Search for Lepton Flavour Violating Processes with Lepton Pairs in pp Collisions at $\sqrt{s} = 13\,\text{TeV}$ with the CMS Experiment at the LHC

Von der Fakultät für Mathematik, Informatik und Naturwissenschaften der RWTH Aachen University zur Erlangung des akademischen Grades eines Doktors der Naturwissenschaften genehmigte Dissertation

vorgelegt von

Sebastian Wiedenbeck, M. Sc. RWTH

aus

Moers

Berichter:
Univ.-Prof. Dr. rer. nat. Thomas Hebbeker
Apl.-Prof. Dr. rer. nat. Oliver Pooth

Tag der mündlichen Prüfung: 06.12.2023

Abstract

This thesis presents the search for lepton flavour violating processes with charged lepton pairs in proton-proton collisions at the center-of-mass energy of 13 TeV. It uses the full Run 2 data collected by the CMS detector at LHC at CERN. The $\mu\tau$ channel was analysed using two different file formats and the different outcomes are compared. As no significant deviations from the Standard Model prediction have been observed in the three channels ($e\mu$, $e\tau$,$\mu\tau$), their mass spectra are used for statistical interpretation, using various models.

For the production of a heavy boson Z', a lower mass limit was set at 5.0, 4.3 and 4.1 TeV at 95 % confidence level (CL) for the $e\mu$, $e\tau$ and $\mu\tau$ channel, respectively. A supersymmetric R-parity violating tau sneutrino with masses up to 2.2 TeV is excluded for the $e\mu$ channel and up to 1.6 TeV in both τ channels, assuming coupling parameters of $\lambda = \lambda' = 0.01$. For $\lambda = \lambda' = 0.1$, the lower limit is set at 4.2, 3.7 and 3.7 TeV for the $e\mu$, $e\tau$ and $\mu\tau$ channel. For the production of Quantum Black Holes with $n = 4$ extra dimensions, masses below 5.6 TeV in the $e\mu$ channel, 5.2 TeV in the $e\tau$ channel and 5.3 TeV in the $\mu\tau$ channel can be excluded.

For the first time, a limit on the pre-exponential factor of the production of a sphaleron has been set in these specific channels at 0.63 for a sphaleron energy of 9 TeV. Additionally, the first model-independent limits for all three channels are presented.

Zusammenfassung

Diese Dissertation präsentiert die Suche nach Lepton Flavour verletzenden Prozessen mit geladenen Leptonpaaren in Proton-Proton Kollisionen bei einer Schwerpunktsenergie von 13 TeV. Sie benutzt den gesamte Datensatz von Run 2, gesammelt am CMS Detektor am LHC am CERN. Der $\mu\tau$ Kanal wurde mit Hilfe zweier unterschiedlicher Dateiformate analysiert und die Ergebnisse werden verglichen. Da keine signifikanten Abweichungen von der Standardmodell-Vorhersage in den drei Kanälen ($e\mu$, $e\tau$,$\mu\tau$) beobachtet wurden, werden die Massenspektra, unter Einbezug verschiedener Modelle, für die statistische Interpretation genutzt.

Für die Produktion eines schweren Bosons Z' wurde ein unteres Massenlimit von 5.0, 4.3 und 4.1 TeV, für den $e\mu$, $e\tau$ und $\mu\tau$ Kanal, mit einem Konfidenzniveau von 95 % gesetzt. Ein supersymmetrisches R-Parität verletzendes Tau Sneutrino kann mit Massen bis 2.2 TeV für den $e\mu$ Kanal und 1.6 TeV für beide τ Kanäle ausgeschlossen werden, unter der Annahme der Kopplungsparameter $\lambda = \lambda' = 0.01$. Die untere Massengrenze für $\lambda = \lambda' = 0.1$ wurde bei 4.2, 3.7 und 3.7 TeV für den $e\mu$, $e\tau$ und $\mu\tau$ Kanal gesetzt. Für die Produktion von mikroskopischen schwarzen Löchern mit $n = 4$ Extradimensionen können Massen unter 5.6 TeV für den $e\mu$ Kanal, 5.2 TeV für den $e\tau$ Kanal und 5.3 TeV für den $\mu\tau$ Kanal ausgeschlossen werden.

Eine obere Ausschlussgrenze für den prä-exponetiellen Faktor der Produktion eines Sphalerons wurde zum ersten Mal in diesen speziellen Kanälen bei 0.63 für eine Sphaleron Energie von 9 TeV gesetzt. Zusätzlich wird das erste Modell-unspezifische Limit für alle drei genannten Kanäle präsentiert.

Eidesstattliche Erklärung

Sebastian Wiedenbeck erklärt hiermit, dass diese Dissertation und die darin dargelegten Inhalte die eigenen sind und selbstständig, als Ergebnis der eigenen originären Forschung, generiert wurden.

Hiermit erkläre ich an Eides statt

- Diese Arbeit wurde vollständig oder größtenteils in der Phase als Doktorand dieser Fakultät und Universität angefertigt;
- Sofern irgendein Bestandteil dieser Dissertation zuvor für einen akademischen Abschluss oder eine andere Qualifikation an dieser oder einer anderen Institution verwendet wurde, wurde dies klar angezeigt;
- Wenn immer andere eigene- oder Veröffentlichungen Dritter herangezogen wurden, wurden diese klar benannt;
- Wenn aus anderen eigenen- oder Veröffentlichungen Dritter zitiert wurde, wurde stets die Quelle hierfür angegeben. Diese Dissertation ist vollständig meine eigene Arbeit, mit der Ausnahme solcher Zitate;
- Alle wesentlichen Quellen von Unterstützung wurden benannt;
- Wenn immer ein Teil dieser Dissertation auf der Zusammenarbeit mit anderen basiert, wurde von mir klar gekennzeichnet, was von anderen und was von mir selbst erarbeitet wurde;
- Ein Teil oder Teile dieser Arbeit wurden zuvor veröffentlicht und zwar in:

  CMS Collaboration, "Search for heavy resonances and quantum black holes in eμ, eτ, and $\mu\tau$ final states in proton-proton collisions at $\sqrt{s}$ = 13 TeV", JHEP 05 (2023) 227, arXiv:2205.06709. DOI: 10.1007/JHEP05(2023)227.

Datum:

_____

Unterschrift:

_____

Contents

1. Introduction **11**

2. Theoretical Foundation **13**
2.1. The Standard Model of Particle Physics . . . 13
2.1.1. Parton Distribution Function . . . 16
2.2. Sphaleron as Non-perturbative Effects in the Electroweak Sector . . . 16
2.3. Beyond the Standard Model . . . 20
2.3.1. Sequential Standard Model (SSM) . . . 20
2.3.2. R-parity violating Supersymmetry (RPV) . . . 21
2.3.3. Quantum Black Holes (QBH) . . . 22
2.4. Existing Limits on Charged Lepton flavour Violation . . . 24
2.4.1. Muon transitions . . . 24
2.4.2. Tau Flavour Violation at Low Masses . . . 24
2.4.3. High Energy Searches . . . 24

3. Experimental Setup **27**
3.1. Large Hadron Collider . . . 27
3.2. Compact Muon Solenoid . . . 29
3.2.1. General Concept . . . 29
3.2.2. Superconducting Magnet . . . 30
3.2.3. Tracker System . . . 30
3.2.4. Calorimeters . . . 32
3.2.5. Muon System . . . 35
3.2.6. Trigger & Data Acquisition . . . 37

4. Particle Reconstruction and Identification **41**
4.1. Tracks . . . 41
4.2. Electron . . . 42
4.2.1. Reconstruction . . . 42
4.2.2. Identification . . . 42
4.2.3. HEEP Identification in 2018 . . . 44
4.3. Muon . . . 44
4.3.1. Reconstruction . . . 44
4.3.2. Identification . . . 45
4.3.3. Isolation . . . 46
4.3.4. Muon Momentum Scale . . . 46
4.4. Tau . . . 47
4.4.1. Jets . . . 47
4.4.2. Reconstruction . . . 48
4.4.3. Identification . . . 50
4.5. $\vec{p}_T^{\,\text{miss}}$ (Missing Transverse Momentum) . . . 51

5. Analysis **55**
5.1. Datasets . . . 55
5.2. Simulation Chain in CMS . . . 56
5.3. Background Description . . . 57
5.4. Signal Production . . . 60
5.4.1. SSM Z′ . . . 60
5.4.2. RPV SUSY . . . 62
5.4.3. QBH . . . 64
5.4.4. Sphaleron . . . 66
5.4.5. Signal Efficiency . . . 69
5.5. Normalization and Corrections . . . 70
5.5.1. Pileup . . . 70
5.5.2. Prefiring . . . 72
5.5.3. Trigger . . . 72
5.5.4. Top Background . . . 72
5.5.5. Object Related Corrections . . . 73
5.6. Discriminating Variable . . . 77
5.7. Mass Resolution . . . 79
5.8. Event selection . . . 80
5.8.1. $\mu\tau$ channel . . . 81
5.8.2. eμ channel . . . 81
5.8.3. eτ channel . . . 82
5.9. Estimation of jet $\rightarrow \tau$ Fake Contribution in the $\mu\tau$ Channel . . . 83
5.9.1. Validation of the fake rate estimation method . . . 85
5.10. Systematic Uncertainties . . . 87
5.11. Kinematic Distributions of the $\mu\tau$ channel . . . 91
5.12. Collinear Mass of the $\mu\tau$ channel . . . 97
5.12.1. Comparison between `NanoAOD` and `MiniAOD` . . . 99
5.13. Mass Distributions of the Electron Channels . . . 101

6. Statistical Interpretation **103**
6.1. Frequentist & Bayesian Statistics . . . 103
6.2. Limit Calculation with Bayesian Statistics . . . 104
6.2.1. Likelihood of a Counting Experiment and Nuisance . . . 105
6.2.2. Markov Chain Monte Carlo . . . 107
6.2.3. Metropolis Hastings Algorithm (MH) . . . 108
6.3. Result of the Statistical Interpretation . . . 109
6.3.1. Impacts . . . 109
6.3.2. Sequential Standard Model . . . 114
6.3.3. R-parity violating Supersymmetry . . . 117
6.3.4. Quantum Black Hole . . . 123
6.3.5. Sphaleron Pre-Exponential Factor . . . 126
6.3.6. Model Independent Limit . . . 128

7. Summary **131**

A. Appendix **133**
A.1. Background Table 133
A.2. $e\tau$ Trigger Scale Factors 135
A.3. Fake Rate for 2016 and 2017 137
A.4. Single Year Distributions 139
A.4.1. 2016 139
A.4.2. 2017 143
A.4.3. 2018 147

Bibliography **151**

1 | Introduction

Physics is driven by the search for answers on how the world around us functions. Over hundreds of years, the knowledge about the universe, how it behaves and what it is made of has grown. But with each answer that is found, new questions arise about the functioning of the world.

The Standard Model (SM) of particle physics offers a well-established and tested description of the physical phenomena at very small magnitudes. Nevertheless, it is not able to explain certain questions and observed behaviour in nature. Thus, particle physicists try to modify and extend the SM which leads to the prediction of "new physics".

This thesis presents the search for such new phenomena in the context of lepton flavour violation (LFV) with the production of lepton pairs. In the SM, the lepton flavour is conserved while no specific underlying principle exists to support this assumption. Measurements of neutrino oscillations indicate that the lepton flavour is not conserved in the neutral sector. Thus, the assumption that it also might be not conserved for charged leptons comes as a natural consequence.

The presented search uses data from proton-proton collisions from the Large Hadron Collider (LHC) at CERN, measured by the Compact Muon Solenoid (CMS) experiment. The center-of-mass energy ($\sqrt{s}$) is at 13 TeV, giving the opportunity to search in a very high energy regime. The combined collected data of Run 2, taken in the years 2016 to 2018, offer an extensive quantity of collected events and might show hints of new physics. The search is divided into three channels, containing either an electron (e) and a muon (μ), an electron and a tau (τ) or a muon and a tau. As the tau decays before reaching the detector, its reconstruction from the measured detector response is challenging.

Multiple theories have been developed that predict lepton flavour violation. This thesis puts focus on the search for a heavy boson Z', predicted by the Sequential Standard Model (SSM), the production and decay of a supersymmetric tau sneutrino with R-parity violation (RPV) and Quantum Black Holes (QBH) with extra dimensions. In addition, a non-perturbative effect in the electroweak sector of the SM, called "sphaleron", is looked at. The choice of models offers a variety of different potential signal shapes of the measured invariant mass of the lepton pairs. They are also used to perform a statistical interpretation of the findings of this search. For the first time in these channels, a model-independent limit will be provided.

Some of the results presented in this thesis have been published in the "Journal of High Energy Physics" (JHEP) as "Search for heavy resonances and quantum black holes in $e\mu$, $e\tau$, and $\mu\tau$ final states in proton-proton collisions at $\sqrt{s} = 13$ TeV" [1]. The author of this thesis is a co-author of the publication. Plots labelled with "*Private Work*" are not part of the publication and are created specifically for this thesis.

This thesis starts with a short introduction into the theoretical foundation of the presented search (Chapter 2). After a short summary of the Standard Model, the non-perturbative effect leading to the sphaleron, as well as the three beyond the Standard Model (BSM) models will be discussed. Afterwards, the experimental setup with the Large Hadron Collider and the Compact Muon Solenoid will be described in Chapter 3. Chapter 4 covers the reconstruction and identification of the objects used in this thesis. After these foundations are established, Chapter 5 will explain the

analysis strategy, containing a description of the relevant background processes and the Monte Carlo simulation. The main focus of this chapter will lie on the $\mu\tau$ channel. The used, specific event criteria are presented and the final distributions of the discriminating variable for all three channels are shown. Chapter 6 will then introduce the methods to interpret the results of the analysis in a statistical sense leading to the exclusion limits for the different interpretations. The thesis ends with a summary of the results in Chapter 7.

2 | Theoretical Foundation

The following chapter will give a short introduction to the theoretical background of this thesis.

The first section will give an overview of the status quo of the theoretical description of elementary particles and their interactions, the so called Standard Model (SM) of particle physics. This theory is one of the most tested theories in physics to date and builds the foundation to existing knowledge of particle physics. Therefore, it is used to describe the background when comparing a measurement to the expectation while searching for new physics deviating from the SM prediction.

The second section will cover a specific solution of the SM which allows the lepton flavour violating (LFV) production of multiple leptons in a regime that is rarely looked at in experimental searches. This section also covers certain theories beyond the Standard Model (BSM) which allow final states with two leptons of different flavours due to LFV. These particular theories are usually additions to the SM rather than fully independent models. The choice of these models is motivated by the different expected signal shapes that they produce, as well as by already existing searches to make the results of this thesis comparable.

The introduction to the SM will mostly be based on "Introduction to Elementary Particles" by David Griffith [2]. Quantities coming from measurements, like particle masses or lifetimes, are taken from "The Review of Particle Physics" in its latest version [3].

Throughout this thesis, the unit system commonly employed in particle physics will be used. Energies will be given in terms of electron volts ($1\,\text{eV} = 1.60218 \cdot 10^{-19}\,\text{J}$). Planck's constant ($\hbar = 6.58212 \cdot 10^{-22}\,\text{MeV s}$) and the speed of light ($c = 2.99792 \cdot 10^{8}\text{m/s}$) are set to 1. Thus, properties like the momentum or the mass of a particle are also given in the unit of eV. The electric charge will be given in terms of the elementary charge ($e = 1.60218 \cdot 10^{-19}\,\text{C}$).

2.1 The Standard Model of Particle Physics

The Standard Model (SM) of particle physics describes the fundamental particles that we know of today and the interactions between them. Fundamental, in this context, means that it is assumed that such particles are not a composition of particles. The present form of the SM dates back to the 1960's when the latest addition, the Higgs boson, was added to the particle zoo [4–6] as a possible explanation on how masses are created in the Standard Model. It was first observed at the LHC by the CMS and the ATLAS experiments in 2012[1] [7,8]. The SM content can be divided into two groups: fermions, with half-integer spin, and bosons, with integer spin. The bosons are mediators of the interactions between the particles whereas fermions build up the matter in our universe.

The group of fermions is made up of 12 distinct particles, namely six quarks and six leptons. The leptons can be further grouped by their electric charge Q and their lepton family number, also called *lepton flavour*, L. The charged leptons are the electron e, muon μ and tau τ with their uncharged electron neutrino ν_e, muon neutrino ν_μ and tau neutrino ν_τ. The grouping of

[1] More information about these experiments can be found in Chapter 3

a charged lepton with its corresponding same-flavour neutrino is also called generation. The leptons can be seen in Table 2.1.

Table 2.1.: The three lepton generations of the SM with their corresponding charge Q, lepton number L and masses. (Values taken from [3])

particle	Q (e)	L_{family}	mass
e	-1	$L_e = 1$, $L_\mu = L_\tau = 0$	$\approx 0.511\,\text{MeV}$
ν_e	0	$L_e = 1$, $L_\mu = L_\tau = 0$	$< 1.1\,\text{eV}$
μ	-1	$L_\mu = 1$, $L_e = L_\tau = 0$	$\approx 105.66\,\text{MeV}$
ν_μ	0	$L_\mu = 1$, $L_e = L_\tau = 0$	$< 0.19\,\text{MeV}$
τ	-1	$L_\tau = 1$, $L_e = L_\mu = 0$	$\approx 1776.86\,\text{MeV}$
ν_τ	0	$L_\tau = 1$, $L_e = L_\mu = 0$	$< 18.2\,\text{MeV}$

The quarks can also be divided into three generations. The first generation contains the d (down) and the u quark (up). The s (strange) and the c quark (charm) are part of the second generation while the b (bottom) and the t quark (top) quark define the third generation. The d, s and b quark carry an electric charge of $-\frac{1}{3}e$ whereas the u, s and t carry $\frac{2}{3}e$. The properties of the quarks are summarized in Table 2.2. Unlike leptons, quarks carry a colour charge and take part in the strong interaction, mediated by the gluon g.

Fermions that carry an electric charge participate in the electromagnetic interaction via the photon γ as a mediator. Furthermore, all fermions take part in the weak interaction via its corresponding mediators, the $W^\pm$ and Z bosons. The interaction of the particles with the Higgs field via the Higgs boson creates the masses in the SM. The photon and the gluon do not interact with the Higgs field and therefore do not carry any mass. The bosons of the Standard Model with their corresponding masses can be found in Table 2.3.

Table 2.2.: The three quark generations of the SM with their corresponding charges Q and masses. (Values taken from [3])

particle	Q (e)	mass
up (u)	$2/3$	$\approx 2.3\,\text{MeV}$
down (d)	$-1/3$	$\approx 4.8\,\text{MeV}$
charm (c)	$2/3$	$\approx 1275\,\text{MeV}$
strange (s)	$-1/3$	$\approx 95\,\text{MeV}$
top (t)	$2/3$	$\approx 173200\,\text{MeV}$
bottom (b)	$-1/3$	$\approx 4180\,\text{MeV}$

Each particle in the SM has its corresponding anti-particle, which carries the same mass but opposite charges. In the SM, there is no mechanism to give mass to neutrinos, which also means that the lepton numbers are assumed to be conserved. But the observation of neutrino oscillations shows that neutrinos carry a non-zero mass indicating that the lepton flavour number conservation is in fact violated [9–12]. This is a strong motivation for the search for lepton flavour violating processes as well as to look for possible extensions to the SM to explain the observations.

The SM is constructed as a quantum field theory (QFT) where the particles mentioned above

Table 2.3.: The different bosons of the Standard Model as the mediating particles with their electric charge and their masses. (Values taken from [3])

Boson	Q (e)	mass
photon γ	0	0
gluon g	0	0
$W^{\pm}$	± 1	$\approx 80.4\,\text{GeV}$
Z	0	$\approx 91.2\,\text{GeV}$
Higgs H	0	$\approx 125.7\,\text{GeV}$

are quanta of their corresponding quantum fields. The underlying structure is a gauge theory with the groups $SU(3)_C \times SU(2)_L \times U(1)_Y$ with the colour charge C, weak isospin L and weak hypercharge Y. An invariance under a local gauge transformation then gives rise to a corresponding interaction in this formalism.

$SU(2)_L \times U(1)_Y$ are the unification of the weak and the electromagnetic interaction. It contains four massive fields, of which two are charged, the W^1 and W^2, and two are neutral, the W^3 and B. These fields combine as linear combinations to the gauge fields:

$$A = B\cos(\theta_w) + W^3\sin(\theta_w,) \tag{2.1}$$

$$Z = -B\sin(\theta_w) + W^3\cos(\theta_w), \tag{2.2}$$

$$W^{\pm} = \frac{1}{\sqrt{2}}(W^1 \mp iW^2). \tag{2.3}$$

The field A corresponds to the electromagnetic field and gives rise to the photon γ while Z and $W^{\pm}$ are the weak bosons as they appear in nature. They as well take part in the weak interaction and therefore couple to themselves. The appearance of the gauge fields through linear combinations is the consequence of something called *spontaneous symmetry breaking*. To give particles masses in the SM, Brout, Englert and Higgs as well as Guralnik, Hagen and Kibble proposed the addition of a scalar field ϕ, the Higgs field [4–6]. The ground vacuum state of this field does not share the same symmetry as the underlying Lagrangian, thus breaking the symmetry. The interaction of the corresponding spin-0 Higgs boson then solves the problem of the existence of heavy bosons and massive fermions whereas the gluon and the photon do not interact with the Higgs field and therefore stay massless.

$SU(3)_C$ corresponds to quantum chromodynamics (QCD), where the invariance gives rise to the gluon. Since it carries a colour charge, it interacts with itself. The coupling α_s of the strong interaction increases as the interacting particles get further apart. This leads to a rise in the energy of the system to a point at which new quark-antiquark pairs are created. As a result of this effect called *confinement*, only colourless particle combinations are stable, meaning that no free quarks appear in nature. At very short distances, α_s decreases for increasing momenta and quarks behave similarly to free particles, e.g. at hadron colliders.

Calculations of cross sections σ of SM processes are usually done using perturbation theory. The first order value of the perturbation series, also called *leading-order (LO)*, of the corresponding coupling usually dominates the calculation. Continuing to higher orders (*next-to-leading order (NLO)*, *next-to-next-to-leading order (NNLO)*,...) adds corrections to the LO calculation. In Feynman

calculus, this is equivalent to adding more Feynman diagrams containing additional higher-order contributions to the process.

2.1.1 Parton Distribution Function

As this thesis uses experimental data from proton-proton collisions, the colliding particles are not of fundamental nature but a composition of quarks. The constituents of the proton take part in *deep inelastic scattering* and do not carry the full beam energy E_{beam}. Thus, the center-of-mass energy of such a collision of two so called partons (quarks or gluons) is:

$$\sqrt{\hat{s}} = \sqrt{x_1 x_2 s}, \tag{2.4}$$

with s being the center-of-mass energy($\sqrt{s} = 2E_{beam}$) of the proton-proton collision and x_1 and x_2 are the momentum fractions of the partons. This also means that the initial energy of the parton is not known. To still have a theoretical description of the process one uses the probability that a parton carries a fraction x of the available momentum at the momentum scale Q^2. The cross section for a hard process, a process of high momentum transfer at the high energy regime where quarks can be approximated as free particles, and can be calculated by [13, 14]:

$$\sigma(P_1, P_2) = \sum_{i,j} \int_0^1 dx_1 \int_0^1 dx_2 f_i(x_1, Q^2, \mu_F) f_j(x_2, Q^2, \mu_F) \hat{\sigma}_{i,j}(x_1 P_1, x_2 P_2, Q^2, \alpha_s(\mu_R)). \tag{2.5}$$

It sums over all initial parton states (i, j) and integrates over the *parton distribution function* (PDF) $f_{i,j}$, which describes the probability to obtain a parton at a momentum scale Q^2 with a certain momentum fraction x, and the parton-level-cross section $\hat{\sigma}$. P_1 and P_2 indicate the four momenta of the initial hadrons. To avoid ultraviolet divergences due to loop integration and infrared divergences, arising in the amplitude calculation when massless particles radiate additional massless particles, the PDF additionally depends on the factorization scale μ_F and the renormalization scale μ_R.

The PDF dependency on the variable x can not be determined from theory itself and thus needs to be derived from data. Multiple measurements from different experiments like HERA [15] and LHC [16–18] are combined from different groups to provide an accurate description of the PDF, some of which use modern deep neural network approaches for higher accuracy [19]. One issue with the latter approach is a lack of data in the very high energy regime. As the neural network needs a significant amount of data in the specific region to offer an accurate description, neural network driven PDF sets have shown some issues with unphysical (e.g. negative cross sections) for high energies [20].

2.2 Sphaleron as Non-perturbative Effects in the Electroweak Sector

As mentioned in the last section, calculations in the SM are mostly done using perturbation theory. But additionally, a quantum field theory can also contain non-perturbative effects. In the electroweak sector, one of these effects predicts a violation of the Baryon and the Lepton number. This effect was first described in 1975 which predicts a new particle called *instaton* [21].

A simplified version of the electroweak Lagrangian is [22]:

$$\mathcal{L} = -\frac{1}{2}\mathrm{Tr}[F_{\mu\nu}F^{\mu\nu}] + \frac{1}{2}(D_\mu\Phi)^\dagger D^\mu\Phi - \frac{\lambda}{4}(\Phi^\dagger\Phi - v^2)^2 + i\bar{\psi}_L^{(i)}\gamma^\mu D_\mu\psi_L^{(i)}, \tag{2.6}$$

with

$$\begin{aligned} F^a_{\mu\nu} &= F^a_{\mu\nu}\frac{\sigma^a}{2} = \partial_\mu A_\nu - \partial_\nu A_\mu - ig\left[A_\mu, A_\nu\right], & (2.7)\\ D_\mu\Phi &= \partial_\mu\Phi - igA_\mu\Phi, & (2.8)\\ D_\mu\psi_L^{(j)} &= \partial_\mu\psi_L^{(j)} - igA_\mu\psi_L^{(j)}, & (2.9) \end{aligned}$$

where $A_\mu(x) = A^a_\mu\frac{\sigma^a}{2}$. A^a_μ are the $SU(2)$ weak interaction gauge fields with $a = 1,2,3$ and σ^a are the three Pauli matrices. $\Phi(x)$ is the doublet Higgs field and $\psi_L^{(j)}$ are the left-handed fermion doublets with $j = 1,2,...,12$. Classically, this produces 12 conserved $U(1)$ currents $J^{(j)\mu}$, but a presence of an anomaly breaks this conservation:

$$\partial_\mu J^{(j)\mu} = \frac{g^2}{16\pi^2}\mathrm{Tr}\left[F_{\mu\nu}\tilde{F}^{\mu\nu}\right]. \tag{2.10}$$

Here, $\tilde{F}^{\mu\nu} = \frac{1}{2}\epsilon^{\mu\nu\lambda\gamma}F^{\lambda\gamma}$ [21]. With the instaton solution one can define:

$$N = \frac{g^2}{16\pi^2}\int d^4x\mathrm{Tr}\left[F_{\mu\nu}\tilde{F}^{\mu\nu}\right], \tag{2.11}$$

where N is often called the *Chern-Simons-Number (CS)* or N_{CS}. For the instaton, this number is an integer and describes the tunnelling from one potential minimum to another minimum with a change ΔN of the CS number. A change in the CS number thus leads to a change in the lepton number L of

$$\Delta N_e = \Delta N_\mu = \Delta N_\tau = \Delta N \tag{2.12}$$

and a change in the baryon number B by

$$\Delta B = 3\Delta N \tag{2.13}$$

as each quark has $B = \frac{1}{3}$ times a factor of three for the existing families and the three colours. As the electric charge is still conserved, the final changes can be written as:

$$\begin{aligned} \Delta(B+L) &= 6\Delta N, & (2.14)\\ \Delta(B-L) &= 0. & (2.15) \end{aligned}$$

Another possible solution is called the *sphaleron* [23–25], which describes a static, unstable solution not tunnelling through the potential barrier. The sphaleron therefore describes the peak of the potential. A transition like this can be modelled by a one-dimensional Schrödinger equation [22]

$$\left(-\frac{1}{2m}\frac{\partial^2}{\partial Q^2} + V(Q)\right)\psi(Q) = E\psi(Q), \tag{2.16}$$

where $Q = \mu/m_W$ is used to redefine the CS number to μ/π. μ is a number defined by $N\mu = \mu - \sin(2\mu)/2$ and m corresponds to an effective mass parameter and m_W to the W boson mass. This parametrization leads to an effective potential of [22]:

$$V(Q) \simeq 4.75\,\text{TeV}\left(1.31\sin^2(m_W Q) + 0.60\sin^4(m_W Q)\right), \tag{2.17}$$

with

$$E_{sph} = \max\left[V(Q)\right] = V\left(\frac{\pi}{2m_W}\right) = 9.11\,\text{TeV}. \tag{2.18}$$

The potential $V(Q)$ can be seen in Figure 2.1. It shows the periodic structure of the potential with its maxima, corresponding to the sphaleron, at $N = \mu/\pi + 1/2$ with a height of $E_{sph} = V\left(\frac{\pi}{2m_W}\right) = 1.91 \cdot 4.75\,\text{TeV} \approx 9\,\text{TeV}$. This periodic nature of the Cherm-Simons potential leads to a reduced suppression of the production cross section at energies $< E_{sph}$ with no suppression at all at energies $\geq E_{sph}$ [26]. This opens up the opportunity to observe sphaleron transitions with colliders like the LHC. With a change in the CS number of -1, a sphaleron process induced by parton scattering would create a high multiplicity final state:

$$qq \to \bar{\ell}_e\bar{\ell}_\mu\bar{\ell}_\tau\bar{q}\bar{q}\bar{q}\bar{q}\bar{q}\bar{q}\bar{q} + X, \tag{2.19}$$

with one anti-lepton for each generation and nine anti-quarks, one for each generation and colour. Two anti-quarks annihilate with the two initial quarks, leaving only seven anti-quarks in the final state plus an undefined number of particles X. These particles fulfil $B = L = 0$, and carry a certain electric charge such that the electric charge is conserved in the process. A specific $\Delta N = +1$ process could be:

$$u + u \to \nu_e\mu^-\tau^- tbbcscduu + uu + X, \tag{2.20}$$

resulting in a lepton flavour violating final state of a μ and a τ plus additional particles.

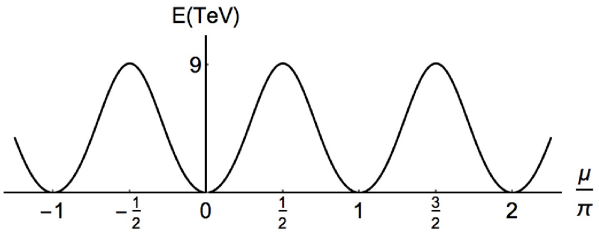

Figure 2.1.: Potential $V(Q)$ of the sphaleron process with an $E_{sph} = 9\,\text{TeV}$, corresponding to the barrier height of the potential. The maxima of the potential are at $\frac{\mu}{\pi} = \frac{1}{2}, \frac{3}{2}, \frac{5}{2}, \ldots$ (taken from [22]).

The cross section of a sphaleron process at the LHC can be described by the parametrization [26]:

$$\sigma(\Delta N_{CS} = \pm 1) = \frac{p}{m_W^2}\sum_{ab}\int dE\frac{d\mathcal{L}_{ab}}{dE}\exp\left(c\frac{4\pi}{\alpha_W}S(E)\right), \tag{2.21}$$

where $\frac{d\mathcal{L}_{ab}}{dE}$ is defined as:

$$\frac{d\mathcal{L}_{ab}}{dE} = \frac{2E}{E_{CM}^2} \int_{\ln\sqrt{\tau}}^{-\ln\sqrt{\tau}} dy f_a\left(\sqrt{\tau}e^{y}\right) f_b\left(\sqrt{\tau}e^{-y}\right), \tag{2.22}$$

with the parton distribution function $f(x)$ of the colliding quarks (a,b) at the momentum fraction x. The variable τ is defined as E^2/E_{CM}^2 with E_{CM} being the center-of-mass energy and α_W is the weak coupling constant and $c \approx 2$. Moreover, S(E) is defined as:

$$S(E) = (1-a)\hat{E} + a\hat{E}^2 - 1, \tag{2.23}$$

for $0 \leq \hat{E} \leq 1$ with $\hat{E} \equiv \frac{E}{E_{\text{Sph}}}$ and $a = -0.005$. For $\hat{E} > 1$, $S(E) = 0$, describing the suppression of the sphaleron production for energies smaller than E_{sph}. The parameter p is called *pre-exponential factor* and is unknown. It can be understood as the ratio of produced sphalerons compared to all final states of the proton-proton collision.

2.3 Beyond the Standard Model

Even though the Standard Model provides an extensive description of our world and has been tested to tremendous precision so far, there are multiple phenomena that can not be explained by the SM in its current form.

One observation that is not in agreement with the Standard Model has been already mentioned in Section 2.1, namely the findings of neutrino oscillations, which point to a violation of the lepton flavour number conservation.

Additionally, in the SM, it is assumed that the gauge coupling of the three different lepton generations is the same which is called *lepton universality*. Measurements from *BABAR* [27, 28], *Belle* [29–31] and *LHCb* [32–34] show tension in the Standard Model prediction of the ratio of the decay rates of B-hadrons into D-mesons [35]. The average measurement over the three experiments shows a deviation of 3.3σ compared to the Standard Model calculation. Adding new measurements from *LHCb* [36, 37], a new preliminary result of this average updated this value to 3.2σ. Previous measurements by the *LHCb* experiment of the decay rate ratio of B-hadrons into K-mesons have shown similar tensions [38, 39] but the latest updated results, containing data taken between 2011 and 2018, are consistent with the SM prediction with a maximum difference of 1σ [40].

Another problem that so far is not understood is the so called *hierarchy problem* of the Standard Model. It raises the question of why the gravitational force is much weaker than, for example, the weak force. It is actually expected that the Higgs mass lies close to the Planck mass ($\mathcal{O}(10^{19})$ GeV) instead of 125 GeV. This is solved by additional loop diagrams that lead to cancellations but involves the usage of specifically tuned parameters (*fine-tuning*).

To conquer these, and other, problems of the Standard Model, many additions to the SM, so called *Beyond the Standard Model* (BSM) theories have been developed. The following subsections will cover the three used examples in this thesis that lead to a final state with two charged leptons of different flavours under the assumption of lepton flavour violation.

2.3.1 Sequential Standard Model (SSM)

One possible extension to the Standard Model is the addition of an extra $U(1)$ gauge symmetry which leads to the creation of a neutral massive vector boson often called Z' [41]. Various different models can predict the production of this type of particle.

In most searches, the Sequential Standard Model (SSM) is chosen as a benchmark model to test for the existence of the Z' [42]. In this scenario, the new heavy vector boson has the same properties as the SM Z partner except for its mass, that can result in a resonant production of the vector boson. In this thesis, the coupling κ_{ij} (ij stands for the different lepton flavours) is also modified allowing only charged lepton flavour violating decays. For each channel, κ is set to 1 for the combination of leptons looked at ($e\mu$, $e\tau$ and $\mu\tau$) and to 0 for the others. Regarding the production, all quark flavour combinations that are in agreement with the conservation laws known from the SM are allowed. Figure 2.2 shows the production of the Z' boson and the decay into a pair of leptons via lepton flavour violation.

The branching ratio $\mathcal{B}$ into the leptonic channels is set to 10% and is assumed to stay constant over the whole mass range with a decay width of $\approx 3\% \cdot M_{Z'}$, similar to the SM Z.

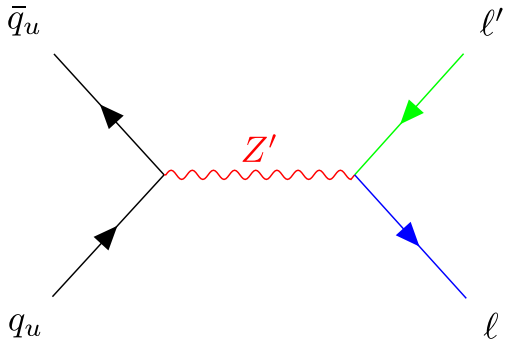

Figure 2.2.: Feynman diagram of the production of an SSM massive vector boson Z' decaying via lepton flavour violation into a pair of leptons of different flavour.

2.3.2 R-parity violating Supersymmetry (RPV)

Instead of adding only one partner to a SM particle in the SSM, in the Minimal Supersymmetric Standard Model (MSSM) each Standard Model particle gets its supersymmetric partner [43]. Supersymmetry (SUSY) can solve multiple problems with the SM, including the hierarchy problem and the existence of dark matter. This is one of the reasons that supersymmetry became a famous and promising addition to the SM, especially prior to the data taking at the LHC.

As mentioned above, in the MSSM each SM particle gets its own supersymmetric partner creating a spin symmetry. This means that each half integer spin particle has an integer spin supersymmetric partner and each integer spin particle a half integer partner. Therefore, each SM fermion has a bosonic SUSY partner and vice versa. Supersymmetric partner particles of the fermions are usually called *sparticles*, while the partners of the bosons end with "ino" (e.g. *Gluino*).

Since no *sparticle* has been observed to date, it can be assumed that SUSY is actually a broken symmetry as the masses of the SUSY partners seem to differ significantly from the SM particles.

Usually, in the most general and renormalizable supersymmetric models a problem arises as they introduce interactions that violate the lepton number as well as the baryon number [43]. The latter would open up the possible decay of the proton which is strongly constrained by experimental measurements [3]. This is solved by introducing a new symmetry called R-parity which eliminates the violating terms:

$$R = (-1)^{3(\mathrm{B}-\mathrm{L})+2\mathrm{s}} \tag{2.24}$$

with s being the spin of the particle, B being the baryon and L being the lepton number. This thesis assumes that the R-parity actually is not conserved which leads to R-parity violation (RPV). This creates three different couplings in the MSSM superpotential, namely λ, λ' and λ''. λ and λ' lead to the violation of the lepton number, whereas the λ'' coupling introduces baryon number violation to the superpotential. To ensure the stability of the proton, the introduction of a discrete symmetry called *Baryon Triality Symmetry* B_3 [44] is used, cancelling out the λ'' terms, leading to the final trilinear part of the superpotential [45]:

$$W_{RPV} = \frac{1}{2}\lambda_{ijk} L_i L_j \bar{E}_k + \lambda'_{ijk} L_i Q_j \bar{D}_k, \tag{2.25}$$

where i,j and k describe the generation of the particles, L and Q are the doublet superfields of the leptons and quarks and $\bar{E}_k$ and $\bar{D}_k$ are the singlet superfields of the charged leptons and down-type quarks.

For simplicity and comparability to earlier analyses, the RPV SUSY model used in this thesis allows the resonant, lepton flavour violating production of a single sparticle from SM particles via the λ'_{ijk} coupling by down-type quarks. The produced sparticle is the τ sneutrino, as it provides a valid candidate for the lightest supersymmetric particle (LSP) [46]. Thus, the produced sparticle can only decay into SM particles, either into leptons via the λ_{i3k} coupling or into quarks via λ'_{i3k}. Additionally, to be comparable with [47], λ_{i3k} and λ_{k3i} are assumed to be the same for all leptons and that the τ sneutrino decays promptly. All other RPV couplings are assumed to vanish. A Feynman diagram of this τ sneutrino production and the subsequent decay can be seen in Figure 2.3.

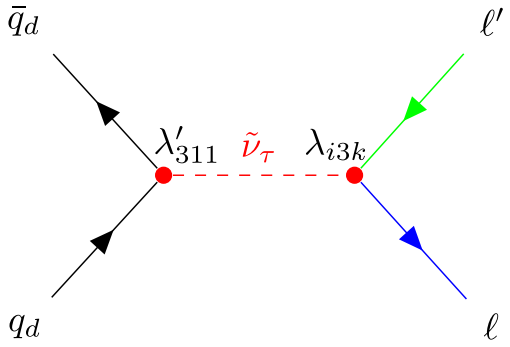

Figure 2.3.: Feynman diagram of the production of a τ sneutrino from two down quarks via λ'_{311} with a decay into a lepton pair of different flavour via λ_{i3k}.

Using the narrow-width approximation[2], the cross section times branching ratio scales with the couplings [48]:

$$\sigma(pp \to \tilde{\nu}_\tau) \times \mathcal{B}(\tilde{\nu}_\tau \to \ell_i \ell_k) \propto \frac{(\lambda'_{311})^2 \left((\lambda_{i3k})^2 + (\lambda_{k3i})^2\right)}{3(\lambda'_{311})^2 + \left((\lambda_{i3k})^2 + (\lambda_{k3i})^2\right)}. \tag{2.26}$$

2.3.3 Quantum Black Holes (QBH)

Another way to extend the SM is to allow the production of black holes at hadron colliders. Trying to unify electromagnetism with gravity, which is described by *General Relativity*, Kaluza and Klein added an additional spatial dimension to the four dimensional space-time [49]. The addition of extra dimensions creates the opportunity of observable quantum gravity effects. For example, Arkani-Hamed, Dimopoulos, Dvali and Kaloper developed a model (ADD) which contains $n > 1$ compact extra dimensions with radii R of $\sim 1\,\text{mm}$ [50]. This leads to the reduction of the Planck Scale M_P to the reduced Planck Scale $M_D \sim 1(\text{TeV})$, where the classical Planck scale represents the strength of gravity observed in three spatial dimensions [51].

[2]The narrow-width approximation assumes, that the width of the decays is negligible compared to the detector resolution (see Section 5.4.2).

A Planck scale of the order of M_D opens up the production of black holes at hadron colliders if the energy is greater than the gravity scale. For $\sqrt{s} \gg M_P$, they are described as semi-classical black holes. If the impact parameter is smaller than the Schwarzschild radius r_S, the production cross section of such black holes follows $\sigma \sim \pi r_S^2$ [52]. These black holes create final states of high multiplicity by Hawking radiation. As it would need multiple M_D to produce semi-classical black holes and only a fraction of the initial energy is available for the scattering partons, the PDF is falling fast and an observation of these types of black holes at the LHC is considered unlikely [52, 53].

Instead, *quantum black holes* (QBH) can be produced at scales around M_D and are expected to have final states of low multiplicity (two or three particles in the final state) [54]. The ADD model predicts the production of QBH under the assumption of $n \geq 2$ with $M_P^2 \sim r_n^n M_{D(4+n)}^{n+2}$, where $M_{D(4+n)}$ is the reduced Planck scale with n extra dimensions and r_n is the size of the extra dimensions [50]. For $n = 2$, the size is $\sim 1\,\text{mm}$. By assuming that QBH behave similar to semi-classical black holes with vanishing significance of radiation the cross section of QBH production at proton-proton collisions can be written as [54]:

$$\sigma^{pp} = \int_0^1 2z dz \int_{\frac{(x_{min} M_D)^2}{y(z)^2 s}}^1 du \int_u^1 \frac{dv}{v} \times F(n) \pi r_s^2(us, n, M_D) \sum_{i,j} f_i(v, Q) f_j(u/v, Q), \tag{2.27}$$

with $z = b/b_{max}$, $x_{min} = M_{BH,min}/M_D$ and $F(n)$ and $y(z)$ being additional factors coming from the calculation of classical black holes at high energy collisions [55]. Their values are calculated in [56]. f_i and f_j are again the parton distribution functions with momentum fractions u and v and momentum transfer Q. The Schwarzschild radius r_s is given by:

$$r_s(us, n, M_D) = k(n) M_D^{-1} \left[\sqrt{us}/M_D\right]^{1/(1+n)}, \tag{2.28}$$

with

$$k(n) = \left[2^n \sqrt{\pi}^{n-3} \frac{\Gamma(3+n)/2}{2+n}\right]^{1/(1+n)}. \tag{2.29}$$

As mentioned before, a similar behaviour of the QBH compared to the semi-classical black hole is assumed for this calculation. $M_{BH,min}$ is then the minimal black hole mass at which this extrapolation holds.

A diagram of the QBH production with a final state of exclusively two charged leptons with different flavour can be seen in Figure 2.4.

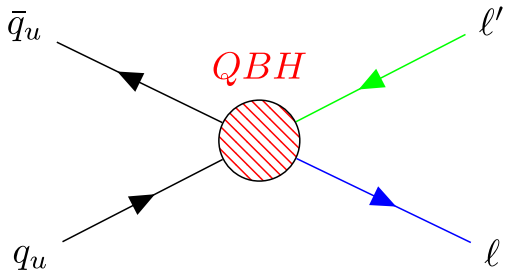

Figure 2.4.: Diagram of the production of a quantum black hole from two up quarks which then decays into a lepton pair of different flavour.

2.4 Existing Limits on Charged Lepton flavour Violation

The search for charged lepton flavour violation has a long history in experiments as the underlying conservation results from an assumption that neutrinos are massless. Additionally, as shown before, even calculations in the framework of the SM can lead to LFV processes. This section summarizes some of the searches for charged LFV and their experimental results using [3] and [57] as guidelines.

2.4.1 Muon transitions

The main transitions for lepton flavour violation in muon decays are $\mu^+ \to e^+\gamma$, $\mu^+ \to e^+e^-e^+$ and $\mu^- N \to e^- N$, where the latter describes the muon conversion in the presence of a nucleus N:

- $\mu^+ \to e^+\gamma$: The best limit on the branching ratio ($\mathcal{B}$) is set at $\mathcal{B}(\mu^+ \to e^+\gamma) < 4.2 \times 10^{-13}$ at a confidence level of 90% by the MEG experiment [58]. Future updates are expected to push this limit below $\mathcal{O}(10^{-14})$ [59].
- $\mu^+ \to e^+e^-e^+$: The SINDRUM experiment set a limit to the branching ratio at $\mathcal{B}(\mu^+ \to e^+e^-e^+) < 1.0 \times 10^{-12}$ [60]. The future Mu3e experiment plans to exclude branching fractions above $\mathcal{O}(10^{-16})$ [61].
- $\mu^- N \to e^- N$: In the search for the muon conversion into an electron, an experimental bound is set on the conversion rate compared to the regular muon capture:

$$R_{\mu e} = \frac{\Gamma(\mu^- + N(A,Z) \to e^- + N(A,Z))}{\Gamma(\mu^- + N(A,Z) \to \text{all captures})} \tag{2.30}$$

  with A and Z being the mass and the atomic number of the target nucleus, respectively.

  The current limit is set at $R_{\mu e} < 7 \times 10^{-13}$ at 90% CL by the SINDRUM-II experiment [62]. The Mu2e experiment, currently in construction, plans to reach a sensitivity of $\approx 3 \times 10^{-13}$ [63] while the COMET collaboration aims for $\mathcal{O}(10^{-15})$ [64].

2.4.2 Tau Flavour Violation at Low Masses

The upper limits on the branching fractions of lepton flavour violation including a tau (e.g. $\mathcal{B}(\tau \to \mu^-\mu^+\mu^-)$ or $\mathcal{B}(\tau \to e^-\pi^0)$) are mainly coming from the BaBar experiment [65–70], the Belle experiment [71–79] and the LHCb experiment [80, 81] and are of the order of 10^{-8} to 10^{-7} at 90 % CL. Future upgraded detectors at the LHC at 14 TeV are expected to reach a sensitivity of $\mathcal{O}(10^{-9})$ for the $\tau^- \to \mu^-\mu^+\mu^-$ branching fraction [82–84].

2.4.3 High Energy Searches

Searches at the high energy regime include Z and Higgs boson decays as well as top decays and BSM searches:

- **Z boson:** Lepton flavour violating Z boson decays have been looked for at LEP [85, 86] and the ATLAS experiment [87–89]. The limit on the branching ratio $\mathcal{B}(Z \to \ell\ell')$ was set at $0.75 - 5.0 \times 10^{-6}$ for the $e\mu$, $e\tau$ and $\mu\tau$ final states at 95 % confidence level.

- **Higgs boson:** The LFV decay of the Higgs boson into lepton pairs has been looked at by the CMS collaboration for the $e\tau$ and $\mu\tau$ final state and the ATLAS collaboration for the $e\mu$ final state. The limit for the $e\mu$ channel has been set at $\mathcal{B}(\mathrm{H} \to e\mu) < 6.1 \times 10^{-5}$ [90], at $\mathcal{B}(\mathrm{H} \to e\tau) < 2.2 \times 10^{-3}$ for the $e\tau$ channel and $\mathcal{B}(\mathrm{H} \to \mu\tau) < 1.5 \times 10^{-3}$ [91] for the $\mu\tau$ channel at 95 % CL, using full Run 2 data.
- **top quark:** The CMS collaboration has set limits on the $t \to u\mu e$ and $t \to c\mu e$ channels at the order of 10^{-7} and 10^{-6} at 95 % CL [92].
- **BSM searches:** Direct searches for the Z′ at the LHC have set upper limits at 95 % CL in the mass of the new heavy boson for the $e\mu$ channel by the CMS collaboration at 4.4 TeV [93] and for the $e\mu$, $e\tau$ and $\mu\tau$ channel by the ATLAS collaboration at 4.5 TeV, 3.7 TeV and 3.5 TeV [47], respectively.

  Searches for Quantum Black Holds of both collaborations set upper limits at 95 % CL on the threshold mass for $n = 4$, in the $e\mu$ channel at 5.3 TeV [93] and, for $n = 6$, at 5.6, 4.9 and 4.5 TeV for all three channels.

  Additionally, upper limits at 95 % CL on the mass of the tau sneutrino for the RPV SUSY model were set by the CMS collaboration at 1.7 TeV, for $\lambda = \lambda' = 0.01$, for the $e\mu$ channel [93]. The ATLAS collaboration sets limits at 3.4, 2.9 and 2.6 TeV, for $\lambda'_{311} = 0.11$ and $\lambda = 0.07$, at 95 % CL for the $e\mu$, $e\tau$ and $\mu\tau$ final state [47].
- **Sphaleron:** A high-multiplicity search from the CMS collaboration has set an upper limit on the pre-exponential factor of the sphaleron production at 0.021 at 95 % CL for a sphaleron energy of $\mathrm{E_{Sph}} = 9$ TeV [94].

3 | Experimental Setup

3.1 Large Hadron Collider

The Large Hadron Collider (LHC) is a particle collider located at the European Organization for Nuclear Research (CERN[1]) between Lake Geneva in Switzerland and the French Jura mountains [95]. It is built inside the tunnel of the discontinued Large Electron-Positron (LEP) collider with a circumference of about 26.7 km at a depth of 50 to 175 m below the surface [96]. It is designed for proton-proton collisions with a beam energy of 7 TeV per nucleus, resulting in a center-of-mass energy of 14 TeV, and for heavy ion collisions with a beam energy of 2.76 TeV per nucleon, yielding a center-of-mass energy of 1.15 PeV for Pb-Pb collisions.

To reach these energies, the LHC relies on a chain of multiple accelerators. Until November 2018, the injected protons started at the Linear Accelerator 2 (Linac2), which accelerated particles to an energy of up to 50 GeV. After reaching that energy, they pass the Booster and the Proton Synchrotron (PS) where they reach energies up to 25 GeV. The last step in the chain, before the proton bunches get injected into the LHC, is the Super Proton Synchrotron (SPS). After passing this pre-accelerator, the proton bunches reach an energy of up to 450 GeV. They are then injected into the LHC where they reach their final energy of up to 7 TeV.

The first full data taking period at the LHC took part from the years 2009 to 2013 and is called Run 1, running at a center-of-mass energy of 7 TeV. In the following run period, Run 2, the beam energy was risen to 6.5 TeV, resulting in a center-of-mass energy of 13 TeV.

Around the LHC ring, four experiments are installed at the collision points of the accelerator. Firstly, there are two "general purpose" detectors which are designed to cover a wide range of measured particles and tested processes: the A Toroidal LHC ApparatuS (ATLAS) [97] and the Compact Muon Solenoid (CMS) detector [98]. The latter will be discussed in more detail in the following section. The other two are the A Large Ion Collider Experiment (ALICE) detector [99], which main focus lies on the measurements in connection with the strong force using collisions of heavy irons, and LHCb [100], an experiment dedicated to rare B decays and measurements of CP violation.

The whole accelerator complex located at CERN with the different facilities can be seen in 3.1.

[1] The acronym "CERN" originates from the french name "Conseil européen pour la recherche nucléaire" of the founding council of the organization

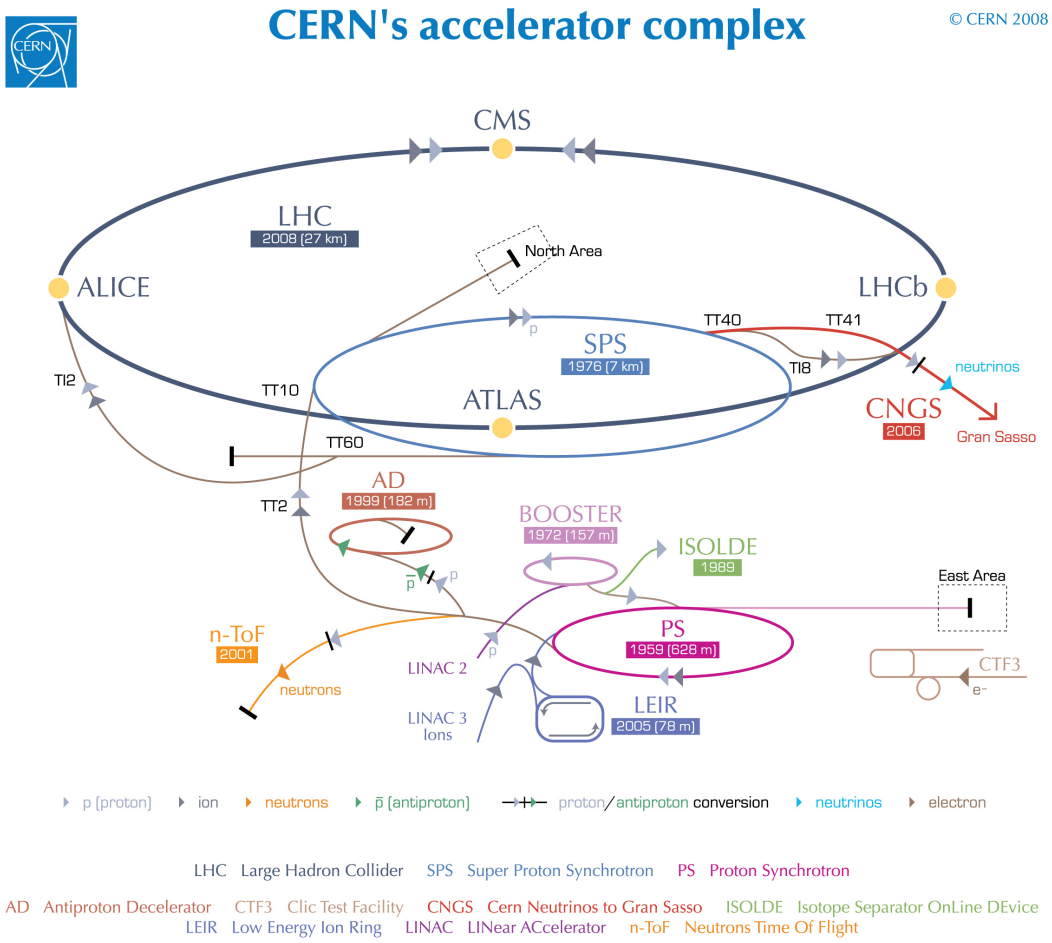

Figure 3.1.: Overview of the whole accelerator complex located at CERN. Taken from [101]

3.2 Compact Muon Solenoid

Located 100 m below the surface close to the French village Cessy, the CMS detector, shown in Figure 3.2, weights 12,500 t and measures 21.6 m in length with a diameter of 14.6 m.

As a "general-purpose" detector, the CMS is built to reconstruct all standard model particles except only weakly interacting neutral particles. To accomplish this, it is made up of multiple subdetectors with different purposes which, in combination, provide a nearly full picture of the constituents of the produced particles or their decay products during the proton-proton collisions.

This section will describe the CMS layout with its different subdetectors as well as relevant upgrades made during the Run 2 period of the LHC and is mostly based on [98].

3.2.1 General Concept

The detector has a cylindrical "onion like" layout, which means that the single subcomponents are built in different layers around the collision point in the center of the CMS. An overview of the layout of the CMS detector can be seen in Figure 3.2.

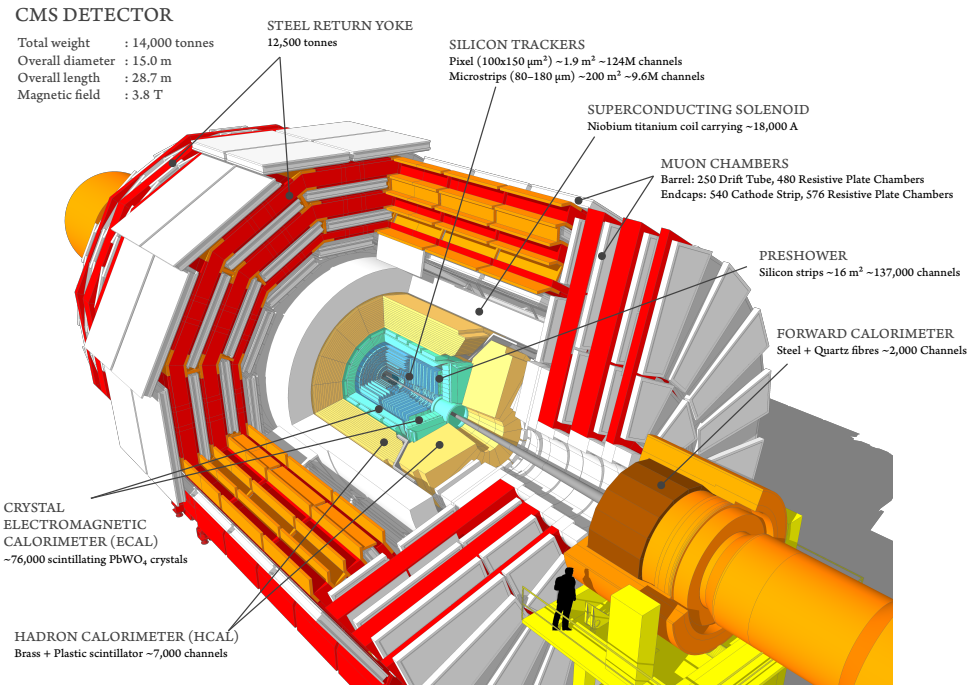

Figure 3.2.: Schematic view of the CMS detector, showing the "onion like" structure with the beam pipe in the center and the different detector parts following around it. Taken from [102]

Due to its shape, the detector can be divided into one Barrel region and two Endcap regions which cover the forward region of the beam pipes. Most detector parts lie inside the solenoid magnet. Only the muon system is located outside the magnet. Therefore, it is the outer layer of the detector.

To describe the measured objects and their position in space, the CMS experiment adopted a coordinate system with its center lying in the nominal collision point. The x-axis points inward into the center of the LHC ring whereas the y-axis points upwards to the surface. The z-axis points along the beam pipes in the direction of the Jura mountains.

Due to its cylindrical shape, it is helpful to use angular coordinates. The azimuthal angle ϕ lies in the x-y plane and is measured from the x-axis while the polar angle θ is measured from the z-axis. The radial component r also lies in the x-y plane.

Using the polar angle θ, one can define the pseudorapidity η as:

$$\eta = -\ln\left(\tan\left(\frac{\theta}{2}\right)\right). \tag{3.1}$$

For particles with a momentum much greater than its mass the pseudorapidity is approximately the rapidity[2]. One of its benefits is that the angular distance of two particles can be described as:

$$\Delta R = \sqrt{\Delta\phi^2 + \Delta\eta^2}. \tag{3.2}$$

Assuming that $p \gg m$, the distance ΔR is invariant under a Lorentz boost.

In this coordinate system, the momentum transverse to the direction of the beam is called transverse momentum p_T:

$$p_T = \sqrt{p_x^2 + p_y^2}. \tag{3.3}$$

3.2.2 Superconducting Magnet

The magnet inside the CMS detector has a length of 12.5 m and a diameter of 6.3 m. A current of 18 kA creates a magnetic field of 3.8 T. The cables are made of Niobium-Titanium (NbTi) which are reinforced with aluminium. They operate at a temperature of about 4.5 K, using helium as a cooling agent for the NbTi to perform as a superconductor.

The cold mass of the magnet is 220 t with a stored energy of 2.6 GJ.

The iron return yoke outside of the solenoid has a total mass of 10,000 t and guides the magnetic field and additionally serves as a support structure for the muon system.

The main purpose of the solenoid is to create a magnetic field which bends the trajectory of charged particles in the detector to provide high resolution of the transverse momentum measurement and allows the distinction between charged and neutral particles.

3.2.3 Tracker System

With a length of 5.8 m and a diameter of 2.5 m, the tracking system is the first detector part of the CMS, built directly around the interaction point. Its purpose is to measure the trajectory of charged particles with a $p_T > 1$ GeV in a pseudorapidity range of $|\eta| < 2.5$ as well as secondary vertices from the collision. Together with other detector parts it plays an important role in the reconstruction and identification of leptonic and hadronic particles.

A sketch of the original tracker layout can be seen in Figure 3.3.

[2] "Rapidity" is the "relativistic velocity" which, at colliders, is defined as $y = \frac{1}{2}\ln\frac{E+p_z}{E-p_z}$ [3]

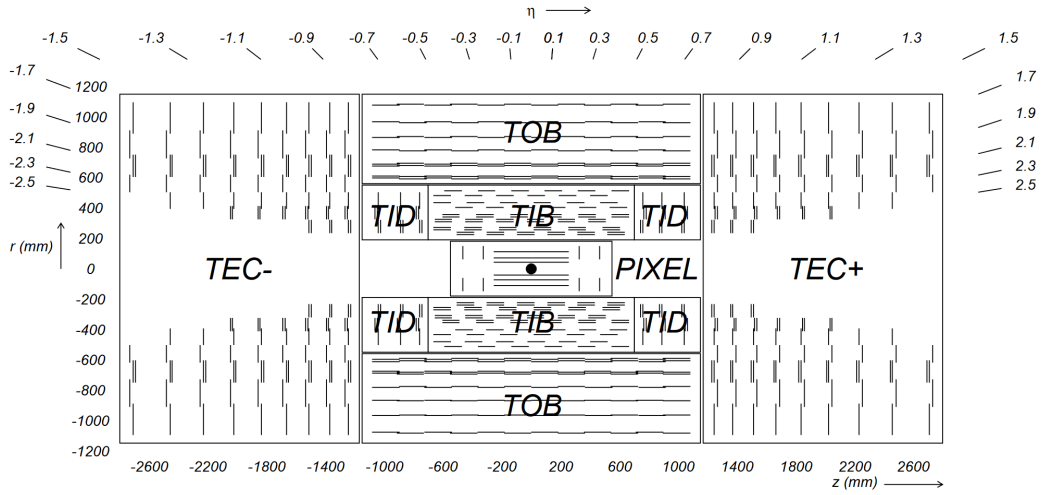

Figure 3.3.: Schematic view of the layout of the tracker system. The pixel detector is shown closest to the beam pipe, which is located at $r = 0\,\text{mm}$, surrounded by different parts of the silicon tracker. Taken from [98]

Pixel Detector

The innermost part of the tracker system is the pixel detector. The original design consists of three cylindrical layers respectively placed at radii of 4.4, 7.3 and 10.2 cm around the interaction point building the Barrel. Additionally, two discs of pixel modules cover the Endcaps of the pixel detector at $z = \pm 34.5$ and $z = \pm 46.5\,\text{cm}$.

The pixel detector covers an area of about $1\,\text{m}^2$ with roughly 66 million single pixels of a size of $100 \times 150\,\mu\text{m}^2$. In total, 1440 pixel modules are built into the tracker system which provides a spatial resolution of $15 - 20\,\mu\text{m}$. The main purpose of the pixel detector is the reconstruction of primary and secondary vertices and to build seeding tracks for particle reconstruction.

During the technical stop from the end of 2016 to the beginning of 2017, the pixel detector of the tracker system was updated to withstand the higher pileup and deliver more robust tracking under those more difficult circumstances [103]. The upgraded Phase-1 tracker system is expected to perform on this level until the end of Run 3, when the whole tracker system will receive an update to be used for the high luminosity LHC. A comparison of the pixel tracker before and after the upgrade can be seen in Figure 3.4.

The update also included the addition of an extra layer in the Barrel as well as in the Endcaps for higher precision of the measurement. Additionally, the first layer was moved closer to the interaction point. This upgrade delivered a positional resolution of $9.5\,\mu\text{m}$ in the $r - \phi$ and $22.2\,\mu\text{m}$ in the z direction, and a four-hit coverage up to $|\eta| = 2.5$ [103].

Silicon Strip Tracker

Outside of the pixel detector, the silicon strip tracker is built in a radius region between 20 to 116 cm. It consists of three different subsystems: the tracker inner Barrel (TIB) and disk (TID), the tracker outer Barrel (TOB) and Endcaps (TOC), with a total length of about 160 cm.

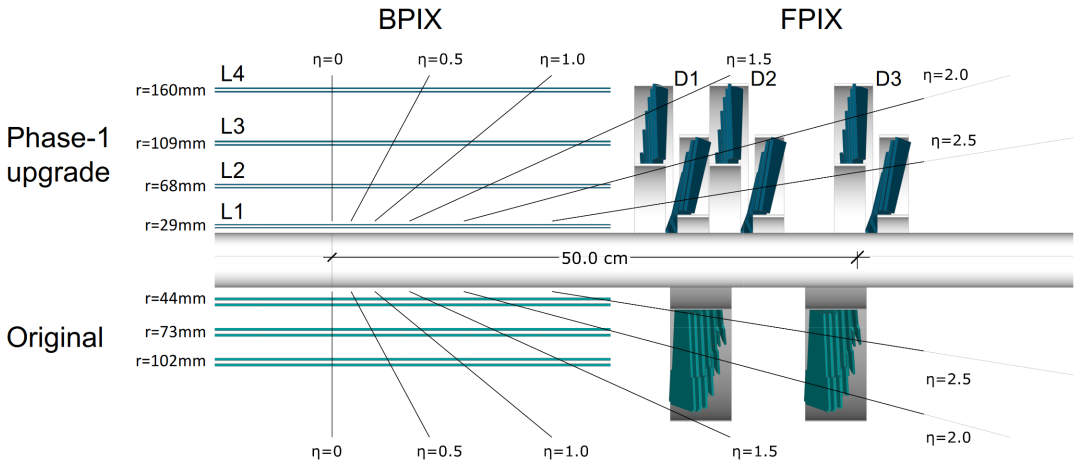

Figure 3.4.: Comparison of the pixel tracker before and after the upgrade, showing the added layers in the Barrel and the forward region of the detector. Taken from [103].

The TIB and TID use four Barrel layers and three Endcap discs with silicon micro strip sensors of 320 μm thickness. They provide a measurement of the r-ϕ coordinates with a single point resolution of 23 μm and 35 μm for the Barrel and 100 μm and 141 μm for the Endcaps.

Outside of the inner tracker, the outer Barrel and Endcaps are built out of 6 layers and 9 disks with up to 7 disks of strip sensors. The single point resolution of the 6 point measurement in the Barrel is 53 μm for r and 35 μm for ϕ.

Overall, the resolution of the tracker system for high momentum tracks with a p_T of 100 GeV is about $1-2\,\%$ up to $|\eta| \approx 1.6$, decreasing for higher momenta.

3.2.4 Calorimeters

Electromagnetic Calorimeter

The electromagnetic calorimeter (ECAL) is installed outside of the tracking detector. Its main purpose is to measure the energy and position of electrons, photons and the electromagnetic products of hadronic jets. It is a homogeneous calorimeter made of lead tungstate ($PbWO_4$) crystals and photomultipliers to measure light emission due to energy deposition. A preshower detector is installed in front of the Endcaps. A sketch of the ECAL layout can be seen in Figure 3.5.

With a volume of 8.14 m^3 and a weight of 67.4 t, the ECAL Barrel (EB) covers a range of $|\eta| < 1.479$ with a number of 61200 crystals with each crystal having a front face cross section of $22 \times 22\,mm^2$ and a rear face cross section of $26 \times 26\,mm^2$. The crystals are assembled into supermodules with about 1700 crystals each. Avalanche photodiodes (APD) are used to collect the light emitted from the crystals in the Barrel. With an active area of $5 \times 5\,mm^2$, one pair of these APDs is installed per crystal.

The ECAL Endcaps (EE) cover a range of $1.479 < |\eta| < 3.0$, at a distance of 315.4 cm to the interaction point. Crystals in units of 5×5 (so called "supercrystals" or "SC") are used with a

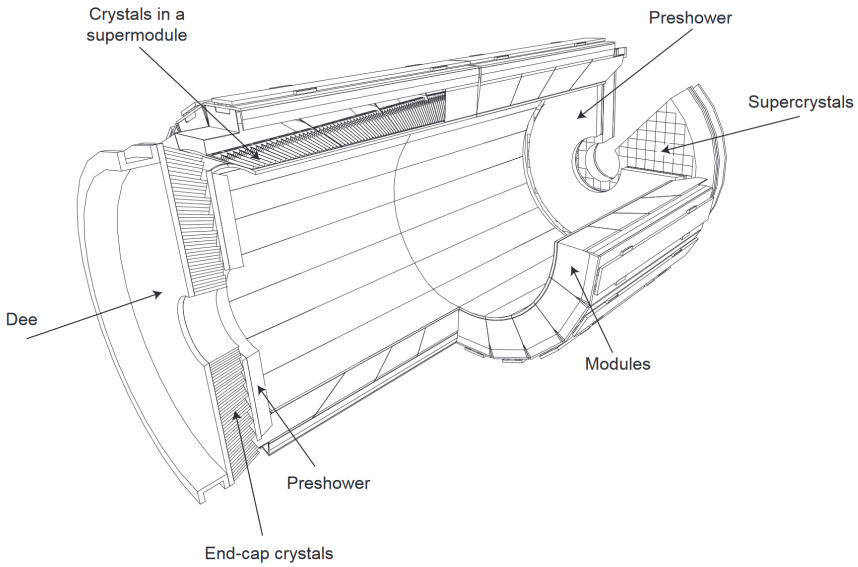

Figure 3.5.: Schematic view of the layout of the electromagnetic calorimeter showing the Barrel and the Endcap with its modules and crystals. Taken from [98]

front face cross section of $28.62 \times 28.62\,\mathrm{mm}^2$ and a rear face cross section of $30 \times 30\,\mathrm{mm}^2$ of a single crystal. Each EE is divided into two halves, called Dees, which contain 3662 crystals each. One vacuum phototriode (VPT) is installed per crystal with a diameter of 25 mm and an active area of $\approx 280\,\mathrm{mm}^2$.

High radiation and particle fluxes during the proton-proton collisions lead to ionizing radiation which may cause absorption bands in the crystals. These lead to a loss of light transmission which can be tracked and corrected by measuring the transparency of the crystals with a laser system, since this loss does not change the scintillator mechanism.

The operating temperature lies at 18° Celsius and is kept stable by using a water cooling system.

The energy resolution of the ECAL can be parametrized by

$$\left(\frac{\sigma}{E}\right)^2 = \left(\frac{S}{\sqrt{E}}\right)^2 + \left(\frac{N}{E}\right)^2 + C^2. \tag{3.4}$$

S describes a stochastic term, covering event-to-event fluctuations within the shower containment, photostatistic contributions and fluctuations in the preshower absorber energy deposition. N is a noise term, describing noise coming from electronics, digitization and pileup. The last term, C, is a constant term, taking into account non-uniformity of the light collection in the longitudinal direction, intercalibration errors and energy leakage through the crystal back parts. The parameters were determined by test beam measurements leading to the final energy resolution parametrization of

$$\left(\frac{\sigma}{E}\right)^2 = \left(\frac{2.8\,\%}{\sqrt{E}}\right)^2 + \left(\frac{0.12}{E}\right)^2 + (0.3\,\%)^2, \tag{3.5}$$

where E is in units of GeV.

Hadron Calorimeter

The hadronic calorimeter (HCAL), built around the ECAL, uses brass absorption layers with plastic scintillators. The scintillator light is converted by wavelength shifting (WLS) fibres and was originally detected by hybrid photodiodes (HPDs). The purpose of the HCAL is to measure the energy deposition of hadronic jets as well as to provide measurements for the calculation of missing energy in the sum of all measured energy[3] (e.g. from neutrinos or exotic new particles).

A sketch of the original layout of the hadronic calorimeter can be seen in Figure 3.6.

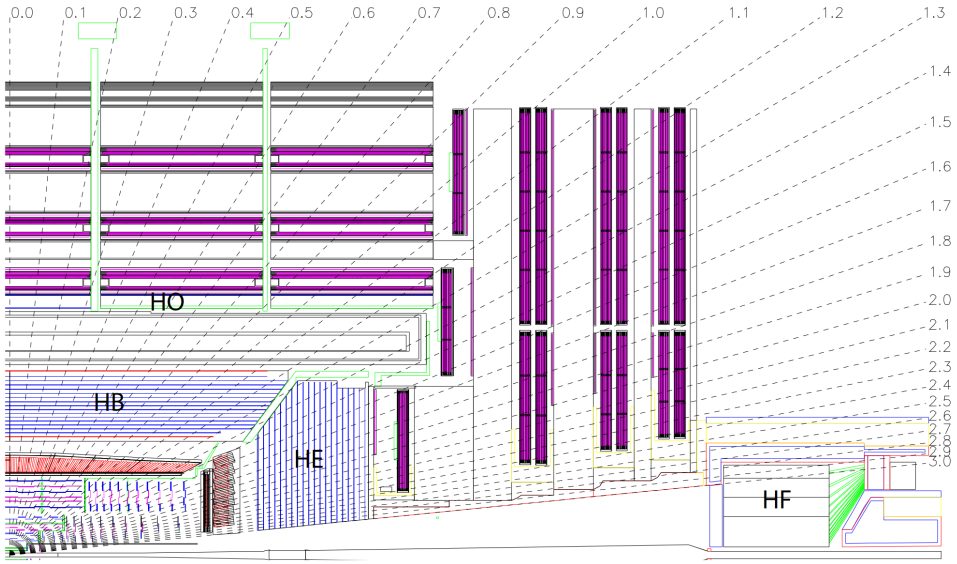

Figure 3.6.: Schematic view of the layout of the hadronic calorimeter showing the Barrel (HB), Endcaps (HE) and forward (HF) region of the HCAL as well as the part reaching outside of the solenoid (HO). The beam pipe is visible at the bottom of the sketch with the collision point at the left bottom corner. The dashed lines indicate the η coordinate. Taken from [98]

The HCAL can be divided into four different parts. The central part of the calorimeter is the hadron Barrel (HB) covering the pseudorapidity range of $|\eta| < 1.3$. The HB can be further divided into two half-Barrels (HB+ and HB-) with a total number of 36 identical parts called wedges, which contain the detector material.

The inner and the outermost plate of these wedges are made of stainless steel increasing the overall strength of the system. There are in total 16 η sectors for the plastic scintillators with a crack size smaller than 2 mm between the wedges. The effective thickness of the HB increases with the angle θ up to 10.6 interaction lengths at $|\eta| = 1.3$. Adding the ECAL material leads to a total thickness of 11.8 interaction lengths.

The first layer of the HB scintillators is built in front of the steel plates to give the opportunity to measure the shower in the material between the EB and the HB.

The second part of the HCAL is the hadron Endcaps (HE). They cover a range of $1.3 < |\eta| < 3$, a region that contains about 34 % of the final state particle content produced during a proton-proton interaction. The HE brass absorber geometry is built to minimize the crack size between the HB

[3] This is called "missing transverse momentum, see Section 4.5.

and the HE as the resolution of hadronic jets is primarily limited by parton fragmentation, pileup and magnetic field effects. The total effective thickness of the HE is ≈ 10 interaction lengths.

As the stopping power of the EB and the HB combined is not sufficient to contain all hadron showers in the central η region, an additional calorimeter part was added outside of the solenoid, called hadron outer calorimeter (HO). The HO extends the HCAL to measure late starting showers as well as the energy of showers that is deposited after the HB.

As the absorber depth of the HB is minimal at $\eta = 0$, the HO has two layers at this position instead of one. It contains 12 identical ϕ sectors following roughly the same geometry as the HB.

The last part of the HCAL is the forward hadron calorimeter (HF). It is installed in a region where the particle fluxes are very high. The average energy deposition per p-p interaction is 760 GeV. Due to this high amount of radiation and energy, quartz fibres were chosen as the active medium, collecting Cherenkov light emitted by secondary particles.

During the long shutdown 2 (LS2), which started in December 2018 and ended in 2022, the HCAL was updated. The HPDs were replaced by silicon photomultipliers (SiPMs) which provide higher light yields and radiation tolerance with better noise levels [104].

For the combination of the EB and HB, the energy resolution was measured to be [105]:

$$\left(\frac{\sigma}{E}\right)^2 = \left(\frac{115.3\%}{\sqrt{E}}\right)^2 + (5.5\%)^2, \tag{3.6}$$

where E is in units of GeV.

3.2.5 Muon System

As the name of the experiment already suggests, muon detection plays an important role in CMS. The main functions of the muon system are the identification of muons, the measurement of their momentum and the triggering of events with muons. To fulfil this purpose, it uses three different types of gaseous particle detectors. The layout of the muon system can be seen in Figure 3.7. To handle the expected high particle fluxes in the forward region expected in Phase-2 of the LHC, starting in 2026, an additional detector type called gas electron multipliers (GEM) will be installed in the muon Endcap region. A first station was installed during LS2 and is used during the data taking of Run 3 [106].

Drift Tube System

In the Barrel region, drift tubes (DT) are installed and cover a range of $|\eta| < 1.2$. They are divided into four cylindrical stations surrounding the inner detector parts. 12 sectors are defined in the r-ϕ plane, each containing four chambers per wheel. Chambers are made of superlayers (SL), the smallest independent part of the DT detector containing four layers each. These layers are made of multiple DT cells. The cells use a gold-plated steel wire in the middle, electrode strips at the top and at the bottom and cathode strips at each side. They are filled with a mixture of 85 % argon and 15 % carbon dioxide. With a maximum transverse path of 21 mm, the DTs have a drift time of about 380 ns.

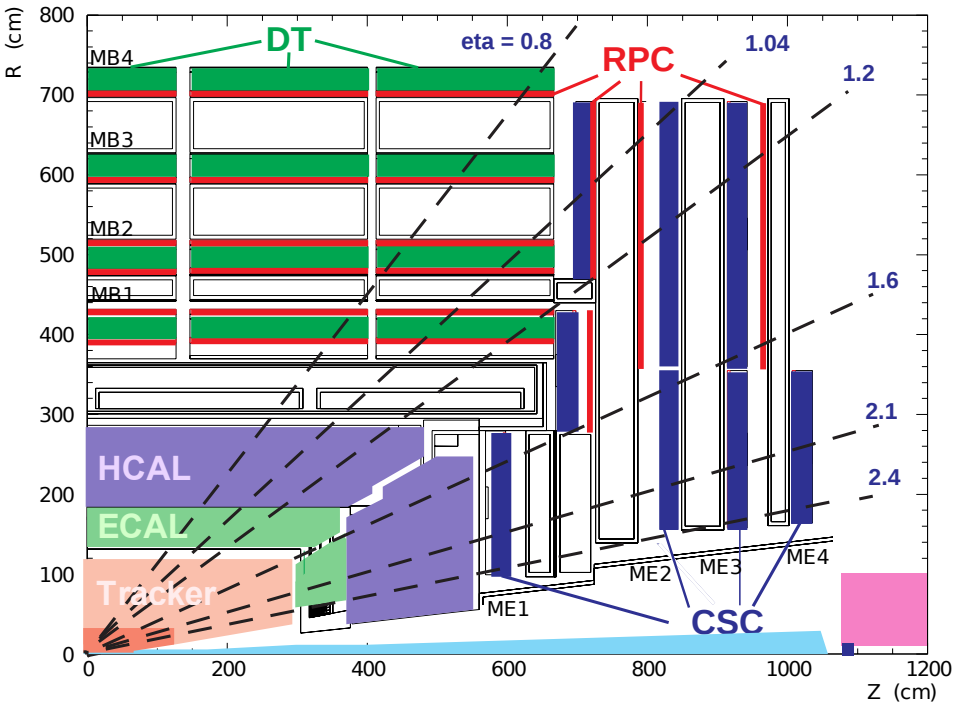

Figure 3.7.: Sketch of the muon system showing the Barrel stations (MB) with their drift tubes (DT) and resistive plate chambers (RPC) and the Endcap stations (ME) with the cathode strip chambers (CSC). The collision point is at $z = 0$ and $r = 0\,\text{cm}$. The dashed lines indicate the η coordinate. Taken from [107]

The wires of the outer SL are parallel to the beam axis to provide a measurement of the muons r-ϕ coordinate. The inner SL wires, on the other hand, are orientated orthogonal to the beam axis to provide a measurement in the z direction. As it is shown in Figure 3.8, a muon originating from the interaction point passes the first SL, which delivers a ϕ measurement, travels through the honeycomb plate, enters the inner SL, which provides the z measurement, and, in the end, reaches the second ϕ measuring SL.

Cathode Strip Chambers

In the Endcap region of the muon system, cathode strip chambers (CSC) are used. They are multi-wire proportional chambers with six anode wire planes and seven cathode panels. With each of the chambers covering 10 or 20 degrees, the overlap provides a contiguous coverage in the range of $0.9 < |\eta| < 2.4$. The position of the CSC in the CMS detector can be seen in Figure 3.7. The wires are arranged azimuthally and used to measure the radial coordinate of the track. This is done by interpolating the charges that are induced on the strips which are milled on the cathode panels. The total number of channels sums up to 468, with 234 chambers in each Endcap.

Resistive Plate Chambers

In addition to the DT and the CSC, resistive plate chambers (RPC) are used in the Barrel and in both Endcaps. These gaseous parallel plate detectors combine good spatial and time resolution

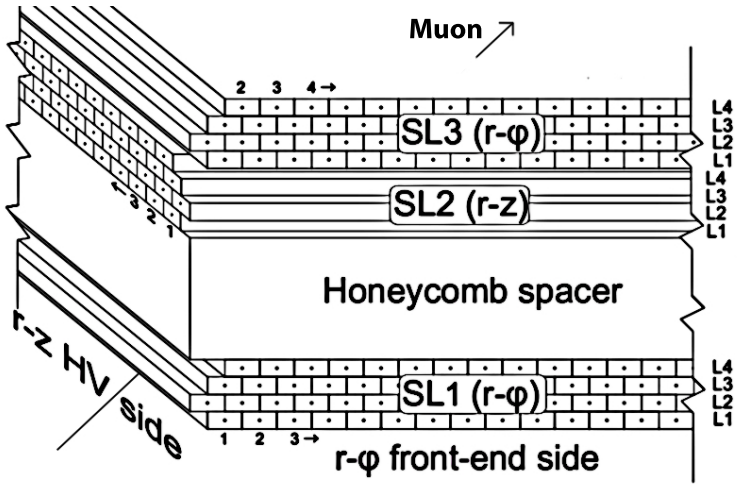

Figure 3.8.: Sketch of the structure of a drift tube chamber, showing three superlayers and the honeycomb plate. Adapted from [108]

and provide the capability of measuring the arrival time of an ionizing event. The time needed to trigger such an event is significantly shorter than the time between a single bunch crossing of 25 ns. Therefore, the RPC can identify the corresponding event for the reconstructed muon track, being essential for the triggering of muon events.

The RPC use basic double gap modules, with two gaps called "up" and "down", in avalanche mode. The total signal contains the sum of both single gap signals which provides a better detector efficiency than using only single gaps. Six RPC layers are installed in the Barrel iron yoke, where two are in each of the first and second muon stations and another in each of the last two stations. Having two layers of RPCs in the first stations ensures that the trigger algorithm can perform the reconstruction always on four layers in an $|\eta|$ range up to 2.1. The position of the RPCs can also be seen in Figure 3.7.

The overall resolution of the muon system combined with tracker information was estimated using cosmic rays. It is about 1 % for muons with a p_T of 100 GeV, 2 % for a p_T of 200 GeV and rises up to 6 % for muons with a p_T of 1 TeV [109].

3.2.6 Trigger & Data Acquisition

With a bunch crossing frequency of 40 MHz at the LHC and multiple collisions during each crossing, the amount of data to store the information of all activity would be too big. Therefore, the data needs to be filtered before it is stored to reduce the rate to the order of 100 Hz. This is achieved by using a two step trigger system.

The first step is the Level 1 (L1) trigger. It is a custom designed, programmable hardware trigger that uses input from the calorimeters and the muon system. A sketch of the L1 trigger flow can be seen in Figure 3.9.

The L1 uses local, regional and global inputs, combined into the muon and the calorimeter triggers.

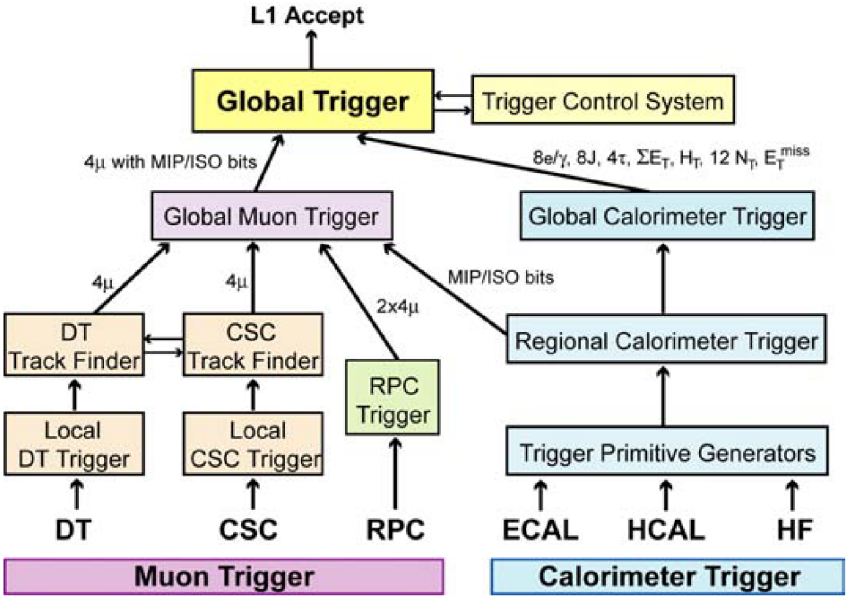

Figure 3.9.: Sketch showing the information flow of the Level 1 (L1) trigger using the information coming from the different parts of the muon system and the calorimeters to build separated global triggers leading to the overall global trigger. Taken from [98]

The local triggers from the muon system are coming from the DT and CSC detector parts. The calorimeter part combines information from the ECAL, HCAL and HF into the so called Trigger Primitive Generators (TPG), taking the energy deposition in the calorimeter trigger towers and track segment and hit patterns into account.

The information from the local muon triggers is passed to the DT and CSC track finder which are then combined with the information from the RPC trigger to the global muon trigger. The regional triggers combine their information with pattern logic and rank their specific trigger objects. For example, electrons or muons, are ordered by their energy or momentum and their quality. The global muon trigger also uses input from the regional calorimeter trigger which gets its input from the TPG and is used as a single input for the global calorimeter trigger. Both global triggers deliver their output to the main global trigger where the highest ranked object of the event is chosen and the event is either rejected or accepted. The global trigger is supported by the Trigger Control System (TCS) which provides readiness information of the subsystems and the data acquisition.

The output rate of the L1 has a maximum of 100 kHz. Its information is used in step two of the reduction of data rates: the High-Level-Trigger (HLT) of the data acquisition (DAQ) system. As the rate of data is already reduced by a significant amount by the L1 hardware trigger system, the second step can be done by slower, but more precise, software triggers that use about 1000 processors to filter the L1 output. The HLT uses information from the complete readout data from the detector and runs calculations similar to offline analyses. Developed for specific needs (for example to select events with at least one "good" muon), the output rate of the HLT is of the order of 1000 Hz [110]. This rate is low enough to store the measured data and save it for later access.

For data storage and computing, a tier system is used. The first layer in this system is the Tier-0 installed at CERN. Its purpose is to accept the data coming from the HLT and to perform prompt data reconstruction. The events are sorted depending on their HLT path and saved to the Tier-0. Additionally, they are also forwarded to the next layer, the Tier-1, to be safely stored as a copy. The Tier-1 combines multiple computation centres outside of CERN, providing storage for the taken data as well as for simulated background events. The last level of the computing system is the Tier-2, consisting of multiple centres distributed all over the world at local research facilities, offering storage and computing power for analysis activities, calibration tasks and simulation which can be transferred to the Tier-1 for long term storage. One of this Tier-2 facilities can be found at the RWTH Aachen University [111].

4 Particle Reconstruction and Identification

The information from the different detector parts described in the previous section is used to reconstruct and identify the particle content of the measured collision events. The main algorithm used to reconstruct the particles and their properties at CMS is called Particle Flow algorithm (PF) [112]. It uses the information of all detector parts to reconstruct the final state constituents of the events. The basic elements, like tracks and clusters, are combined to get the most precise reconstruction of the different types of particles.

4.1 Tracks

The reconstruction of tracks in the innermost part of the detector is needed for most of the more complex descriptions of specific objects. The procedure for track reconstruction used in CMS is called Combinatorial Track Finder (CTF) [113]. It starts off with a seed, followed by track finding and fitting using Kalman Filters (KF) [114]. The final stage of track reconstruction is the selection of well reconstructed tracks using quality criteria to reduce the number of wrongly reconstructed tracks.

Seeding is done by either using pairs or triplets of the detector layers. In the first case, the seeding is accepted if track parameters of the hit pair (one hit in each of the detector layers building a pair) are consistent with the requirements of the specific region where the possible track was measured. These requirements include the minimum p_T and the distances to the assumed production point of the particle. For the latter case, the inner layers of the seeding layers are used to search for a third hit in the outer layer. Again, the seed is accepted if the track parameters of the track calculated from all three layers fulfil the tracking region requirements.

The track finding uses the seed together with an extrapolation of the trajectory to determine the most probable next layer of the track. From that extrapolation, intercepted silicon modules in the layers, which are compatible within the uncertainty of the track, are searched for. As a next step, a group of hits is formed, containing all hits from one of the module groups. Using the original track candidates, one compatible hit of the group is added, new track candidates are formed and the trajectory parameters are updated. All new candidates are then propagated to the following layer, repeating the described procedure and building the final track candidates.

After all possible hits are known, the trajectory is refitted starting at the innermost point and running iteratively through all hits corresponding to the track candidate and updating the track parameters. This procedure is followed by a smoothing stage. The procedure uses a Runge-Kutta[1] propagator to obtain the best precision of the extrapolation between the hits, taking into account the effects of the material and the magnetic field. Finally, the number of tracks is reduced by applying a track-selection procedure with requirements on the minimum number of layers with associated hits, the maximum number of layers without a hit and various requirements on the track parameters. Using this track selection, the number of fake tracks is significantly reduced.

[1] The Runge-Kutta method is an often used method to approximate solutions of non-linear equations [115] due to its easy computational implementation.

4.2 Electron

4.2.1 Reconstruction

The reconstruction of electron tracks using the tracker system presents some challenges. On its way to the ECAL, the electron loses a significant amount of energy due to Bremsstrahlung. As this loss in energy is non-Gaussian distributed, the standard Kalman-Filter driven reconstruction leads to a lower resolution and affects the efficiency of correctly reconstructing existing electron tracks.

To find the seed for the electron track reconstruction, two different methods are used. As Bremsstrahlung from high energetic electrons is usually boosted into the same η direction as the electron, the deposition of the energy of the electron and the Bremsstrahlung is expected to be in the same η coordinate but in different ϕ regions due to the bending of the electron track. Therefore, so called "superclusters" (SC) are built that merge clusters in an area in ϕ in the ECAL in the same η direction. The position of these SCs already adds a constraint on the track reconstruction of the electron in the tracker system under the assumption that the electron originated from the center of the collision. This seed is also called "ECAL-driven".

The second method uses the main tracks from the iterative KF approach, checks their compatibility with electrons and associates them to the close-by ECAL cluster. Thus, it is known as a "track-driven" seed.

The "ECAL-driven" seeding has an efficiency for isolated high-E_T electrons coming from Z boson decays (where E_T stands for "transverse energy", similar to $\vec{p}_T^{\,\text{miss}}$) of more than 95% [116] whereas the "track-driven" seed only offers an efficiency of less than 5% at $E_T > 10\,\text{GeV}$ [112]. The latter can be used to recover track reconstruction efficiency at low-E_T or in critical regions like the Barrel-Endcap overlap region of the ECAL. In contrast to the usual PF Kalman filter method for the final trajectory fit, the electron fit uses an adapted KF method called Gaussian Sum Filter (GSF) [117].

Starting from the seed, tracks are built using the KF method including iteratively each tracker layer information. The energy loss due to Bremsstrahlung is modelled using a Bethe-Heitler function [118]. This method collects compatible hits per layer and creates trajectory candidates.

After all hits are collected, the GSF fit is performed, approximating the energy loss per layer by a sum of Gaussian distributions, each of which is weighted with a probability associated factor. This procedure is continued to the ECAL hit to create the final electron GSF track. All the information from the track reconstruction of the electron goes into the particle flow algorithm to calculate the different properties of the reconstructed electron.

4.2.2 Identification

This thesis uses high energy electrons. Therefore, the high energy electron pairs[2] (HEEP) identification is chosen [120]. The HEEP ID is built for electrons with $E_T > 35\,\text{GeV}$ up to more than 2 TeV and uses only the calorimeter information for the energy measurement. The variables used in the HEEP identification are the same for all three years of Run 2 and can be found in Table 4.1.

[2]The name originates from the fact that this identification was first developed for the $Z' \to ee$ search, which contains a pair of high energy electrons in the final state [119].

Table 4.1.: Requirements of the high-E_T selection to fulfil the HEEP identification [121].

Variable	Barrel	Endcap
E_T	$> 35\,\text{GeV}$	$> 35\,\text{GeV}$
η range	$\lvert\eta_{SC}\rvert < 1.4442$	$1.566 < \lvert\eta_{SC}\rvert < 2.5$
isEcalDriven	$= 1$	$= 1$
$\lvert\Delta\eta_{in}^{seed}\rvert$	< 0.004	< 0.006
$\lvert\Delta\phi_{in}\rvert$	$< 0.06\,\text{rad}$	$< 0.06\,\text{rad}$
H/E	$< 1\,\text{GeV}/E_{SC} + 0.05$	$< 5\,\text{GeV}/E_{SC} + 0.05$
$\sigma_{i\eta i\eta}$	n/a	< 0.03
E_{2x5}/E_{5x5}	> 0.94 OR $E_{1x5}/E_{5x5} > 0.83$	$<$ n/a
$I_{ECAL} + I_{HCAL}$	$< 2\,\text{GeV} + 0.03 \cdot E_T + 0.28 \cdot \rho$	$< 2.5\,\text{GeV} + 0.28 \cdot \rho$ for $E_T < 50\,\text{GeV}$ else $< 2.5\,\text{GeV} + 0.03 \cdot (E_T - 50\,\text{GeV}) + 0.28 \cdot \rho$
$I_{tracker}$	$< 5\,\text{GeV}$	$< 5\,\text{GeV}$
Number of missing hits	≤ 1	≤ 1
$\lvert d_{xy}\rvert$	$< 0.02\,\text{mm}$	$< 0.05\,\text{mm}$

The HEEP ID uses subdetector-based isolation instead of the isolation coming from the PF algorithm (which is used for example in the cut-based electron identification):

- E_T: The transverse energy deposition measured in the ECAL, that is consistent with a single electron, has to be greater than 35 GeV.
- isEcalDriven: The seed used for the electron track reconstruction has to be "ECAL-driven", as mentioned in Section 4.2.1.
- $\lvert\Delta\eta_{in}^{seed}\rvert$ & $\lvert\Delta\phi_{in}^{seed}\rvert$: The difference in η and ϕ between the extrapolated track from the inner system and the seeding supercluster has to be smaller than 0.004 and smaller than 0.06 rad respectively.
- H/E: In the direction of the electron, the sum of HCAL tower energies within a cone of $\Delta R < 0.15$ has to be small compared to its energy deposition in the ECAL supercluster.
- $\sigma_{i\eta i\eta}$ & E_{2x5}/E_{5x5}: To distinguish between electromagnetic and hadronic showers, the spread of energy in the crystals in the ECAL is constrained. In the Barrel, this is achieved by comparing the spread of energy in crystal arrays of 2x5 and 5x5 around the seed crystal. In the Endcaps, the width of the shower in an array around the seeding crystal has to be smaller than 0.03.
- $I_{ECAL} + I_{HCAL}$: To suppress jets that are misidentified as electrons, the energy deposition of the prompt electron should be isolated from other sources in the ECAL and HCAL. These depositions are collected in a cone of $\Delta R = 0.3$, excluding an inner cone of three crystals in the ECAL and HCAL towers in a radius of 0.15. The sum of these depositions has to be smaller than $2\,\text{GeV} + 0.03 \cdot E_T + 0.28 \cdot \rho$ in the Barrel and smaller than $2.5\,\text{GeV} + 0.28 \cdot \rho$ in the Endcap if the E_T of the electron is smaller than 50 GeV. Else, it must be smaller than $2.5\,\text{GeV} + 0.03 \cdot (E_T - 50\,\text{GeV}) + 0.28 \cdot \rho$ in the Endcap. Here, ρ is defined as the average energy density in the event.
- $I_{tracker}$: To further suppress misidentified jets, the sum of the E_T of all tracks in a cone of $\Delta R = 0.3$ excluding an inner cone of 0.04 around the electron track has to be smaller than 5 GeV.

- Number of missing hits: To distinguish between prompt electrons and those coming from pair production, no more than one hit must be missing in the inner tracker system.
- $|d_{xy}|$: The transverse impact parameter, a measure of the distance of the track to the primary vertex, has to be smaller than 0.02 mm (0.05 mm) in the Barrel (Endcap) to make sure that the reconstructed electron is a prompt electron.

The HEEP identification performance may vary when comparing Monte Carlo simulation to measured data. Therefore, recommended event weight scale factors are used to correct for this effect in MC [122] and can be found in Section 5.5.5.

4.2.3 HEEP Identification in 2018

In 2018, a disagreement between Monte Carlo and measured data in the HCAL was observed in the Endcaps for the HEEP identification. In order to have a flat scale factor, the HEEP identification was adjusted for the Endcap region in 2018. To address this issue, an η and ρ dependency in the H/E and the ECAL and HCAL isolation requirements in the Endcaps for 2018 were introduced:

Table 4.2.: Changed requirements (red) of the high-E_T selection to fulfil the HEEP identification in 2018 [122].

Variable	Barrel	Endcap
E_T	$> 35\,\text{GeV}$	$> 35\,\text{GeV}$
η range	$\lvert\eta_{SC}\rvert < 1.4442$	$1.566 < \lvert\eta_{SC}\rvert < 2.5$
isEcalDriven	$= 1$	$= 1$
$\lvert\Delta\eta_{in}^{seed}\rvert$	< 0.004	< 0.006
$\lvert\Delta\phi_{in}\rvert$	$< 0.06\,\text{rad}$	$< 0.06\,\text{rad}$
H/E	$< 1\,\text{GeV}/E_{SC} + 0.05$	$< (-0.4 + 0.4\lvert\eta\rvert) \cdot \rho\ \text{GeV}/E_{SC} + 0.05$
$\sigma_{i\eta i\eta}$	n/a	< 0.03
E_{2x5}/E_{5x5}	> 0.94 OR $E_{1x5}/E_{5x5} > 0.83$	$<$ n/a
$I_{ECAL} + I_{HCAL}$	$< 2\,\text{GeV} + 0.03 \cdot E_T + (0.15 + 0.07) \cdot \lvert\eta\rvert \cdot \rho$	$< 2.5\,\text{GeV} + (0.15 + 0.07)\lvert\eta\rvert \cdot \rho$ for $E_T < 50\,\text{GeV}$ else $< 2.5\,\text{GeV} + 0.03 \cdot (E_T - 50\,\text{GeV}) + 0.28 \cdot \rho$
$I_{tracker}$	$< 5\,\text{GeV}$	$< 5\,\text{GeV}$
Number of missing hits	≤ 1	≤ 1
$\lvert d_{xy}\rvert$	$< 0.02\,\text{mm}$	$< 0.05\,\text{mm}$

The analyses presented in this thesis use the requirements shown in Table 4.1 for the years 2016 and 2017 while the adjusted HEEP ID presented in Table 4.2 is used for the year 2018.

4.3 Muon

4.3.1 Reconstruction

The reconstruction of muon objects also starts with the track reconstruction. The muon is reconstructed using the muon system outside of the return yoke. The inner parts of the detector (e.g. the calorimeters) already stop most particles from reaching the muon system, leaving only muons and neutrinos present in that area of the detector [123].

There are three different types of track-reconstructed muons [112] [123]:

- Standalone muons: Standalone muon tracks are reconstructed using the detector information from the muon system. Hits in the DT, CSC or RPC are collected to form track segments. The track segments are used to reconstruct the trajectory of the muon by using Kalman filters.
- Tracker muons: Tracker muons are built from the propagation of the inner track to the muon system. They are loosely matched to at least one DT or CSC segment. This track reconstruction is more efficient for muons with a p_T below 10 GeV. However, it has a higher probability of misidentifying hadrons as muons as hadrons can sometimes reach the first muon station.
- Global muons: If the track from standalone muons can be matched to a track measured in the inner tracking system, the reconstructed muon is called "global muon". In that case, the final fit of the trajectory uses the combined information from the inner tracker and the muon system. Global muons are designed for high energy muons and therefore create multiple hits in the muon stations, reducing the probability of muon misidentification when compared to tracker muons.

Before the start of Run 2, the muon track reconstruction was updated by adding two specifically developed calculations [112] to cope with the high pileup conditions during Run 2.

The information from the track reconstruction is fed into the particle flow algorithm together with all other available detector information to reconstruct the particle quantities of the measured muon. To determine the measured p_T of the muon, the "Tune-P" algorithm is used [124]. This algorithm chooses between the tracker-only p_T measurement and the three additional p_T reconstruction strategies by comparing the goodness-of-fit of the tracks coming from the different approaches and their relative p_T uncertainty. The additional strategies are [109]:

- Tracker-Plus-First-Muon-Station fit: The Tracker-Plus-First-Muon-Station (TPFMS) fit starts with the global-muon track but ignores all muon stations besides the innermost one, which contains hits.
- The Picky fit: This algorithm cleans hits from chambers that seem to originate from showers. This is done by a χ^2 comparison and only hits in these chambers are kept if the extrapolated trajectory is compatible.
- Dynamic-Truncation fit: Energy loss of the muon causes bending of the trajectory which can show up as a kink in the reconstructed track. After propagating the track coming from the tracker and refitting by adding hits from the closest compatible chamber, the algorithm repeats for the next station and stops if there is no compatible hit found in two consecutive stations.

4.3.2 Identification

There are different types of muon identification depending on the need for purity as well as efficiency for the specific analysis. This analysis uses muons with high momentum. Therefore, the identification of choice is the "High momentum muon ID" or "high-p_T ID" [125].

This identification was developed for muons with $p_T > 200\,\text{GeV}$, which are both, a global and a tracker muon. The tracker track has to have at least one pixel hit as well as hits in at least six layers in the inner tracking system. In at least two muon stations, the track has do fulfil the

"track-to-segment" matching where the difference of the position of the track and a segment in the x coordinate is smaller than 3 cm or the distance to its uncertainty ratio is smaller than five [123].

For Run 2, this requirement was extended to cases where the inner track is expected to match, at most, zero or one segment when the extrapolation from the tracker muon predicts a pass through to the muon system gaps. In this case, one matching segment still fulfils the identification requirement. An additional change to the Run 1 high-p_T ID was the added requirement that the used final fit, either the global muon fit or the one coming from the TuneP algorithm, includes at least one valid muon system hits [125].

To make sure that the high-p_T muon originates from a primary vertex, the transverse and longitudinal impact parameters, $|d_{xy}|$ and $|d_z|$, have to be smaller than 0.3 cm and 20 cm, respectively.

In comparison to the "tight muon ID", the high-p_T ID does not have a requirement on the χ^2/dof[3] of the global muon fit to cope with efficiency loss due to additional hits from the radiation of electromagnetic showers [123]. To ensure a good quality of the momentum measurement, the relative p_T uncertainty has to be smaller than 30%.

4.3.3 Isolation

Isolation can be used to further distinguish between prompt muons and muons from weak decays appearing inside of jets. This is done by calculating the sum of the energy in a cone around the muons relative to its p_T, also called "relative isolation". There are two different approaches to the calculation of the muon isolation: Tracker based and PF based.

The track based isolation uses the sum of all reconstructed tracks within a cone of $\Delta R < 0.3$. For the LOOSE working point, the ratio of the summed p_T of the tracks and the muon p_T has to be smaller than 0.1, while for the TIGHT working point it has to be smaller than 0.05.

Instead of reconstructed tracks, the PF isolation uses the sum of the p_T of charged hadrons from the primary vertex and the sum of the energy of all neutral particles. To correct for the impact of pileup to the neutral particles, the deposition of charged hadrons from pileup vertices is summed and scaled by a factor of 0.5 [123]. This is then subtracted from the sum of neutral particles giving the pileup corrected sum of the neutral particle energy contribution. The cone size for the PF isolation is $\Delta R < 0.4$ with the loose working point value for the p_T ratio of 0.25 and the tight working point value of 0.15.

The analyses presented in this thesis use the tracker based isolation for the muon selection.

4.3.4 Muon Momentum Scale

The measurement of high energy muons is subjected to inaccurate track curvature determinations arising from energy loss, variations in the magnetic field and detector misalignments [123]. To calibrate the momentum scale, all these three effects are included by modifying the curvature, either with an additive correction k_b to the curvature $\kappa = q/p_T$ (detector misalignment), where q is the muon charge, a multiplicative factor (magnetic field variation) and a charge independent additive term (energy loss) [125].

[3] "dof" means "degrees of freedom"

The method to cope with detector misalignments is called the "generalized endpoint method" [123] and uses muons from Drell-Yan events that fulfil certain selection criteria. The resulting q/p_T distribution of measured events is compared to multiple simulated muon samples i that have an additional bias k_b^i injected in steps of 0.01/ TeV between -1.00/ TeV and $+1.00$/ TeV. The resulting curvature becomes:

$$q/p_T \rightarrow q/p_T + k_b^i. \tag{4.1}$$

The k_b^i that leads to the minimum fit χ^2 from the comparison between data and the weighted simulation is chosen as the curvature bias in the measured data [123].

4.4 Tau

Due to their short lifetime ($\tau_\tau = 290.3 \pm 0.5 \cdot 10^{-15}$ s [3]) and the resulting average flight length of $\approx 87 \cdot 10^{-4}$ m for $\gamma = 1$, taus produced in proton-proton collisions in the LHC usually decay before they can reach any of the detector material. The tau reconstruction and identification in CMS focuses on hadronic tau decays as they make up most of the branching fraction of tau decays (see Table 4.3). As the decay products are hadrons, one needs to understand the reconstruction of hadronic jets before reconstructing the tau object.

Table 4.3.: Branching fractions ($\mathcal{B}$) of different tau decay channels. The decays are shown for τ^- but apply for τ^+ as well [3].

Decay Mode	Resonance	$\mathcal{B}$
Leptonic Decays		35.2 %
$\tau^- \rightarrow e^- \bar{\nu}_e \nu_\tau$		17.8 %
$\tau^- \rightarrow \mu^- \bar{\nu}_\mu \nu_\tau$		17.4 %
Hadronic Decays		64.8 %
$\tau^- \rightarrow h^- \nu_\tau$		11.5 %
$\tau^- \rightarrow h^- \pi^0 \nu_\tau$	$\rho(770)$	25.9 %
$\tau^- \rightarrow h^- \pi^0 \pi^0 \nu_\tau$	$a_1(1260)$	9.5 %
$\tau^- \rightarrow h^- h^+ h^- \nu_\tau$	$a_1(1260)$	9.5 %
$\tau^- \rightarrow h^- h^+ h^- \pi^0 \nu_\tau$	$\rho(1450)$	4.8 %
Other		3.3 %

4.4.1 Jets

After the PF algorithm has identified electrons, muons and isolated photons, the remaining information is used to identify hadrons and non-isolated photons [112]. ECAL and HCAL depositions that can not be connected to a track are considered to come from neutral hadrons and photons. If there is a connection to be found between an ECAL and an HCAL cluster, they are assumed to originate from the same "hadronic shower". Otherwise, the ECAL cluster is considered to originate from photons.

To reconstruct the direction and energy of the initial parton, different approaches called "jet clustering algorithms" were developed. The one used by the CMS collaboration is called "anti-k_t"

algorithm [126], using the FastJet package [127]. All so called "recombination algorithms", which also include the k_t and the Cambridge/Aachen algorithm, define two distances [126]:

$$d_{ij} = \min(k_{ti}^{2p}, k_{tj}^{2p}) \frac{\Delta_{ij}^2}{R^2}, \tag{4.2}$$

$$d_{iB} = k_{ti}^{2p}. \tag{4.3}$$

Δ_{ij}^2 is defined as $\Delta_{ij}^2 = (y_i - y_j)^2 + (\phi_i - \phi_j)^2$. k_{ti} is the transverse momentum, y_i the rapidity and ϕ_i the azimuthal angle of the entity i, coming from the remaining objects in the PF algorithm particle list. The anti-k_t algorithm uses the parameter $p = -1$, whereas the k_t algorithm uses $p = 1$ and the Cambridge/Aachen algorithm uses $p = 0$ [128, 129].

d_{iB} is defined as the distance between the entity i and the beam. Both distances, d_{ij} and d_{iB}, are calculated for the remaining objects in the particle list. If d_{ij} corresponds to the smallest distance, the two entities i and j are recombined into a so called "protojet". Instead, if d_{iB} is the smallest distance, the entity i is called a jet and removed from the list. This procedure is repeated until the list of entities is empty.

The resulting list of jets from the anti-k_t algorithm, using a distance parameter $R = 0.4$, is then used in the reconstruction of the tau candidates.

4.4.2 Reconstruction

To reconstruct hadronic tau candidates, the hadron-plus-strips algorithm is used [130]. As a first step, seeding regions are defined by using the jets from the list build by the anti-k_t algorithm previously discussed. A cone in the $\eta - \phi$ plane with $\Delta R = 0.5$ is defined and all particles within it are used for the next steps of the reconstruction.

As explained before, the tau can decay into charged hadrons plus neutral π^0. These π^0 candidates are reconstructed using information from the ECAL. The π^0 decays promptly into a pair of photons. These photons have a high probability to create e^+e^- pairs. While going through the tracker, the electrons will be spatially separated due to the magnetic field in the CMS [131]. To reconstruct the full energy of the neutral hadron, electrons and photons in an $\Delta\eta \times \Delta\phi$ plane are clustered together. These clusters are called "strips". A sketch of the hadron-plus-strips algorithm can be seen in

For Run 2, the algorithm was updated to a dynamic strip reconstruction. Before, the plane was defined by the fixed values 0.05×0.20. The dynamic strip approach uses the electron or photon with the highest p_T that has not yet been included in a strip as a seed for a new strip. The electron or photon with the second highest p_T in a dynamic strip area around the initial position is then merged into this new strip. This dynamic strip area is defined as:

$$\Delta\eta = f(p_T^{e/\gamma}) + f(p_T^{\text{strip}}) \tag{4.4}$$

$$\Delta\phi = g(p_T^{e/\gamma}) + g(p_T^{\text{strip}}). \tag{4.5}$$

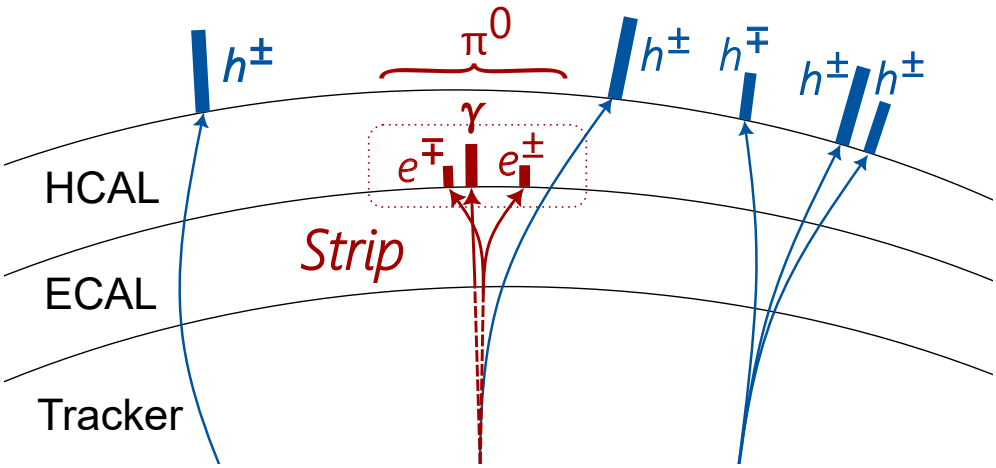

Figure 4.1.: Simplified sketch of the tau reconstruction algorithm for three different decay modes. The first one shows the $\tau^{\pm} \to h^{\pm}\nu_{\tau}$ where only the charged hadron is reconstructed in the HCAL, the ν_{τ} stays undetected an contributes to the $\vec{p}_T^{\,\text{miss}}$. The second one shows the $\tau^{\pm} \to h^{\pm}\pi^0\nu_{\tau}$ decay, where the π^0 decays into two photons. One of the photons creates an e^+e^- pair. The remaining photon and the electrons are measured in the ECAL and build the "strip" for the hadron-plus-strips algorithm. The last shown decay is the $\tau^{\pm} \to h^{\pm}h^{\mp}h^{\pm}\nu_{\tau}$ decay.

The functions f and g result from a fit of the form $a/(p_T)^{-b}$ [131]:

$$f(p_T) = 0.20 \cdot \left(\frac{p_T}{\text{GeV}}\right)^{-0.66}, \tag{4.6}$$

$$g(p_T) = 0.35 \cdot \left(\frac{p_T}{\text{GeV}}\right)^{-0.71} \cdot (\text{rad}). \tag{4.7}$$

Note that $\Delta\eta$ has to be between 0.05 and 0.15 and $\Delta\phi$ has to be between 0.05 and 0.3.

After this merge, the strip position is recalculated as:

$$\eta_{\text{strip}} = \frac{1}{p_T^{\text{strip}}} \sum p_T^{e/\gamma} \eta_{e/\gamma} \tag{4.8}$$

$$\phi_{\text{strip}} = \frac{1}{p_T^{\text{strip}}} \sum p_T^{e/\gamma} \phi_{e/\gamma}. \tag{4.9}$$

The search for additional constituents in the $\Delta\eta \times \Delta\phi$ area is carried on until no additional e/γ candidate is found. The procedure then starts over with the reconstruction of a new strip.

The resulting strips are combined with the charged hadrons and checked against the different hadronic tau decay chains that can be seen in Table 4.3. The visible hadronic components have to be reconstructed in a specific mass window that has to agree with the $\rho(770)$, $\rho(1450)$ or $a_1(1260)$ meson [131] [130], depending on the reconstructed decay mode as shown in Table 4.3. Additionally, the reconstructed electric charge of the tau candidate has to be ± 1 and all $h^{\pm}$ and π^0 have to be in a cone with a radius $\Delta R = 3.0/p_T(\text{GeV})$ with $0.05 \leq \Delta R \leq 0.1$.

4.4.3 Identification

For Run 2, a new tau identification algorithm was developed [130]. It uses a deep neural network instead of a cut-based or multi-variant approach and is therefore called DeepTau. The output of this neural network is the probability of the hadronic tau (τ_h) candidate being a genuine tau or an electron, muon or jet being misidentified as a tau. This is already a significant change from the previous approach where a specific algorithm for each of these classes was developed [131] while the DeepTau uses only one deep neural network for all discriminators.

Another difference is the usage of "lower-level", more fundamental, information of all reconstructed particles which are close to the τ_h candidate. If there are multiple particles of the same type close to the τ_h candidate, the information from the particle object with the highest p_T is chosen for the algorithm.

Additionally, the network also uses "higher-level" information like the τ_h 4-momentum or the compatibility with the leading track from the primary vertex. This helps to substantially reduce the number of events necessary to train the network [130].

The network uses convolutional layers [132], since they offer computational benefits and are well implemented in machine learning frameworks. As these types of layers need partitioned inputs in two dimensions, two $\eta - \phi$ grids around the τ_h candidate axis are created, shown in Figure 4.2, and used to process the particle information. Each of the cells contains information about the reconstructed particles which is then used as the input of the deep neural network.

Overall, three subnetworks are created, one for the high level information, one for the inner grid cells and one for the outer grid cells. These different networks are then combined into four fully connected layers with 200 nodes each. The output of these layers is then fed into the final 4 node layer. A softmax activation function gives the probability that the candidate belongs to a given output class (tau, electron, muon or jet). In total, the number of inputs into the neural network sums up to over 100,000.

The reconstructed taus are sorted into different decay modes (DM) which refer to the different tau decays shown in Table 4.3. The definition of the different DM numbers is following:

$$DM = 5 \times (N_c - 1) + N_p, \tag{4.10}$$

where N_c is the number of charged hadrons (also called "prongs") and N_p is the number of neutral pions. Additionally to the DM shown in Table 4.3, experimental DM are created with only two prongs where one prong of the decay is lost during the reconstruction. These DM, namely 5 and 6, are not used in this analysis.

The performance of the DeepTau in comparison to the multi-variant approach was checked using simulation and measured data of $t\bar{t}$ processes as these events contain a large amount of b quarks and gluon jets combined with a busy event topology [130]. A comparison between both approaches in simulation can be seen in Figure 4.3. It shows the τ_h identification efficiency on the x-axis and the jet mis-identification probability on the y-axis. The graphs show the discrimination against jets for the DeepTau (red), the original MVA (green) and the MVA with updated decay modes (blue). Each point represents a working point of the identification.

The DeepTau delivers a reduction in the mis-identification rate by at least a factor of 1.8 with higher factors in the high-p_T regime. This shows the power of the deep neural network approach.

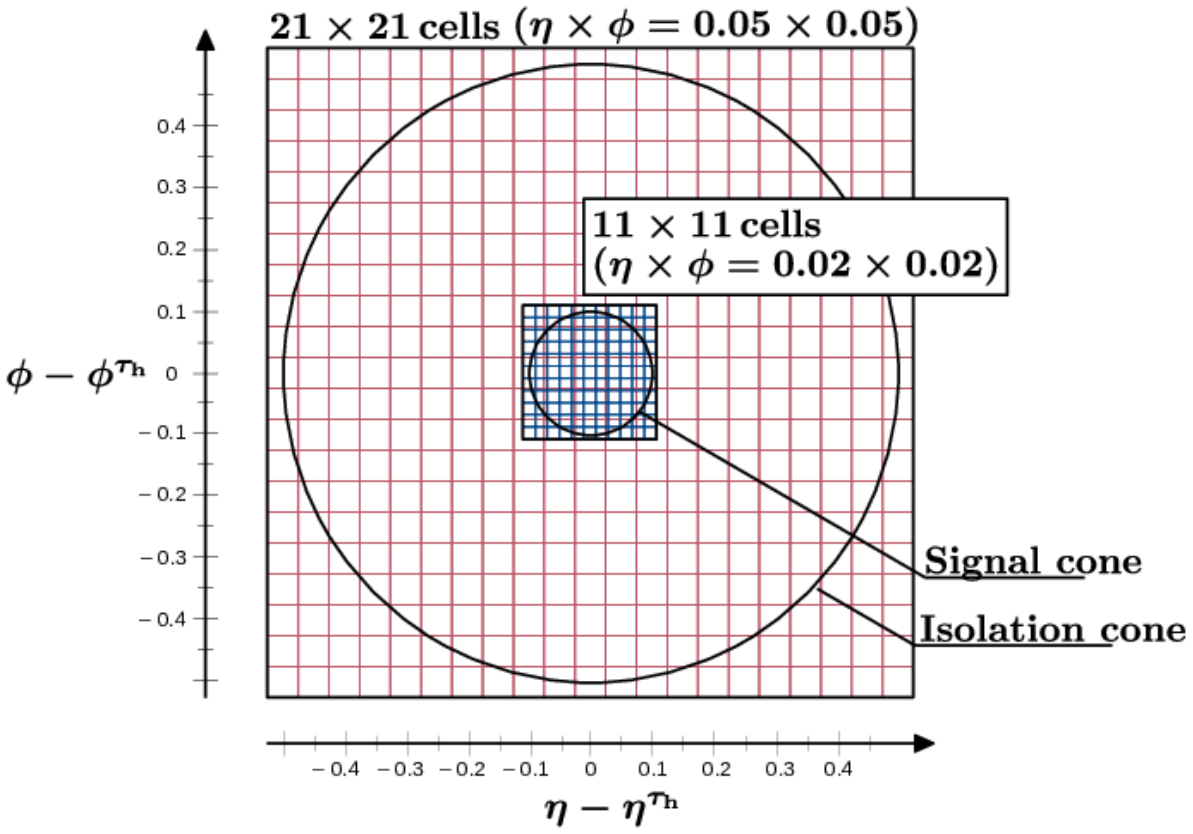

Figure 4.2.: Sketch of the 11×11 $\eta - \phi$ grid with a size of 0.02×0.02 and the 21×21 grid with a size of 0.05×0.05 around the τ_h candidate axis which is used as an input into the deep neural network [130].

A comparison of the DeepTau performance in simulation and measured data from 2018 can be seen in Figure 4.4. It shows the jet mis-identification probability for simulation (black) and data (red) as a function of the jet p_T for the tight working point. The observed probability shows good agreement to the expected probability from simulation, especially in the high-p_T regime which this analysis is most interested in. Additionally, as mentioned before, discriminator values against mis-identifying a muon or an electron as a tau are provided by the deep neural network. Each discriminator has multiple working points with different requirements, for instance regarding the isolation, ranging from VERY VERY VERY LOOSE (VVVLOSE) to VERY VERY TIGHT (VVTIGHT) for the anti-jet and anti-electron discriminator and from VERY LOOSE (VLOSE) to TIGHT for the anti-muon discriminator.

Monte Carlo to data comparisons allow the calculation of scale factors which correct the behaviour of the simulation, such that it follows the actual measurement [130] and are described in Section 5.5.5.

4.5 $\vec{p}_T^{\,\text{miss}}$ (Missing Transverse Momentum)

Some particles in a collision event might escape the CMS apparatus undetected, for example neutrinos which do not interact with the detector material. As the amount of transverse

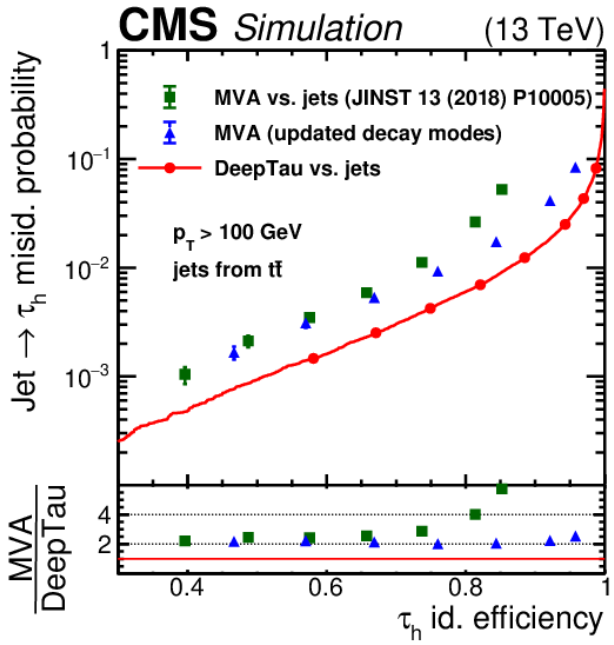

Figure 4.3.: τ_h identification efficiency and the jet mis-identification probability for τ_h with a p_T greater than 100 GeV in DeepTau and MVA. In DeepTau, the mis-identification probability is reduced by a factor of at least 1.8, becoming a higher factor for high-p_T taus, compared to the MVA [130].

momentum at the time of the collision is assumed to be 0, summing up all reconstructed particle information in the event leads to "missing transverse momentum" or $\vec{p}_T^{\text{miss}}$.

$\vec{p}_T^{\text{miss}}$ is therefore defined as the negative vector sum of all PF candidates in the event [133]:

$$\vec{p}_T^{miss} = -\sum_{\text{PF}} \vec{p}_T, \tag{4.11}$$

with its magnitude defined as :

$$p_T^{miss} = |\vec{p}_T^{miss}|. \tag{4.12}$$

The $\vec{p}_T^{\text{miss}}$ plays an important role in the final reconstruction of the invariant mass of the two lepton state with a tau, since the neutrino created during the tau decay will contribute to the $\vec{p}_T^{\text{miss}}$ in the event.

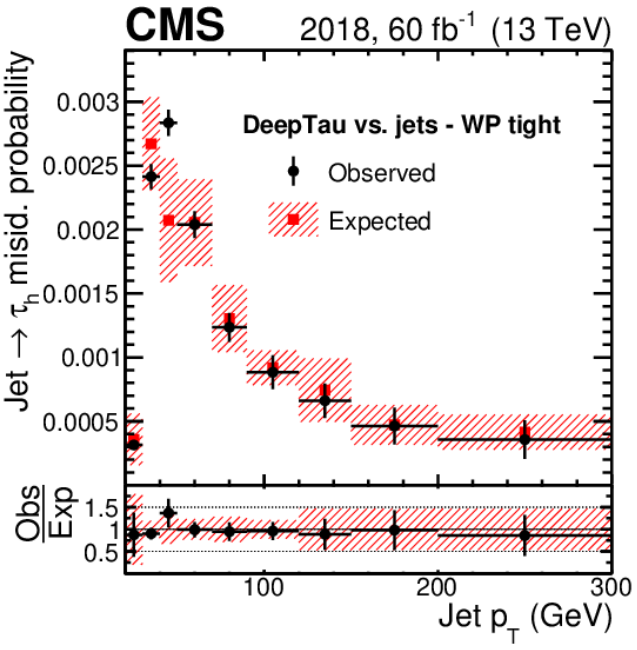

Figure 4.4.: Comparison of the jet mis-identification probability in simulation and measured data from 2018 as a function of the jet p_T. The measurements support the expected identification performance as the comparison delivers a good observed to expected ratio [130].

5 | Analysis

This chapter describes the analysis of the search for lepton flavour violation with two charged leptons of different flavours in the final state. The analysis of the eμ channels was performed by Xuyang Gao [1] and the eτ channel was analysed by Amandeep Kaur Kalsi [1]. The $\mu\tau$ channel was analysed with the `NanoAOD` format by the author of this thesis while an analysis using the `MiniAOD` format was performed by Diego Beghin [1]. The difference between both formats will be described in Section 5.2. As the `NanoAOD` format is supposed to become the standard workflow for most of the CMS analysis, a verification in comparison to the known `MiniAOD` format is of particular importance.

All three channels will be presented, as the results of these analyses will serve as input for the statistical interpretation (Chapter 6), while the main focus will be on the $\mu\tau$ analysis using the `NanoAOD` file format, performed by the author of this thesis. Additionally, a short comparison between the final results from both approaches of this channel will be presented. More details about the $e\mu$ and $e\tau$ analysis can be found in the corresponding publication [1] and the analysis note [134].

5.1 Datasets

In this thesis, the data taken by the CMS experiment in the years 2016, 2017 and 2018 are analysed. The channels including a muon are based on the `SingleMuon` dataset whereas the $e\tau$ channel is based on the `SingleElectron` and `SinglePhoton` dataset in the years 2016 and 2018. These two sets were merged together into one single dataset in 2018, called `EGamma`.

Only events certified by the physics data and MC validation (PDMV) group in their recommended reconstruction version are used [135]. The cleaning for certified events is done by only accepting events present in the so called `goldenJSON`. The integrated luminosity of certified events for each year can be found in Table 5.1. The recommended value of the Luminosity Physics Object Group (LUM POG) for the final total integrated luminosity is 138 fb^{-1} [136].

Table 5.1.: Integrated luminosity for all three years used in this analysis. The value of the combination of all years is rounded to 138 fb^{-1} following the recommendation of the Luminosity Physics Object Group.

Year	Integrated Luminosity
2016	35.9 fb^{-1}
2017	41.3 fb^{-1}
2018	59.7 fb^{-1}
$\sum$	138 fb^{-1}

5.2 Simulation Chain in CMS

The event simulation of proton-proton collisions and their measurement with the CMS detector are done by following a step-by-step routine [137].

- Hard event generation: The first step is the simulation of the proton-proton collision under the assumption of a specific model (e.g. SM, SSM, RPV SUSY, ...). The propagation of the initial momentum of the incoming particles to the particles produced in the collision is calculated using the specific Feynman diagrams corresponding to the chosen model and the resulting probability function. The information on the incoming, produced and outgoing particles is saved in a *Les Houches* file format [138]. Different generators have different precision in the order of the calculated Feynman diagrams.
- Generation: The generation calculates additional radiation either from the initial or the final state particles, called parton showering. Quarks and gluons can not be observed as free particles but will form colour free particles, called hadrons. This hadronization and the resulting creation of jets of hadrons is also calculated. The information saved contains all final state particles which reach the detector material.
- Simulation: After having generated all final state particles and their specific kinematic information, this step simulates the response of the detector. For that, the full CMS was built in the `GEANT4` [139] software package. `GEANT4` is short for "Geometry and Tracking" and provides the possibility to recreate a detector's geometry with its specific materials, simulating the response of each of the detector parts.
- Digitisation: This step emulates the response of the read-out electronics of the detector to the final response of the detector parts created in the simulation step. The output is in the same format as the measured data coming from the experiment.

Since the simulated events are now in the same format as measured data, the following steps are the same for both.

- Reconstruction:The constituents of the events are reconstructed using the particle reconstruction algorithms described in Chapter 4.
- `MiniAOD`: The now fully reconstructed event information is reduced in size by only saving the necessary parts for analysis and potentially needed rerunning of specific reconstruction algorithms. This reduced format is called `MiniAOD` and was developed in 2014 for Run 2 [140].[1]
- `NanoAOD`: The `MiniAOD` format was used by most analyses in CMS as an input for private file productions, applying corrections (e.g. electron energy corrections) and further reduction of the needed storage space. By the end of Run 2, CMS developed a new data format called `NanoAOD` whose purpose is to provide a format that can be directly analysed outside of the CMS software environment[2]. It provides all the necessary event information for most of the analyses and includes the most important corrections. Additionally, it reduces the average size of an event from $40 - 50\,\text{kB}$ using the `MiniAOD` format to $1 - 2\,\text{kB}$ in `NanoAOD` [140, 141].

[1] "AOD" is an acronym for "Analysis Object Data", which was the data format used in Run 1. `MiniAOD` describes a reduced version of this data format.

[2] This environment is called CMSSW which stands for "CMS SoftWare".

This chain is used for the production of Monte Carlo samples describing the Standard Model background expectation as well as for the multiple signal models that are tested in this thesis.

5.3 Background Description

As the final state that is searched for includes two leptons of a different flavour, Standard Model processes that contain either these two leptons, called prompt background, or objects that can be mis-identified as leptons, called fake background, contribute to the background expectation of this analysis. Namely:

- $t\bar{t}$: The main background producing two leptons with different flavours is coming from $t\bar{t}$ production. The top quark decays to a W boson and almost always a b quark [3]. The W boson can then further decay into a lepton and neutrino pair. If both W bosons from the top pair production decay in this leptonic way, they can create two leptons of different flavours.

  The simulation of the $t\bar{t}$ background is done in the generator Powheg [142–148]. For the hadronization, Pythia8 [149] is used. These $t\bar{t}$ samples producing two leptons are binned in the invariant mass of the dilepton pair to achieve better statistical precision in the high mass regime. The cross section of the $t\bar{t}$ process is corrected to NNLO level for QCD and NLO level for electroweak effects [150].

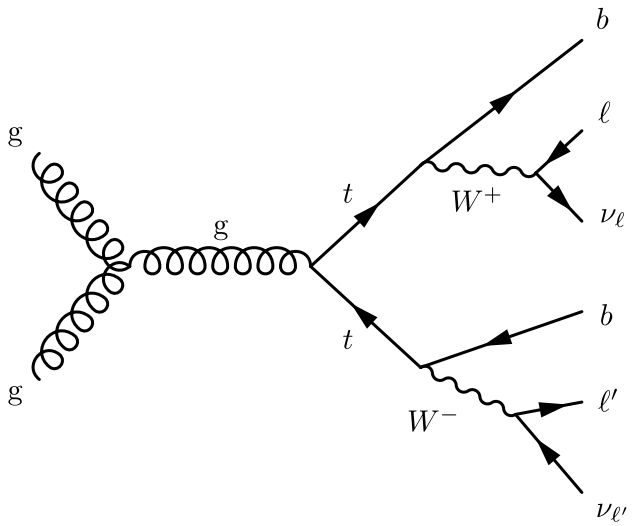

Figure 5.1.: One possible Feynman diagram for the production of a $t\bar{t}$ pair decaying into a final state with two leptons of different flavour (ℓ and ℓ').

- Diboson: The second largest prompt background arises from the production of boson pairs (WW, WZ, ZZ), with the WW production being the dominant one.

  The WW samples are binned in the mass of the lepton pair and are generated with Powheg. The WZ and ZZ samples are either generated with Powheg ($3\ell\nu$, $2\ell 2\nu$ and 4ℓ) or MadGraph5_aMC@NLO [151] ($2\ell 2q$ and $2q2\nu$). Figure 5.2 shows an example of each of the Diboson channels for the production of multiple leptons in the final state.

  The WW and WZ cross sections are corrected to NLO precision [152] [153] whereas the ZZ background cross section is calculated at NNLO level [154].

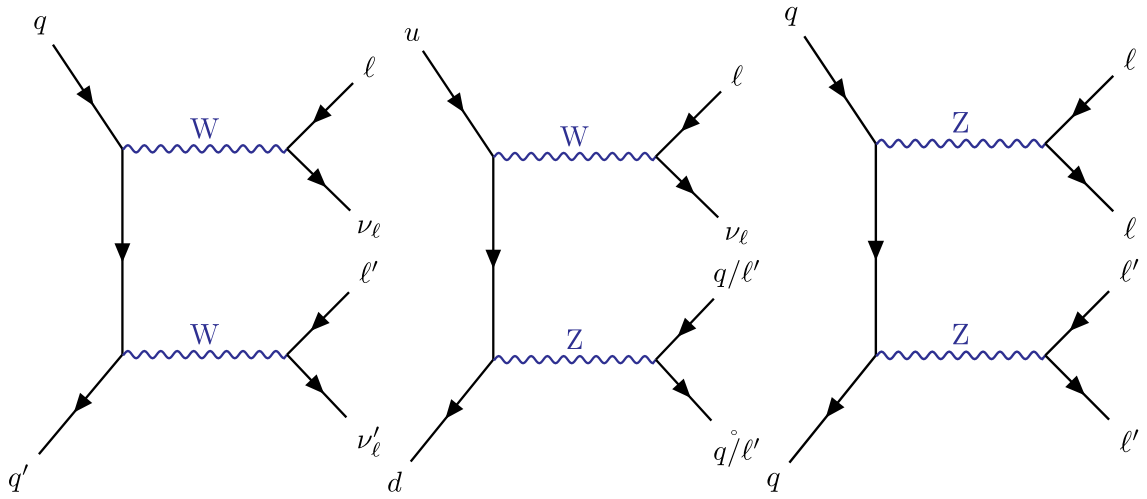

Figure 5.2.: Possible Feynman diagrams for the production of a WW, WZ or ZZ Diboson pair which decay into a final state with multiple leptons. The outcoming leptons can either have the exact final state with two leptons of different flavour (WW) or have multiple leptons where the additional leptons escape the reconstruction or do not fulfil the required quality of the identification. An additional possibility to mimic the final state of interest is the misidentification of jets from quarks as leptons or through the production of a tau lepton that decays into a muon or electron.

- Single top: An additional, but subleading background, is coming from single top production. The production of a single top can happen in association with a W boson in the tW channel (see Figure 5.3). In combination with the further decay of the top quark this can create a W boson pair that, in the end, can lead to the required final state. As the other channels (s and t channel) only contribute via the misidentification of leptons their contribution to the background description is very small.

  The single top background is produced with Powheg, separately for the top and antitop quark. The cross section is calculated at NNLO level [155].

- Drell-Yan: The last background is the Drell-Yan background with additional jets. It only contributes to the final state if the produced lepton pair is of the tau flavour and one of the taus decays into an electron or a muon or if one of the jets is misidentified as a lepton while one of the leptons of the pair production is not reconstructed or does not fulfil the identification requirements. The Drell-Yan background has therefore the smallest contribution to the background description.

  The Drell-Yan samples are binned in the mass of the lepton pair and produced with MadGraph5_aMC@NLO. The cross section is calculated at NLO level [156].

  A Feynman diagram of a Drell-Yan production can be seen in Figure 5.3.

Another important contribution to the Standard Model background is coming from jets misidentified as taus. This background makes up about 20 % of the total background events in the $\mu\tau$ channel. These would mainly be described by the W+jets background. As the difference in simulation to data for jets faking taus was estimated to be around 30 % [157], the CMS tau particle objects group recommends evaluating the fake rate of the specific analysis using a data

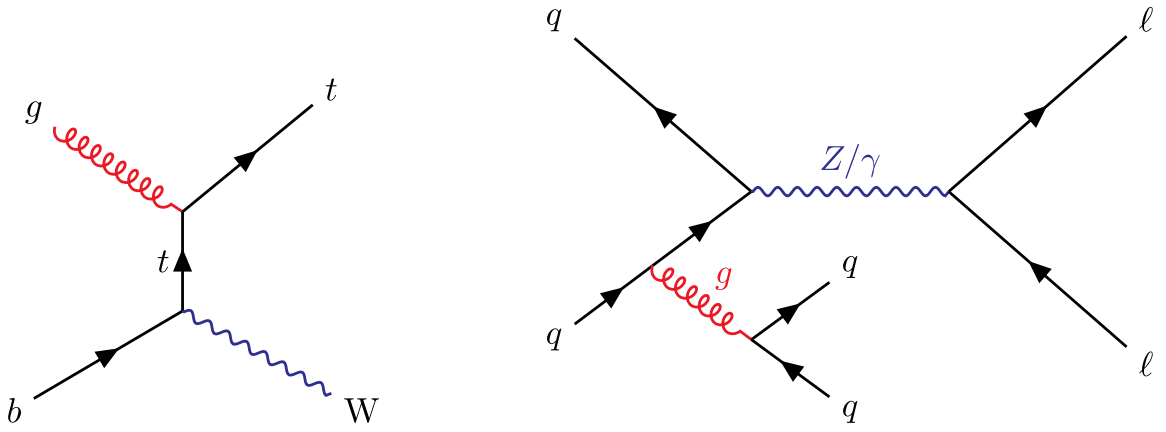

Figure 5.3.: Feynman diagram of single top production in the tW channel (left) and a Drell-Yan process with additional jets (right). The top quark of the tW channel can further decay which adds an additional W boson, ending up with a WW pair that can recreate the final state of two leptons with different flavour. The Drell-Yan process could produce a tau pair where one of the taus decays into another charged lepton.

driven technique in a control region similar to the signal region. This method will be described in more detail in Section 5.9.

The used background Monte Carlo samples can be found in Section A.1 with their corresponding cross sections.

5.4 Signal Production

This section describes the produced Monte Carlo simulation of different signal models investigated in this analysis. First, the production of the SSM Z′, RPV SUSY and QBH samples is discussed. Afterwards, the private production of the Sphaleron signal samples is explained in more detail.

5.4.1 SSM Z′

The production of the SSM Z′ signal Monte Carlo simulation is done on leading-order (LO) using Pythia8 [149] with the tune CP5, where "tune" describes the different settings of the parameters used in the generator [158]. Pythia8 is a tool to generate high-energy collision events including the interaction between the generated particles, parton showers, interactions, fragmentation and decay. It also allows the usage of different parton density functions (PDF). The specific "TuneCP5", which is the standard tune used in CMS for the years 2017 and later, uses the NNPDF 3.1 at NNLO [19]. The usual PDF set used for this tune is the "NNPDF31_nnlo_as_0118_luxqed". For the production done in CMS, this is changed to the "NNPDF31_nnlo_as_0118" set [19, 159].

The Z′ signal is produced for a Z′ mass of 500 GeV up to 6000 GeV. All mass points with their corresponding cross section can be seen in Table 5.2.

Figure 5.4 shows the invariant mass distribution of the lepton pair at the generator level for three different Z′ masses. The distributions are not normalized to a specific cross section and luminosity as they should only show the specific shape of the signal. Thus, the y-axis has "arbitrary units" (a.u.). The SSM Z′ produces a narrow resonance together with off-shell production which is visible at the lower mass regime and becomes more and more significant as the mass of the Z′ increases. The relative width of the Z′ is set to 3 % of its mass, similar to the SM Z.

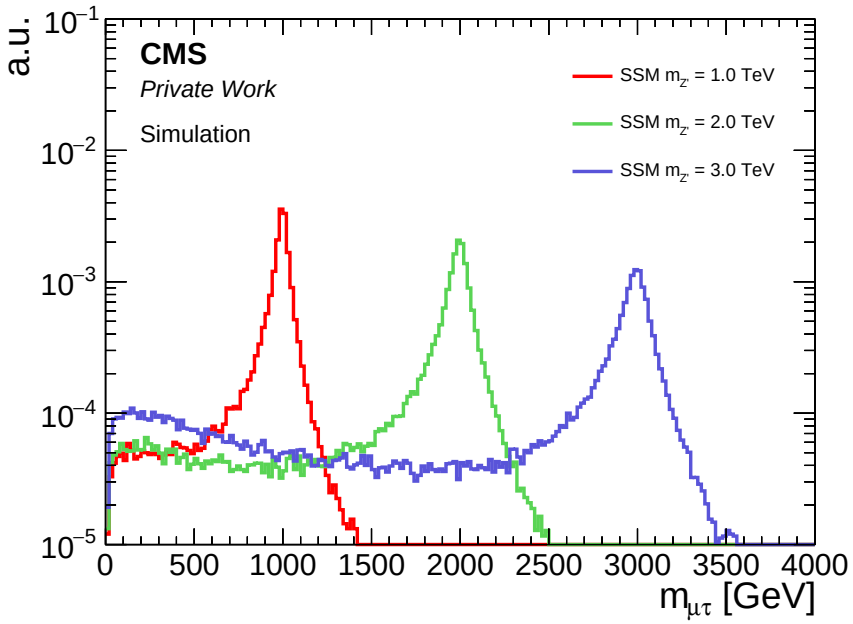

Figure 5.4.: SSM Z′ invariant mass of the lepton pair at the generator level for three different Z′ masses, namely for $m_{Z'} = 1$ (red), 2 (green) and 3 TeV (blue).

Table 5.2.: Different produced Z′ masses with their corresponding cross section calculated using the Pythia8 generator [149].

Z′ Mass (GeV)	$\sigma\,(q\bar{q} \to Z' \to \ell^{\pm}\ell^{\mp})$ (pb)
500	9.59
600	5.03
700	2.83
800	1.70
900	1.08
1000	0.71
1100	0.48
1200	0.33
1300	0.23
1400	0.17
1500	0.12
1600	$9.1 \cdot 10^{-2}$
1700	$6.8 \cdot 10^{-2}$
1800	$5.1 \cdot 10^{-2}$
1900	$3.9 \cdot 10^{-2}$
2000	$3.0 \cdot 10^{-2}$
2200	$1.8 \cdot 10^{-2}$
2400	$1.1 \cdot 10^{-2}$
2600	$7.2 \cdot 10^{-3}$
2800	$4.7 \cdot 10^{-3}$
3000	$3.1 \cdot 10^{-3}$
3500	$1.1 \cdot 10^{-3}$
4000	$4.8 \cdot 10^{-4}$
4500	$2.2 \cdot 10^{-4}$
5000	$1.1 \cdot 10^{-4}$
5500	$6.2 \cdot 10^{-5}$
6000	$3.9 \cdot 10^{-5}$

5.4.2 RPV SUSY

Instead of Pythia8, the RPV SUSY samples are generated with CALCHEP [160] which simulates high energy physics events at the parton level at LO. For the following parton shower and hadronization simulation, Pythia8 is used again.

CTEQ6L [161] is used as the parton density function for the production of the RPV SUSY signature. The samples are produced in a mass range of 200 GeV up to 6500 GeV.

Each produced mass point can be seen in Table 5.3, together with its corresponding cross section. The cross sections are corrected to NLO using the mass of the $\tilde{\nu}_\tau$ as the factorization and renormalization scales [162].

The invariant mass distribution on the generator level for three different masses of the RPV SUSY $\tilde{\nu}_\tau$ is shown in Figure 5.5. Again, this interpretation produces a very narrow resonance. Unlike the Z′, the RPV SUSY does not produce off shell $\tilde{\nu}_\tau$ due to its longer lifetime, also leading to a considerably smaller decay width. As mentioned in Section 2.3.1, the width of the Z′ is about 3 % of its mass while for the RPV SUSY $\tilde{\nu}_\tau$ it is at $\mathcal{O}(10^{-6} - 10^{-4})$ [163]. For the coupling of $\lambda = \lambda' = 0.01$, this interpretation produces a very narrow, delta-function like, peak at the resonance mass. Thus, this signal shape is well suited to test the reconstruction resolution of this analysis (see Section 5.7).

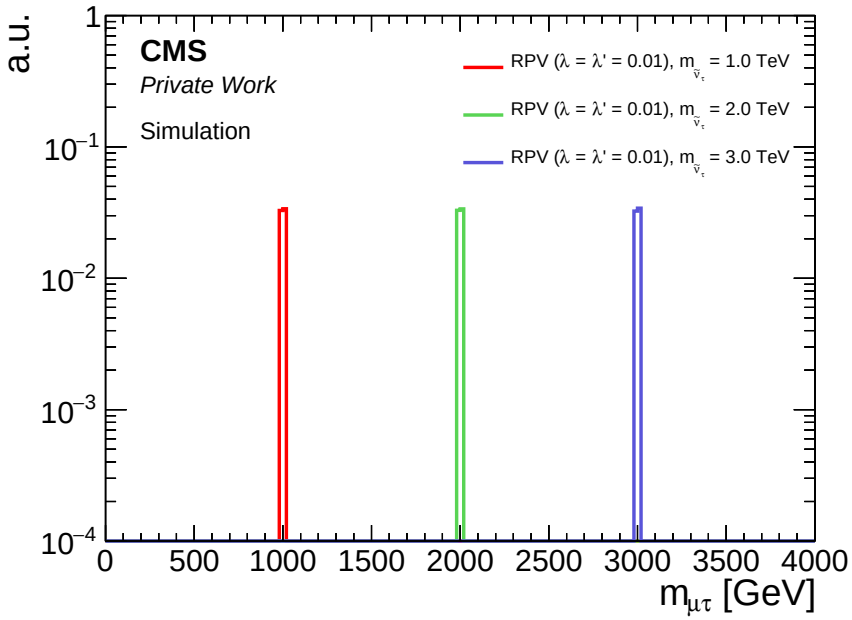

Figure 5.5.: Invariant mass distribution for three different $\tilde{\nu}_\tau$ masses using the RPV SUSY interpretation, namely for $m_{\tilde{\nu}_\tau} = 1$ (red), 2 (green) and 3 TeV (blue)

Table 5.3.: Cross sections of the production of a RPV SUSY $\tilde{\nu}_\tau$ for different masses at LO and their corresponding NLO k-factor [162].

RPV ($\lambda = \lambda' = 0.01$) $\tilde{\nu}_\tau$ mass (GeV)	$\sigma\,(q\bar{q} \to \tilde{\nu}_\tau \to \ell^\pm \ell^\mp)$ (pb)	k-factor
200	585	1.34
300	158	1.36
400	60.0	1.37
500	27.6	1.37
600	14.4	1.37
700	8.18	1.37
800	4.95	1.36
900	3.13	1.35
1000	2.06	1.34
1200	0.97	1.32
1400	0.49	1.3
1600	0.27	1.27
1800	0.15	1.25
2000	$8.6 \cdot 10^{-2}$	1.22
2500	$2.4 \cdot 10^{-2}$	1.16
3000	$7.2 \cdot 10^{-3}$	1.11
3500	$2.1 \cdot 10^{-3}$	1.08
4000	$6.4 \cdot 10^{-4}$	1.05
4500	$1.8 \cdot 10^{-4}$	1.05
5000	$5.1 \cdot 10^{-5}$	1.08
5500	$1.3 \cdot 10^{-5}$	1.17
6000	$3.3 \cdot 10^{-6}$	1.36
6500	$7.9 \cdot 10^{-7}$	1.68

5.4.3 QBH

For the production of the ADD quantum black hole signals, a dedicated generator `QBH3.0` [164] is used together with the `CTEQ6L` [161] PDF set. `QBH3.0` calculates the production of quantum black holes at leading order level and passes the events on parton level to Pythia8 for showering and hadronization, using the Les Houches accord (LHA) [165].

QBH samples are produced for different threshold masses, starting with 200 GeV up to 10 TeV. The produced mass points with their corresponding cross sections with $n = 4$ extra dimensions can be seen in Table 5.4. Unlike the two other interpretations mentioned so far, there is no resonant behaviour in the production of the QBH. Figure 5.6 shows the invariant mass distribution on the generator level. Until a specific threshold mass is reached, no production of QBH takes place, creating a sharp edge of the distribution with a falling tail.

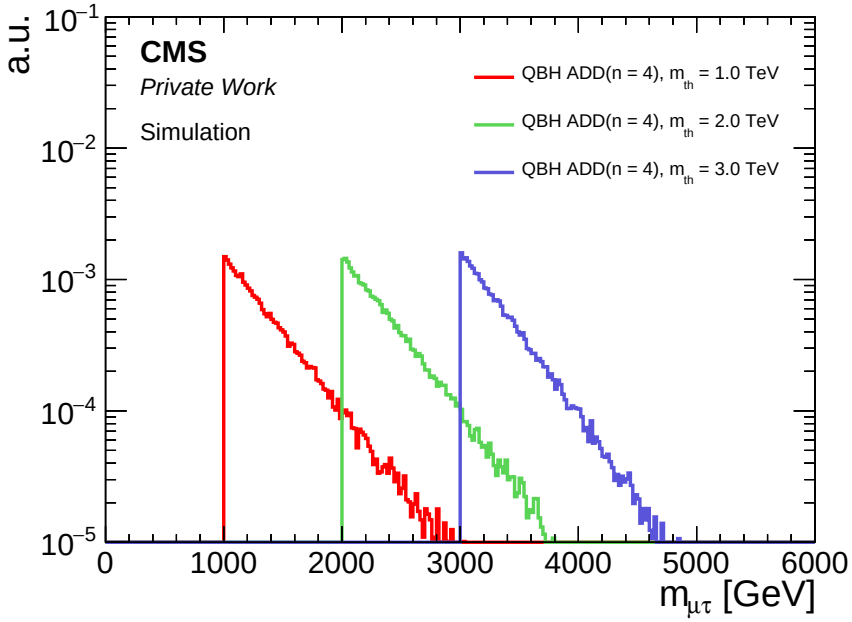

Figure 5.6.: Invariant mass distribution for the threshold masses of $m_{th} = 1$ (red), 2 (green) and 3 TeV (blue) using the QBH interpretation with $n = 4$ additional dimensions.

Table 5.4.: Cross section of the different QBH threshold masses with 4 extra dimensions at LO using the `QBH3.0` [164] generator.

QBH threshold Mass (GeV)	$\sigma\,(q\bar{q} \to \text{QBH} \to \ell^{\pm}\ell^{\mp})$ (pb)
200	$2.4 \cdot 10^{4}$
400	$1.7 \cdot 10^{3}$
600	$3.3 \cdot 10^{2}$
800	94.1
1000	33.2
1200	13.3
1400	5.96
1600	2.81
1800	1.42
2000	0.74
2500	0.17
3000	$4.2 \cdot 10^{-2}$
3500	$1.2 \cdot 10^{-2}$
4000	$3.2 \cdot 10^{-3}$
4500	$9.4 \cdot 10^{-4}$
5000	$2.7 \cdot 10^{-4}$
5500	$7.8 \cdot 10^{-5}$
6000	$2.2 \cdot 10^{-5}$
7000	$1.6 \cdot 10^{-6}$
8000	$9.3 \cdot 10^{-8}$
9000	$4.5 \cdot 1^{-9}$
10000	$1.6 \cdot 10^{-10}$

5.4.4 Sphaleron

The signal production of the sphaleron samples was not done using an official injection into the CMS computation chain but was instead computed on the Aachen Grid system using the same software and commands as in the official production. Thus, the chain of production is the same as described at the beginning of this chapter.

For the hard event production, the dedicated `BaryoGEN` [166] generator was used. This generator was also used to produce the signal samples of the latest sphaleron search publication from CMS [94]. `BaryoGEN` produces proton-proton collision events with sphaleron-like transitions and saves them in the *Les Houches* file format. Therefore, they can serve as an input to the production line for the full simulation which, in the end, results again in `NanoAOD` files which can be used later in the analysis workflow.

The generator allows us to set the center-of-mass energy, the threshold energy of the sphaleron, and the probability of positive changes in the Chern-Simons Number ($\Delta N = +1$) and also allows to turn off parton cancellations. For this thesis, the center-of-mass energy is set to 13 TeV with a probability of positive changes in the Chern-Simons number of 0.5 (which leads to the same probability for positive and negative changes) together with the option of parton cancellations. In total, five signal samples with different threshold energies (8 to 10 TeV in steps of 500 GeV) with $\approx$ 150.000 events each were created. The high number of events is needed for statistical reasons, as specific selections of each of the three final states reduce the number of events significantly.

The final particle content of this signal is significantly different to those described previously. Instead of a two particle final state, a sphaleron decay produces events with a high multiplicity as described in Section 2.2. The particle content and the number of particles per event can be found in Figure 5.7. The number of up quarks is significantly higher than other particles, as the sphaleron is mostly created by colliding up quarks. In the case of $\Delta N_{CS} = +1$, these up quarks do not cancel out (see for example Equation 2.20 in Section 2.2). Equation 2.20 also shows why the number of quarks is higher than the number of leptons as at least nine quarks are generated compared to only three leptons. Additionally, the shape of the collinear mass does not show a peak like structure, like the Z' or RPV, but a widespread, falling distribution over the whole mass spectrum (see Figure 5.8) more similar to the one in the QBH interpretation.

The cross section is calculated using the parametrization described in Section 2.2. The code for the cross section calculation and the results were developed and checked in close contact with Kazuki Sakurai, the main author of [26]. The script can be found at [167].

The CT14 PDF set was chosen, following the recommendation from the CMS MC group and the previously published CMS sphaleron search. The CT14 PDF set does not use modern machine learning techniques e.g. the `NNPDF`, which could lead to a problem since the signal lies mainly in the high energy regime where the amount of data is not sufficient to train a machine learning network. The result of the cross section calculation using the CT14 PDF set can be seen in Table 5.5.

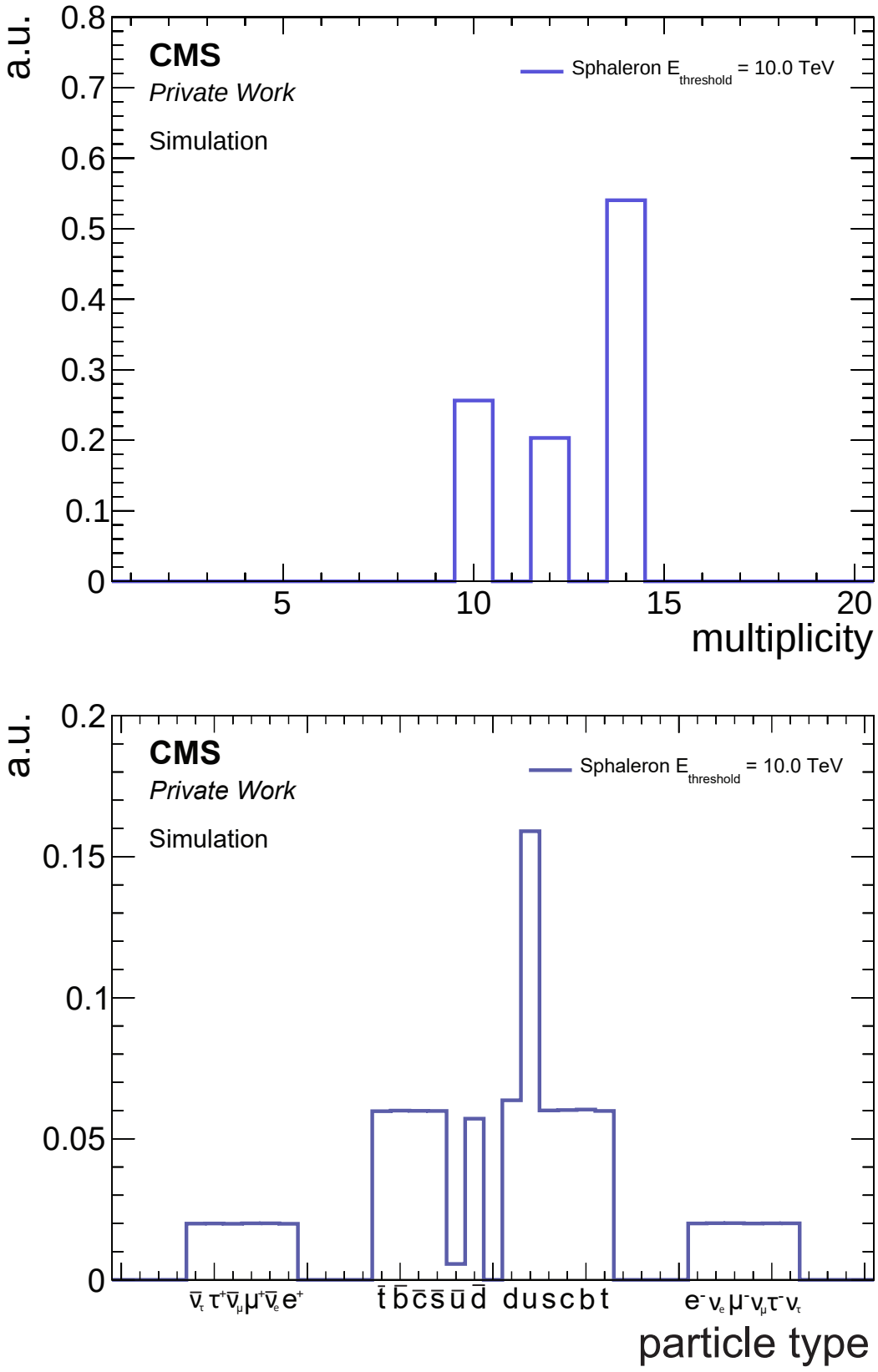

Figure 5.7.: Multiplicity distribution (top) and particle types (bottom) from sphaleron decays at $\sqrt{s} = 13\,\text{TeV}$ with a $E_{Sph} = 10\,\text{TeV}$ on generator level.

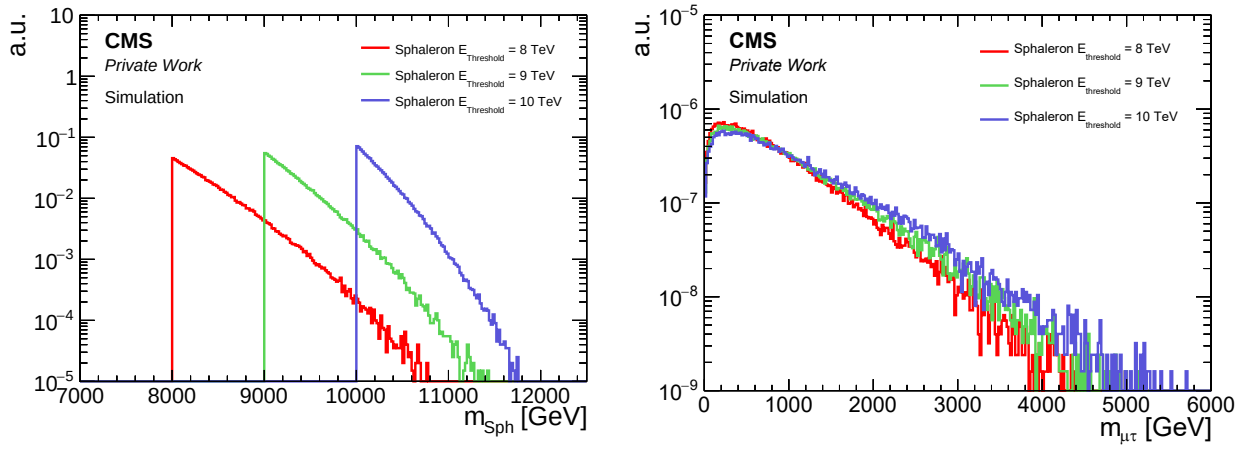

Figure 5.8.: Mass distribution of the sphaleron decay using all outgoing particles (left) and only a muon and a tau (right). For the left plot, the threshold at the potential maximum is clearly visible as a sharp edge while for the right plot the edge is strongly smeared out leaving a wide, falling distribution over the full mass range.

Table 5.5.: Cross section of the different sphaleron energies E_{Sph} using the CT14 PDF set.

E_{Sph} (GeV)	$\sigma(q\bar{q} \to Sph \to X)$ (fb)
8000	150
8500	48.8
9000	13.96
9500	3.34
10000	0.63

5.4.5 Signal Efficiency

Figure 5.9 shows the acceptance times efficiency ($A \times \epsilon$) of the selection of a $\mu\tau$ pair for all four different interpretations as the function of the theoretical mass m_{theo} corresponding to the mass points shown in the cross section tables in Section 5.4. In the case of the sphaleron, $m_{theo} = E_{sph}$. The SSM Z' signal shows a curved shape due to its significant off-shell production for higher energies, reaching a maximum of about 23 % at 2 TeV and then going down again. Instead, the RPV and the QBH interpretation show a rise in efficiency for lower energies which then saturates in the high energy regime at 1 TeV with around 25 % followed by a slowly falling slope.

Due to its rather flat signal shape with a significant amount of events to be found in the low energy regime, the resulting selection efficiency of the sphaleron signature lies at around 9 to 10 %, which is approximately half of the average efficiency of the SSM Z'.

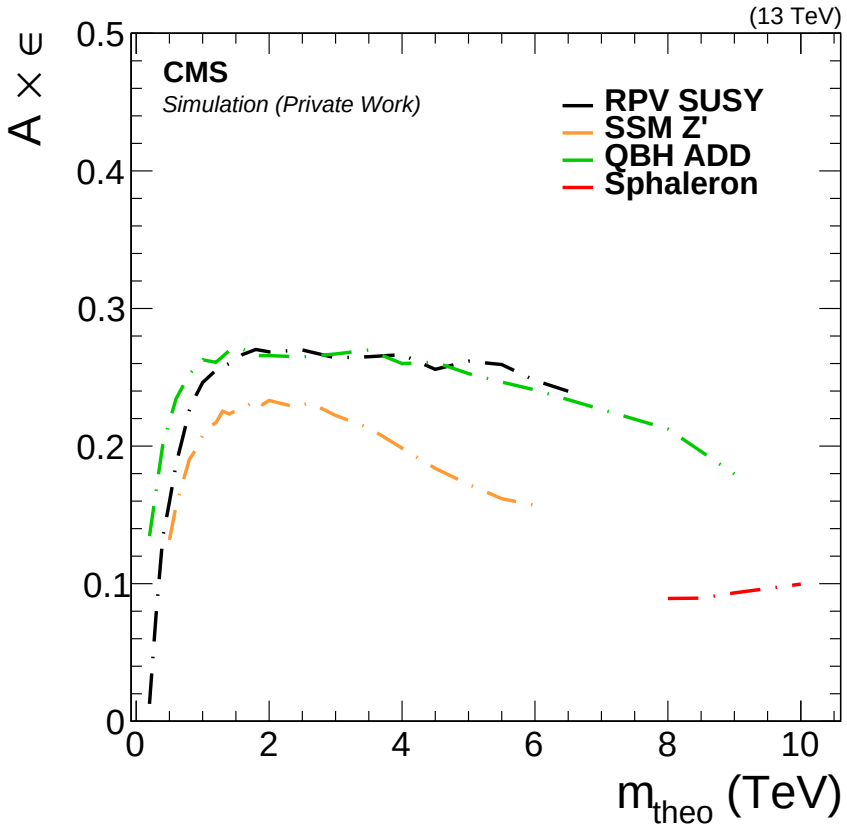

Figure 5.9.: Plot of the acceptance times efficiency for the four different interpretations. The SSM Z' (orange) signal shows a curved shape due to its significant off-shell production for higher energies whereas the RPV (black) and the QBH (green) interpretation show a rise in efficiency for lower energies which then saturates in the high energy regime. The sphaleron signal (red) shows a significantly smaller efficiency due to its signal shape.

5.5 Normalization and Corrections

Even though the simulation of Standard Model background processes is done at a high precision level, it can not reproduce all effects and unforeseen impacts of the detector and data taking. To account for these effects, and to get a better description of the actual measurement, one uses corrections or scale factors.

These include higher order cross section calculations of the relevant processes as well as weights calculated from the comparison of the simulation and the measured data.

Lastly, the simulated background also needs to be normalized to the actual measured luminosity for each single year. The final normalization factor, assuming all corrections and additional weights are already applied, is:

$$w = \frac{\sigma \cdot L}{N_{gen}}, \tag{5.1}$$

with σ being the cross section of the specific process, L the integrated luminosity of the data collected and N_{gen} the total number of generated events.

The following section will describe all corrections and scale factors applied in this analysis.

5.5.1 Pileup

During proton-proton collisions, more than one single interaction happens per bunch crossing. It is possible to have multiple collisions at nearly the same time. The additional interactions, which are not the hard process one is interested in, are called pileup [168]. The higher the instantaneous luminosity, the higher the number of such pileup interactions. An example of the distribution in the simulation and in the measured data of the pileup, represented by the number of reconstructed vertices per event, can be seen in Figure 5.10. Simulated events are created assuming a total inelastic cross section (also called mini bias cross section) of 69.2 mb [169]. As one can see, the simulation differs from the measured data. Therefore, the MC is corrected to create a better representation of the actual measurement by applying an event weight correction factor on the simulated samples.

A comparison of the distribution of the number of primary vertices before and after applying the pileup correction can be seen in Figure 5.11. This correction is applied per single event to the Monte Carlo, depending on the number of primary vertices reconstructed in the event. It does not change the normalization of the process but instead affects its shape. The application of this correction does not necessarily lead to better data to Monte Carlo agreement in the number of primary vertex distributions at the final stage of the analysis. Especially, in the high pileup regime, it is difficult to model such distribution even using data driven techniques.

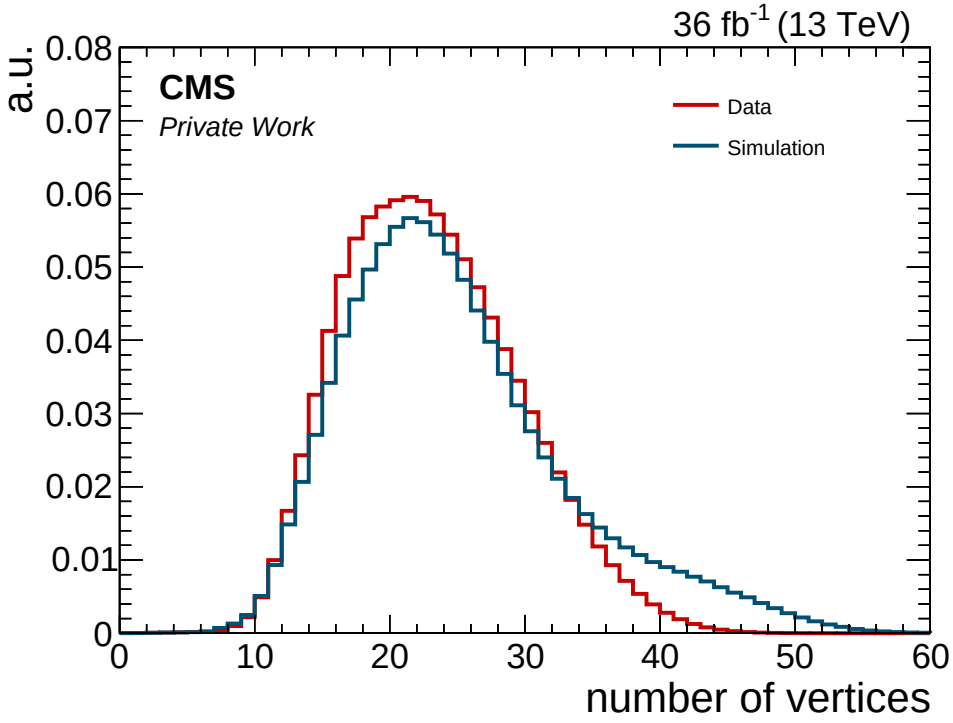

Figure 5.10.: Example of the pileup distribution in the simulation (blue) and the measured data (black) from the year 2016. From these distributions, a correction factor is calculated and later applied to the simulation on an event by event basis.

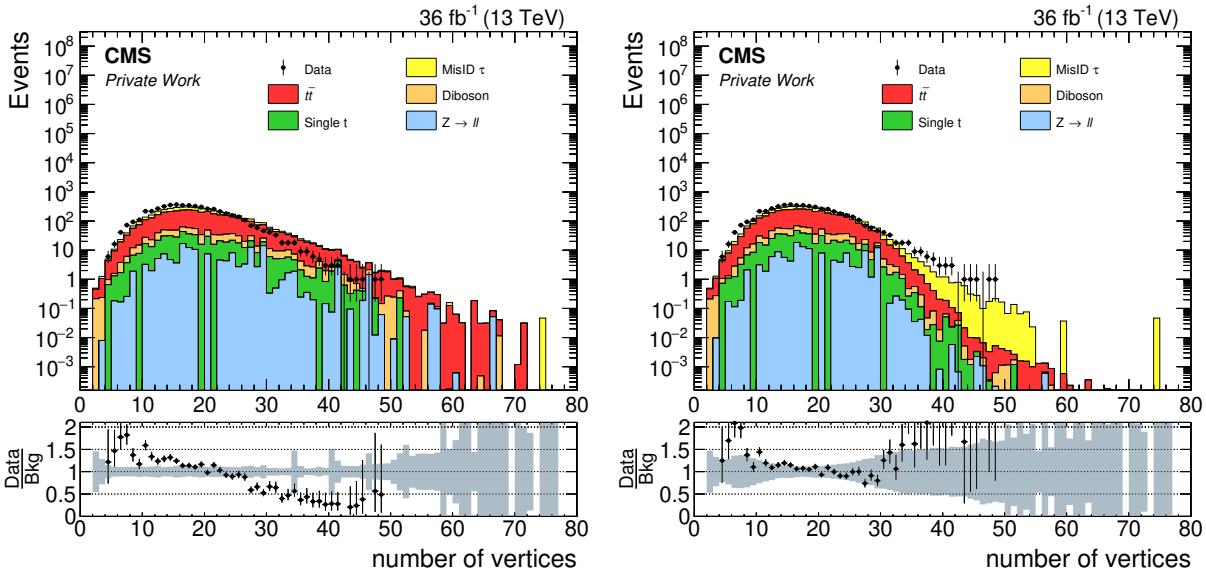

Figure 5.11.: Distribution of the number of primary vertices before (left) and after (right) applying the pileup correction for the year 2016.

5.5.2 Prefiring

In the years 2016 and 2017, a radiation induced transparency loss in the ECAL crystals led to a shift of the ECAL pulse shape. This pulse shift introduced a rising timing calibration offset, which was not corrected online for the ECAL trigger primitives (TP). The shape would move into the edge of the trigger bunch crossing assignment, leading to a wrong assignment of energy deposition to the previous bunch crossing. This could lead to the acceptance of the earlier bunch crossing as the "interesting" one, whereas the actual bunch crossing would be rejected due to the dead time of the trigger and the low energy deposition. Such an effect is called "prefiring" and was corrected in early 2018 [170].

As prefiring is not well simulated, additional corrections have been introduced for 2016 and 2017 to take this phenomenon into account [171].

5.5.3 Trigger

To ensure a well fitting description of the behaviour of the chosen combination of triggers for the different final states, the trigger efficiency in simulation and measured data is compared.

Differences between the modelling of the trigger and the actual measurement are taken into account by applying a trigger scale factor to the Monte Carlo description, achieving a consistent efficiency curve.

These scale factors are approved and provided by the different CMS physics object groups (POG) [121, 172]. The trigger scale factors used in the $e\tau$ channel were calculated by Amandeep Kaur Kalsi and can be found in Section A.2.

All trigger combinations show a so-called "turn-on" effect at low p_T which describes the area of the rising edge where the efficiency has not yet reached its plateau. As this part is difficult to simulate, a suitable low p_T threshold to avoid this turn-on range is introduced for the triggering object.

An example of this "turn-on" effect from the single muon trigger used in this thesis can be seen in Figure 5.12, showing the L1 + HLT efficiency as a function of the muon p_T. The efficiency is at zero for $p_T < 40\,\text{GeV}$ and then starts to rise reaching its plateau around 50 GeV.

5.5.4 Top Background

As mentioned in Section 5.3, the top background is the dominant process to produce a final state with two leptons of different flavours. Therefore, it is important to have a precise description of its contribution and shape. Therefore, a formula was derived to include NNLO QCD and NLO EW corrections to the shape of the top background [150].

The correction takes the top and antitop transverse momentum into account and uses the geometrical average of both weights:

$$w_{top,antitop} = e^{0.0615 - 0.0005\,\text{GeV}^{-1} \cdot p_T^{top,antitop}}, \; w = \sqrt{w_{top} \cdot w_{antitop}}. \tag{5.2}$$

This weight factor introduces additional systematic uncertainties, which result from the theory calculation. These include the uncertainty from the chosen PDF set by varying the weight, as

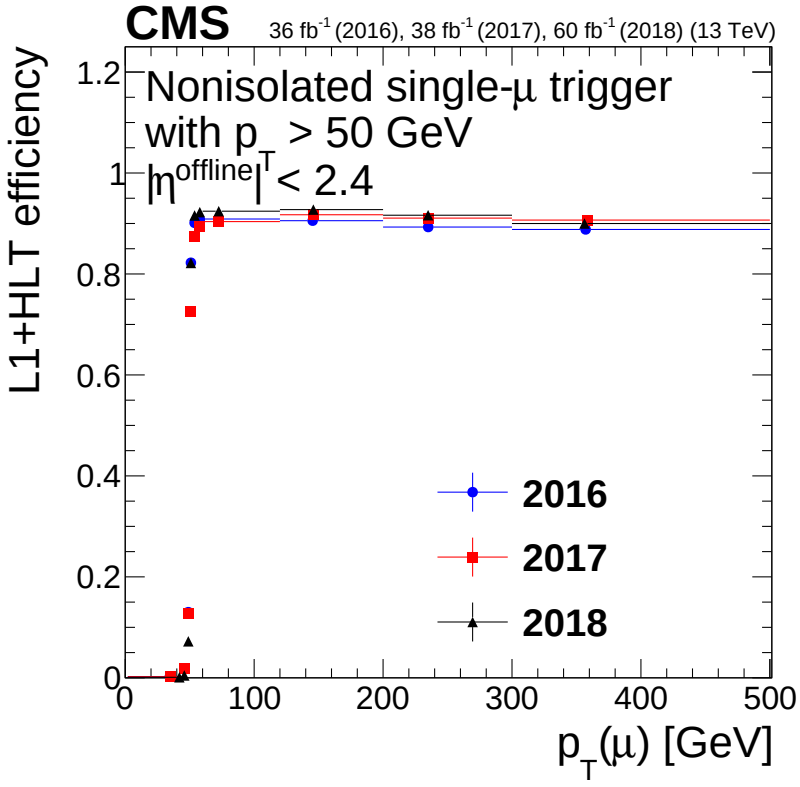

Figure 5.12.: L1 + HLT efficiency of the non-isolated single muon trigger as a function of the muon p_T. The efficiency starts at zero for muons with a $p_T < 40\,\text{GeV}$ and then begins to rise, reaching its plateau around 50 GeV. Taken from [173]

well as the uncertainty on the Q scale by varying the renormalization and factorization factor between 0.5 and 2. These uncertainties can be seen in Figure 5.13.

5.5.5 Object Related Corrections

Similar to trigger scale factors, the reconstruction and identification of physical objects can differ between the simulation and the actual detector response and measurement. To correct these discrepancies, each POG provides scale factors for their ID and the reconstruction.

Electron

The efficiency of reconstructing an electron object differs between the MC simulation and the measured data. To correct this, the E/Gamma POG provides "reco scale factors" binned in the super cluster η of the electron object. The sizes of the correction vary between 1-2 % and are provided for each year [122].

The scale factors on the HEEP identification efficiency of the electron are found to be flat in p_T. They are provided for the Barrel and the Endcap for each year of Run 2 and can be seen in Table 5.6.

Additionally, differences in the scale and resolution, mainly measured in $Z \to ee$ events, are observed and corrected. This can be done by smearing the resolution in the simulation to fit the

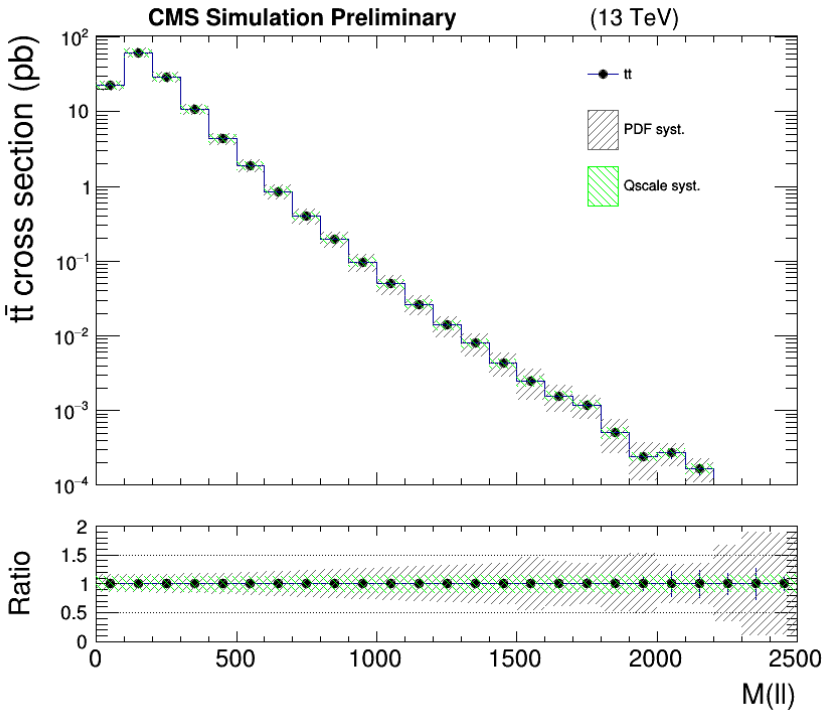

Figure 5.13.: Shape of the NNLO QCD + NLO EW $t\bar{t}$ background with the PDF and Q scale systematic uncertainties shown in gray and green, respectively. These can rise to over 50% at high invariant masses and provide the dominant uncertainty for this background (taken from [134], by Reza Goldouzian).

Table 5.6.: Scale factors for the HEEP identification efficiency to correct for differences between Monte Carlo simulation and measured data for all three years of Run 2 with their corresponding statistical uncertainty provided by the CMS EGamma POG [122].

Year	Barrel	Endcap
2016	0.971 ± 0.001 (stat.)	0.983 ± 0.001 (stat.)
2017	0.967 ± 0.001 (stat.)	0.973 ± 0.002 (stat.)
2018	0.969 ± 0.000 (stat.)	0.984 ± 0.001 (stat.)

measured one. This correction from the E/Gamma POG is already applied "out-of-the-box" to the official `NanoAOD` samples.

Muon

Similar to the electron object, the muon object also needs corrections to mimic the behaviour of the data in the simulation. The CMS Muon POG provides scale factors for the reconstruction and identification efficiency. Moreover, it also provides scale factors for the isolation efficiency of the muon [174–176].

The differences between simulation and data for the reconstruction efficiency lie between 0.8 % and 2 % for increasing momenta. For the identification efficiency, the difference is between 0.8 %

for small values in η and up to 2.7 % for high η muons, independent of the p_T. The difference in the isolation efficiency lies around 0.1 % or lower.

Additionally, an extra Gaussian smearing is applied to the simulation to match the measured resolution. This smearing is applied to muons with an $|\eta| > 1.2$ where the measured resolution in boosted Z events shows a difference between data and simulation, where the resolution in MC appears to be more narrow. Therefore, an additional smearing of 15 % is applied to the muon momentum by drawing a random number from a Gaussian distribution:

$$p_{new} = p \cdot (1 + G(0, 0.57 \cdot \sigma(p, \eta))) \tag{5.3}$$

where p is the muon momentum and G the Gaussian function with a mean 0. The σ in this case corresponds to the parametrization of the momentum resolution which depends on η and the momentum p, varying for each year [174–176]. A 4th degree polynomial is chosen for the parametrization:

$$\sigma(p) = a + b \cdot \left(\frac{p}{\text{GeV}}\right) + c \cdot \left(\frac{p}{\text{GeV}}\right)^2 + d \cdot \left(\frac{p}{\text{GeV}}\right)^3 + e \cdot \left(\frac{p}{\text{GeV}}\right)^4. \tag{5.4}$$

The parameters a, b, c, d and e can be found in Table 5.7 depending on the η and the year.

Table 5.7.: Parameters of the muon momentum resolution for different ranges of η, per year of Run 2, provided by the Muon POG. This parameters are used for the smearing of the Monte Carlo simulation, as well as to estimate the resolution uncertainty [174–176].

2016

	a	b	c	d	e
$0.0 \leq \lvert\eta\rvert < 1.2$	0.006	0.00001	$-1.0 \cdot 10^{-7}$	$-5.7 \cdot 10^{-11}$	$-1.1 \cdot 10^{-14}$
$1.2 \leq \lvert\eta\rvert < 2.1$	0.0134	0.000063	$-4.7 \cdot 10^{-8}$	$-2.6 \cdot 10^{-11}$	$-5 \cdot 10^{-15}$
$2.1 \leq \lvert\eta\rvert < 2.4$	0.0151	0.000114	$-3.7 \cdot 10^{-8}$	$-3.9 \cdot 10^{-12}$	$1 \cdot 10^{-15}$

2017

	a	b	c	d	e
$0.0 \leq \lvert\eta\rvert < 1.2$	0.0053	0.00011	$-1.3 \cdot 10^{-7}$	$+6.9 \cdot 10^{-11}$	$-1.3 \cdot 10^{-14}$
$1.2 \leq \lvert\eta\rvert < 2.1$	0.0136	0.000063	$-2.6 \cdot 10^{-8}$	$-1.3 \cdot 10^{-11}$	$3 \cdot 10^{-15}$
$2.1 \leq \lvert\eta\rvert < 2.4$	0.0170	0.000084	$2.6 \cdot 10^{-9}$	$-2.3 \cdot 10^{-14}$	$8 \cdot 10^{-15}$

2018

	a	b	c	d	e
$0.0 \leq \lvert\eta\rvert < 1.2$	0.0062	0.000096	$-9.7 \cdot 10^{-8}$	$-4.9 \cdot 10^{-11}$	$9 \cdot 10^{-15}$
$1.2 \leq \lvert\eta\rvert < 2.1$	0.0136	0.000052	$-2.4 \cdot 10^{-8}$	$-5.5 \cdot 10^{-11}$	0
$2.1 \leq \lvert\eta\rvert < 2.4$	0.0174	0.000087	$-3.3 \cdot 10^{-9}$	$-1.6 \cdot 10^{-11}$	$5 \cdot 10^{-15}$

Regarding the p_T assignment, the muon system becomes more important for high-p_T muons. The Rochester method, which was used in earlier years and for low to medium-p_T muons to estimate the scale bias from the Z peak measurement, is not reliable anymore. A new momentum scale measurement, named "Generalized Endpoint" (GE), was developed for high-p_T muons [123]. Rather than providing a scale correction, this method calculates uncertainties on the scale which

cover the differences between the simulation and the measured data.

Tau

As explained in Section 4.4.3, the tau identification provides three discriminators, namely against jets, muons and electrons. Each of these performs slightly differently in simulation compared to the measurement. These differences depend on the decay mode but are flat in p_T, especially in the regime which is of interest for this thesis. The size of the difference between data and MC for the anti jet discriminator ranges from 5 to 12%. The impact of the scale factors of the anti-electron and anti-muon discriminator is small. They only apply to tau objects coming from electrons or muons and the discrimination performance is very strong.

Additionally, the simulated tau energy scale is corrected to mimic the behaviour of the actual measurement. For taus with a $p_T < 34\,\text{GeV}$, the corrections are coming from the measurement of $Z\rightarrow \tau\tau$, whereas for taus with a $p_T > 170\,\text{GeV}$ they come from $W^*\rightarrow \tau\nu$, correcting a shift in the energy measurement of the tau object. For taus in between these p_T values, the correction factor is calculated as a linear interpolation between these two extrema.

The energy scale correction depends on the p_T, as well as on the decay mode of the tau.

$\vec{p}_T^{\,\text{miss}}$ & Jets

The quantity $\vec{p}_T^{\,\text{miss}}$, described in Section 4.5, depends on the reconstructed objects in the event. Specifically, changes in the quantities connected to jet objects lead to significant changes in the $\vec{p}_T^{\,\text{miss}}$ calculation.

The difference arising from the jet energy correction is taken into account to calculate the so called "type-1" $\vec{p}_T^{\,\text{miss}}$:

$$\vec{p}_T^{\,miss,JECcorrected} = \vec{p}_T^{\,miss} - \sum_{i\in jets} (\vec{p}_T^{\,i,JEC} - \vec{p}_T^{\,i}) - \sum_{i\in unclustered} \vec{p}_T^{\,i}. \tag{5.5}$$

Here, in the first sum, $\vec{p}_T^{\,i,JEC}$ corresponds to the jet p_T including the jet energy correction whereas $\vec{p}_T^{\,i}$ is the p_T of the uncorrected jet object. The second sum describes the amount of p_T originating from PF candidates where the algorithm was not able to associate them to neither an electron, muon, photon, hadronic tau nor jet [133].

Jet energy corrections are applied in different steps. Initially, the object is corrected for additional energy coming from pileup by comparing events with and without pileup overlay in simulated events. To determine the necessary correction in data, differences between the actual measurement and the simulation are calculated using a random cone method in zero-bias events. These events are triggered without considering a specific event content.

Additionally, a response correction is calculated by comparing generator jets to the simulated detector response for different jet sizes. Afterwards, the data is corrected to the residual difference between the measurement and the simulation using dijet, Drell-Yan and multijet events, using the p_T balancing and the missing transverse momentum projection fraction method [177]. These corrections are then propagated to the $\vec{p}_T^{\,\text{miss}}$ calculation following Equation 5.5.

As this thesis uses high-p_T muons with the Tune-P p_T (see Section 4.3), the $\vec{p}_T^{\,\text{miss}}$ calculation coming from the PF algorithm also needs to be corrected by the difference between the PF muon p_T and the Tune-P p_T:

$$\vec{p}_T^{\,miss,final} = \vec{p}_T^{\,miss,JECcorrected} - \sum_{i \in muons} (\vec{p}_T^{\,i,Tune-P} - \vec{p}_T^{\,i,PF}). \tag{5.6}$$

Due to an interplay between the ECAL ageing, the pileup, and the LHC bunch structure, an enhanced $\vec{p}_T^{\,\text{miss}}$ tail in the measurement was observed in 2017, which was not visible in the simulation. To cope with this so called "EE Noise", an additional correction for the $\vec{p}_T^{\,\text{miss}}$ was introduced for the year 2017. This problem was not present in 2016 and was fixed after the 2017 run was completed [178].

5.6 Discriminating Variable

The discriminating variable between the signal and the background for this analysis is the invariant mass of the lepton pair. Regarding tau channels, the invariant mass calculation of the actual tau and the other lepton is more difficult than for the eμ channel, since the tau decays before reaching the detector and only the visible, hadronic part can be reconstructed.

To take this effect into account, a new variable is defined called "collinear mass", which approximates the four momentum of the tau object. Besides the visible decay product τ_{vis}, a neutrino is produced showing up as $\vec{p}_T^{\,\text{miss}}$ in the measurement. As the tau object is assumed to have high momentum, the decay products are boosted in the same direction and, most likely, propagate in the same direction. The $\vec{p}_T^{\,\text{miss}}$ vector is projected onto the $\boldsymbol{p}_T$ vector of the tau ($\vec{p}_T^{\,\tau}$) to create the $\vec{p}_T^{\,\text{miss}}$ object going in the same direction as the tau, called $\vec{p}_{T,\text{coll}}^{\,miss}$. A correction factor x is defined as the ratio of the magnitude of the visible tau momentum p_T^τ and the sum of p_T^τ and the magnitude of the collinear missing transverse momentum $p_{T,\text{coll}}^{miss}$:

$$x = \frac{p_T^\tau}{p_T^\tau + p_{T,\text{coll}}^{miss}}. \tag{5.7}$$

Now, the four momentum of the visible tau $\boldsymbol{\tau_{vis}}$ can be rescaled to approximate the tau four momentum including the neutrino, $\boldsymbol{\tau_{\text{coll}}}$, using this correction factor x:

$$\boldsymbol{\tau_{\text{coll}}} = \frac{\boldsymbol{\tau_{vis}}}{x}. \tag{5.8}$$

The final discriminating variable is then the invariant mass of this new tau object τ_{coll} and the light lepton:

$$m^2_{\ell\tau_{\text{coll}}} = (\boldsymbol{\ell} + \boldsymbol{\tau_{\text{coll}}})^2, \tag{5.9}$$

with $\boldsymbol{\ell}$ representing the four momentum of the light charged lepton and $\boldsymbol{\tau_{\text{coll}}}$ being the tau four momentum from the collinear approximation.

Figure 5.14 shows the resolution of three different approaches to reconstruct the mass of the two lepton system. The resolution is derived by subtracting the reconstructed mass from the mass on

generator level and further dividing this difference by the generator mass:

$$(m - m_{gen})/m_{gen}. \tag{5.10}$$

The first blue curve uses the visible reconstructed objects, in this case the muon and the visible reconstructed hadronic tau. The "visible mass" approach, pictured in green, includes the $\vec{p}_T^{\,\text{miss}}$ of the events by adding the four momenta of the three objects[3] (muon, tau and $\vec{p}_T^{\,\text{miss}}$) and calculating the invariant mass. Lastly, the red curve shows the resolution for the presented collinear mass approach.

Using only the visible objects of the event, a significant amount of information is lost, smearing out the resolution significantly. While adding the $\vec{p}_T^{\,\text{miss}}$ information recovers most of this information, the collinear mass approach provides the best way of reconstructing the invariant mass of the muon and the underlying tau object since it includes the approximation of the neutrino and its direction.

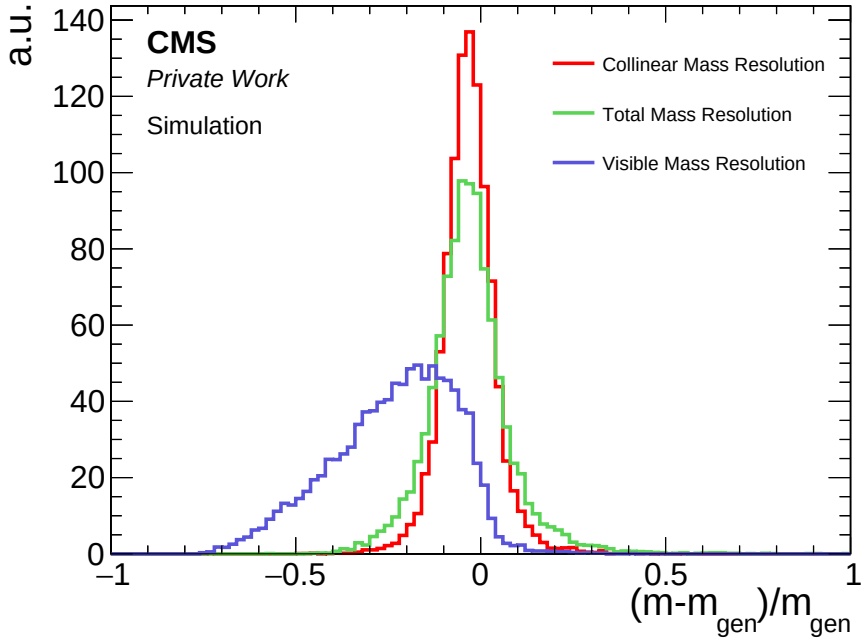

Figure 5.14.: Resolution of the different approaches to reconstruct the invariant mass of the $\mu\tau$ system, using a simulated sample of an SSM Z' with a mass of 1.5 TeV. The blue curve uses only the visible reconstructed objects (visible mass), the green curve additionally includes the $\vec{p}_T^{\,\text{miss}}$ (total mass) and the red curve shows the resolution using the collinear mass approach.

[3] As $\vec{p}_T^{\,\text{miss}}$ is only measured in the x-y-plane, the η component of the four vector is set to 0 to create an usable four vector object.

5.7 Mass Resolution

Using the produced RPV signal samples, a study was done on the mass dependency of the resolution. For each mass point, the reconstructed mass was compared to the generated mass, using Equation 5.10.

To determine the relative resolution per mass point, a Gaussian fit was performed, using the standard deviation as the mass resolution. This procedure is illustrated in Figure 5.15 (left) for the RPV signal point with the tau sneutrino mass of 1000 GeV. Figure 5.15 (right) shows all mass points with their corresponding relative resolution. At lower masses, the assumption that the reconstructed tau object and the neutrino are necessarily boosted in the same direction (as they both carry a high momentum) does not hold anymore, leading to a lower mass resolution. At very high masses, where the collinear approximation holds, the object resolution of the muon and the tau dominate leading to a slowly declining resolution.

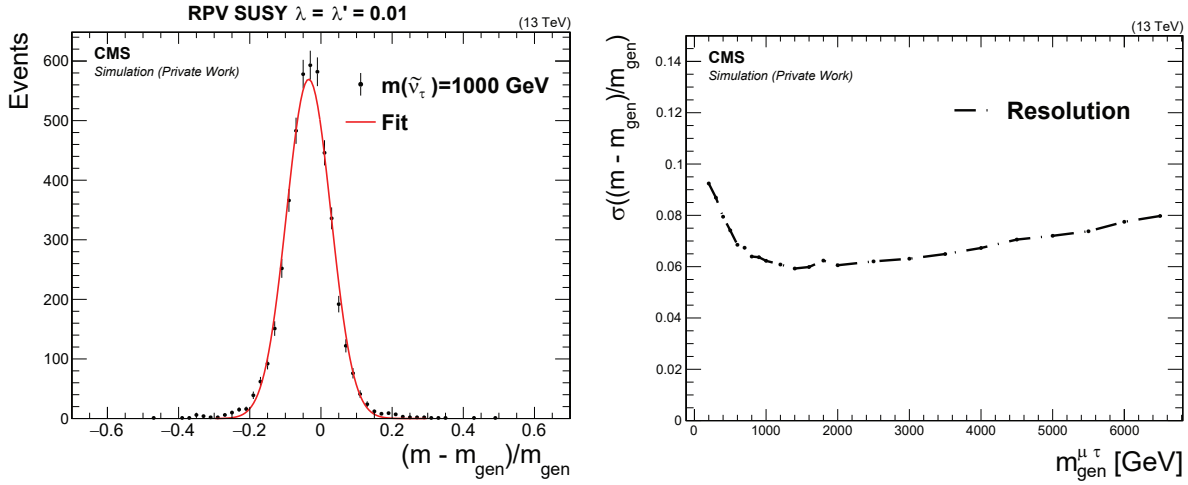

Figure 5.15.: Relative resolution of one RPV signal mass point for a tau sneutrino mass of 1000 GeV (left), and for all mass points (right) for the $\mu\tau$ channel. The resolution at the lower mass regime is worse as the assumption of a collinear tau does not hold for low energies.

The bin width of the collinear mass is chosen according to this measurement of the relative resolution, choosing a minimum step width of 50 GeV at low masses. At high masses, the provided background statistics need to be accounted for as well, leading to wider bins compared to the calculated resolution.

5.8 Event selection

This section will describe the selection criteria for each of the three channels, to accept an event for the final stage of the analysis. As explained previously, all three possible leptonic channels, $e\mu$, $e\tau$ and $\mu\tau$, will be described, since the final mass distribution of the eμ and the eτ channel is used in the statistical interpretation. All channels contain, exclusively, certified events which are additionally filtered for harmful detector effects or reconstruction problems. These filters are developed by the CMS JetMET particle objects group, as these issues usually show up in the measurement of the $\vec{p}_T^{\,\text{miss}}$ and, therefore, these filters are called $\vec{p}_T^{\,\text{miss}}$-filter[4] [133].

The recommended filters are:

- Primary Vertex Filter: Only events with primary vertices of good quality are accepted. Problematic events are, for example, events with high energy deposition in the calorimeters while lacking hits in the tracker system or hard collisions that happened outside of the detector center.
- Beam Halo Filter: Secondary particles produced by the interaction between the beam and the residual gas or with the pipe of the LHC can create a halo, depositing energy in the calorimeter system. If these halo interactions are identified, the event is vetoed.
- HBHE Noise Filters: The scintillator system of the HCAL is known to create sporadic noise, regardless of the beam condition. By taking into account the number of occupied pixels, the quality of the shape and the topology of the signal, these noise events are selected and vetoed.
- ECAL TP Filter: Some crystals in the ECAL are marked as single noise crystals during the reconstruction. This can be due to radiation which can turn single crystals into "dead" cells or due to a missing data link to the front end of the electronics. Using trigger primitive (TP) information the energy can still be approximated. As the TP E_T saturates at 127.5 TeV, events with ECAL towers from the affected regions close to the TP saturation are vetoed.
- Bad PF Muon Filter: The quality of a muon candidate can be sufficiently high to be considered as a PT muon but still fail the later muon identification quality criteria. This muon is still used in the PF $\vec{p}_T^{\,\text{miss}}$ calculation. Events with such muons with a p_T greater than 100 GeV are vetoed.
- EE badSC Noise Filter: Two Endcap supercrystal regions in the ECAL show anomalously high energy spikes, appearing in several channels simultaneously. Events showing these spikes in these specific regions are vetoed. This filter only affects events from measured data and not simulation.
- ECAL bad calibration filter: Some crystals in the high η region of the ECAL Endcap show large laser calibration corrections in the years 2017 and 2018. Events showing this issue in these two years are vetoed.

After selecting certified events and vetoing events containing the described $\vec{p}_T^{\,\text{miss}}$ effects, additional channel specific selections are applied which will be described in the following subsection. The selections are chosen to keep the analysis as model independent as possible.

[4] For historical reasons these filters are often called MET-filters, as $\vec{p}_T^{\,\text{miss}}$ used to be referred to as "missing transverse energy".

5.8.1 $\mu\tau$ channel

For 2016 data, the $\mu\tau$ channel uses a combination of the Muon POG recommended high-p_T muon triggers `HLT_Mu50` and `HLT_TkMu50`[5] In 2017 and 2018, the tracker muon trigger threshold was changed to 100 GeV. Additionally, it is recommended to add the `HLT_OldMu100` trigger. The `HLT_Mu50` is the main trigger while the `HLT_TkMu50/100` and `HLT_OldMu100` recover small inefficiencies observed in the high-p_T regime.

After the trigger selection, the events have to contain at least one high-p_T muon and one `DeepTau` tau fulfilling the identification criteria of the TIGHT working point as mentioned in Chapter 4. The muons must have a $p_T > 53$ GeV to stay out of the turn-on region of the single muon trigger, while the tau has to have a $p_T > 50$ GeV and an $|\eta| < 2.4$. Events containing a `HEEP` electron with $p_T > 35$ GeV are vetoed to avoid overlap with the other channels.

To reduce Drell-Yan background, events containing well-separated di-muon pairs are rejected. These pairs are defined by passing the high-p_T muon ID with a $p_T > 10$ GeV, $|\eta| < 2.4$ and a tracker-based isolation smaller than 0.15 with a ΔR between both muons bigger than 0.2.

It was observed that the regime of low transverse masses m_T of the light lepton and the $\vec{p}_T^{\,\text{miss}}$ are dominated by fake tau events. The transverse mass is defined as:

$$m_T = \sqrt{2 p_T^{\ell} p_T^{miss} (1 - \cos\left(\Delta\phi(\vec{p}_T^{\,\ell}, \vec{p}_T^{\,miss})\right)} \tag{5.11}$$

where p_T^{ℓ} is the transverse momentum of the light lepton. The final signal region with reduced fake tau contamination is set at $m_T > 120$ GeV.

If the event contains more than one $\mu\tau$ pair, the combination with the highest collinear mass is chosen for the final analysis.

5.8.2 eμ channel

The eμ channel uses the same muon trigger combination as mentioned in the $\mu\tau$ channel in combination with a single photon trigger `HLT_Photon175` to recover small efficiency losses in the high invariant mass regime. In 2017, the threshold of the single photon trigger was also raised for these two years to 200 GeV, which was kept for 2018.

The next step in the selection regards the two leptons in the final state. All events need to have at least one electron and one muon fulfilling the identification criteria described in Chapter 4, including the relative track-based isolation of 0.1. To stay above the turn-on regime of the single muon trigger and to stay inside the acceptance region, the muon must have a $p_T > 53$ GeV and an $|\eta| < 2.4$.

The electron p_T has to be greater than 35 GeV to fulfil the HEEP requirements. An electron candidate is rejected if a muon candidate has a $p_T > 5$ GeV and the ΔR muon track relative to the electron track is smaller than 0.1. These criteria reject muons that can be misidentified as electrons due to their production of Bremsstrahlung in the ECAL.

[5] The `Mu` stands for the triggering object, the `Tk` specifies that the triggering muon is a tracker muon (see Section 4.3) and the number 50 defines the trigger p_T threshold in GeV.

If the event contains more than one eμ pair, the combination with the highest invariant mass is chosen for the final analysis.

5.8.3 eτ channel

For the channel with an electron and tau in the final state, the trigger combination consists of two single electron triggers and one single photon trigger to ensure the highest efficiency in the high-p_T regime. The recommended triggers were chosen, namely the `HLT_Ele27_WPTight_Gsf` which uses a tight isolation criterium on the electron, and the `HLT_Ele115_CaloIdVT_GsfTrkIdT`, which has a higher threshold but no isolation requirement. To recover some efficiency loss at the high-p_T regime, the same single photon trigger as in the eμ channel is used with a threshold of 175 GeV for 2016 and 200 GeV for 2017 and 2018.

After the trigger selection, the events must contain at least one electron and one tau fulfilling the identification described in Chapter 4. Both leptons are required to have a $p_T > 50$ GeV. To avoid overlapping with the other channels, events containing additional high-p_T muons with a $p_T > 35$ GeV, $|\eta| < 2.4$ and relative tracker base isolation < 0.15 (see Section 4.3) are vetoed.

Additionally, to reduce the contamination of Drell-Yan background, events with well-separated di-electron pairs fulfilling a looser cut base electron identification [120] with a p_T greater than 10 GeV inside of the acceptance of $|\eta| < 2.5$ and a $\Delta R < 0.5$ are rejected.

To reduce the amount of fake tau contamination, as in the $\mu\tau$ channel, the transverse mass of the electron and the $\vec{p}_T^{\,\text{miss}}$ have to be greater than 120 GeV. Again, in the events containing more than one eτ pair, the combination with the highest collinear mass is chosen.

5.9 Estimation of jet $\rightarrow \tau$ Fake Contribution in the $\mu\tau$ Channel

As taus are reconstructed from jets, genuine jets misidentified as a tau present a relevant contribution to the background of this analysis. Despite the strong discrimination against these jets by the reconstruction and identification algorithms, the huge amount of jets produced during proton-proton collisions make this a non-negligible background.

This analysis uses a so called "ABCD-method" to determine the fake rate estimation ("MisID τ") from data. One main assumption of this method is that the Monte Carlo simulation is working well for reconstructed tau objects originating from actual taus. The background enhanced region is defined by flipping the $m_T > 120\,\text{GeV}$ requirement, therefore defining the signal region (SR) as $m_T > 120\,\text{GeV}$ and the control region (CR) as $m_T < 120\,\text{GeV}$, as this region is highly populated by fake events.

Furthermore, each of the two regions gets divided into an isolated and a non-isolated region. The isolated region is defined by using the tight working point of the tau id (Section 4.4.3). Therefore, the tau candidate in that region has to fulfil the tight working point, while for the non-isolated region, the candidate must fail the tight working point but fulfil the loose working point.

To calculate the contribution from jets faking taus, one has to subtract events from simulation where the reconstructed tau object originates from a genuine tau lepton.

The second assumption to be made is that the ratio of events fulfilling the tight working point to events failing the tight but fulfilling the loose working point (also called "Tight-to-Loose-Ratio") does not change between the CR and the SR. The final regions used for the data driven method are:

- Region A (non-isolated SR): In this region, all the selection criteria explained in Section 5.8.1 stay the same except for the tau identification requirement. This means that the tau candidate is failing the tight `DeepTau` working point but fulfilling the loose working point.
- Region B (isolated SR): This region corresponds to the final signal region used in the analysis as explained in Section 5.8.1.
- Region C (non-isolated CR): This region contains events with $m_T < 120\,\text{GeV}$, failing the tight `DeepTau` working point but fulfilling the loose working point.
- Region D (isolated CR): The isolated control region contains events with tau candidates that fulfil all requirements described in Section 5.8.1, but with $m_T < 120\,\text{GeV}$.

A sketch of these regions can be seen in Figure 5.16.

The fake rate FR is then defined dividing the number of events N_D by the number of events N_C. This ratio is then applied to region A, resulting in the final fake contribution ("MisID τ") in the SR of the analysis:

$$FR = \frac{\mathrm{N}_D}{\mathrm{N}_C} \stackrel{!}{=} \frac{\mathrm{N}_B}{\mathrm{N}_A} \rightarrow N_B = FR \cdot N_A = \frac{\mathrm{N}_D}{\mathrm{N}_C} \cdot N_A, \tag{5.12}$$

where N_i (with i = A,B,C,D) corresponds to the number of data events per bin in the specific region after subtracting the non-jet contribution from simulation:

$$\mathrm{N}_i = \mathrm{N}_{data,i} - \mathrm{N}_{MC,i}^{non-jets}. \tag{5.13}$$

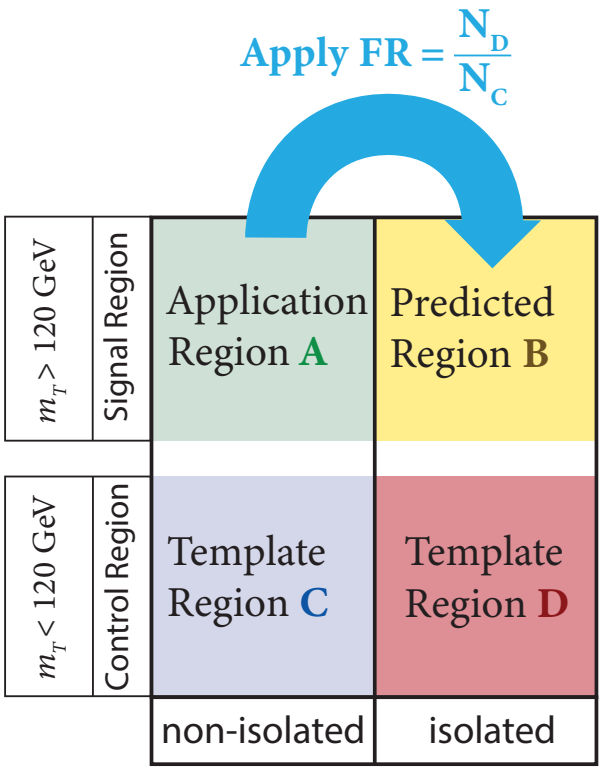

Figure 5.16.: Simplified sketch of the different regions used in the ABCD or Tight-to-Loose method to estimate the jet faking tau contribution from data. The fake rate is estimated in the control regions by dividing the number of events N_D by the number of events N_C and is then applied to the signal region A.

The calculated FR is binned in the p_T of the tau candidate as well as in the ratio between the p_T of the tau candidate and the p_T of its underlying jet. Moreover, it is taken into account if the tau candidate was found in the Barrel or the Endcap region. The binning size is chosen such that each bin contains enough statistics to avoid negative entries.

The ratio between the p_T of the tau candidate and the p_T of the jet object that is used to reconstruct the tau (underlying jet) is introduced to take the dependence of the fake factor from the underlying jet activity into account. If the ratio is small, the underlying jet has a greater p_T than the tau candidate. Therefore, the tau candidate is built only from parts of the jet which indicates high activity in the region of the tau candidate. This high activity decreases the probability that the tau candidate is identified as a well isolated tight tau leading to a small fake factor.

As an example, the final FR in the mentioned binning for the year 2018 can be seen in Table 5.8, while the years 2016 and 2017 can be found in Section A.3.

Table 5.8.: Calculated fake rates FR obtained for the year 2018 for the different tau p_T and tau p_T over jet p_T bins in the barrel and Endcap region. The error shown is of statistical nature only.

2018

p_T^τ [GeV]	p_T^τ / p_T^{jet}	fake rate (barrel)	fake rate (endcap)
$50-80$	$0-0.5$	0.032 ± 0.001	0.032 ± 0.002
	$0.5-0.6$	0.042 ± 0.001	0.041 ± 0.002
	$0.6-0.65$	0.047 ± 0.001	0.042 ± 0.002
	$0.65-0.7$	0.048 ± 0.001	0.041 ± 0.002
	$0.7-0.75$	0.050 ± 0.001	0.041 ± 0.002
	$0.75-1.0$	0.063 ± 0.001	0.069 ± 0.003
	$1.0-3.0$	0.093 ± 0.02	0.060 ± 0.013
$80-150$	$0-0.5$	0.019 ± 0.004	0.027 ± 0.006
	$0.5-0.6$	0.025 ± 0.003	0.022 ± 0.004
	$0.6-0.65$	0.030 ± 0.003	0.025 ± 0.004
	$0.65-0.7$	0.031 ± 0.002	0.034 ± 0.004
	$0.7-0.75$	0.036 ± 0.002	0.053 ± 0.004
	$0.75-1.0$	0.063 ± 0.002	0.068 ± 0.004
	$1.0-3.0$	0.083 ± 0.013	0.064 ± 0.013
$150-1000$	$0-0.7$	0.022 ± 0.005	0.035 ± 0.009
	$0.7-1.$	0.078 ± 0.005	0.070 ± 0.009
	$1.-3.$	0.06 ± 0.03	0.08 ± 0.03

5.9.1 Validation of the fake rate estimation method

To validate the method of estimating the tau fake contribution from jets ("MisID τ") one can test its performance on the Monte Carlo simulation using events assumed to be well modelled, namely, events where the tau can be matched to a generator level jet. The resulting distribution is then compared to the Monte Carlo description of this contribution, mainly coming from W+jets.

Thus, instead of data, one uses the full Monte Carlo description split into the regions explained previously. Instead of only jets faking taus, one also uses the orthogonal set of only genuine taus to calculate the fake rate. This so called "closure" FR is then applied to region A of the simulated background. The resulting distribution is then compared to the pure MC description in region B. The outcome of this validation in the p_T of the tau can be seen in Figure 5.17.

Comparing the distributions from the ABCD method to the simulation in the final signal region, one can see a good agreement, considering statistical uncertainties. To take the remaining differences into account, an additional systematic uncertainty of 50 % is added for the description of the misidentified tau background, as recommended by the CMS Exotica (EXO) working group [179].

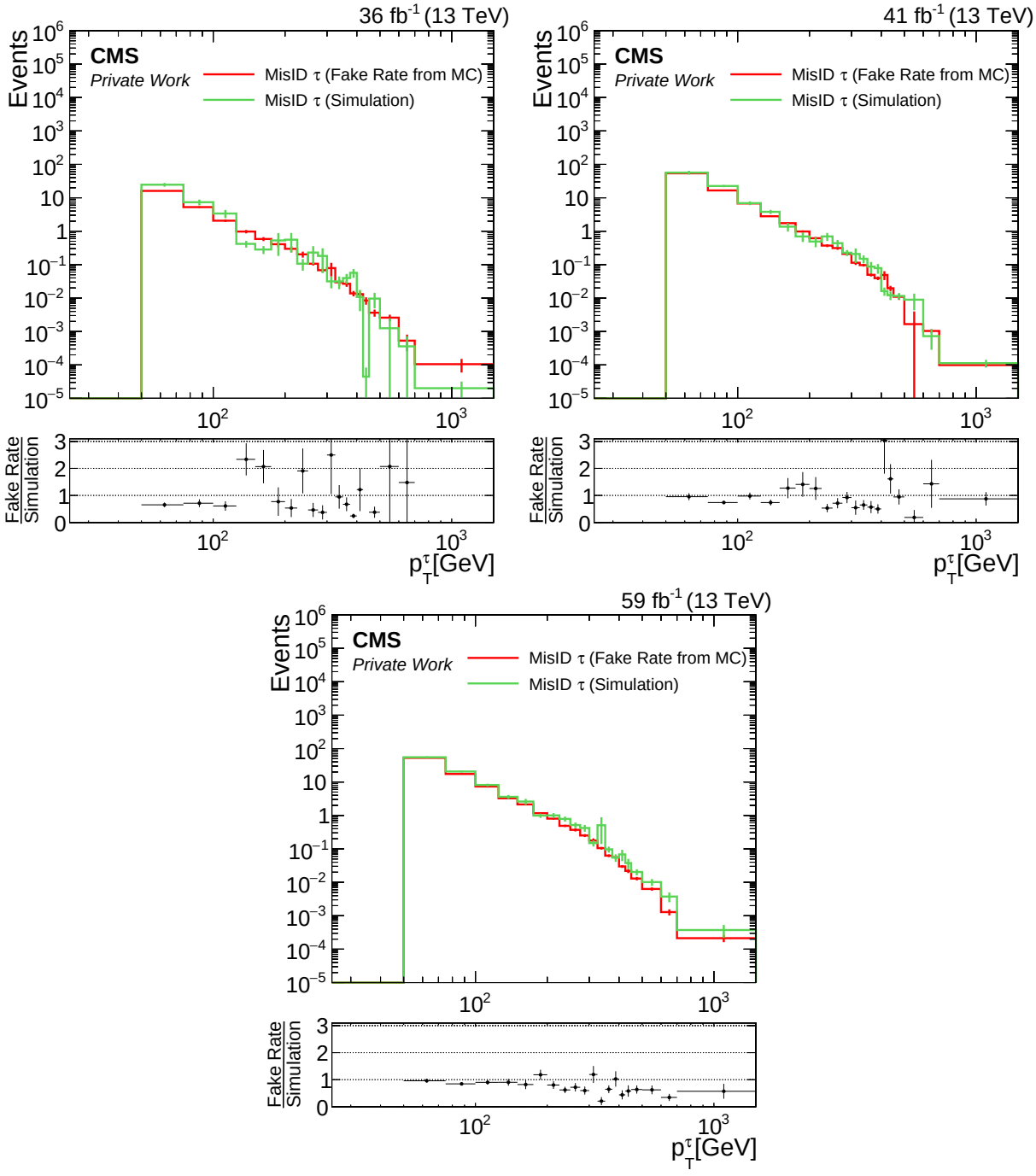

Figure 5.17.: Validation of the fake rate method to determine the tau fake contribution from jets ("MisID τ") using only Monte Carlo simulation in the p_T of the tau. The comparison of the distributions from the ABCD method compared to the simulation in the final signal region shows good agreement considering the statistical uncertainties.

5.10 Systematic Uncertainties

Besides the statistical uncertainty arising from the number of measured or generated events per bin, systematic uncertainties must also be considered. These can be object related uncertainties (e.g. on the momentum scale of the lepton) or general uncertainties (e.g. on the measured luminosity for each year). These uncertainties can affect the normalization (e.g. an uncertainty on the theoretical cross section on a specific background) or the shape, as properties of single objects in an event are shifted.

The systematic uncertainties used in the three channels are:

- **Pileup:** The minimum bias cross section used to create the pileup reweighting mentioned in Section 5.5 is shifted by $\pm 5\,\%$, following the recommendation of the CMS LUMI POG [136]. The effect on the final distribution is evaluated by repeating the analysis with the shifted pileup distribution. The uncertainty is considered to be correlated between the three years and has an impact of about 1 % on the final mass distribution.
- **Luminosity:** The uncertainty on the measured integrated luminosity affects the normalization of the background and signal description. The value is 1.2 % for 2016, 2.3 % for 2017 and 2.5 % for 2018. The uncertainties are treated as uncorrelated between the three years, following the recommendation of the CMS Lumi POG and the CMS Exotica Group combine contact during the publication phase of this analysis.
- **Trigger:** The applied corrections on the trigger combination have associated up and down uncertainties, affecting the shape of the distributions. The uncertainties on the applied scale factors are p_T and η dependent and reach from 0.2 % for low p_T muons and up to 10 % for muons with $p_T > 500\,\text{GeV}$ resulting in an impact on the total background distribution of 0.1 % at low masses up to 4 % at high masses. For electrons, the trigger efficiency is close to 100 %, as its uncertainty is $< 1\,\%$. Thus, this uncertainty can be neglected for the electron triggers, following the recommendation of the CMS EGamma particle object group [122].
- **Prefiring:** The weights correcting the prefiring effect in 2016 and 2017 (Section 5.5.2) also have associated uncertainties. The analysis is repeated using the upwards or downwards uncertainty of these event weights which results in a changed shape of the final distribution. The resulting impact of this uncertainty is around 1 % on the final mass distribution.
- **Background Cross Section:** The uncertainty on the normalization of the background description coming from the theory cross section is taken from their higher order calculations as recommended by the CMS Monte Carlo Generator Group:
  - $\boldsymbol{t\bar{t}}$**:** 4 % [180]
  - **Diboson:** 3 % (WW, ZZ), 4 % (WZ) [181, 182]
  - **Single top:** 4 % [183]
  - **Drell-Yan:** 2 % [182]
- **Top shape:** Besides the cross section uncertainty, the shape uncertainty on the top background from NNLO corrections are also taken into account. As explained in detail in Section 5.5.4, this uncertainty is split into two sources, one coming from the variation of the chosen PDF and one from the uncertainty on the renormalization and factorization scale

of the generator. The one arising from the PDF variation provides the main uncertainty on the $t\dot{t}$ background description, was evaluated to be up to 20 % on the $t\dot{t}$ background at a collinear mass of 2 TeV, resulting in an uncertainty on total background description of $2-5$ % at low masses and 10 % at high masses.

- **WW shape:** Missing corrections to the WW background description are treated by introducing an additional uncertainty on the shape of this process using NLO electroweak calculations [184]. The uncertainty has been parametrized as a second order polynomial as a function of the invariant mass $m_{\ell\ell}$ of the lepton pair:

$$\Delta = 1 - \left(0.993 - 2.001 \cdot 10^{-4} \times m_{\ell\ell} + 2.838 \cdot 10^{-8} \times m_{\ell\ell}\right) \tag{5.14}$$

  This polynomial is applied as an event weight factor $1 \pm \Delta$ on the WW background, creating a symmetric uncertainty. The impact on the total background description is around 0.1 to 2 %.

- **MisID background:** As explained in Section 5.9.1, the background description coming from fakes is associated with an uncertainty that was set to 50 %. Its impact is up to 25 % on the full background description in the low energy regime where fakes dominate the prediction, making it the main uncertainty of the muon channels.

- **Muon Energy Scale:** As mentioned in Section 5.5.5, the scale of the muon differs between simulation and measured data. These differences are addressed by introducing an uncertainty on the scale using the "Generalized Endpoint" method [123], leading to a shift in the muon scale and, therefore, a change in the shape of the distributions. The effect of the muon energy scale uncertainty on the total background description is around below 1 % for low masses and rises up to nearly 20 % for high collinear masses.

- **Muon p_T Resolution:** As mentioned in Section 5.5.5, the resolution of the muon p_T in the simulation is smeared out to match the one measured in data. The uncertainty of this smearing is determined by applying the Gaussian shift using the same parametrization (Table 5.7) as in Section 5.5.5, but with a factor of 0.46 instead of 0.57, corresponding to a 10 % shift up and down. The effect of this shift on the final shape is of the order of 1-3 %.

- **Muon Scale Factors:** The uncertainties arising from the scale factors, namely from the isolation and the identification efficiency of the muon objects, are applied by shifting the value of the scale factor up and down on an event-by-event basis. For the reconstruction efficiency, this uncertainty lies at around 0.07 to 0.4 %, for the ID < 0.3 % and for the ISO it lies below 0.1 % resulting in an impact on the final collinear mass distribution of less than 1 %.

- **Tau Scale Factor:** The tau energy scale factor as well as the `DeepTau` identification scale factors have uncertainties associated with them, dependent on the decay mode and the discriminator type. The size of these uncertainties is about the same as the correction itself, lying in the order of 2 % or less for high p_T taus. These are also applied on an event-by-event basis, leading to a change in the shape of the distributions with an effect on the total background description of 1 to 5 %.

- **Electron Energy Scale:** The electron scale is varied by $\pm 2\,\%$ and the effect on the shape is taken into account as an uncertainty, following the recommendations from the dielectron analysis [20].
- **Electron Scale Factors:** The scale factors for the electron object, namely the HEEP identification and the reconstruction, are also varied within their uncertainties, similar to the muon scale factors. The uncertainty on the HEEP ID scale factor is about 3.1 % in the Barrel and 2.1 % in the Endcaps. The uncertainty on the reconstruction efficiency varies between $1-5\,\%$, depending on the E_T and η of the electron [120].
- **Missing Transverse Momentum:** The main uncertainty on the $\vec{p}_T^{\,\text{miss}}$ comes from the jet energy scale and jet energy resolution (see Section 5.5.5). Shifts in these corrections are propagated into the $\vec{p}_T^{\,\text{miss}}$ calculation, leading to a shape uncertainty for both sources. Additionally, the unclustered energy has an uncertainty of 10 % associated with it.
- **Parton Distribution Function:** Additional to the PDF uncertainty derived for the top and WW background, the uncertainty on the parton distribution function for the additional background processes and the signal is derived using the recommended method from the `PDF4LHC` [185]. The `PDF4LHC_mc` PDF set is used, containing 100 additional replicas $\sigma^{(i)}$ with $i = 1, 2, ..., 100$. These are ordered by size ($\sigma^{(1)} < \sigma^{(2)} < ... < \sigma^{(100)}$) and the final uncertainty is computed as the 68 % confidence level interval midpoint by subtracting the 84th from the 16th value:

  $$\delta^{pdf}\sigma = \frac{\sigma^{(84)} - \sigma^{(16)}}{2} \tag{5.15}$$

  The effect on the final background description is small, as the main backgrounds have their specific, more precise, PDF uncertainty associated with them. For the signal models, only the effect on the acceptance times efficiency of the PDF uncertainty is taken into account.

The size of the relative systematic uncertainty on the total background description and one signal example of the $\mu\tau$ channel as a function of the collinear mass of the muon and the tau for the full Run 2 can be seen in Figure 5.18. Each bin shows the up and down shift of the background description (e.g. a relative uncertainty of 1.2 translates to a value 20 % higher than the nominal one). The object related uncertainties are grouped together for the specific objects (tau, muon and $\vec{p}_T^{\,\text{miss}}$). The leading uncertainty is coming from the jet faking tau background description as it is the leading background with an uncertainty of 50 %. For masses over 1 TeV, the object specific uncertainties from the tau and the muon are the second leading ones.

The effect of the uncertainties on a signal sample (Z' with a mass of 1500 GeV) can also be seen in Figure 5.18. In this case, the leading uncertainties come from the objects, namely the muon, the tau and $\vec{p}_T^{\,\text{miss}}$, with the muon object providing the most significant uncertainty for the signal.

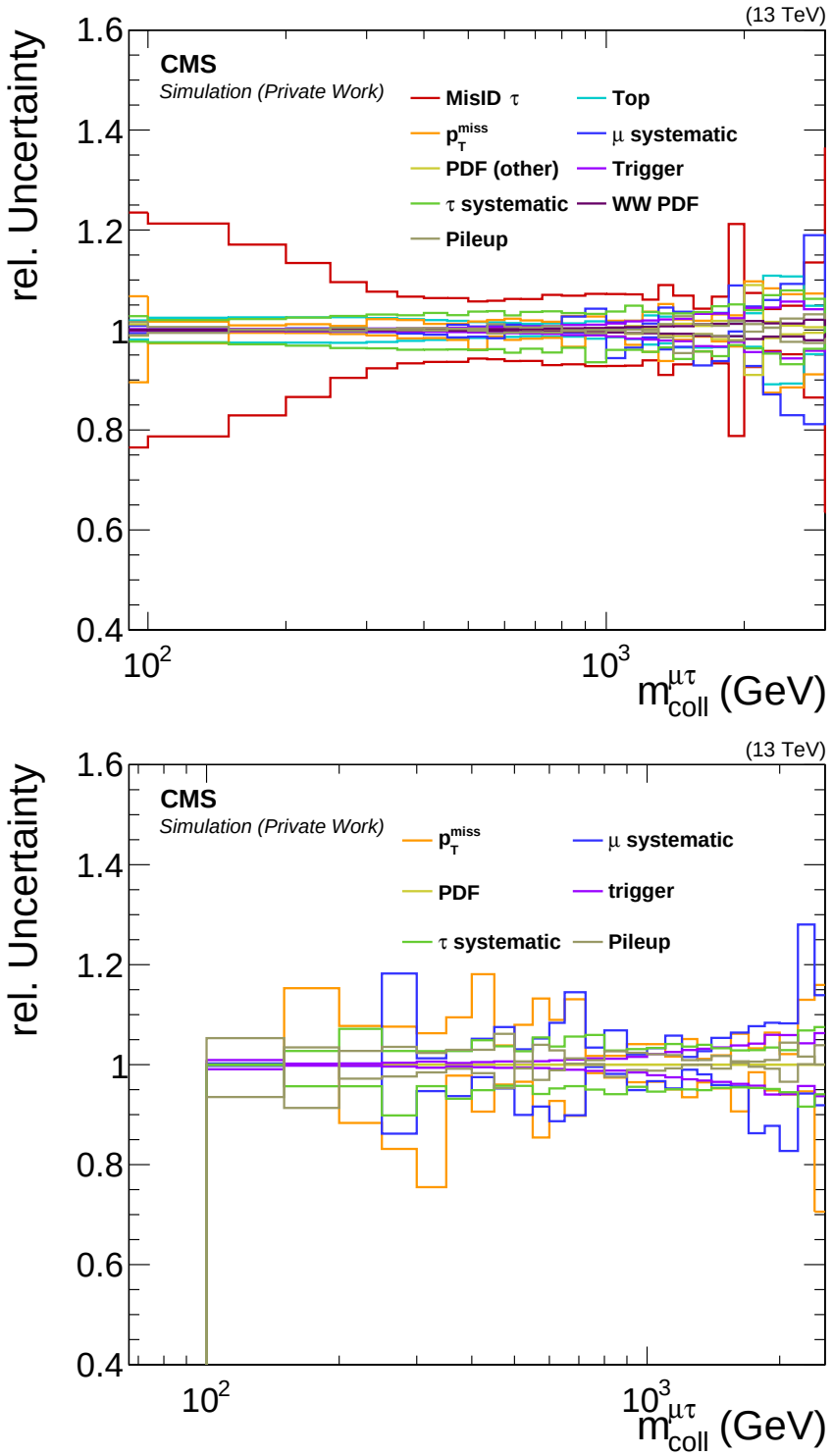

Figure 5.18.: Relative systematic uncertainties on the collinear mass description of the muon and the tau for the full Run 2 combination of the total background prediction (top) and for a signal sample of a Z' with a mass of 1.5 TeV (bottom). The object related uncertainties are grouped together for the specific objects (tau, muon and $\vec{p}_T^{\,miss}$). As the mis-identified jet contribution is the main background of this channel, the 50 % uncertainty is the leading one followed by the object uncertainties for the muon and the tau for masses above 1 TeV for the background prediction. For the signal, the object related uncertainties of the muon, the tau and the $\vec{p}_T^{\,miss}$ play the leading role.

5.11 Kinematic Distributions of the $\mu\tau$ channel

After determining the contribution of jets faking taus using the data driven approach one can now look at the different kinematic variables that will go into the final discriminating variable, the collinear $\mu\tau$ mass. All events fulfil the requirements mentioned in Section 5.8.1. As the systematic uncertainties are also fully defined they are also included in the following distributions.

Figure 5.19 and Figure 5.20 show the measured data in Run 2 in comparison to the Standard Model prediction of the p_T, η and ϕ of the chosen high-p_T muon after applying all corrections and selection steps. The background is divided into the different groups described in Section 5.3, visualized by different colours. At the bottom of each plot, the ratio between the data and the SM prediction is shown, together with a grey band, indicating the combined relative systematic uncertainty. The shape of the background prediction is smooth and shows statistical effects only in the very high p_T regime. Only the single top background might indicate a lack of generated events as no events appear after a $p_T > 750\,\text{GeV}$ and therefore it does not describe the full p_T range where data is measured. The angular variables show a good agreement between the prediction and the measurement. Neither strange behaviour nor significant deviation from the Standard Model prediction has been observed for the muon object.

Figure 5.21 and Figure 5.22 show the p_T, η and ϕ of the chosen tau, after applying all corrections and selection steps in the same way as for the muon object. Around 700 GeV, the Monte Carlo simulation starts to run out of statistics, which does not raise a problem as there is no data observed in this region. As for the muon, no unexpected behaviour or significant variations from the Standard Model prediction were found.

In Figure 5.23, the $|\vec{p}_T^{\,\text{miss}}|$ and the $\phi(\vec{p}_T^{\,\text{miss}})$ are shown for the full Run 2 luminosity. As for the muon and the tau, the shape of the background description is in agreement with the measured data and no significant deviations or unexpected effects were observed.

All three objects show good behaviour in their kinematic regions and will now be used to calculate the final discriminating variable, the collinear mass.

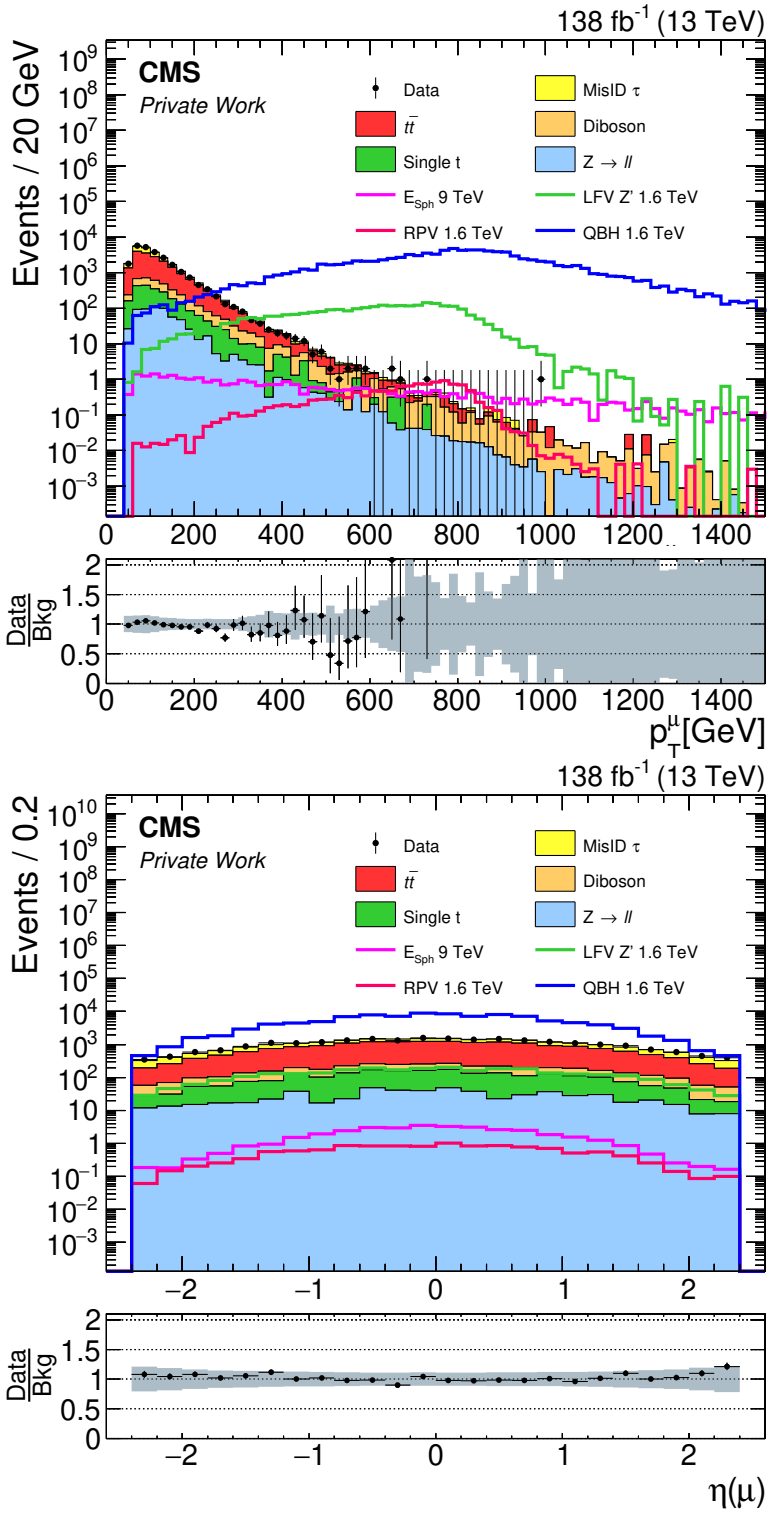

Figure 5.19.: Data and the Standard Model prediction using the contribution from jets that are misidentified as taus derived from data for the muon p_T (top) and muon η (bottom) for the full Run-2 measurement. In the bottom of each plot, a ratio between the measured data and the Standard Model prediction is shown together with the combined relative systematic uncertainties as a grey band. The distributions do not show any unexpected behaviour nor significant variations from the Standard Model prediction.

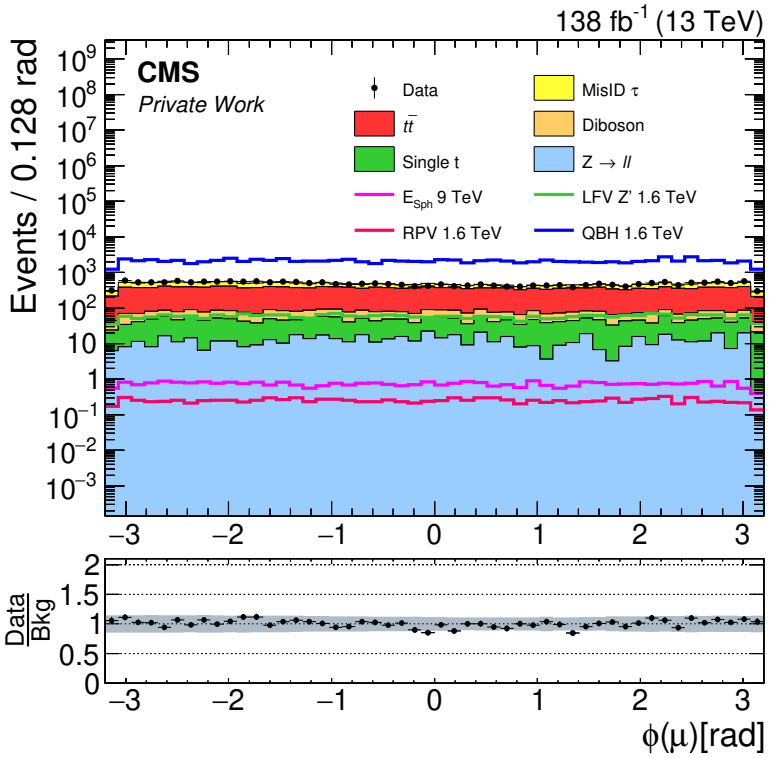

Figure 5.20.: Data and the Standard Model prediction using the contribution from jets that are misidentified as taus derived from data for the muon ϕ for the full Run-2 measurement. In the bottom of the plot, a ratio between the measured data and the Standard Model prediction is shown together with the combined relative systematic uncertainties as a grey band. The distributions do not show any unexpected behaviour nor significant variations from the Standard Model prediction.

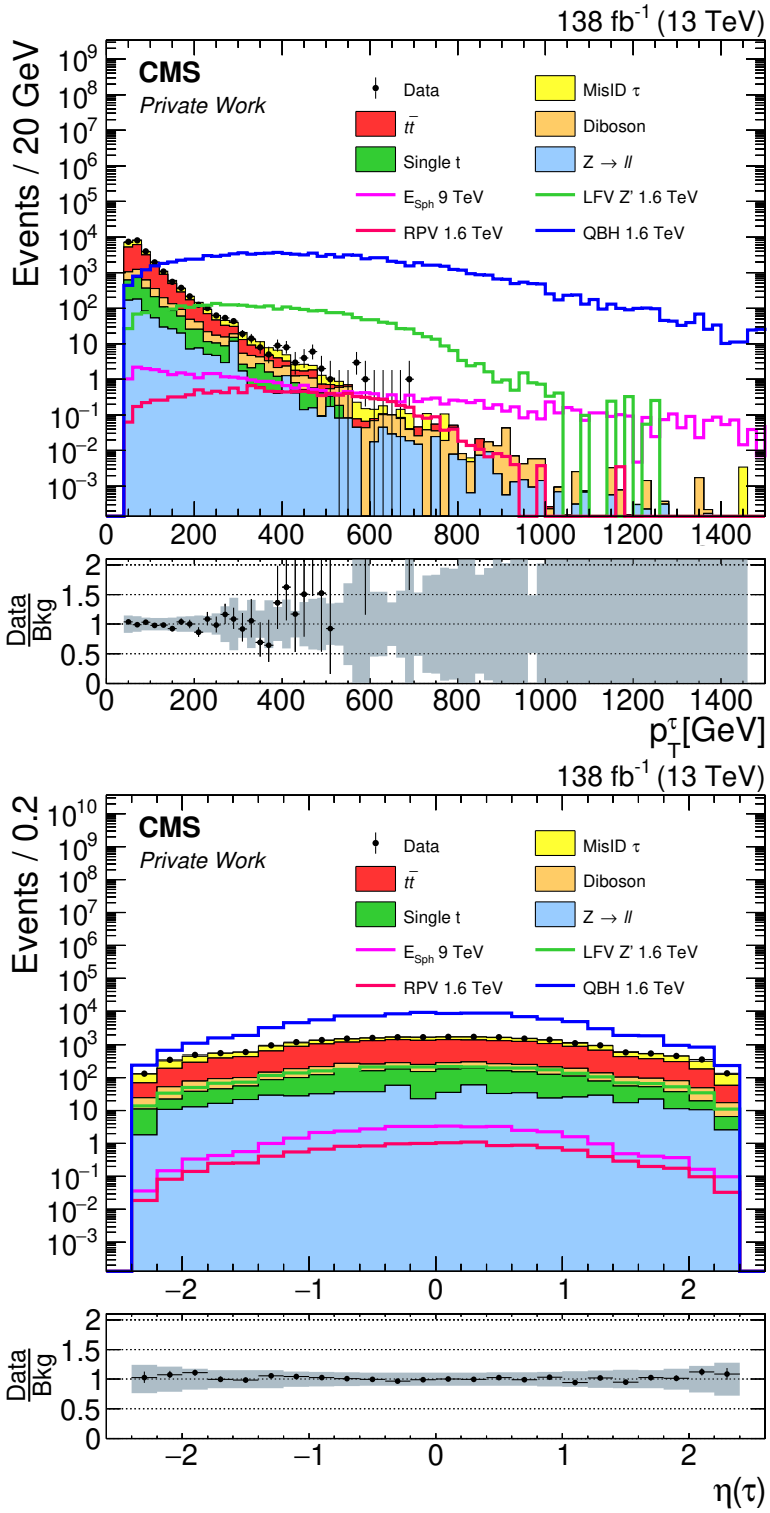

Figure 5.21.: Data and the Standard Model prediction using the contribution from jets that are misidentified as taus derived from data for the tau p_T (top) and tau η (bottom) for the full Run-2 measurement. In the bottom of each plot, a ratio between the measured data and the Standard Model prediction is shown together with the combined relative systematic uncertainties as a grey band. The distributions do not show any unexpected behaviour nor significant deviations from the Standard Model prediction.

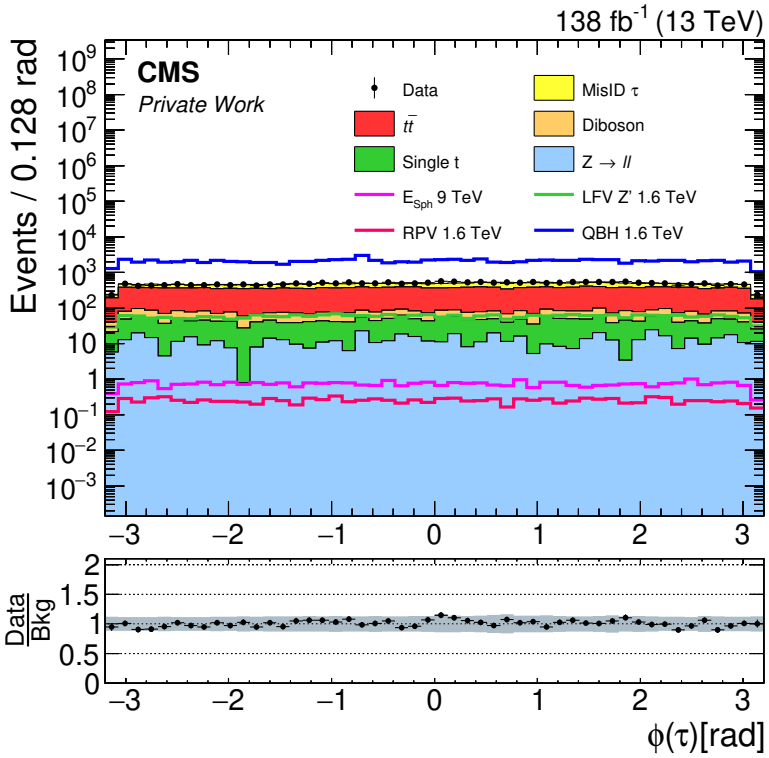

Figure 5.22.: Data and the Standard Model prediction using the contribution from jets that are misidentified as taus derived from data for the tau ϕ for the full Run-2 measurement. In the bottom of the plot, a ratio between the measured data and the Standard Model prediction is shown together with the combined relative systematic uncertainties as a grey band. The distributions do not show any unexpected behaviour nor significant deviations from the Standard Model prediction.

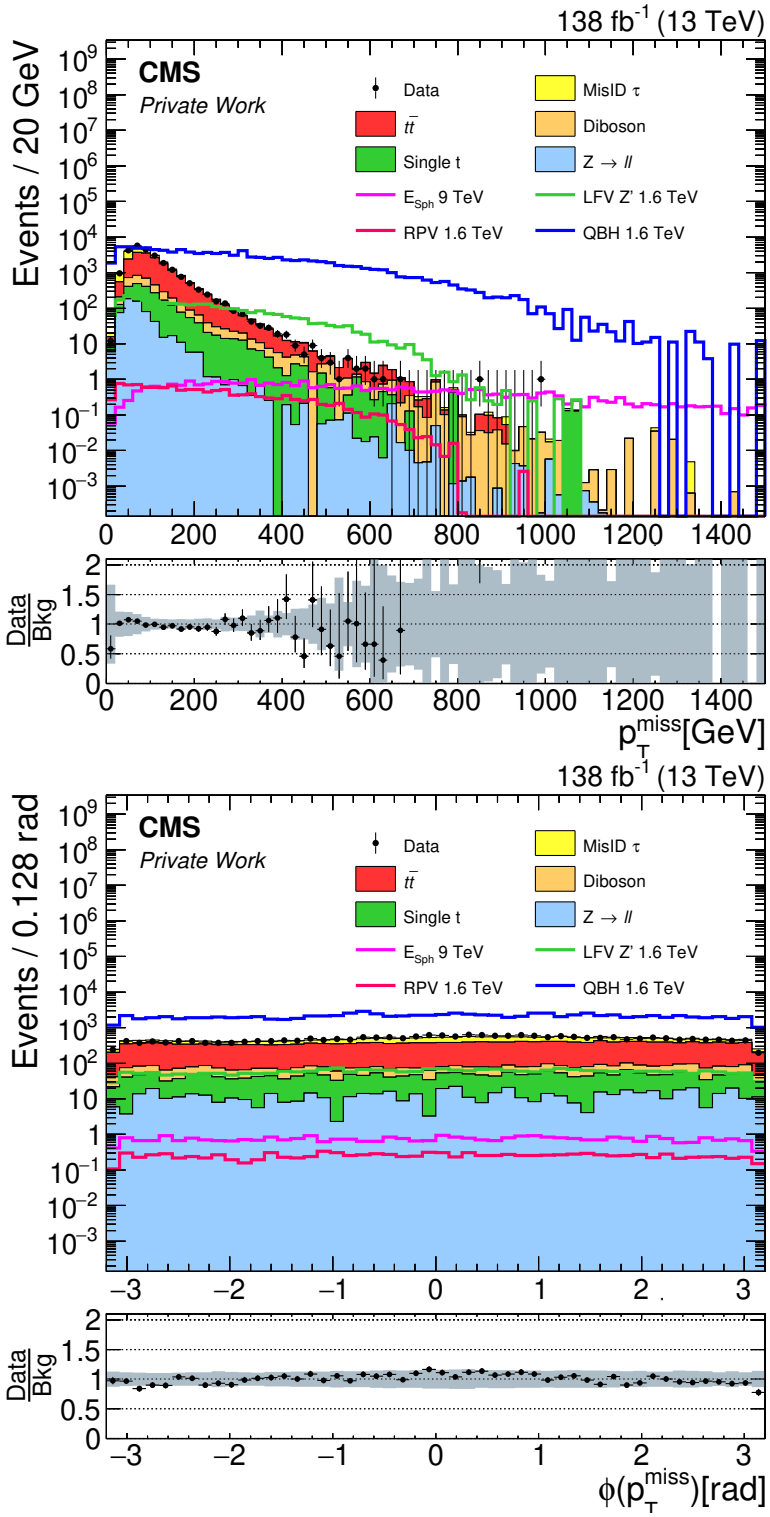

Figure 5.23.: Data and the Standard Model prediction using the contribution from jets that are misidentified as taus derived from data for $|\vec{p}_T^{\,\text{miss}}|$ (top) and the $\phi(\vec{p}_T^{\,\text{miss}})$ (bottom) for the full Run-2 measurement. In the bottom of each plot a ratio between the measured data and the Standard Model prediction is shown together with the combined relative systematic uncertainties as a grey band. The distributions do not show any unexpected behaviour nor significant variations from the Standard Model prediction.

5.12 Collinear Mass of the $\mu\tau$ channel

After selecting the events and looking at the kinematic variables, the final collinear mass distribution of the muon and the tau for the full Run 2 using the `NanoAOD` file format is shown in Figure 5.24. The bin size is chosen using the calculated mass resolution, also taking the Monte Carlo statistics into account, and each bin is normalized to its width. The backgrounds are ordered by the size of their contribution with the leading background at the top. No significant deviation from the Standard Model prediction has been found.

The two biggest deviations arise for the first bin at a very low mass, as this area is difficult to model, and at a mass of 900 to 1000 GeV. The low mass bin has low statistics in data which makes it challenging to evaluate the fake rate using the data driven approach. The excess is covered by the uncertainties with a local significance of 1.1σ with 112 measured data events and 81.4 ± 26.3 expected events.

Similarly, the deficit in the 950 GeV bin, which contains 36 measured events compared to 51.6 ± 6.0 expected events, leads to a local significance of 1.7σ.

The excess at high masses above 2 TeV is covered by statistical uncertainties, as the number of events is very low. Table 5.9 shows 3 observed events with an statistical uncertainty of ± 2, compared to about 1 expected event.

Table 5.9 shows the number of events for each process from the Standard Model prediction after the full selection, together with measured data. The first column shows the full $m_{coll}^{\mu\tau}$ range, whereas the following columns sum up the number of events from the indicated threshold of 500 GeV, 1.5 TeV and 2 TeV. The event number uncertainty reflects statistical uncertainty from the number of weighted generated events and systematic uncertainties, combined by quadratically summing all sources. The last column shows that the slight excess at high $m_{coll}^{\mu\tau}$ is covered by the uncertainties and thus does not show a significant deviation from the prediction.

Table 5.9.: Number of events from the Standard Model prediction for each process and the measured data for the full $m_{coll}^{\mu\tau}$ range (first column), for a threshold of 0.5, 1.5 and 2 TeV. The second value in each cell shows the combination of the statistical uncertainty from the number of weighted generated events and systematic uncertainty.

Process	all $m_{coll}^{\mu\tau}$	$m_{coll}^{\mu\tau} > 500$ GeV	$m_{coll}^{\mu\tau} > 1.5$ TeV	$m_{coll}^{\mu\tau} > 2$ TeV
Data	24505	1572	12	3
MisID τ	5827.7 ± 2914.7	198.2 ± 100.1	1.6 ± 1.6	0.24 ± 0.52
$t\bar{t}$	14397.9 ± 798.5	1036.2 ± 62.6	3.4 ± 0.6	0.38 ± 0.18
Diboson	1591.3 ± 100.7	204.6 ± 16.4	3.8 ± 0.7	0.48 ± 0.12
single t	1681.4 ± 175.7	128.0 ± 37.1	1.05 ± 1.05	-
$Z \to ll$	604.1 ± 113.4	42.3 ± 4.8	0.47 ± 0.23	0.05 ± 0.04
Sum background	24102.4 ± 3054.6	1609.1 ± 124.9	10.3 ± 2.1	1.15 ± 0.59

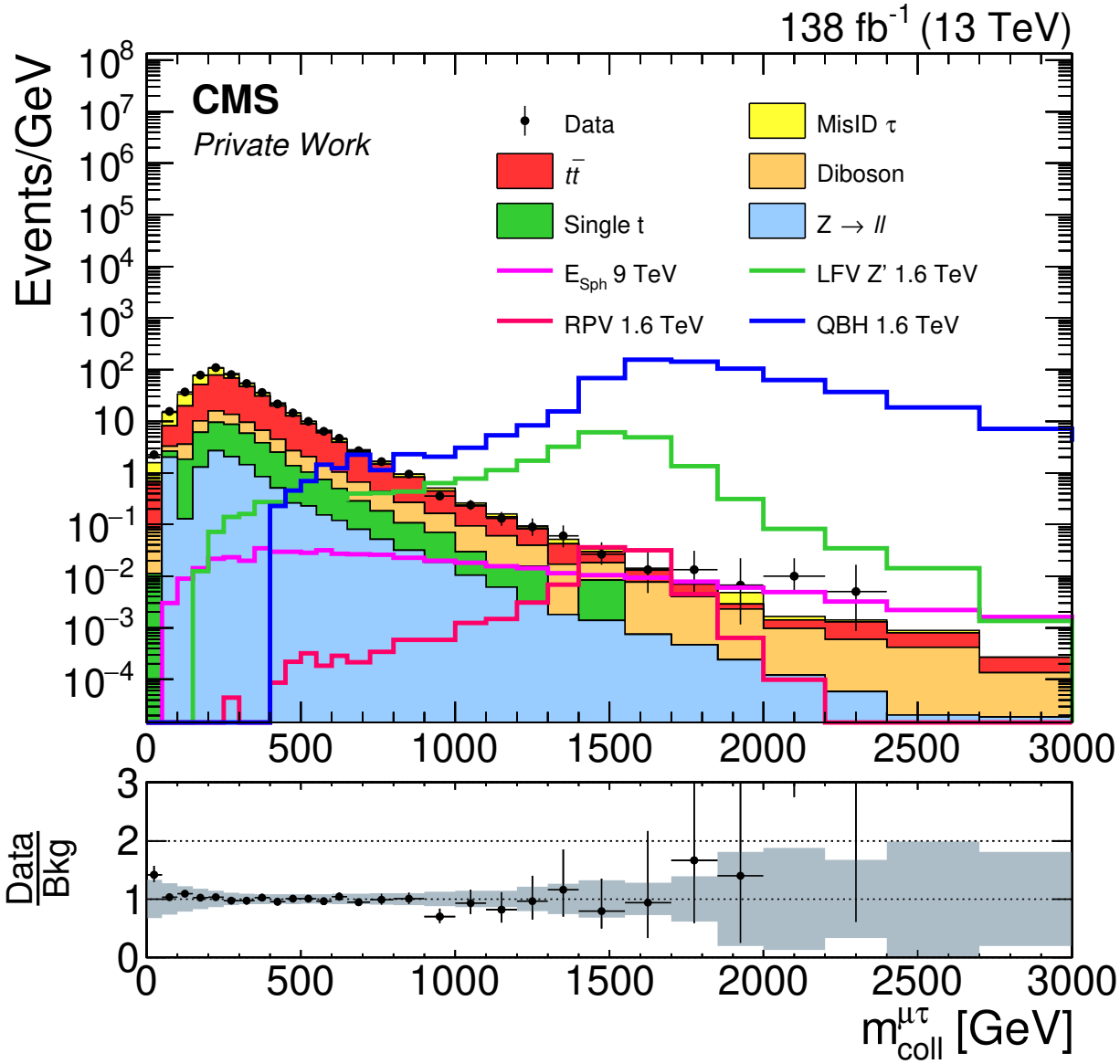

Figure 5.24.: Collinear mass distribution of the muon and the tau after all selection steps. The distribution is shown with a binning following the mass resolution and underlying statistics. Each bin is normalized to its width. The different backgrounds are ordered by their contribution. The lower part of the plot shows the ratio between the measured data and the Standard Model prediction. The grey band in the ratio represents the combined relative systematic uncertainty. The last two data points have a data to background ration of > 3 and are outside of the shown ratio range. The statistical error bar of the last point reaches the ratio of one, shown as the black line at 2300 GeV.

5.12.1 Comparison between NanoAOD and MiniAOD

As mentioned in the introduction of this chapter, the $\mu\tau$ channel was analysed using both file formats, MiniAOD and NanoAOD. The difference between these formats is in the accuracy with which different variables are saved and, in the case of this analysis, in the version of the jet corrections that are applied (Section 5.5.5). Figure 5.25 shows both final $m_{coll}^{\mu\tau}$ distributions, coming from NanoAOD (left) and from MiniAOD (right). The MiniAOD plot is taken from [1]. As one can see, the differences in the distributions are minimal and were calculated to be smaller than 1 % on the full mass range.

Figure 5.26 (left) shows the ratio of the measured data of Run 2 for both file formats. Visible differences can be found between masses of 600 GeV and 1200 GeV and for the two highest mass bins, where one event changes from the 2000 − 2200 GeV bin into the 2200 − 2400 GeV bin. Figure 5.26 (right) shows the comparison between the two different background descriptions, including Monte Carlo and the data driven tau mis-identification description, also showing a very good agreement with only small differences. The smaller number of expected background events in the 2700 − 3000 GeV bin, together with slightly more data in the range of 800 − 1000 GeV, impacts the outcome of the statistical interpretation at high masses, leading to differences in the observed and expected limit for the two different formats (see Section 6.3). These differences between data and simulated background are coming from the updated jet corrections applied to the NanoAOD version and the slightly smaller accuracy of this file format.

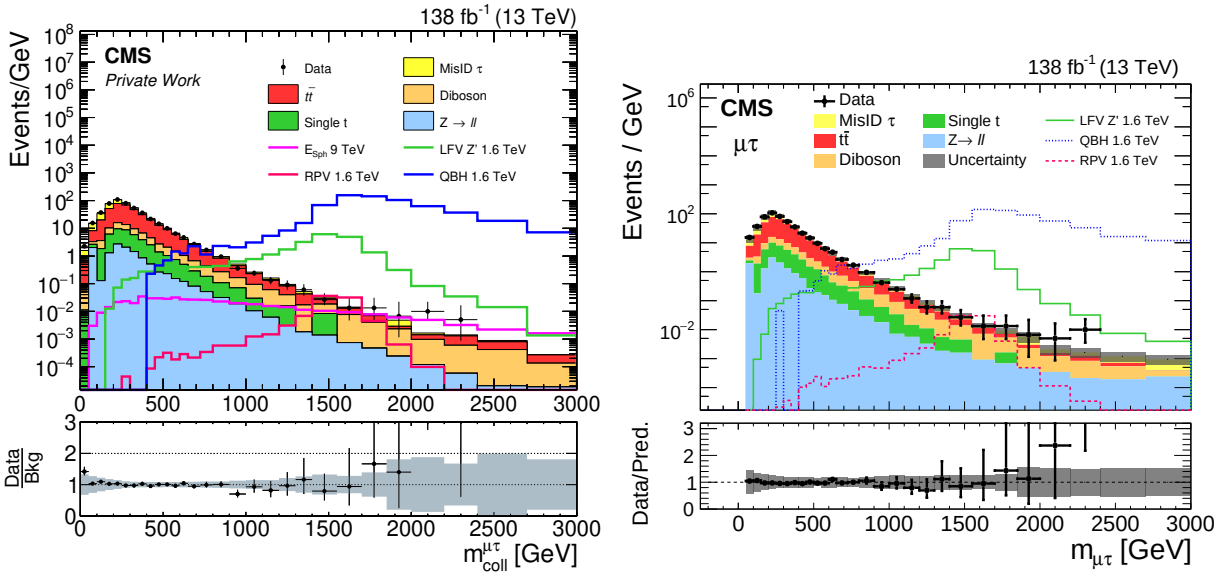

Figure 5.25.: Collinear mass distribution of the muon and the tau after all selection steps for the two different file formats with the NanoAOD version on the left and the MiniAOD version on the right, which is taken from [1]. The differences are very small and are less than 1 % on the full mass range.

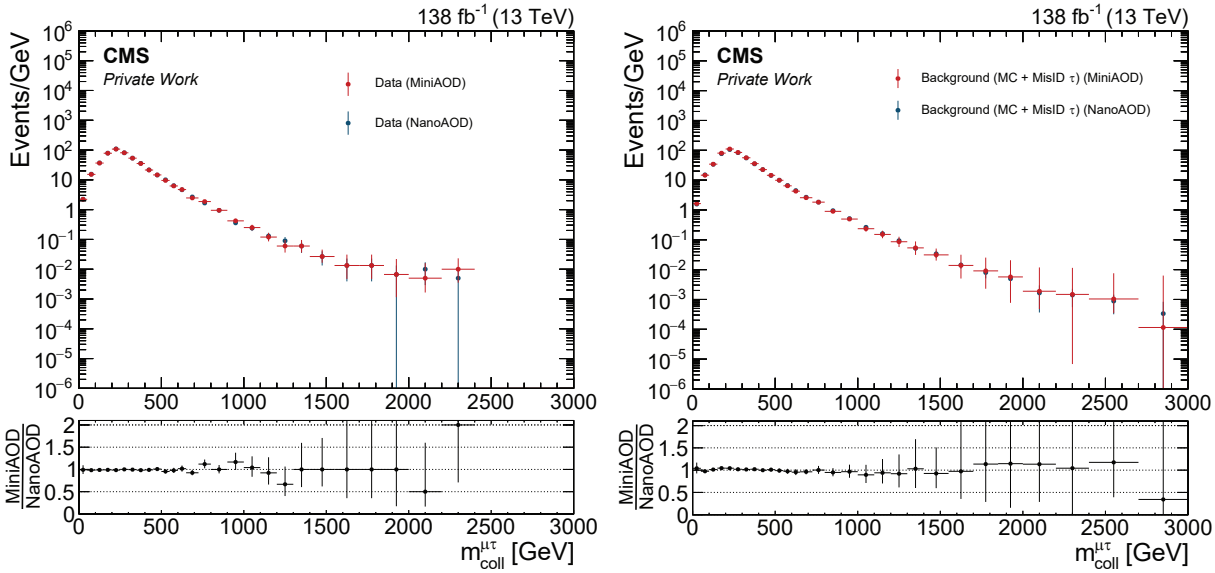

Figure 5.26.: Ratio of the collinear mass distribution of the measured data (left) and the background, including Monte Carlo and the data driven tau mis-identification description, (right) of Run 2 for the two different file formats. Only small differences are visible that are coming from mainly from the updated jet energy corrections for the `NanoAOD` version and the slightly lower accuracy in this file format.

5.13 Mass Distributions of the Electron Channels

This section presents the final mass distributions for the electron channels, after applying all selections, as they are later used in the statistical interpretation. Figure 5.27 show the eμ channel (left) and the eτ channel (right), in a similar plotting style as used for the $\mu\tau$ channel. Both are taken from the publication of the lepton flavour analysis [1]. Similar to the $\mu\tau$ channel, no significant deviations from the Standard Model have been found.

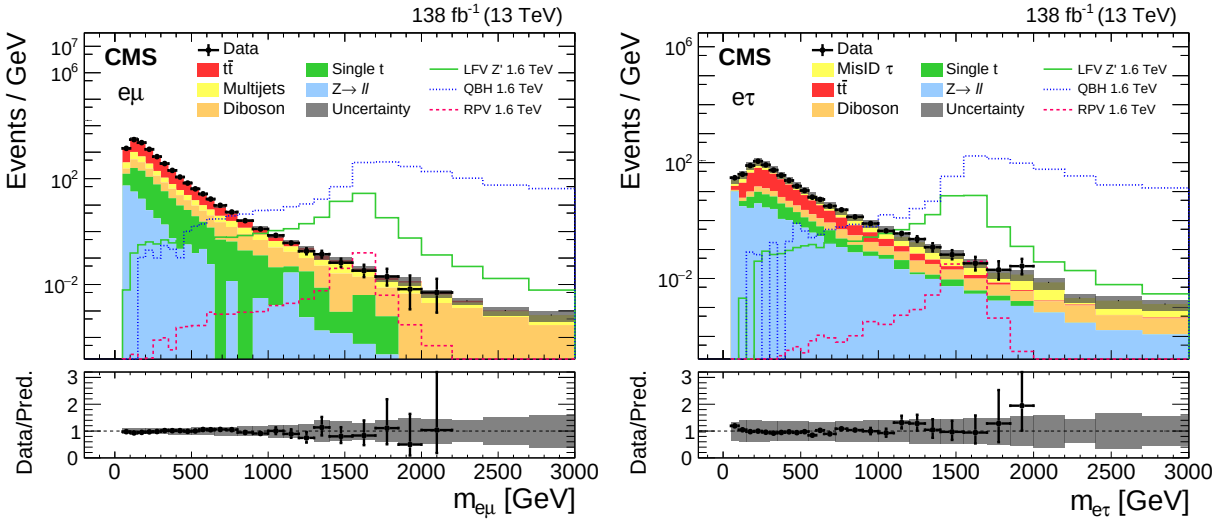

Figure 5.27.: Collinear mass distributions of the two electron channels after all selection steps. The eμ channel is shown on the left whereas the eτ channel is shown in the right. The measured data is in good agreement to the Standard Model prediction without significant deviations being observed. Taken from [1]

As the prediction is in good agreement with the measured data for all three channels, the single year distributions for all channels are used for the statistical interpretation of the different models explained in Section 2.2 and Section 2.3.

6 | Statistical Interpretation

After deriving the final mass distribution of the lepton pair, the outcome is statistically interpreted and new information about our knowledge of physics is drawn. For instance, one can calculate the significance of an observed deviation from the null hypothesis, or test the compatibility of such deviation with different new physics models.

As no significant deviation from the Standard Model expectation has been observed, the resulting mass spectra are used to calculate exclusion limits on signal model parameters. This is usually done by determining an interval of confidence or a confidence level (CL). Drawing information from a resulting measurement using statistical methods is called "statistical interpretation" or "statistical inference". This chapter describes the methods and tools used in this analysis, including a detailed summary of the underlying algorithm used to determine the exclusion limit.

For the fundamental statistical ideas, mainly reference [186] is used while a detailed description of the algorithm can be found in [187] and [188]. The following section will combine information from these references with additional sources to describe the computation which derives the final statistical results of this thesis.

The tool used to perform the statistical calculation is COMBINE [189] which uses the RooStats toolkit [190]. A detailed manual on how to use the COMBINE tool can be found at [191].

6.1 Frequentist & Bayesian Statistics

The realm of statistical interpretation can be divided into two approaches with different interpretations of probability. The first approach is called "Frequentist", following from the interpretation of probability as a limiting relative frequency. Consider a sample space S, where the elements of S are the measurements of a repeatable experiment, and the subset A$\in S$, with A being a single outcome of the experiment. The probability of A, $P(A)$, is defined as [186]:

$$P(A) = \lim_{n\to\infty} \frac{\#\text{ outcome A in } n \text{ measurements}}{n}. \tag{6.1}$$

The measurement always has to deliver some outcome which leads to $P(S) = 1$. The probability $P(A)$ is usually a function of unknown model parameters which are assumed to have a fixed value (which is not necessarily known). Thus, in the Frequentist approach, probabilities are only associated with the outcome of observations.

The second interpretation in statistical inference is the "Bayesian" interpretation. In contrast to the Frequentist idea, the Bayesian approach adds a factor of subjectivity to the probability. In Bayesian statistics, the sample space S consists of hypotheses which can either be true or false. The hypotheses of the sample space must be mutually exclusive, meaning that only one hypothesis can be true. The probability associated with such a hypothesis A, which is a subsample of S, is called "degree of belief" $P(A)$ [186]:

$$P(A) = \text{degree of belief that } A \text{ is true.} \tag{6.2}$$

Since one of the subsamples of S must be true, $P(S) = 1$.

The Frequentist interpretation can be taken as part of the Bayesian approach if the fraction of a specific outcome A, while repeating a measurement multiple times, can be defined as a hypothesis. Additionally, a subjective probability can also be assigned to unknown parameters of a model, e.g. describing the degree of belief that the unknown parameter lies in a specific interval.

6.2 Limit Calculation with Bayesian Statistics

Bayesian statistics is closely connected to Bayes Theorem [186]:

$$P(A|B) = \frac{P(B|A)P(A)}{P(B)}, \tag{6.3}$$

where A and B are subsets of the sample space S and $P(A|B)$ is the conditional probability of A given B [1]. Assuming S can be divided into disjoint subsets, A_i, so that the union of all subsets A_i gives S ($\cup_i A_i = S$), and that these subsets do not intersect ($A_i \cap A_j = \emptyset$ for $i \neq j$), one can write an arbitrary subset B from S as [186]:

$$B = B \cup S = B \cup (\cap_i A_i) = \cup_i (B \cap A_i). \tag{6.4}$$

$$\tag{6.5}$$

Consequently:

$$P(B) = P(\cup_i (B \cap A_i)) = \sum_i P(B \cap A_i) = \sum_i P(B|A_i)P(A_i). \tag{6.6}$$

Equation 6.6 is called the "law of total probability". One now can rewrite Equation 6.3 to:

$$P(A|B) = \frac{P(B|A)P(A)}{\sum_i P(B|A_i)P(A_i)}. \tag{6.7}$$

In the case of Bayesian inference, one can interpret B as the measured data x and A as the model hypothesis H. The sum in the denominator becomes an integral over all possible hypotheses [3]

$$P(H|x) = \frac{P(x|H)P(H)}{\int P(x|H')P(H')dH'}. \tag{6.8}$$

As the measurement x is known and fixed, $P(x|H)$ is called the "likelihood" of H, $P(H)$ is called the prior of H (before the measured data is known) and $P(H|x)$ is called the posterior (after the measurement). Bayes theorem, therefore, allows us to update our knowledge, or degree of belief, in our hypothesis with the use of data from measurements.

Most of the time, one is interested in a specific parameter that determines the hypothesis H, called "parameter of interest" θ. Therefore, one is interested in the posterior distribution of such parameter θ. As experiments are not perfectly accurate, they have uncertainties associated with them. To take these effects into account, additional parameters are added to the model

[1] Also defined as $P(A|B) = \frac{P(A \cap B)}{P(B)}$

hypothesis, called "nuisance parameters" $\vec{\nu}$. $\vec{\nu}$ contains all single nuisance parameters ν, each with an individual prior $P(\nu)$ which will be explained in Section 6.2.1. All single individual priors are combined into $P(\vec{\nu})$. The likelihood $P(x|H)$ then becomes $P(x|\theta,\vec{\nu})$. To handle the uncertainties, the "marginal" likelihood is constructed where the nuisance parameters $\vec{\nu}$ are integrated out of the likelihood [3]:

$$P(x|\theta) = \int P(x|\theta,\vec{\nu}')P(\vec{\nu}')d\vec{\nu}', \tag{6.9}$$

with the prior of the nuisances $P(\vec{\nu}')$. This gives the posterior distribution of the model θ:

$$P(\theta|x) = \frac{P(x|\theta)P(\theta)}{\int P(x|\theta')P(\theta')d\theta'}. \tag{6.10}$$

For an upper limit with a CL of 95 % on θ, one writes:

$$\int_0^{\theta_{upper}} P(\theta|x)d\theta = 0.95. \tag{6.11}$$

6.2.1 Likelihood of a Counting Experiment and Nuisance

As events from proton-proton collisions measured in the CMS are independent counts, they can be assumed to be Poisson distributed. Thus, the likelihood without any nuisances becomes:

$$P(\mathbf{x}|\theta) = \prod_{i\in bins} \frac{(s_i(\theta)+b_i)^{x_i} e^{-(s_i(\theta)+b_i)}}{x_i!}, \tag{6.12}$$

where s_i and b_i give the expected number of events per bin for the signal and background prediction, respectively. Note that s_i is dependent on the parameter of interest θ. Moreover, x_i is the measured number of events.

The prior degree of belief for $P(\theta)$ is chosen to be uniform, giving the same probability for all values of $\theta > 0$ and 0 otherwise [192]. As mentioned before, this likelihood needs to be extended for the case of a non-perfect experiment. This leads to the introduction of nuisances as additional parameters to the likelihood:

$$P(\mathbf{x}|\theta,\vec{\nu}) = \prod_{i\in bins} \frac{(s_i(\theta,\vec{\nu})+b_i(\vec{\nu}))^{x_i} e^{-(s_i(\theta,\vec{\nu})+b_i(\vec{\nu}))}}{x_i!} \times \prod_j^{N_\nu} \pi(\nu_i). \tag{6.13}$$

Now s and b are functions of the nuisance parameters $\vec{\nu}$, which are also called "response functions". The product $\prod_j^{N_\nu} \pi(\nu_i)$ is introduced to take the presence of parameters that are derived from additional measurements into account. $\pi(\nu)$ represents the priors of the specific nuisance parameters.

Depending on the type of nuisance, the prior changes. For nuisances describing an uncertainty on the normalization of the spectrum (e.g. on the luminosity or the cross section), a log-normal prior is chosen as it provides a safe implementation of positively defined observables. The prior

probability density function (pdf) for nuisances like this is defined as [193]:

$$\pi(\nu) = \frac{1}{\sqrt{2\pi}\ln(\kappa)} \exp\left(-\frac{(\ln(\nu/\tilde{\nu}))^2}{2(\ln(\kappa))^2}\right)\frac{1}{\nu}\,, \tag{6.14}$$

where $\tilde{\nu}$ is the measured value of the nuisance parameter and $\kappa = 1 + \Delta x/x$ with $\Delta x/x$ being the relative uncertainty.

Uncertainties on the actual shape of the distribution (e.g. object scale uncertainties or jet energy corrections) use the "vertical template morphing" technique [194]. For that, the distribution shifted up and down by one σ is provided together with the nominal. For shifts bigger than one σ, linear extrapolation is applied. For shifts in the $\pm 1\sigma$ range, a spline is used for interpolation [191]:

$$f(\nu) = (\frac{1}{2}\left((\delta^+ - \delta^-)\nu + \frac{1}{8}(\delta^+ + \delta^-)(3\nu^6 - 10\nu^4 + 15\nu^2)\right). \tag{6.15}$$

Here, f is the fraction of events in a specific bin, ν is the normalized nuisance parameter value ($\nu = 1$ means a shift of one σ up and $\nu = -1$ a shift one σ down) and $\delta^{\pm}$ are defined as:

$$\delta^+ = f(\nu = 1) - f(\nu = 0) \tag{6.16}$$
$$\delta^- = f(\nu = -1) - f(\nu = 0). \tag{6.17}$$

Therefore, the deltas δ^+ and δ^- describe the difference between the up and down shifted bin compared to the nominal one. This interpolation is used as the response function for the specific nuisance parameter together with a unit Gaussian prior. If the method provides a negative value for the bin, the value is set to 0.

Statistical uncertainties on the yield of each bin are incorporated using the Barlow-Beeston-lite approach, where the "lite" means that one nuisance is used to scale the sum of all processes instead of using separate parameters per process [194, 195]. For that, each background contribution to a bin gets summed together to a total number of events per bin n_{tot}. The errors of each background get summed quadratically e_{tot}. The quadratic ratio of these two values is then compared to a threshold number $n^{threshold}$. If the ratio is smaller than the threshold, uncertainties per background will be evaluated independently using a Poisson-constrained parameter. Otherwise, a Barlow-Beeston-lite parameter is used with a Gaussian-constraint [191]. This offers the evaluation of the statistical uncertainty per bin and, if needed, for each process separately, while keeping the computational demand at a reasonable level by minimizing the number of necessary parameters.

Equation 6.9 and the complex form of Equation 6.13 already hint at multiple challenges. The determination of the posterior distribution for θ as the normalization integral over all possible hypotheses can usually not be calculated. Additionally, the integral of the likelihood and the different nuisance parameters are also problematic, often making the analytic calculation impossible. This is solved by using a method called "Markov Chain Monte Carlo" or "MCMC" [188].

6.2.2 Markov Chain Monte Carlo

As the integration in equation Equation 6.9 often can not be performed analytically, especially if the number of nuisance parameters is large, a sampling method to approximate the integral is used.

Considering that one wants to perform the integration of some function $f(x)$: $F = \int f(x)dx$. The integral can be approximated by the expected value of F_N [196], defined as:

$$F_N = \frac{1}{N}\sum_{i=1}^{N}\frac{f(X_i)}{p(X_i)}, \tag{6.18}$$

where X_i is a random variable with the arbitrary probability density function $p(x)$ and $f(x)$ is the function one wants to integrate. The expected value of F_N is:

$$\begin{aligned} E[F_N] &= E\left[\frac{1}{N}\sum_{i=1}^{N}\frac{f(X_i)}{p(X_i)}\right] && (6.19)\\ &= \frac{1}{N}\sum_{i=1}^{N}\left[\frac{f(X_i)}{p(X_i)}\right] && (6.20)\\ &= \frac{1}{N}\sum_{i=1}^{N}\int\frac{f(x)}{p(x)}p(x)dx && (6.21)\\ &= \frac{1}{N}N\int\frac{f(x)}{p(x)}p(x)dx && (6.22)\\ &= \int f(x)dx. && (6.23) \end{aligned}$$

This method of calculating an integral by sampling over random values X_i is also called "Monte Carlo Integration". A way to implement this MC integration is by using a construction called "Markov Chain" [188].

Consider a state space $S = \{s_1, s_2, ..., s_N\}$, where s_i with $i \in \mathbb{N}$ is called a state. A "Markov Chain" is then a construct where the probability of being in state s_n, $P(s_n)$, is only dependent on the state s_{n-1}, hence [188]:

$$P(s_n) = \sum P(s_n|s_{n-1}) \cdot P(s_{n-1}). \tag{6.24}$$

Assuming a finite state space with states numbered from 1 to N, and the Markov Chain to be time invariant, the one step transition probability from one state to the next can be written as the matrix:

$$\boldsymbol{P} = \begin{bmatrix} p_{1,1} & \cdots & p_{1,N} \\ \cdots & & \cdots \\ p_{N,1} & \cdots & p_{N,N} \end{bmatrix},$$

with $p_{i,j}$ being the probability of going to the state s_j from s_i, i.e. $p_{i,j} = P(s_j|s_i)$. Following the Chapman-Kolmogorov equation, the transition probability matrix at step n $\boldsymbol{P}^{[n]}$ can be written as

the transition probability matrix to the power of n [188]:

$$\boldsymbol{P}^{[n]} = \boldsymbol{P}^{n}. \tag{6.25}$$

One can define the occupation probability function at the starting step of the chain $\boldsymbol{\alpha}^{(0)}(\alpha_1^{(0)}, ..., \alpha_K^{(0)})$, where $\alpha_i^{(0)}$ is the probability of the chain being in the state s_i at step 0. The occupation probability function at step n can then be written as the product of the starting point and the transition probability matrix:

$$\boldsymbol{\alpha}^{(n)} = \boldsymbol{\alpha}^{(0)} \times \boldsymbol{P}^{n}. \tag{6.26}$$

Assuming that, as $n \to \infty$, the Markov Chain has a limiting distribution, one can define the so-called "long run distribution":

$$\pi = \lim_{n\to\infty} \alpha^{(n)}. \tag{6.27}$$

If this limit exists for the present Markov Chain, one can write:

$$\boldsymbol{P}^{[n+1]} = \boldsymbol{P}^{[n]} \times \boldsymbol{P}, \tag{6.28}$$

which, as $n \to \infty$, becomes:

$$\boldsymbol{\pi} = \boldsymbol{\pi} \times \boldsymbol{P}. \tag{6.29}$$

Thus, the occupation probability function $\boldsymbol{\pi}$ does not change anymore. Equation 6.29 is called the steady state equation. The conditions under which a Markov Chain has a steady state can be found in [188]. If a long run distribution exists, the posterior probability distribution can be calculated using an algorithm called "Metropolis-Hastings".

6.2.3 Metropolis Hastings Algorithm (MH)

The Metropolis Algorithm [197], modified by Hastings [198], provides a method to draw a random sample from a posterior distribution where the actual normalization of the distribution is unknown and only the shape can be used. Namely, a Markov Chain is applied to a continuous state space, assuming the existence of a long run distribution [188].

Looking at Equation 6.29 and Equation 6.10, one can identify the posterior $P(\theta|x)$ as the desired long run distribution π. It is possible to show that the posterior is the long run distribution of the Markov Chain if, for a chosen candidate distribution $q(\theta', \theta)$ which generates a candidate θ' using a starting point θ, the reversibility condition is satisfied [188]:

$$P(\theta|x)q(\theta', \theta) = P(\theta'|x)q(\theta, \theta'). \tag{6.30}$$

However, most of these candidate distributions do not fulfil the reversibility condition. The Metropolis-Hastings Algorithm solves this problem by introducing a *probability of moving* α[2] [188]:

$$\alpha(\theta, \theta') = min\left[\frac{P(\theta'|x)q(\theta', \theta)}{P(\theta|x)q(\theta, \theta')}\right]. \tag{6.31}$$

[2]Note that here, α is not a matrix and a different probability then $\boldsymbol{\alpha}$ used in Equation 6.29.

The new candidate distribution $\alpha(\theta,\theta')q(\theta,\theta')$ now fulfils the reversibility condition and $P(\theta|x)$ is the long run distribution of the Markov Chain. Additionally, as the algorithm introduces a ratio, the normalization is defined as an integral over all possible hypotheses in Equation 6.10 cancels out solving the integral calculation challenge, discussed in Section 6.2. The full Metropolis Hastings Algorithm to draw from an unknown posterior with the use of a Markov Chain follows the following steps [188]:

1. Choose an initial value θ^0.
2. For each step i of the Markov Chain, up to a specified maximum step, repeat:
   a) Draw a value θ' from the chosen candidate distribution $q(\theta^{i-1},\theta')$,
   b) Calculate the *probability of moving* $\alpha(\theta^{i-1},\theta')$,
   c) Draw a random number u from a uniform distribution between 0 and 1,
   d) If u is smaller than $\alpha(\theta^{i-1},\theta')$ then accept θ' as a new step value, otherwise set it to the value from the previous step $\theta^i = \theta^{i-1}$.

The candidate distribution q is chosen to be a multivariate Gaussian, built from the product of multiple independent Gaussians, one for each parameter of interest and nuisance parameter. To keep the chain acceptance rate high, only one nuisance is varied at each step of the Markov Chain.

After a number of steps in the Markov Chain, and using Equation 6.10 in Equation 6.31, one draws samples of θ following the posterior $P(\theta|x)$ using only $P(x|\theta)P(\theta)$, without having to analytically solve the integration of the marginalized likelihood. The resulting distribution of θ can then be integrated to calculate the upper limit of the parameter of interest.

6.3 Result of the Statistical Interpretation

Now that the fundamental statistics and the computation method have been introduced, this section describes the final results of the statistical interpretation, using the mass distributions presented in Section 5.12 and Section 5.13. As signal models, the Monte Carlo based simulation is used after the final event selection. As no significant deviations have been observed, exclusion limits for the different signal models presented in Section 5.4 will be discussed. Additionally, for the first time in this specific search, model independent exclusion limits will be presented. Each year is analysed separately and combined during the statistical analysis, taking the correlation of the systematic uncertainties, as explained in Section 5.10, between the years into account. For the $\mu\tau$ channel, the `NanoAOD` version is used as the input for the final limit calculation and then compared to the result using the `MiniAOD` format.

6.3.1 Impacts

Before calculating the limit, the impact of the nuisances on the limit is evaluated. Varying the distribution within its uncertainties, changes of the limit parameter r are calculated and are shown in Figure 6.1 for the $e\mu$ channel, in Figure 6.2 for the $e\tau$ channel and in Figure 6.3 for the $\mu\tau$ channel. This is a check on the implementation and importance of the uncertainties as nuisances, as well as on the performance of the nuisances variations. Only the 30 nuisance

parameters with the highest impact on the limit calculation are shown for all three different channels.

Since one is only interested in the performance of the uncertainties, this check does not use the measured data but an Asimov dataset [199]. Thus, in this context, the background prediction is used as the measured data.

In the left plot, the pull indicates the change of the nuisance parameter value to the best postfit value compared to the prefit input for the specific nuisance. The error bar shows the best-fit $\pm 1\sigma$ range for this nuisance. As the data and the background input are the same, the pull on the postfit is zero. Error bars smaller than ± 1 indicate a constrain on the uncertainty by the fit algorithm. Entries which are uncorrelated between the years contain the specific year number. Additionally, for the statistical uncertainty ("MC stat.") the mass range of the corresponding bin is given.

The check shows that the statistical uncertainty on the high mass bins plays a significant role in the derivation of the limit. Additionally, the data is expected to constrain certain uncertainties (e.g. the uncertainty on the fake rate "MisID"). The fake rate uncertainty, moreover, shows the biggest constrain of all nuisances. Although this indicates that the recommended uncertainty of 50 % on the fakerate description overestimates the uncertainty, the COMBINE tool can change this value to a more fitting one in the calculation. Overall, no unexpected behaviour of the nuisances has been observed in all three channels.

It is important to mention that these tests were performed using a Sequential Standard Model Z' signal with a mass of 1000 GeV as a signal model input. The mass range and the width of the chosen signal sample can change the hierarchy of the impact of the nuisances. For instance, if the signal does not occupy a high mass bin, the statistical uncertainty is less likely to play an important role, the overall performance and the general behaviour of the nuisances stays unchanged.

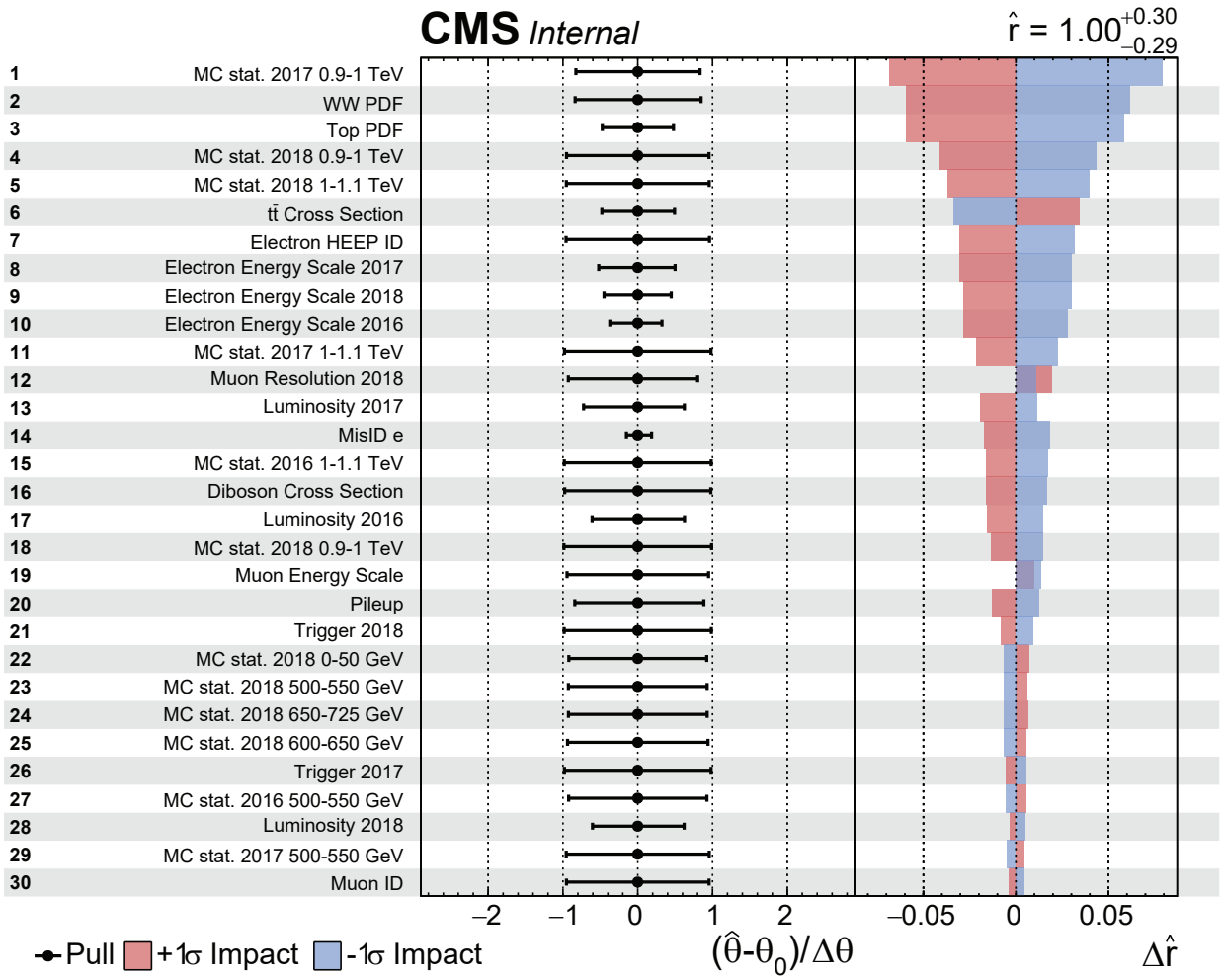

Figure 6.1.: These plots show the 30 nuisance parameters with the highest impact ($\Delta\hat{r}$) on the limit parameter $\hat{r}$ for an example SSM Z′ with a mass $m_{Z'} = 1000\,\text{GeV}$ for the $e\mu$ channel. Entries which are uncorrelated between the years contain the specific year number. Additionally, for the statistical uncertainty, the mass range of the corresponding bin is given.

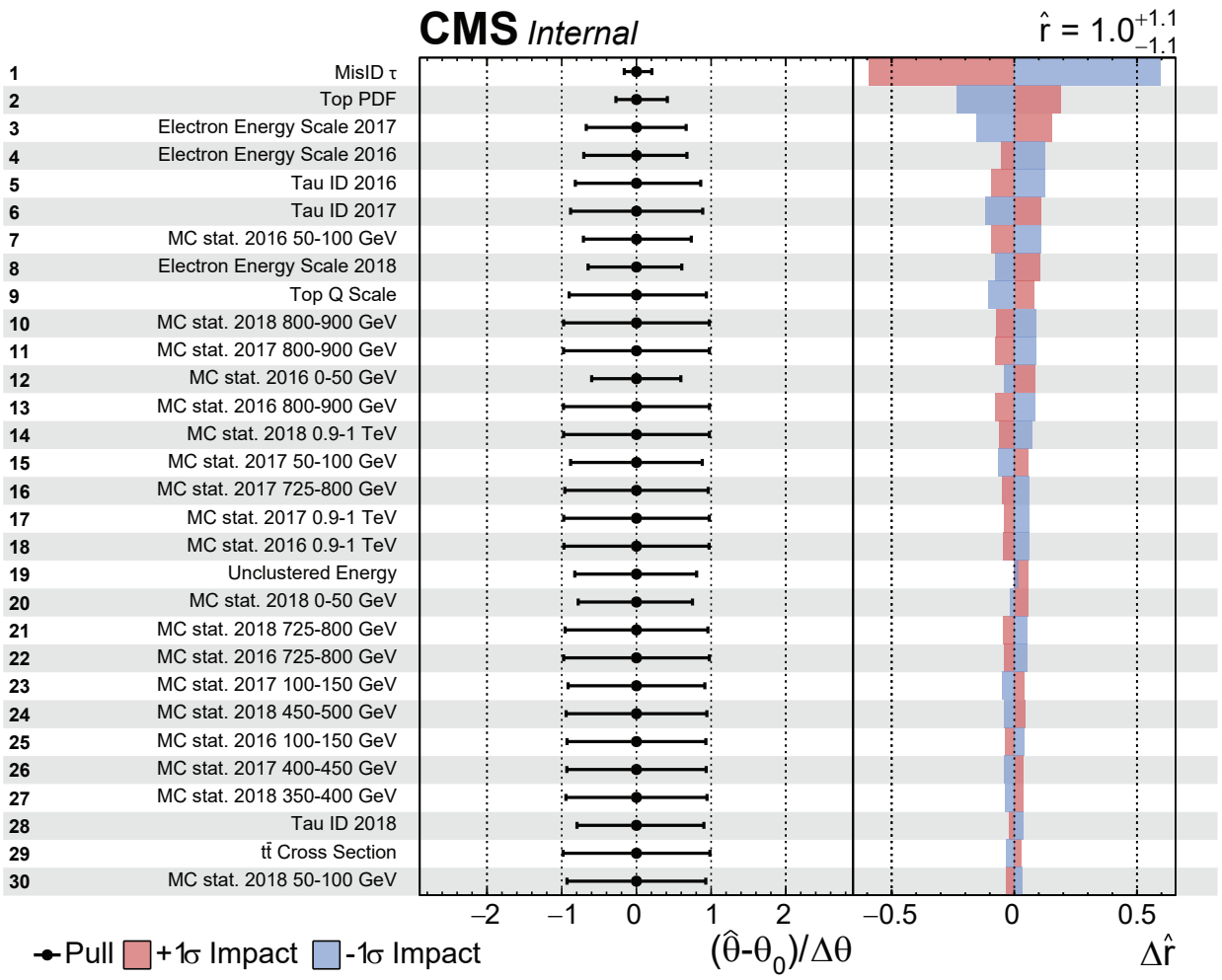

Figure 6.2.: These plots show the 30 nuisance parameters with the highest impact ($\Delta\hat{r}$) on the limit parameter $\hat{r}$ for an example SSM Z′ with a mass $m_{Z'} = 1000\,\text{GeV}$ for the $e\tau$ channel. Entries which are uncorrelated between the years contain the specific year number. Additionally, for the statistical uncertainty, the mass range of the corresponding bin is given.

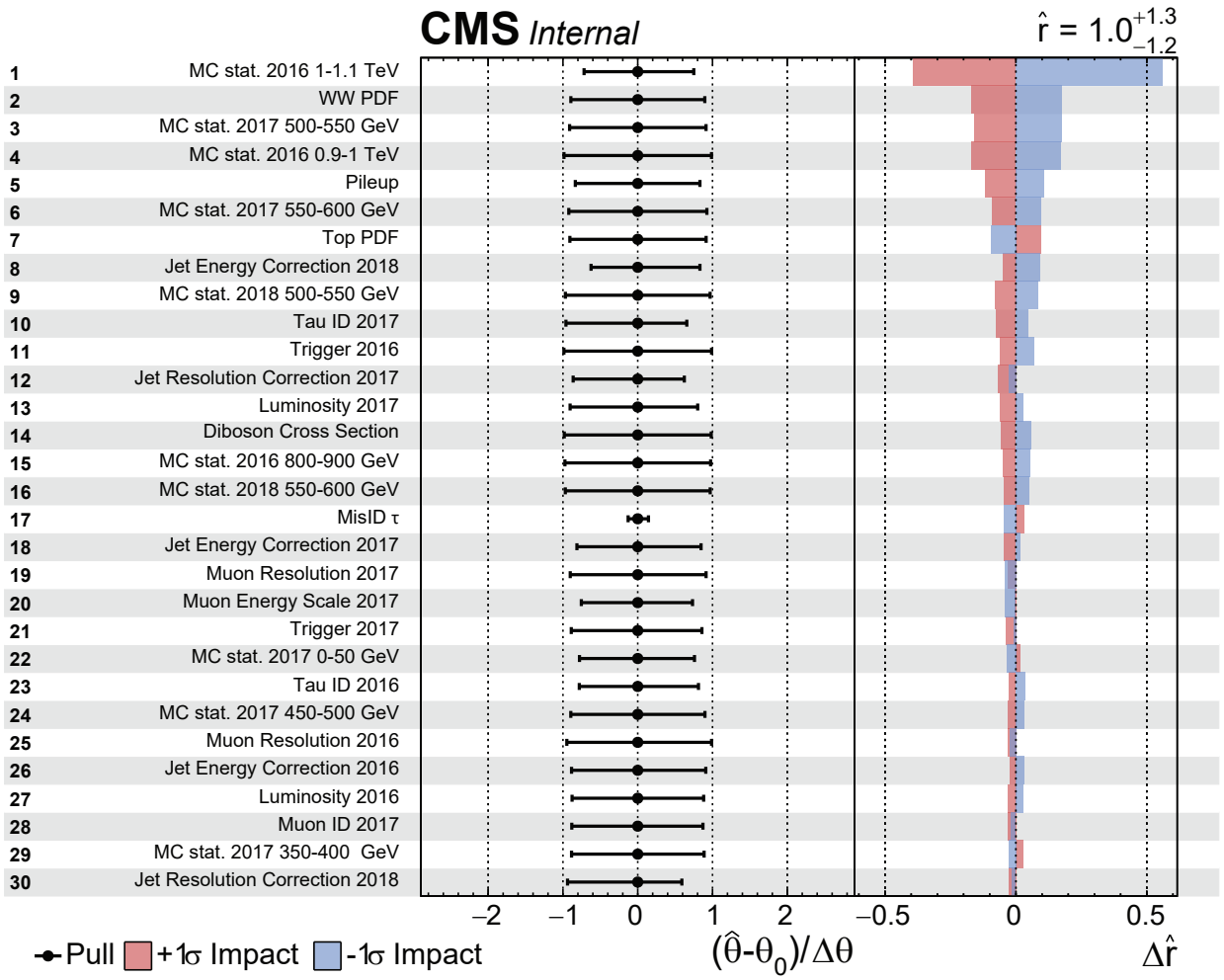

Figure 6.3.: These plots show the 30 nuisance parameters with the highest impact ($\Delta\hat{r}$) on the limit parameter $\hat{r}$ for an exemplary SSM Z′ with a mass $m_{Z'} = 1000\,\text{GeV}$ for the $\mu\tau$ channel. Entries which are uncorrelated between the years contain the specific year number. Additionally, for the statistical uncertainty, the mass range of the corresponding bin is given.

6.3.2 Sequential Standard Model

Using the signal model of a Sequential Standard Model Z′ and the signal points mentioned in Section 5.4.1, an exclusion limit on the cross section as a function of the mass is calculated. The outcome is compared to the cross section coming from the theory prediction to determine the excluded mass limit. The result for the $e\mu$ and the $e\tau$ channel for the full Run 2 exclusion limit can be seen in Figure 6.4. The limit of the $\mu\tau$ channel can be seen in Figure 6.5.

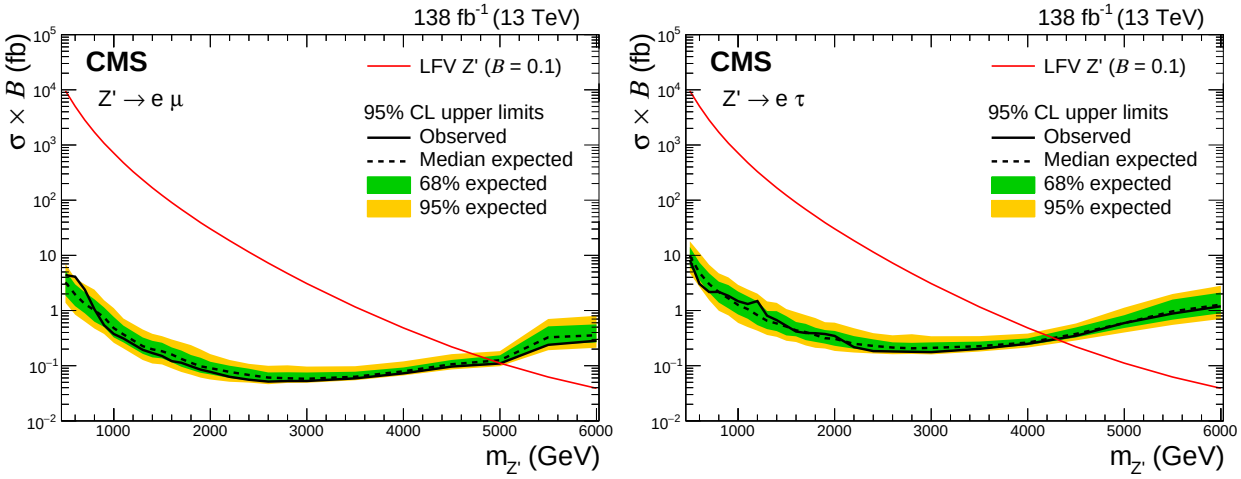

Figure 6.4.: Exclusion limit on the cross section of a Sequential Standard Model Z′ for the $e\mu$ (left) and $e\tau$ (right) for the full Run 2 dataset at 95 % confidence level. The solid black line indicates the observed limit while the dashed black line indicates the median expected limit calculated from the background simulation with repeated toy experiments. The green and yellow band show the 68 and 95 percentile interval from the expected limit distribution. The red line shows the theory cross section for a branching ratio of 10 % for the production of a Z′ decaying into the specific channel.

The figures show the calculated upper limit on the cross section as a function of the specific Z′ mass $m_{Z'}$ for the three channels $e\mu$, $e\tau$ and $\mu\tau$. The intersection between the red curve representing the theory cross section with the black curve indicates the derived observed (solid) and expected (dashed) lower mass limit for Run 2. The upper limit on the cross section decreases as one approaches the high mass regime up to a turning point at around 2.5 TeV after which the limit rises again. For lower masses, the higher upper limit is explained by the higher amount of background events, as well as by the search-specific value of the acceptance and efficiency (see Section 5.4.5). More events in the low mass region will be rejected due to the specific event selection. The rise for higher masses is due to the increasing off-shell production of the Z′, as described in Section 5.4.1. This leads to more signal events in the lower mass bins which introduce more background contribution to the limit calculation. Visible steps in the limit curve are caused by the step size of the mass samples as well as rising uncertainties (e.g. the PDF uncertainty) for high masses which can enlarge the uncertainty band.

The observed lower mass limit for the $e\mu$ channel was determined at a Z′ mass of

$$m_{Z'}^{e\mu} > 5.0\,\text{TeV}\ (95\,\%\ \text{CL}),$$

which offers an improvement of 600 GeV compared to the 2016 CMS result [93] and 500 GeV compared to the 2016 result presented by ATLAS [47]. For the $e\tau$ channel, the observed lower

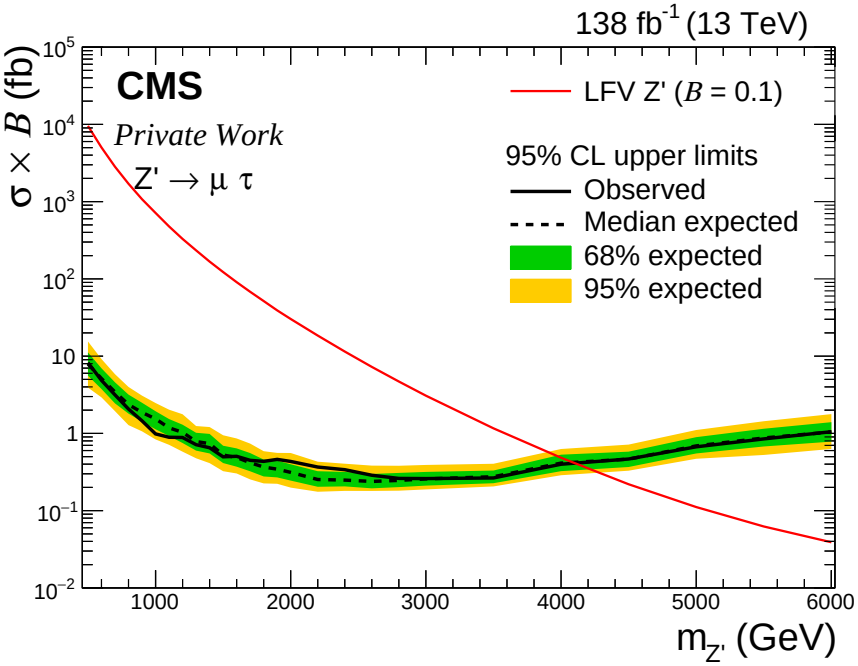

Figure 6.5.: Exclusion limit on the cross section of a Sequential Standard Model Z′ for the $\mu\tau$ channel for the full Run 2 dataset using the `NanoAOD` format at 95 % confidence level. The solid black line indicates the observed limit while the dashed black line indicates the median expected limit calculated from the background simulation with repeated toy experiments. The green and yellow band show the 68 and 95 percentile interval from the expected limit distribution. The red solid line shows the theory cross section for a branching ratio of 10 % for the production of a Z′ and a decay into the specific channel.

mass limit is set at

$$m_{Z'}^{e\tau} > 4.3\,\text{TeV}\ (95\,\%\ \text{CL}),$$

which is the first mass limit on this channel in the CMS Collaboration. This limit delivers an improvement of 300 GeV to the 2016 ATLAS result [47]. A limit of

$$m_{Z'}^{\mu\tau} > 4.1\,\text{TeV}\ (95\,\%\ \text{CL})$$

is set in the $\mu\tau$ channel, which is a gain of 600 GeV to the 2016 ATLAS result [47] and the first set limit for this channel in the LFV regime. As expected, using different data types leads to a very similar outcome regarding the limit calculation, resulting in the same observed exclusion limit.

Recently published results by the ATLAS collaboration set a limit on the Z′ mass at 5.0 TeV, 4.0 TeV and 3.9 TeV for the $e\mu$, $e\tau$ and $\mu\tau$ channels, respectively [200]. For the $e\mu$ channel, both experiments provide the same exclusion limit. In the tau channels, the presented CMS results offer a stronger limit on the Z′ mass, with a difference of 300 GeV for the $e\tau$ channel and 200 GeV for the $\mu\tau$ channel.

One can see that the statistics of the full Run 2 of the LHC measured by the CMS experiment delivers a significant improvement to earlier measurements.

The limits presented in this thesis are the best lower mass limits for a direct search of a lepton flavour violating decay of a Z′ into a pair of leptons to date.

Comparison between MiniAOD and NanoAOD

To compare the outcome of the limit calculations for the different file formats, Figure 6.6 shows the calculated limit using the MiniAOD and the NanoAOD format.

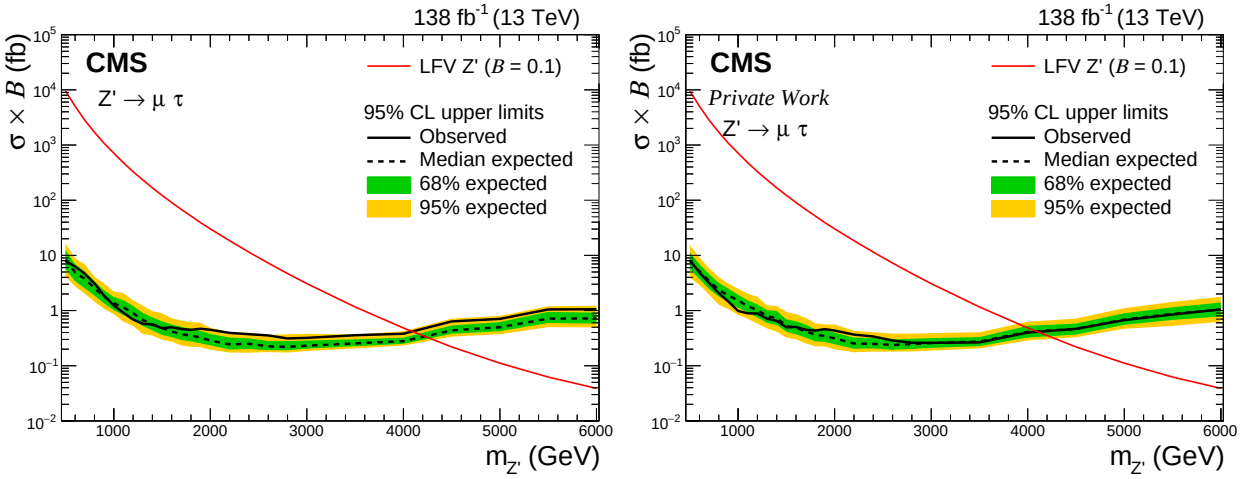

Figure 6.6.: Exclusion limit on the cross section of a Sequential Standard Model Z′ for the $\mu\tau$ channel for the full Run 2 dataset using MiniAOD (left) and NanoAOD (right) at 95 % confidence level. The solid black line indicates the observed limit while the dashed black line indicates the median expected limit calculated from the background simulation with repeated toy experiments. The green and yellow band show the 68 and 95 percentile interval from the expected limit distribution. The red solid line shows the theory cross section for a branching ratio of 10 % for the production of a Z′ and a decay into the specific channel. The limits show very similar behaviour with small differences for the two data types due to the updated corrections in the NanoAOD version.

Differences in the $\mu\tau$ channel are explained by updated corrections (e.g. jet energy corrections), creating an overall slightly better data-to-Monte Carlo agreement in the NanoAOD version. The updates also induce the change of the high mass event as well as a stronger under fluctuation at around 800 GeV. Additionally, as discussed in Section 5.12.1, the number of expected events from simulation at around 3000 GeV is lower for the MiniAOD version (a factor of 0.3). This is due to more expected fake tau events in the high mass regime in the NanoAOD version as the description of the fake tau background using the data driven approach is heavily influenced by the applied jet corrections. Comparing both limit plots, the MiniAOD version shows a slight over fluctuation for Z′ masses smaller than 1000 GeV while the NanoAOD version observed limit stays below the expected one, mainly driven by the 800 GeV bin which negates small over fluctuation appearing in the lower mass region. This becomes important again for masses above 3000 GeV as the off-shell production in the regime below 1000 GeV becomes significant when combined with the lower Monte Carlo expectation, leading to matching values for the expectation to the observation.

6.3.3 R-parity violating Supersymmetry

The outcome of the upper limit calculation using the R-parity violating supersymmetry as the signal model is shown in Figure 6.7 for the electron channels and in Figure 6.8 for the $\mu\tau$ channel. Here, the $\sigma \times B$ limit is calculated as a function of the supersymmetrical tau sneutrino $\tilde{\nu}_\tau$ mass. The theoretical cross section is shown for the case of $\lambda = \lambda' = 0.01$ (red) and $\lambda = \lambda' = 0.1$ (blue).

In comparison to the SSM Z′ limit, one can clearly see a difference in the shape of the limit. The RPV model provides a very narrow resonance without any off-shell production for higher masses. This allows to scan for deviations in the collinear and invariant distribution, being only restricted by the bin width and therefore by the resolution of the measurement and the statistics. Due to the better resolution, these effects are more prominent in the lower mass regime. For instance, the shape of the observed limit in the $\mu\tau$ channel compared to the expected limit at around 2000 GeV is directly connected to the slight excess in the measured data at this mass regime.

A similar statement can be made for the lower mass range of the $e\mu$ channel. Since uncertainties in this regime are significantly smaller than in the higher mass regime, one can observe the effect of slight deviations from the expectation in the observed limit. Additionally, the provided resolution is higher and therefore the bin width in this area is smaller. Thus, slight deviations have a stronger impact on the calculated observed limit leading to a higher discrepancy from the expected one.

As there is no off-shell production in the higher mass regime, the overall signal efficiency becomes flat and the limit stays stable as the background free regime is reached.

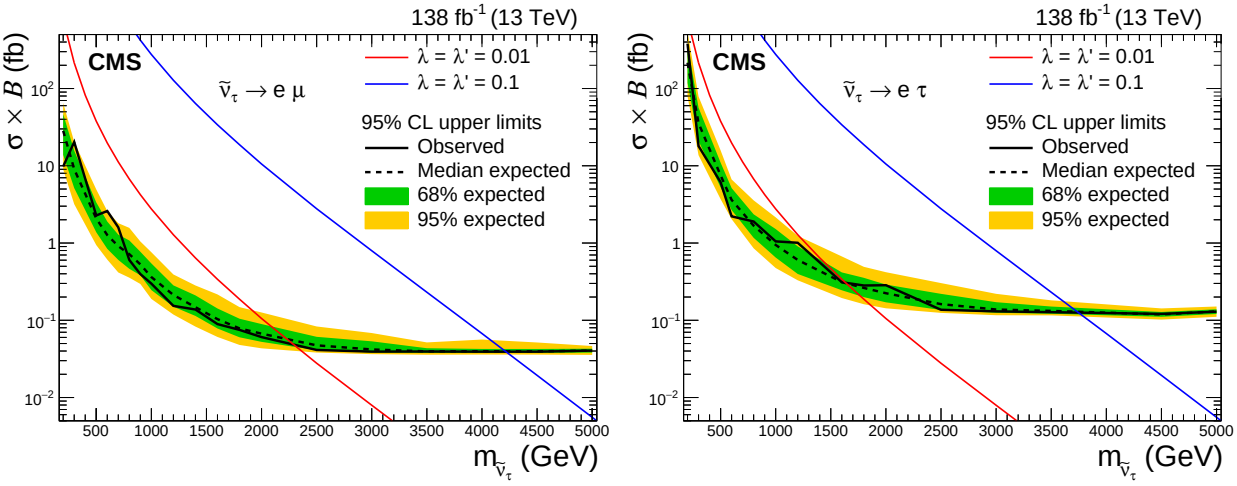

Figure 6.7.: Exclusion limit on the cross section of R-parity violating supersymmatrical stau neutrino $\tilde{\nu}_\tau$ for the $e\mu$ channel (left) and $e\tau$ channel (right) for the full Run 2 dataset at 95 % confidence level. The solid black line indicates the observed limit whereas the dashed black line indicates the median expected limit calculated from the background simulation with repeated toy experiments. The green and yellow band show the 68 and 95 percentile interval from the expected limit distribution. The solid red and the blue line show the theory cross section for the RPV model.

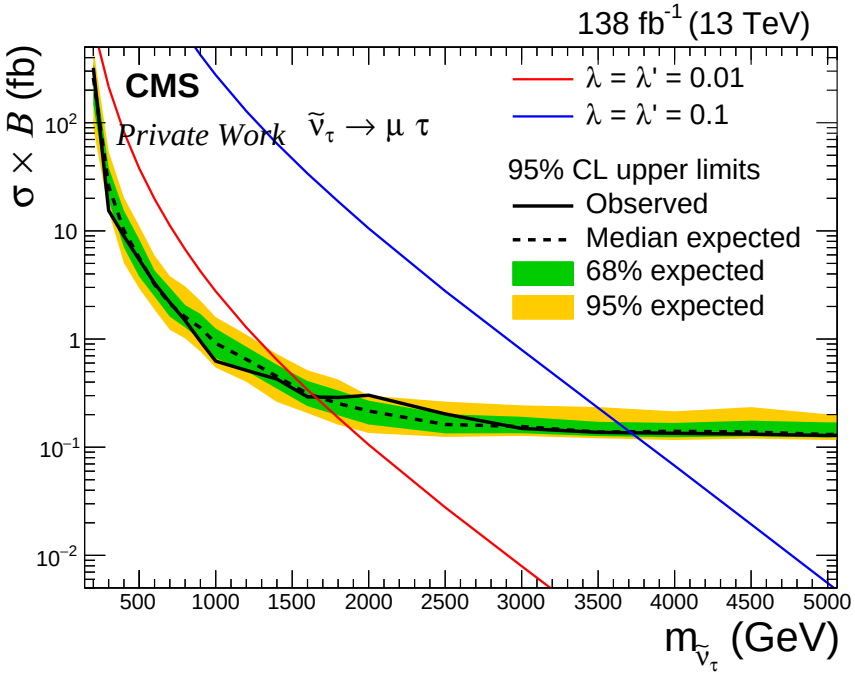

Figure 6.8.: Exclusion limit on the cross section of R-parity violating supersymmatrical stau neutrino $\tilde{\nu}_\tau$ for the $\mu\tau$ channel for the full Run 2 dataset at 95 % confidence level. The solid black line indicates the observed limit whereas the dashed black line indicates the median expected limit calculated from the background simulation with repeated toy experiments. The green and yellow band show the 68 and 95 percentile interval from the expected limit distribution. The solid red and the blue line show the theory cross section for the RPV model.

The final observed exclusion limit for the RPV tau sneutrino $\tilde{\nu}_\tau$ mass in the $e\mu$ channel, for $\lambda = \lambda' = 0.1$, lies at

$$m_{\tilde{\nu}_\tau}^{e\mu} > 4.2\,\text{TeV}\ (95\,\%\ \text{CL}).$$

This represents an improvement of 400 GeV compared to the 2016 CMS result [93]. For $\lambda = \lambda' = 0.01$, the lower mass limit is set at

$$m_{\tilde{\nu}_\tau}^{e\mu} > 2.2\,\text{TeV}\ (95\,\%\ \text{CL}),$$

a difference of 500 GeV to the 2016 CMS result.

The exclusion limit for the $e\tau$ channel is set at

$$m_{\tilde{\nu}_\tau}^{e\tau} > 3.7\,\text{TeV}\ (95\,\%\ \text{CL})$$

for $\lambda = \lambda' = 0.1$ and

$$m_{\tilde{\nu}_\tau}^{e\tau} > 1.6\,\text{TeV}\ (95\,\%\ \text{CL})$$

for $\lambda = \lambda' = 0.01$. These are the first limits for this channel in the search for LFV RPV supersymmetry in CMS.

The $\mu\tau$ lower exclusion mass limits are derived to be

$$m_{\tilde{\nu}_\tau}^{\mu\tau} > 3.7\,\text{TeV}\ (95\,\%\ \text{CL})$$

for $\lambda = \lambda' = 0.1$ and

$$m_{\tilde{\nu}_\tau}^{\mu\tau} > 1.6\,\text{TeV}\ (95\,\%\ \text{CL})$$

for $\lambda = \lambda' = 0.01$. These are also the first limits of this kind in the CMS experiment.

Using the narrow-width approximation (see Section 2.3.2), for fixed values of λ, the cross section limit can be translated into exclusion bounds in the plane of the tau sneutrino mass and the λ' coupling. Equation 2.26 can be translated into a formula to derive the coupling λ'_{311} using a fixed λ_{i3k} and the cross section times branching ratio [201]:

$$\lambda'_{311}\left(m_{\tilde{\nu}_\tau}, (\lambda_{i3k})^2 + (\lambda_{k3i})^2\right) = \sqrt{\frac{\left((\lambda_{i3k})^2 + (\lambda_{k3i})^2\right)}{\frac{k(m_{\tilde{\nu}_\tau})}{(\sigma\times\mathcal{B})_{obs}} \cdot \left((\lambda_{i3k})^2 + (\lambda_{k3i})^2\right) - 3}}, \tag{6.32}$$

with $k(m_{\tilde{\nu}_\tau})$ being a mass dependent constant, taken from [201]. These exclusion bounds can be seen in Figure 6.9. Four different values for the λ coupling are shown, namely 0.007 in black, 0.07 in red, 0.05 in blue and 0.01 in green. Additionally, the expected limit for $\lambda = 0.07$ is plotted as a comparison benchmark between the behaviour of the expected and observed limits. As the differences in the observed limit between the `MiniAOD` and the `NanoAOD` version of the $\mu\tau$ channel are small (see Section 6.3.3), this calculation is only performed using the `MiniAOD` version. The plots are created by Swagata Mukherjee and taken from the LFV CMS paper publication [1], using the limits presented in this section.

With the usage of Equation 6.32, one can derive the lower mass limit for different couplings. In the $e\mu$ channel, for $\lambda = 0.07$ and $\lambda' = 0.11$, the lower limit on the mass is at 4 TeV, while in the $e\tau$ channel is at 3.6 TeV and in the $\mu\tau$ channel also at 3.6 TeV. Compared to the 2016 ATLAS result, this is an improvement of 600 GeV in the $e\mu$ channel, 700 GeV in the $e\tau$ channel and 1000 GeV in the $\mu\tau$ channel [47].

Very recently published results by the ATLAS collaboration set a limit on the tau sneutrino $\tilde{\nu}_\tau$ for $\lambda = 0.07$ and $\lambda' = 0.11$ [200]. Differently to the previous publication, a less simplified approach of the theory model is used. As a result of gauge invariance, an anti-symmetry $\lambda_{ijk} = -\lambda_{jik}$ is introduced [163]. Thus, λ_{331} and λ_{332} have to be zero, reducing the branching ratio $\mathcal{B}$ in the tau channels while the $e\mu$ channel stays unchanged. For the $e\mu$ channel, the ATLAS limit is set at 3.9 TeV, 100 GeV lower than the presented CMS result. In the tau channels, masses below 2.8 TeV and 2.7 TeV are excluded for the $e\tau$ and $\mu\tau$ channels, respectively. Using Equation 6.32 and $\lambda = 0.07$ and $\lambda' = 0.11$ with $\lambda_{331} = \lambda_{332} = 0$, the CMS limit on the tau sneutrino mass is recalculated to be 3.3 GeV for the $e\tau$ channel and 3.3 GeV for the $\mu\tau$ channel. The limits presented in this thesis are more stringent, offering a higher exclusion limit with a difference of 500 GeV in the $e\tau$ and 600 GeV in the $\mu\tau$ channel compared to the ATLAS publication. Therefore, this thesis provides the strongest limits for a direct search of these channels to date.

Using Equation 6.32, the cross section limit from the $e\mu$ channel presented in this thesis can be

transferred into a boundary on $|\lambda'_{311}\lambda_{312}|$, assuming $\lambda = \lambda'$:

$$|\lambda'_{311}\lambda_{132}| < 1.25 \cdot 10^{-5} \text{ (95 \% CL)}. \tag{6.33}$$

For a mass of 1 TeV and assuming that $\lambda = \lambda'$, the search for $\mu - e$ conversion with the SINDRUM II experiment sets an upper limit for the coupling product $|\lambda'_{311}\lambda_{312}|$ at the order of $\mathcal{O}(10^{-7})$ [202][3]. Therefore, the indirect search sets more stringent limits compared to the direct search for a LFV tau sneutrino.

As it has already been shown in [163], the direct search for the τ channels surpasses boundaries set by indirect searches, e.g. from the Belle experiment. Results on the $\tau \to \mu\eta$ decay can be used to obtain an indirect limit on the product of the λ and λ' coupling [72, 163]:

$$|\lambda'_{311}\lambda_{323}| < 2.0 \cdot 10^{-3} \left(m_{\tilde{\nu}_\tau}/\text{TeV}\right)^2 \text{ (90 \% CL)}. \tag{6.34}$$

For a mass of $m_{\tilde{\nu}_\tau} = 1$ TeV, this limit is set at $|\lambda'_{311}\lambda_{323}| < 2.0 \cdot 10^{-3}$ at 90 % CL. Assuming $\lambda = \lambda'$ and using Equation 6.32, one can derive a similar mass limit from the CMS data for the $\mu\tau$ channel at

$$|\lambda'_{311}\lambda_{233}| < 3.2 \cdot 10^{-5} (\text{ 95 \% CL}).$$

For the $e\tau$ channel, the boundary set for a mass of 1 TeV coming from the $\tau \to e\eta$ decay is $|\lambda'_{311}\lambda_{133}| < 2.8 \cdot 10^{-3}$ (90 % CL) [72, 163], while the presented direct search offers

$$|\lambda'_{311}\lambda_{133}| < 8.1 \cdot 10^{-5} \text{ (95 \% CL)}.$$

Thus, both tau channels surpass the boundary set by the indirect search with a stronger confidence level.

[3] Important to mention is that [72, 163, 202] use a different notation of the λ_{ijk} indices. i is the index of the decaying particle and j and k refer to the decay products while in this thesis, i and k refer to the decay products and j corresponds to the decaying particle, in this case the tau sneutrino with $j = 3$.

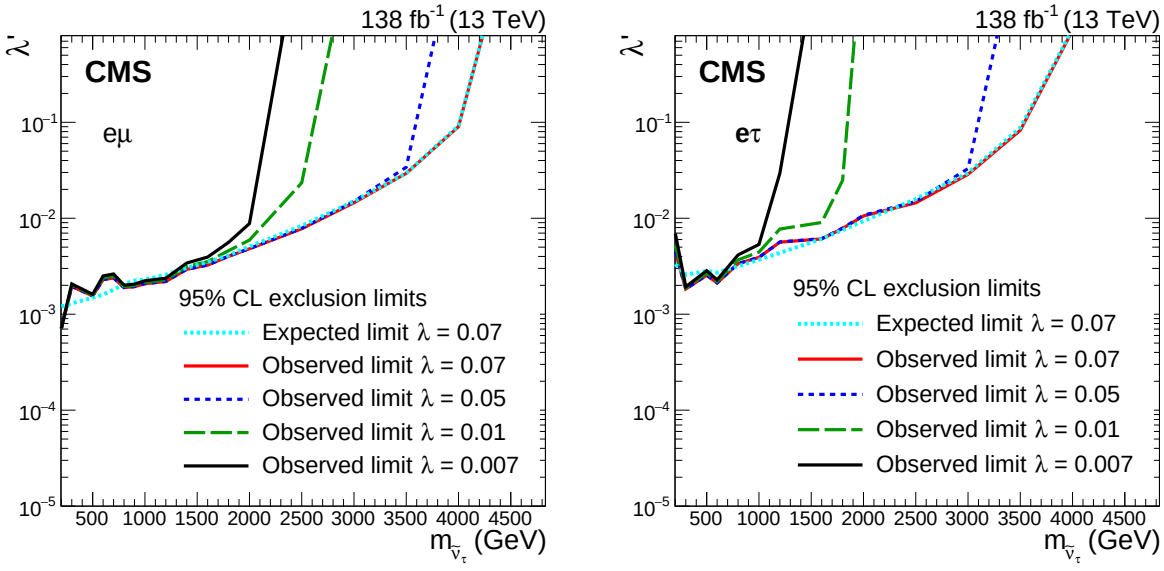

(a)

(b)

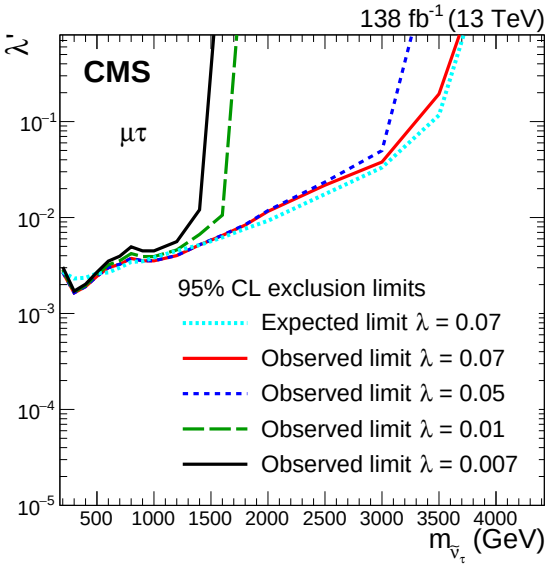

(c)

Figure 6.9.: Exclusion limits at the 95 % confidence level of R-parity violating supersymmatrical tau sneutrino $\tilde{\nu}_\tau$ for the $e\mu$ (a), $e\tau$ (b) and $\mu\tau$ (c) channel for the full Run 2 in the $m_{\tilde{\nu}_\tau}$ plane. The λ coupling is set to 0.007 (black), 0.07 (red), 0.05 (blue) and 0.01 (green). Additionally, one expected limit for $\lambda = 0.07$ is shown in bright blue.

Comparison between MiniAOD and NanoAOD

Figure 6.10 shows the outcome of the limit calculation for the RPV SUSY interpretation using the two different file formats.

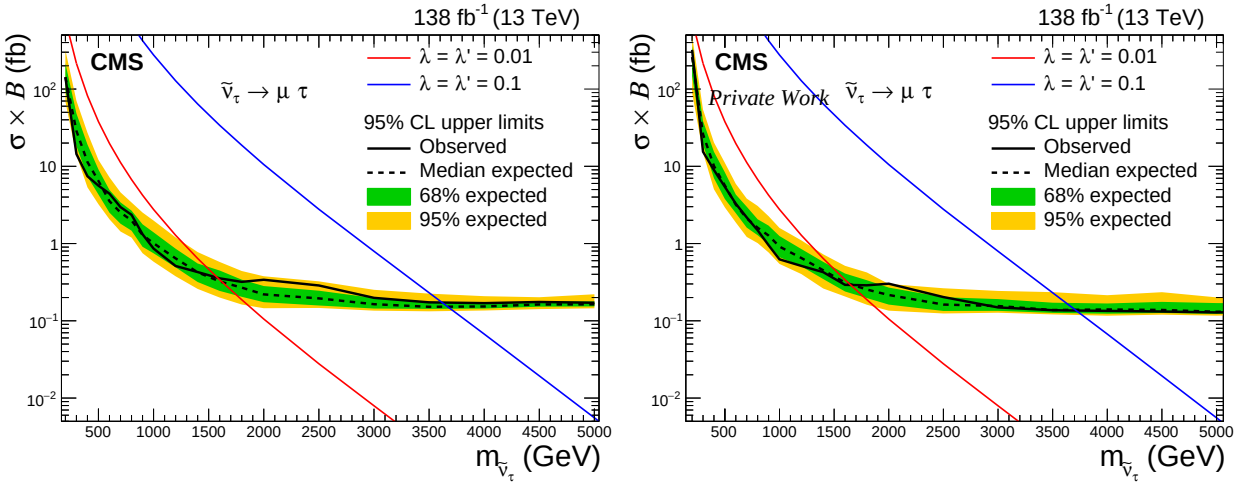

Figure 6.10.: Exclusion limit on the cross section of R-parity violating supersymmatrical stau neutrino $\tilde{\nu}_\tau$ for the $\mu\tau$ channel for the full Run 2 dataset using MiniAOD (left) and NanoAOD (right) at 95 % confidence level. The solid black line indicates the observed limit whereas the dashed black line indicates the median expected limit calculated from the background simulation with repeated toy experiments. The green and yellow band show the 68 and 95 percentile interval from the expected limit distribution. The solid red and the blue line show the theory cross section for the RPV model.The limits show very similar behaviour with small differences for the two data types due to the updated corrections in the NanoAOD version.

As in the SSM case, differences between the MiniAOD and the NanoAOD format in the $\mu\tau$ channel result from updated corrections. In the case of the RPV, as mentioned before, small changes in single bins, especially in the lower mass regime and around 3000 GeV for the simulation, have a significant impact on the limit calculation. While for the MiniAOD format, the data bins around 600 GeV are slightly above the expectation, the NanoAOD format shows an approximated ratio of 1 between data and expectation bins. Thus, the observed and expected limits are in better agreement in the NanoAOD than in the MiniAOD format. For the high mass regime, the event changing its bin from the last into the second last one has a similar effect on the observed limit for masses greater than 3000 GeV. This leads to a difference in the exclusion limit set for $\lambda = \lambda' = 0.1$ of 100 GeV between the NanoAOD and the MiniAOD version.

6.3.4 Quantum Black Hole

Unlike the SSM and RPV signal models, the Quantum Black Hole model does not lead to a resonance but to a steep rise at the threshold mass m_{th} followed by a slowly decreasing tail. Thus, single bin fluctuations do not play a significant role in the limit calculation, as the number of bins with signal occupation is rather high. Figure 6.11 shows the derived 95 % confidence level upper cross section limit for the $e\mu$ and the $e\tau$ channels as a function of the threshold mass m_{th}. Figure 6.12 shows the limit calculated for the $\mu\tau$ channel. The red curve indicates the theory cross section for the ADD case with four extra dimensions (n= 4). All three channels show good agreement between the expected and observed limits within their uncertainty bands. In the $\mu\tau$ channel, the observed limit touches the two sigma band at a threshold mass of 2 TeV, as this is the bin containing three observed data events versus about one expected event.

The lower exclusion limit on the threshold mass for four extra dimensions in the ADD model is set at

$$m_{th}^{e\mu} > 5.6\,\text{TeV}\ (95\,\%\ \text{CL})$$

in the $e\mu$ channel, at

$$m_{th}^{e\tau} > 5.2\,\text{TeV}\ (95\,\%\ \text{CL})$$

in the $e\tau$ channel and at

$$m_{th}^{\mu\tau} > 5.3\,\text{TeV}\ (95\,\%\ \text{CL})$$

in the $\mu\tau$ channel. This is an improvement of 300 GeV for the $e\mu$ exclusion limit when compared to the 2016 CMS result [93]. For $n = 6$, this limit is calculated to 5.9, 5.5 and 5.6 TeV for the $e\mu$, $e\tau$ and $\mu\tau$ channel, respectively. Compared to the ATLAS result from 2016, which sets a corresponding limit at 5.6, 4.9 and 4.5 TeV [47], this result represents an improvement of 300, 600 and 1100 GeV, respectively.

Recently published results by the ATLAS collaboration set a limit on the threshold mass with $n = 6$ at 5.9, 5.2 and 5.1 TeV for the $e\mu$, $e\tau$ and $\mu\tau$ channels, respectively [200]. Therefore, the presented result and the ATLAS publication offer the same exclusion limit for the $e\mu$ channel, while the exclusion limit set in this thesis is 300 GeV higher for the $e\tau$ channel and 500 GeV higher for the $\mu\tau$ channel.

Therefore, this thesis provides the strongest limits for a direct search of Quantum Black Holes decaying into a pair of leptons with LFV to date.

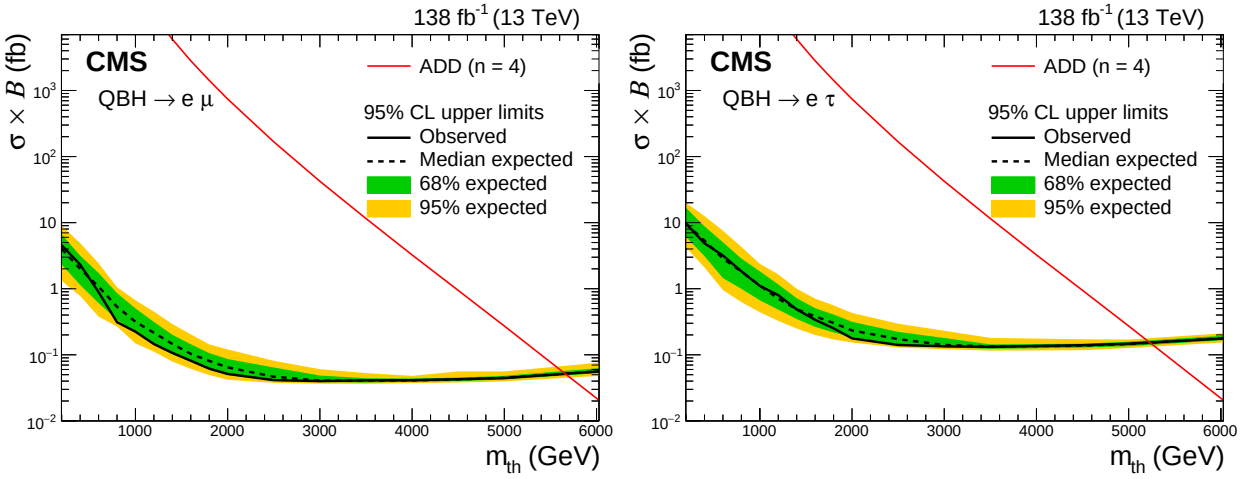

Figure 6.11.: Exclusion limit at 95 % confidence level on the cross section of a Quantum Black Hole for the $e\mu$ (left) and the $e\tau$ (right) channels for the full Run 2 dataset. The solid black line indicates the observed limit while the dashed black line indicates the median expected limit calculated from the background simulation with repeated toy experiments. The green and yellow bands show, respectively, the 68 and 95 percentile interval from the expected limit distribution. The red solid line shows the calculated theory cross section for the ADD model with four additional extra-dimensions.

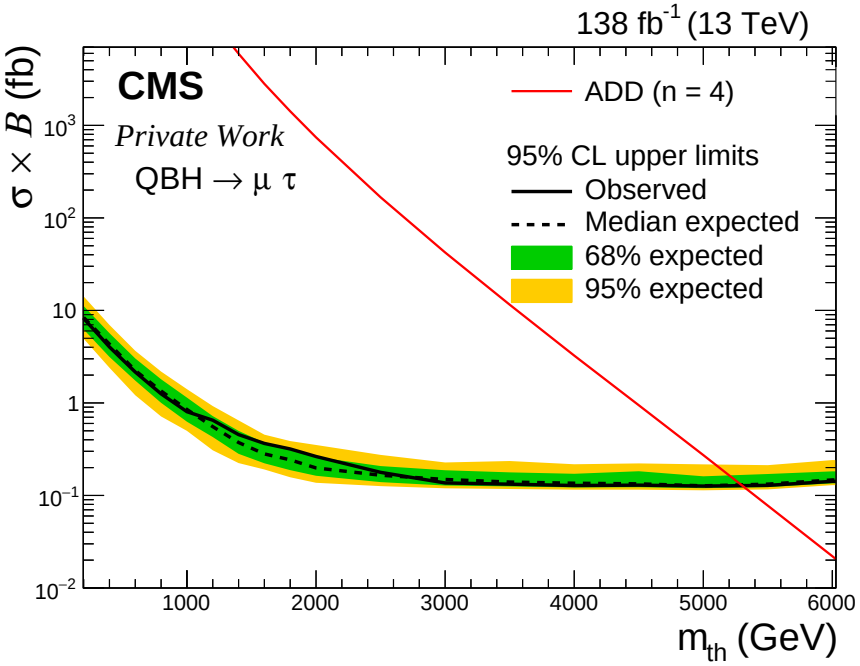

Figure 6.12.: Exclusion limit at 95 % confidence level on the cross section of a Quantum Black Hole for the $\mu\tau$ channel for the full Run 2 dataset. The solid black line indicates the observed limit while the dashed black line indicates the median expected limit calculated from the background simulation with repeated toy experiments. The green and yellow bands show, respectively, the 68 and 95 percentile interval from the expected limit distribution. The red solid line shows the calculated theory cross section for the ADD model with four additional extra-dimensions.

Comparison between MiniAOD and NanoAOD

The outcome of the limit calculation using the MiniAOD and the NanoAOD format can be seen in Figure 6.13 to compare the outcome of the different versions.

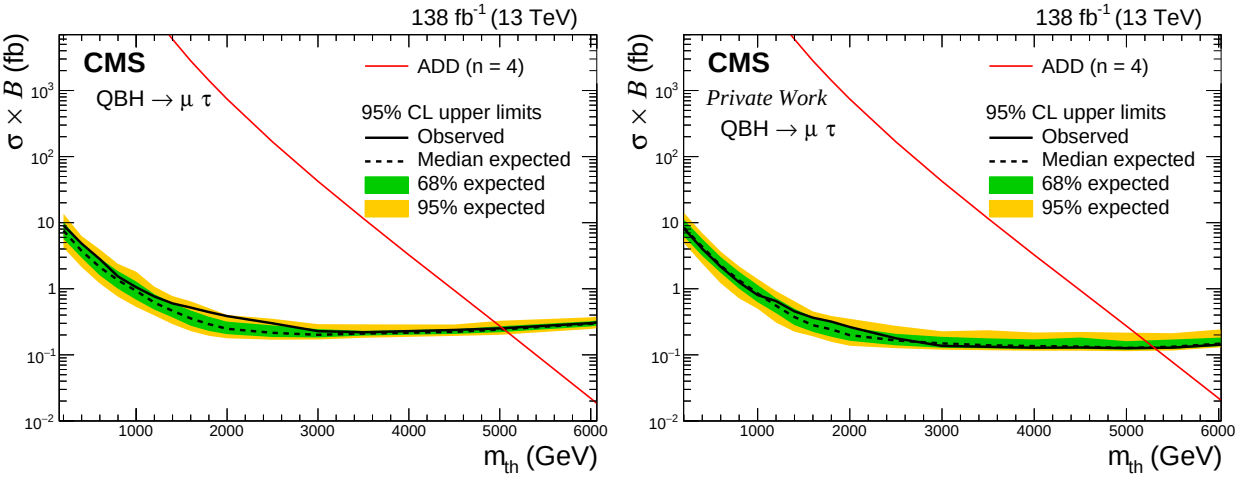

Figure 6.13.: Exclusion limit at 95 % confidence level on the cross section of a Quantum Black Hole for the $\mu\tau$ channel using MiniAOD (left) and NanoAOD (right) for the full Run 2 dataset. The solid black line indicates the observed limit while the dashed black line indicates the median expected limit calculated from the background simulation with repeated toy experiments. The green and yellow bands show, respectively, the 68 and 95 percentile interval from the expected limit distribution. The red solid line shows the calculated theory cross section for the ADD model with four additional extra-dimensions. The limits show very similar behaviour with small differences for the two data types due to the updated corrections in the NanoAOD version, leading to a higher exclusion limit.

In the $\mu\tau$ channel, the under fluctuation at around 800 GeV in the NanoAOD version cancels the over fluctuation at the highest mass bin leading to similar observed and expected limits for lower mass thresholds. As the signal has a clearly defined threshold, this effect disappears after 1000 GeV. The difference in the high mass regime can again be explained by the bin changing high mass event due to the updated corrections. This difference becomes more important for very higher masses as the contribution from low mass bins becomes less and less, as long as there are still signal events found for this mass. Thus, this difference leads to a difference in the excluded threshold mass of 300 GeV between the MiniAOD and the NanoAOD version.

6.3.5 Sphaleron Pre-Exponential Factor

This thesis presents the first exclusion limits of the sphaleron production with the specific search for LFV lepton pairs in the final state. As the only unknown parameter is the pre-exponential factor (PEF), the limit is not presented as a limit on the cross section times branching ratio but on this PEF. Additionally, there is no expected value for the PEF from theory, therefore no theory curve as presented for the SSM Z', RPV SUSY or the QBH interpretation can be drawn. The 95 % CL upper limit on the PEF for all three channels combined for the full Run 2 can be seen in Figure 6.14.

The exclusion limit on the PEF is derived by first calculating the limit on the cross section and then dividing the result by the theoretical production cross section shown in Table 5.5 for the corresponding energy point. Additionally, one also takes into account the branching ratio of the sphaleron production into a final state containing the three leptonic channels analysed in this thesis. The $\mathcal{B}$ is about 22.7 % for each of the channels.

As this signal covers a broad mass range, small differences in single bins do not play a significant role in the limit calculation. Therefore, using the `MiniAOD` or the updated `NanoAOD` analysis for the $\mu\tau$ channel does not lead to significant differences in the $\mu\tau$ channel. Thus, the `NanoAOD` input is used for the combination with the other two channels.

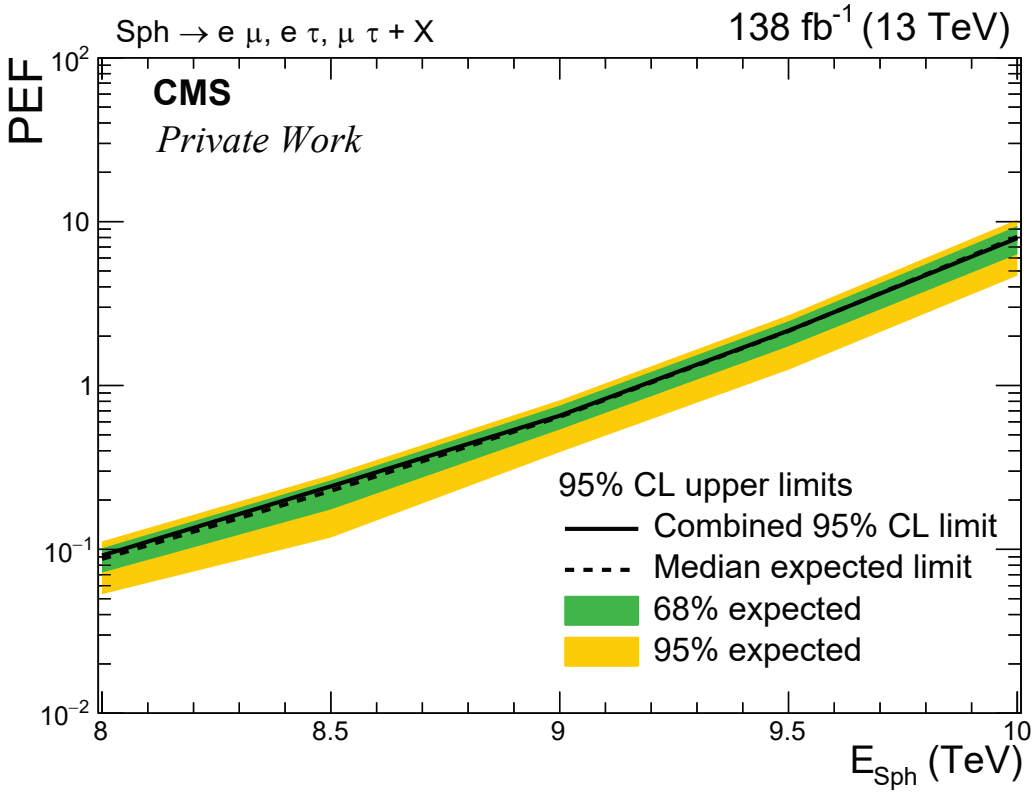

Figure 6.14.: 95 % Exclusion limit on the pre-exponential factor (PEF) of the sphaleron production as a function of the sphaleron energy E_{sph}. This limit considers all three leptonic channels combined for the full Run 2 dataset.

For a sphaleron threshold energy of 9 TeV the upper limit on the PEF is set at

$$\text{PEF} < 0.63 \ (95\,\% \ \text{CL}).$$

This result is the first limit on the pre-exponential factor of the sphaleron production with a final state containing two charged leptons, following a rather model independent approach. This limit is higher than the one presented in the dedicated high multiplicity search from CMS using 2016 data [94], corresponding to a PEF value of 0.021 for $E_{Sph} = 9$ TeV. This analysis uses the information of the full event content, especially on the multiplicity of the event. This is a more model-dependent approach which also includes not necessarily well reconstructed objects. It is therefore possible to increase the sensitivity of this search by applying additional requirements, for example high multiplicity or high sphericity. However, this would also mean becoming more dependent on that specific model search and to a certain phase-space.

This limit would benefit the most from a higher center-of-mass energy, compared to the other interpretations, as the production cross section rises significantly. Figure 6.15 shows the production cross section for sphaleron threshold energies between 8 TeV and 10 TeV at center-of-mass energies of 13, 13.6 and 14 TeV. The rise to 14 TeV would increase the cross section by about one order of magnitude at $E_{Sph} = 9$ TeV. This also shows that repeating this search using Run 3 data, measured at $\sqrt{s} = 13.6$ TeV, should deliver a significant improvement in the limit of the PEF even if the collected number of events is in the same order as for Run 2.

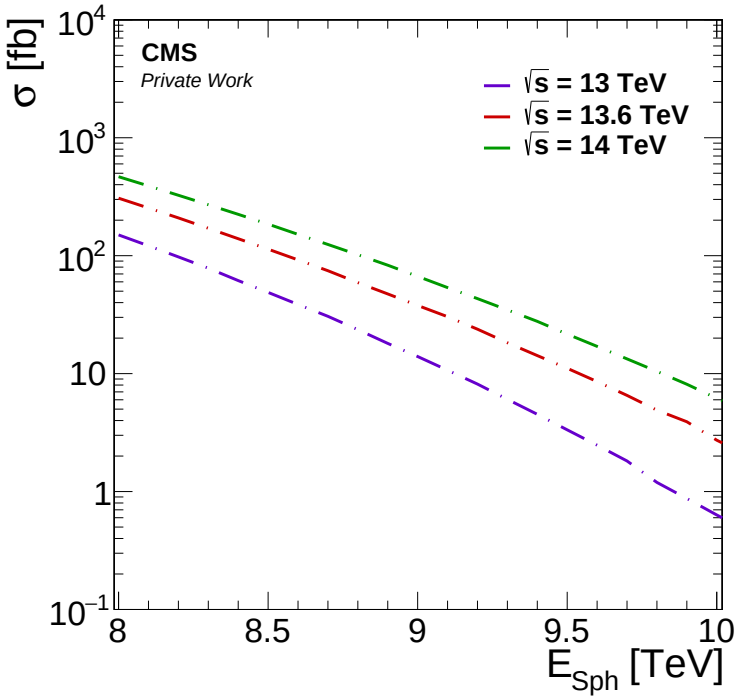

Figure 6.15.: Theoretical cross section of the sphaleron production as a function of E_{sph}, considering three different center-of-mass energies up to the design energy of 14 TeV of the LHC. Note how the cross section is increased by about one order of magnitude when the center-of-mass energy is raised by 1 TeV for $E_{sph} = 9$ TeV.

6.3.6 Model Independent Limit

In addition to the model-dependent exclusion limits presented previously, a model-independent (MI) limit is calculated for each channel. This limit can be used by theorists or others to derive a cross section limit for additional interpretations with similar final states without running a full simulation including the detector and reconstruction, as only generator level information is needed.

The main difference to the specific signal model limits is that the shape is not taken into account. The MI limit is calculated by first summing over the bins of the discriminating distribution from a specific mass threshold, m^{min}, up to infinity. The exclusion limit is then calculated on this single bin distribution. This step is repeated for multiple threshold masses, increasing in intervals of 50 GeV.

Although no signal shape is used, the acceptance times efficiency of a potential signal is assumed to show a flat behaviour as a function of the invariant mass. It is taken from the Z' interpretation and assumed to be 65 % for the $e\mu$ channel, 24 % for the $e\tau$ channel and 23 % for the $\mu\tau$ channel (see Section 5.4.5). Since the experimental $A \times \epsilon$ is already included in the limit, only the $A \times \epsilon$ on generator level needs to be calculated to apply this model independent limit.

The model-independent cross section limit can be seen in Figure 6.16 for the $e\mu$ and $e\tau$ channel and in Figure 6.17 for the $\mu\tau$ channel.

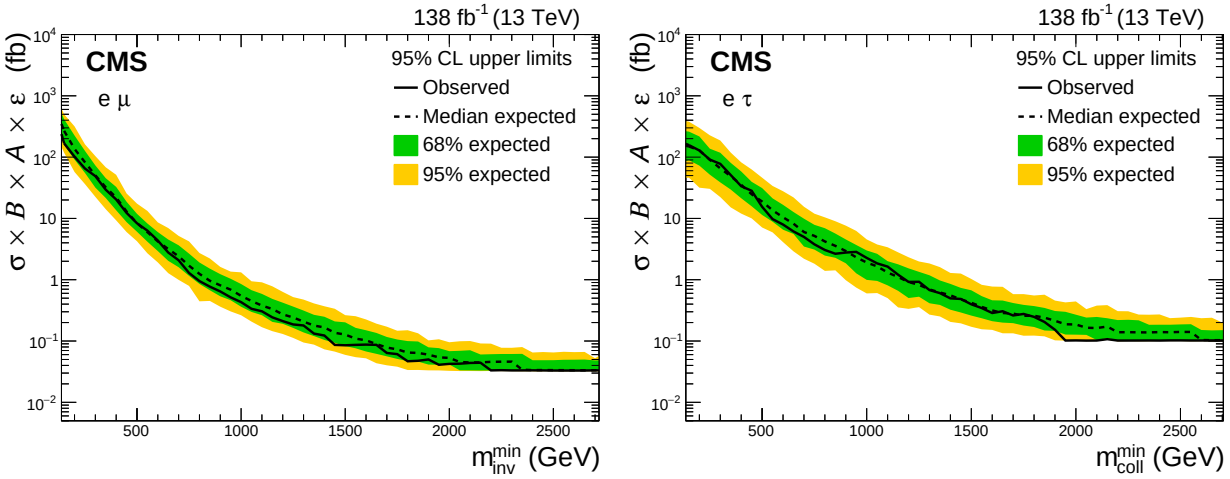

Figure 6.16.: Model-independent 95 % exclusion limit on the cross section for the $e\mu$ (left) and the $e\tau$ (right) channel for the full Run 2 dataset. The solid black line indicates the observed limit while the dashed black line indicates the median expected limit calculated from the background simulation with repeated toy experiments. The green and yellow band show the 68 and 95 percentile interval from the expected limit distribution. The limit is shown as a function of the invariant (collinear) mass.

All three channels show a good agreement between the observed and expected upper limit. The curves are falling for higher mass thresholds, starting from $\mathcal{O}(10^2)$, and becoming flat at $\mathcal{O}(10^{-1})$ once no data above the specific threshold is measured or expected.

A factor $f_m(m^{min})$ representing the effect of the minimum mass threshold m^{min} on the signal distribution is calculated by summing the number of signal events on generator level above the

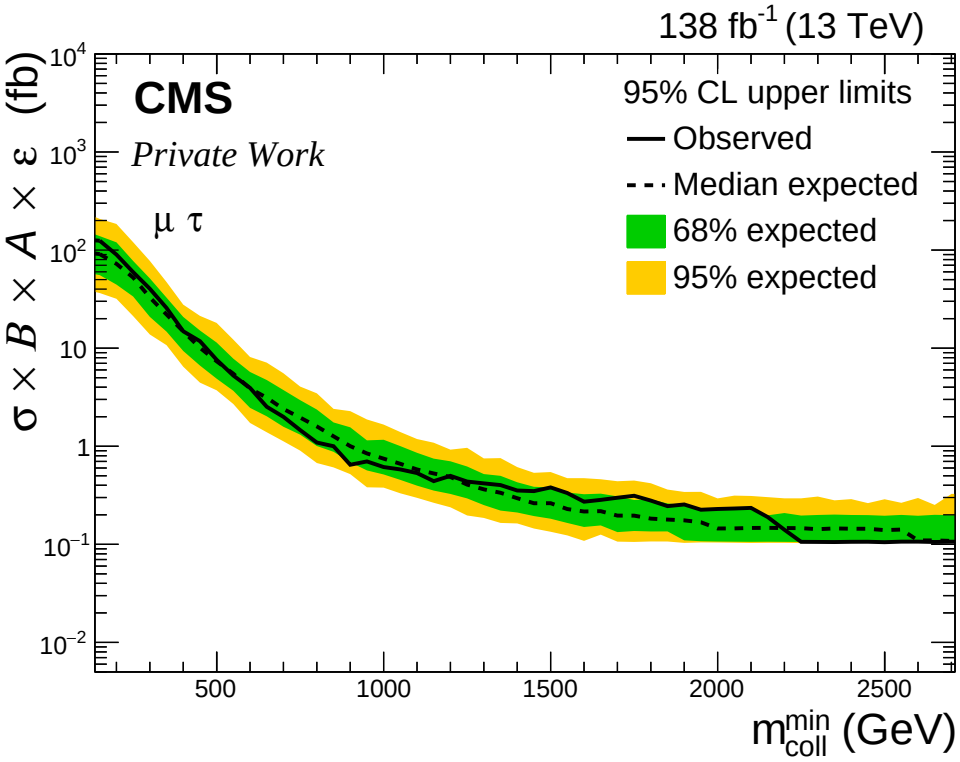

Figure 6.17.: Model-independent 95 % exclusion limit on the cross section for the $\mu\tau$ channel for the full Run 2 dataset. The solid black line indicates the observed limit while the dashed black line indicates the median expected limit calculated from the background simulation with repeated toy experiments. The green and yellow band show the 68 and 95 percentile interval from the expected limit distribution. The limit is shown as a function of the collinear mass.

threshold and dividing the result by the total number of generated events:

$$f_m(m^{\text{min}}) = \frac{\text{number of events } m > m^{\text{min}}}{\text{total number of events}}. \tag{6.35}$$

The exclusion limit on the cross section times branching fraction of the new interpretation $(\sigma\mathcal{B}\text{A}\varepsilon)_{\text{excl}}(\text{total})$ can be determined by dividing the MI exclusion limit by the $f_m(m^{\text{min}})$:

$$(\sigma\mathcal{B}\text{A}\varepsilon)_{\text{excl}}(\text{total}) = \frac{(\sigma\mathcal{B}\text{A}\varepsilon)_{\text{MI}}(m^{\text{min}})}{f_m(m^{\text{min}})}, \tag{6.36}$$

where $(\sigma\mathcal{B}\text{A}\varepsilon)_{\text{excl}}(\text{total})$ is the exclusion limit calculated for the specific new model interpretation and the specific mass threshold and $(\sigma\mathcal{B}\text{A}\varepsilon)_{\text{MI}}$ is the model-independent limit.

The $(\sigma\mathcal{B}\text{A}\varepsilon)_{\text{excl}}(\text{total})$ needs to be determined for all mass threshold values. The minimum of all these exclusion limits is then chosen to be the exclusion limit for the new interpretation. If the theoretical cross section times branching ratio is larger than the exclusion limit derived from the MI limit, this specific model can be excluded.

Comparison between MiniAOD and NanoAOD

Figure 6.18 shows the result of the model-independent limit calculation using the different file formats. The differences in the two $\mu\tau$ channel versions are again due to the updated corrections in the NanoAOD version, leading to a slightly stronger under fluctuation around 800 GeV in the collinear mass and a change in which bin the high mass event belongs to. The expected limit behaves nearly identically in both versions.

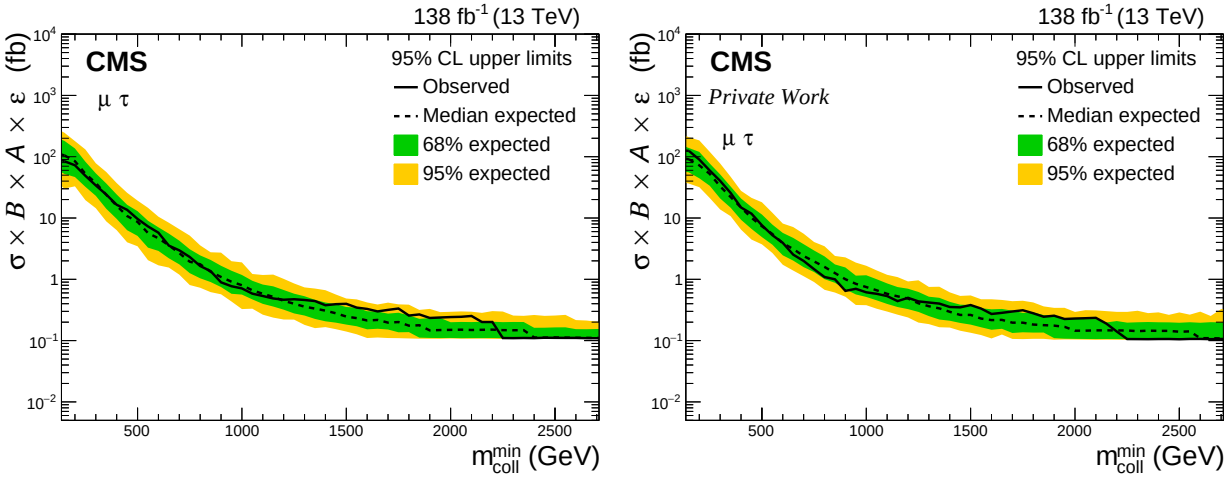

Figure 6.18.: Model-independent 95 % exclusion limit on the cross section for the $\mu\tau$ channel for the full Run 2 dataset in the MiniAOD version (left) and the NanoAOD version (right). The solid black line indicates the observed limit while the dashed black line indicates the median expected limit calculated from the background simulation with repeated toy experiments. The green and yellow band show the 68 and 95 percentile interval from the expected limit distribution. The limit is shown as a function of the collinear mass. Both versions show very similar behaviour with very small differences due to the updated corrections in NanoAOD.

7 | Summary

This thesis presented a search for lepton flavour violation considering two charged leptons with different flavours in the final state, namely the $e\mu$, $e\tau$ and $\mu\tau$ channels. The main focus in the description of the analysis was the $\mu\tau$ channel together with a comparison of two different available data formats, `MiniAOD` and `NanoAOD`. The dataset used in this thesis includes the full Run-2 data recorded by the CMS experiment at $\sqrt{s} = 13\,\text{TeV}$ during the years 2016 to 2018, summing up to an integrated luminosity of $138\,\text{fb}^{-1}$.

Monte Carlo simulations were used to describe the expected Standard Model background of prompt τ objects. For the estimation of the contribution of mis-identified tau objects, a data-driven approach has been presented and tested. The systematic uncertainties playing a role in this analysis were discussed. The leading uncertainty in the $\mu\tau$ channel comes from the mis-identified tau object prediction, together with the uncertainties on the muon object and the parton distribution function in the high energy regime.

No significant deviation from the Standard Model prediction has been found in the three channels. Their final mass distribution was then used as an input for further statistical analyses.

The presented mass limits on the beyond the Standard Model interpretations are the most constraining ones to date in all three channels. Masses of a potential sequential standard model (SSM) Z′ up to 5.0, 4.3 and 4.1 TeV are excluded at a 95 % CL for the $e\mu$, $e\tau$ and $\mu\tau$ channel, respectively, delivering a significant improvement of up to 600 GeV compared to previous searches. In the R-parity violating supersymmetry model, with $\lambda = \lambda' = 0.01$, tau sneutrino masses up to 2.2, 1.6 and 1.6 TeV are excluded at a 95 % CL for the $e\mu$, $e\tau$ and $\mu\tau$ channels, respectively. For $\lambda = \lambda' = 0.1$, masses up to 4.2, 3.7 and 3.7 TeV are also excluded at a 95 % CL for the corresponding channels. Exclusion limits on the threshold mass of the production of Quantum Black Holes were set at 5.6, 5.2 and 5.3 TeV, for the number of extra dimensions $n = 4$ at a 95 % CL, for the $e\mu$, $e\tau$ and $\mu\tau$ channels.

For the first time, a limit on the pre-exponential factor of sphaleron production was set at 0.63 for a sphaleron with $E_{sph} = 9\,\text{TeV}$ for these specific leptonic channels. Additionally, for the first time, a model-independent limit for all three channels was provided. The presented results can now be used to calculate additional exclusion limits based on different interpretations with similar kinematics.

Run 3 of the LHC with a higher center-of-mass energy of 13.6 TeV offers a new opportunity to make a discovery in the high energy regime and therefore see first signs of either new physics or unobserved effects predicted by the SM. The limits presented in this thesis, in the case that no discovery will be made, are expected to stay the most stringent limits for the SSM, RPV and QBH interpretation until the collected statistics at the LHC for Run 3 surpasses the full Run 2 statistics, considering that the rise in the center-of-mass energy from 13 TeV to 13.6 TeV is not expected to deliver a significant change in the production cross sections compared to the also higher production of background in the high energy regime. This is not the case for the

sphaleron interpretation, as the cross section rises by a factor of ≈ 2.7 for the higher center-of-mass energy. Thus, it is expected that a significantly more stringent limit can be set for the sphaleron interpretation even before the end of Run 3.

Even though no deviations from the Standard Model prediction have been found in this analysis, this search should be continued for Run 3 and later runs. These might offer promising results as new physics potentially hides at higher energies or at very low production cross sections, which might show up at very high luminosities at the planned high luminosity LHC (HL-LHC) [203].

A | Appendix

A.1 Background Table

Table A.1.: List of backgrounds and their cross section (in pb) for the year 2016.

Sample name	Cross section (pb)
/DYJetsToLL_M-50_TuneCUETP8M1_13TeV-amcatnloFXFX-pythia8	$6.1 \cdot 10^{3}$
/TTTo2L2Nu_TuneCUETP8M2_ttHtranche3_13TeV-powheg-pythia8	76.7
/TTToSemilepton_TuneCUETP8M2_ttHtranche3_13TeV-powheg-pythia8	$3.2 \cdot 10^{2}$
/TTToHadronic_TuneCUETP8M2_ttHtranche3_13TeV-powheg-pythia8	$3.8 \cdot 10^{3}$
/WWTo2L2Nu_Mll_200To600_13TeV-powheg	10.5
/WZTo2L2Q_13TeV_amcatnloFXFX_madspin_pythia8	5.60
/WZTo3LNu_TuneCUETP8M1_13TeV-amcatnloFXFX-pythia8	4.43
/ZZTo2L2Nu_13TeV_powheg_pythia8	0.56
/ZZTo2L2Q_13TeV_amcatnloFXFX_madspin_pythia8	3.22
/ZZTo4L_13TeV-amcatnloFXFX-pythia8	1.26
/ST_tW_top_5f_NoFullyHadronicDecays_13TeV-powheg_TuneCUETP8M1	19.5
/ST_tW_antitop_5f_NoFullyHadronicDecays_13TeV-powheg_TuneCUETP8M1	19.5
/DYJetsToLL_M-100to200_TuneCUETP8M1_13TeV-amcatnloFXFX-pythia8	$2.3 \cdot 10^{2}$
/DYJetsToLL_M-200to400_TuneCUETP8M1_13TeV-amcatnloFXFX-pythia8	7.77
/DYJetsToLL_M-400to500_TuneCUETP8M1_13TeV-amcatnloFXFX-pythia8	0.41
/DYJetsToLL_M-500to700_TuneCUETP8M1_13TeV-amcatnloFXFX-pythia8	0.23
/DYJetsToLL_M-700to800_TuneCUETP8M1_13TeV-amcatnloFXFX-pythia8	$3.6 \cdot 10^{-2}$
/DYJetsToLL_M-800to1000_TuneCUETP8M1_13TeV-amcatnloFXFX-pythia8	$3.0 \cdot 10^{-2}$
/DYJetsToLL_M-1000to1500_TuneCUETP8M1_13TeV-amcatnloFXFX-pythia8	$1.6 \cdot 10^{-2}$
/DYJetsToLL_M-1500to2000_TuneCUETP8M1_13TeV-amcatnloFXFX-pythia8	$2.2 \cdot 10^{-3}$
/DYJetsToLL_M-2000to3000_TuneCUETP8M1_13TeV-amcatnloFXFX-pythia8	$5.2 \cdot 10^{-4}$
/WJetsToLNu_TuneCUETP8M1_13TeV-madgraphMLM-pythia8	$5.0 \cdot 10^{4}$
/WJetsToLNu_HT-70To100_TuneCUETP8M1_13TeV-madgraphMLM-pythia8	$1.4 \cdot 10^{3}$
/WJetsToLNu_HT-100To200_TuneCUETP8M1_13TeV-madgraphMLM-pythia8	$1.3 \cdot 10^{3}$
/WJetsToLNu_HT-200To400_TuneCUETP8M1_13TeV-madgraphMLM-pythia8	$3.6 \cdot 10^{2}$
/WJetsToLNu_HT-400To600_TuneCUETP8M1_13TeV-madgraphMLM-pythia8	48.8
/WJetsToLNu_HT-600To800_TuneCUETP8M1_13TeV-madgraphMLM-pythia8	12.1
/WJetsToLNu_HT-800To1200_TuneCUETP8M1_13TeV-madgraphMLM-pythia8	5.50
/WJetsToLNu_HT-1200To2500_TuneCUETP8M1_13TeV-madgraphMLM-pythia8	1.33
/WJetsToLNu_HT-2500ToInf_TuneCUETP8M1_13TeV-madgraphMLM-pythia8	$3.2 \cdot 10^{-2}$
/WWTo2L2Nu_NNPDF31_13TeV-powheg	12.2
/WWTo2L2Nu_Mll_200To600_13TeV-powheg	1.39
/WWTo2L2Nu_Mll_600To1200_13TeV-powheg	$5.7 \cdot 10^{-2}$
/WWTo2L2Nu_Mll_1200To2500_13TeV-powheg	$3.6 \cdot 10^{-3}$
/WWTo2L2Nu_Mll_2500ToInf_13TeV-powheg	$5.4 \cdot 10^{-5}$
/TTToLL_MLL_500To800_41to65_13TeV-powheg-pythia8	0.33
/TTToLL_MLL_800To1200_41to65_13TeV-powheg-pythia8	$3.3 \cdot 10^{-2}$
/TTToLL_MLL_1200To1800_41to65_13TeV-powheg-pythia8	$3.1 \cdot 10^{-3}$
/TTToLL_MLL_1800ToInf_41to65_13TeV-powheg-pythia8	$1.7 \cdot 10^{-4}$

Table A.2.: List of backgrounds and their cross section (in pb) for the years 2017 and 2018

Sample name	Cross section (pb)
/DYJetsToLL_M-50_TuneCP5_13TeV-amcatnloFXFX-pythia8	$6.1 \cdot 10^{3}$
/TTTo2L2Nu_TuneCP5_13TeV-powheg-pythia8	87.3
/TTToSemiLeptonic_TuneCP5_PSweights_13TeV-powheg-pythia8	$3.6 \cdot 10^{2}$
/TTToHadronic_TuneCP5_PSweights_13TeV-powheg-pythia8	$3.8 \cdot 10^{2}$
/WWTo2L2Nu_NNPDF31_TuneCP5_13TeV-powheg-pythia8	12.2
/WZTo2L2Q_13TeV_amcatnloFXFX_madspin_pythia8	5.60
/WZTo3LNu_TuneCP5_13TeV-amcatnloFXFX-pythia8	5.05
/ZZTo2L2Nu_13TeV_powheg_pythia8	0.56
/ZZTo2L2Q_13TeV_amcatnloFXFX_madspin_pythia8	3.22
/ZZTo4L_13TeV_powheg_pythia8	1.21
/ST_tW_top_5f_NoFullyHadronicDecays_13TeV-powheg_TuneCP5	19.5
/ST_tW_antitop_5f_NoFullyHadronicDecays_13TeV-powheg_TuneCP5	19.5
/DYJetsToLL_M-100to200_TuneCP5_13TeV-amcatnloFXFX-pythia8	$2.3 \cdot 10^{2}$
/DYJetsToLL_M-200to400_TuneCP5_13TeV-amcatnloFXFX-pythia8	7.77
/DYJetsToLL_M-400to500_TuneCP5_13TeV-amcatnloFXFX-pythia8	0.43
/DYJetsToLL_M-500to700_TuneCP5_13TeV-amcatnloFXFX-pythia8	0.24
/DYJetsToLL_M-700to800_TuneCP5_13TeV-amcatnloFXFX-pythia8	$3.8 \cdot 10^{-2}$
/DYJetsToLL_M-800to1000_TuneCP5_13TeV-amcatnloFXFX-pythia8	$3.2 \cdot 10^{-2}$
/DYJetsToLL_M-1000to1500_TuneCP5_13TeV-amcatnloFXFX-pythia8	$2.0 \cdot 10^{-2}$
/DYJetsToLL_M-1500to2000_TuneCP5_13TeV-amcatnloFXFX-pythia8	$2.3 \cdot 10^{-3}$
/DYJetsToLL_M-2000to3000_TuneCP5_13TeV-amcatnloFXFX-pythia8	$5.4 \cdot 10^{-4}$
/WJetsToLNu_TuneCP5_13TeV-madgraphMLM-pythia8	$6.2 \cdot 10^{4}$
/WJetsToLNu_HT-70To100_TuneCP5_13TeV-madgraphMLM-pythia8	$1.3 \cdot 10^{3}$
/WJetsToLNu_HT-100To200_TuneCP5_13TeV-madgraphMLM-pythia8	$1.4 \cdot 10^{3}$
/WJetsToLNu_HT-200To400_TuneCP5_13TeV-madgraphMLM-pythia8	$4.1 \cdot 10^{2}$
/WJetsToLNu_HT-400To600_TuneCP5_13TeV-madgraphMLM-pythia8	57.4
/WJetsToLNu_HT-600To800_TuneCP5_13TeV-madgraphMLM-pythia8	12.9
/WJetsToLNu_HT-800To1200_TuneCP5_13TeV-madgraphMLM-pythia8	5.37
/WJetsToLNu_HT-1200To2500_TuneCP5_13TeV-madgraphMLM-pythia8	1.07
/WJetsToLNu_HT-2500ToInf_TuneCP5_13TeV-madgraphMLM-pythia8	$8.0 \cdot 10^{-3}$
/WWTo2L2Nu_NNPDF31_13TeV-powheg	12.2
/WWTo2L2Nu_Mll_200To600_NNPDF31_13TeV-powheg	1.39
/WWTo2L2Nu_Mll_600To1200_NNPDF31_13TeV-powheg	$5.7 \cdot 10^{-2}$
/WWTo2L2Nu_Mll_1200To2500_NNPDF31_13TeV-powheg	$3.6 \cdot 10^{-3}$
/WWTo2L2Nu_Mll_2500ToInf_NNPDF31_13TeV-powheg	$5.4 \cdot 10^{-5}$
/TTToLL_MLL_500To800_41to65_NNPDF31_13TeV-powheg-pythia8	0.33
/TTToLL_MLL_800To1200_41to65_NNPDF31_13TeV-powheg-pythia8	$3.3 \cdot 10^{-2}$
/TTToLL_MLL_1200To1800_41to65_NNPDF31_13TeV-powheg-pythia8	$3.1 \cdot 10^{-3}$
/TTToLL_MLL_1800ToInf_41to65_NNPDF31_13TeV-powheg-pythia8	$1.7 \cdot 10^{-4}$

A.2 $e\tau$ Trigger Scale Factors

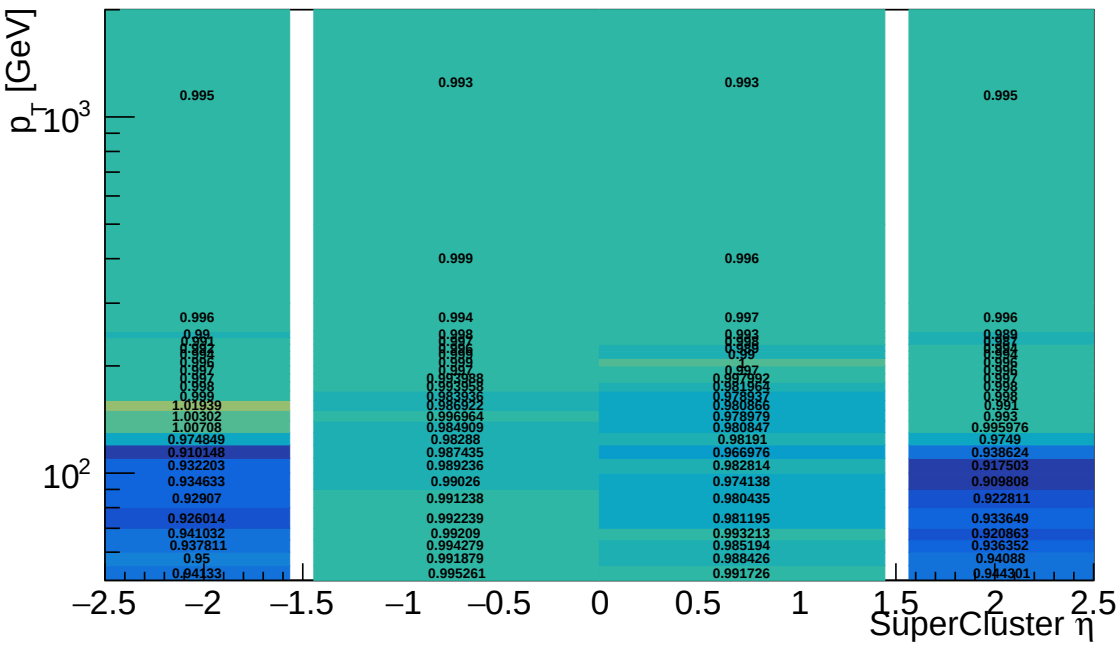

Figure A.1.: Trigger scale factors for the $e\tau$ channel as a function of the supercluster η and the p_T of the electron for the year 2016 (taken from [134].

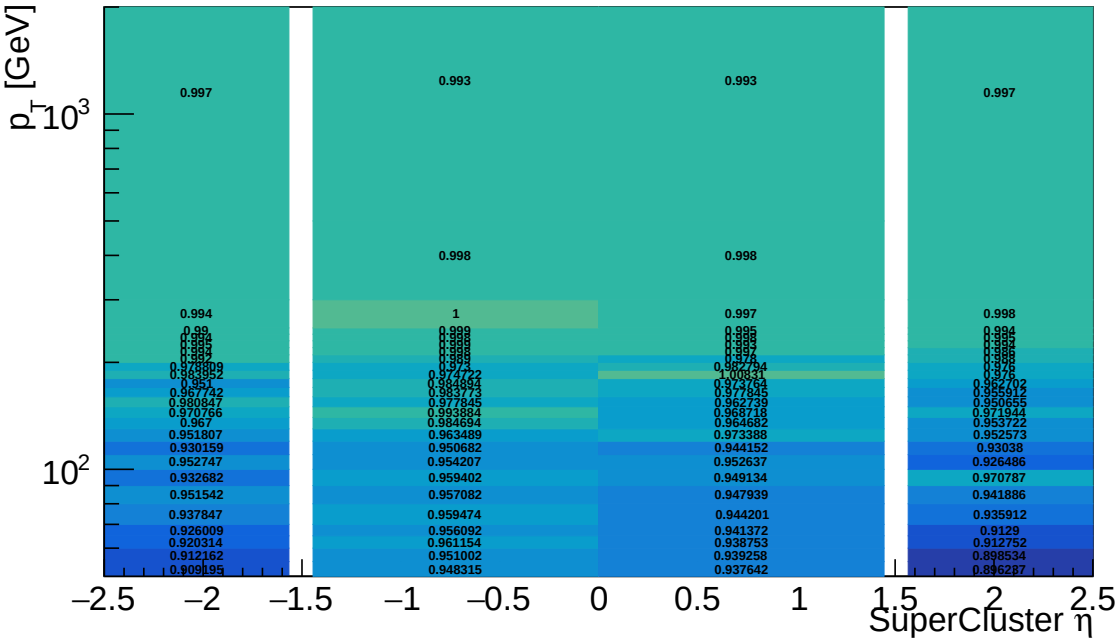

Figure A.2.: Trigger scale factors for the $e\tau$ channel as a function of the supercluster η and the p_T of the electron for the year 2017 (taken from [134].

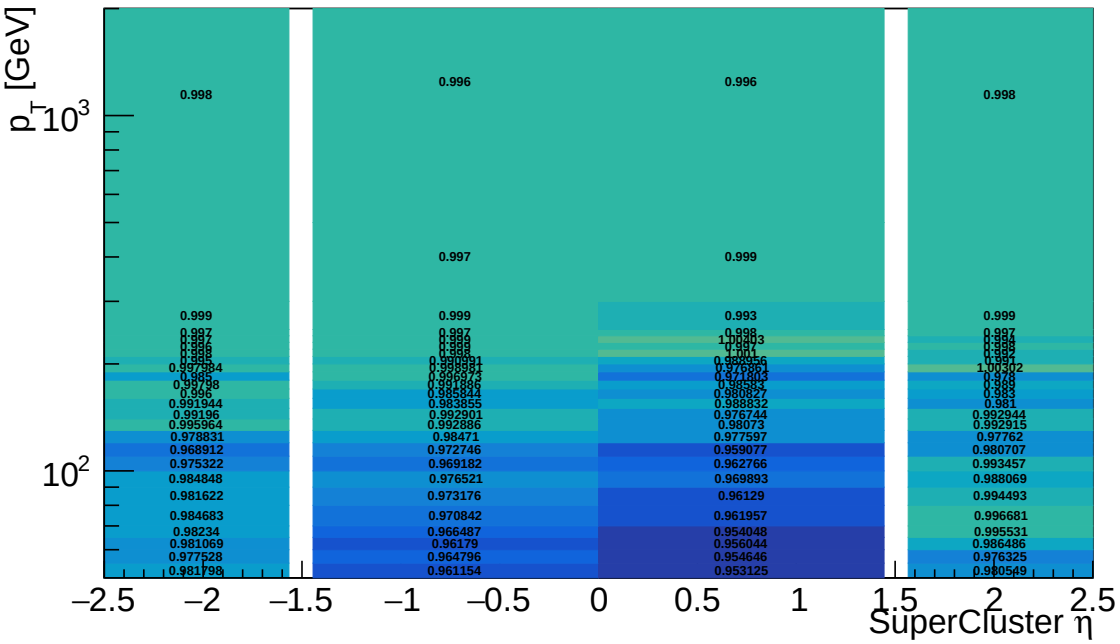

Figure A.3.: Trigger scale factors for the $e\tau$ channel as a function of the supercluster η and the p_T of the electron for the year 2018 (taken from [134].

A.3 Fake Rate for 2016 and 2017

Table A.3.: Calculated fake rates FR obtained for the year 2016 for the different tau p_T and tau p_T over jet p_T bins in the Barrel and Endcap region. The error shown is of statistical nature.

2016

p_T^τ [GeV]	p_T^τ / p_T^{jet}	fake rate (barrel)	fake rate (endcap)
50 - 80	$0 - 0.5$	0.031 ± 0.001	0.028 ± 0.002
	$0.5 - 0.6$	0.043 ± 0.001	0.036 ± 0.002
	$0.6 - 0.65$	0.043 ± 0.002	0.036 ± 0.003
	$0.65 - 0.7$	0.047 ± 0.002	0.043 ± 0.003
	$0.7 - 0.75$	0.046 ± 0.002	0.050 ± 0.003
	$0.75 - 1.0$	0.060 ± 0.002	0.053 ± 0.003
	$1.0 - 3.0$	0.07 ± 0.02	0.05 ± 0.01
$80 - 150$	$0 - 0.5$	0.024 ± 0.005	0.011 ± 0.008
	$0.5 - 0.6$	0.031 ± 0.003	0.031 ± 0.005
	$0.6 - 0.65$	0.027 ± 0.003	0.031 ± 0.005
	$0.65 - 0.7$	0.037 ± 0.003	0.030 ± 0.004
	$0.7 - 0.75$	0.040 ± 0.003	0.041 ± 0.004
	$0.75 - 1.0$	0.062 ± 0.002	0.061 ± 0.005
	$1.0 - 3.0$	0.092 ± 0.02	0.06 ± 0.02
$150 - 1000$	$0. - 0.7$	0.033 ± 0.006	0.026 ± 0.009
	$0.7 - 1.$	0.059 ± 0.006	0.070 ± 0.011
	$1. - 3.$	0.0004 ± 0.04	0.04 ± 0.03

Table A.4.: Calculated fake rates FR obtained for the year 2017 for the different tau p_T and tau p_T over jet p_T bins in the Barrel and Endcap region. The error shown is of statistical nature.

2017

p_T^τ [GeV]	p_T^τ / p_T^{jet}	fake rate (barrel)	fake rate (endcap)
$50-80$	$0-0.5$	0.031 ± 0.001	0.028 ± 0.002
	$0.5-0.6$	0.043 ± 0.001	0.036 ± 0.002
	$0.6-0.65$	0.043 ± 0.002	0.036 ± 0.003
	$0.65-0.7$	0.047 ± 0.002	0.043 ± 0.003
	$0.7-0.75$	0.046 ± 0.002	0.050 ± 0.003
	$0.75-1.0$	0.060 ± 0.002	0.053 ± 0.003
	$1.0-3.0$	0.07 ± 0.02	0.05 ± 0.01
$80-150$	$0-0.5$	0.024 ± 0.005	0.011 ± 0.008
	$0.5-0.6$	0.031 ± 0.003	0.031 ± 0.005
	$0.6-0.65$	0.027 ± 0.003	0.031 ± 0.005
	$0.65-0.7$	0.037 ± 0.003	0.030 ± 0.004
	$0.7-0.75$	0.040 ± 0.003	0.041 ± 0.004
	$0.75-1.0$	0.062 ± 0.002	0.061 ± 0.005
	$1.0-3.0$	0.092 ± 0.02	0.06 ± 0.02
$150-1000$	$0.-0.7$	0.033 ± 0.006	0.026 ± 0.009
	$0.7-1.$	0.059 ± 0.006	0.070 ± 0.011
	$1.-3.$	0.0004 ± 0.04	0.04 ± 0.03

A.4 Single Year Distributions

A.4.1 2016

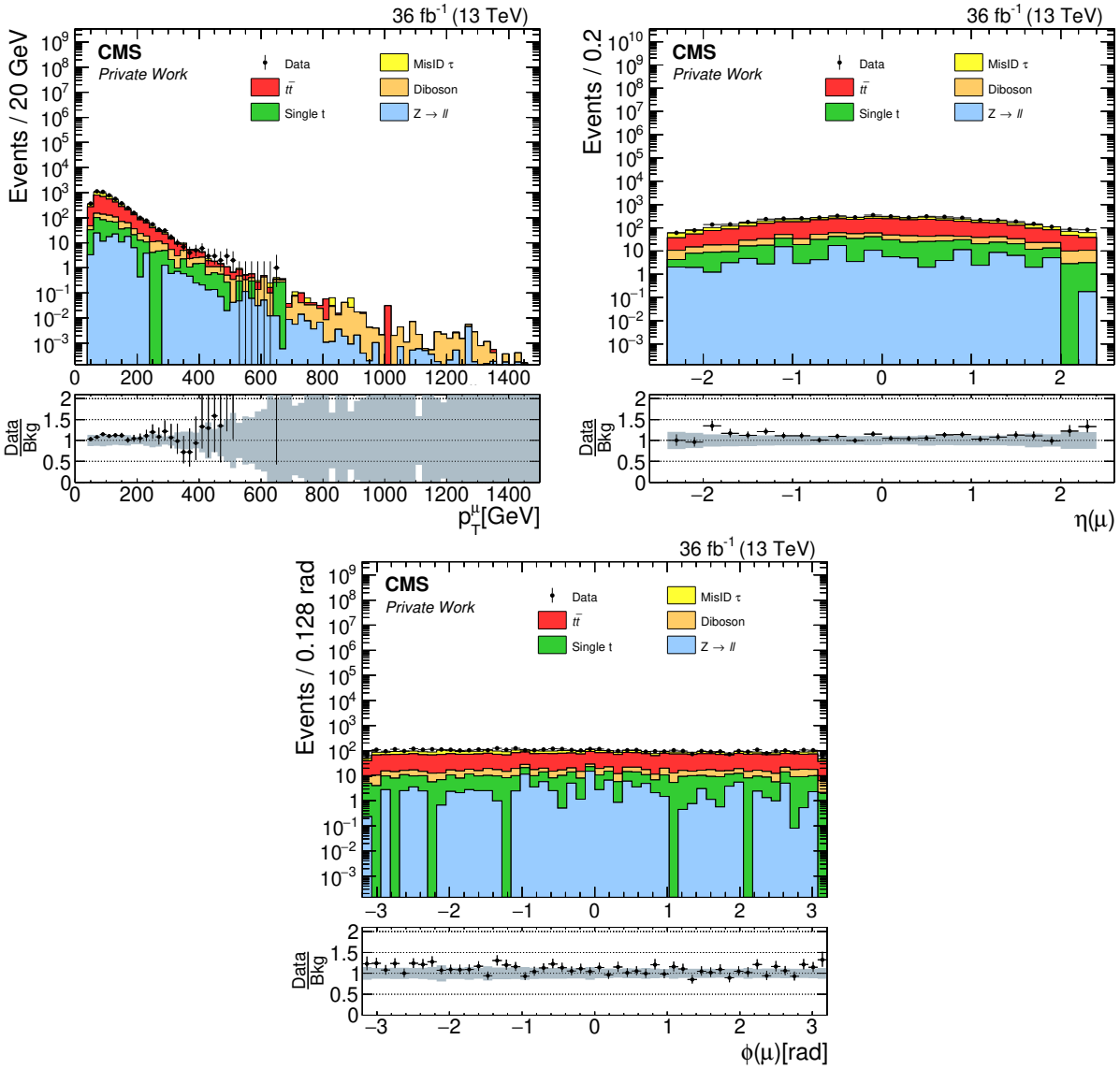

Figure A.4.: Data and the Standard Model prediction using the jet faking taus contribution derived from data for the muon p_T (left), muon η (right) and muon ϕ (bottom) for 2016. In the bottom of each plot, a ratio between the measured data and the Standard Model prediction is shown together with the combined relative systematic uncertainties as a grey band. The distributions do not show any unexpected behaviour nor significant variations from the Standard Model prediction.

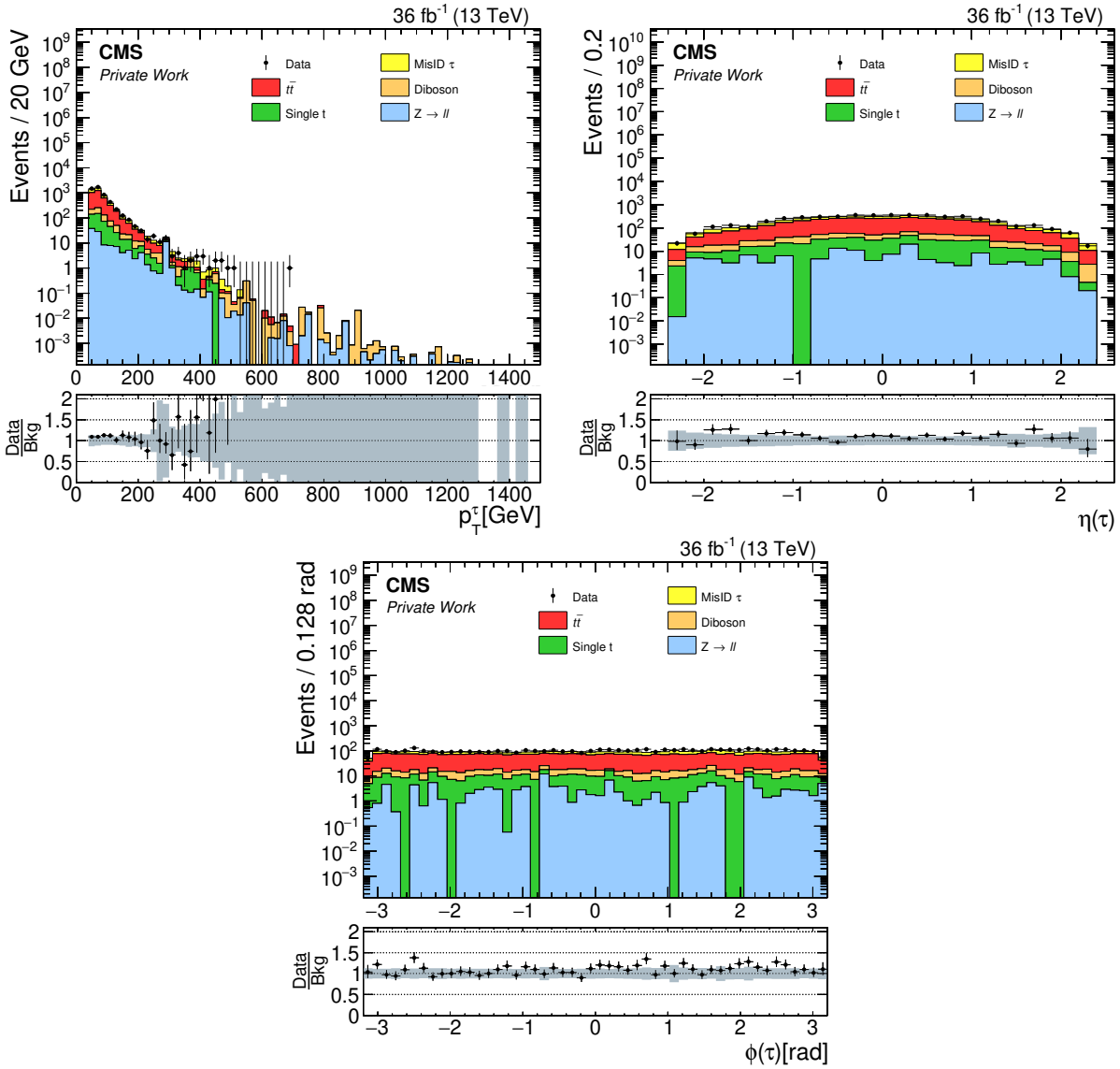

Figure A.5.: Data and the Standard Model prediction using the jet faking taus contribution derived from data for the tau p_T (left), tau η (right) and tau ϕ (bottom) for 2016. In the bottom of each plot, a ratio between the measured data and the Standard Model prediction is shown together with the combined relative systematic uncertainties as a grey band. The distributions do not show any unexpected behaviour nor significant deviations from the Standard Model prediction.

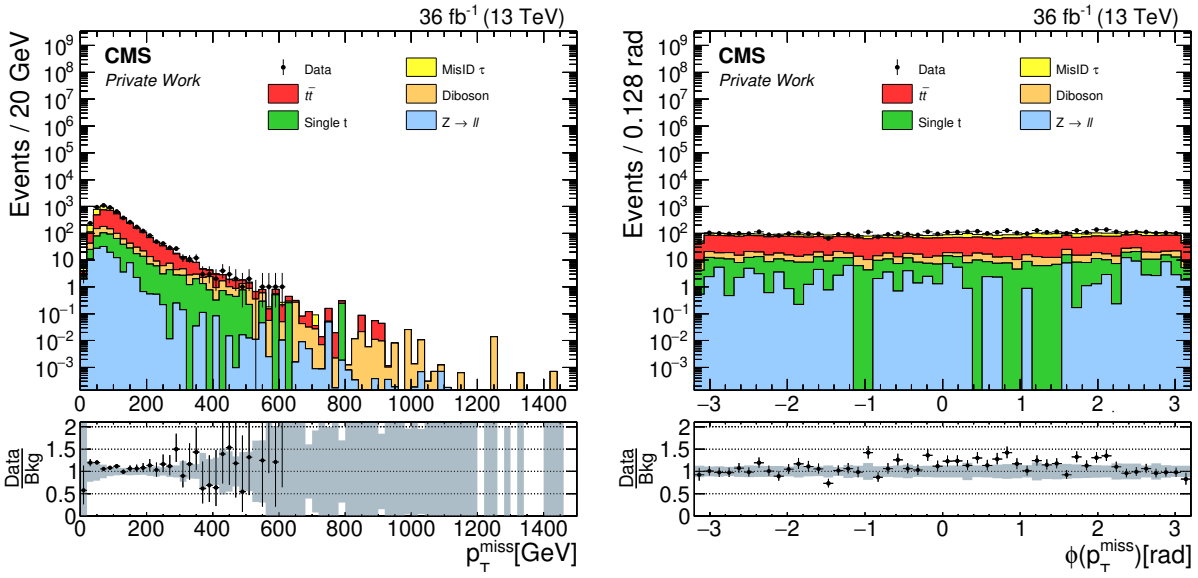

Figure A.6.: Data and the Standard Model prediction using the jet faking taus contribution derived from data for the $\vec{p}_T^{\,\text{miss}}$ (left) and the $\phi(\vec{p}_T^{\,\text{miss}})$ (right) for 2016. In the bottom of each plot a ratio between the measured data and the Standard Model prediction is shown together with the combined relative systematic uncertainties as a grey band. The distributions do not show any unexpected behaviour nor significant variations from the Standard Model prediction.

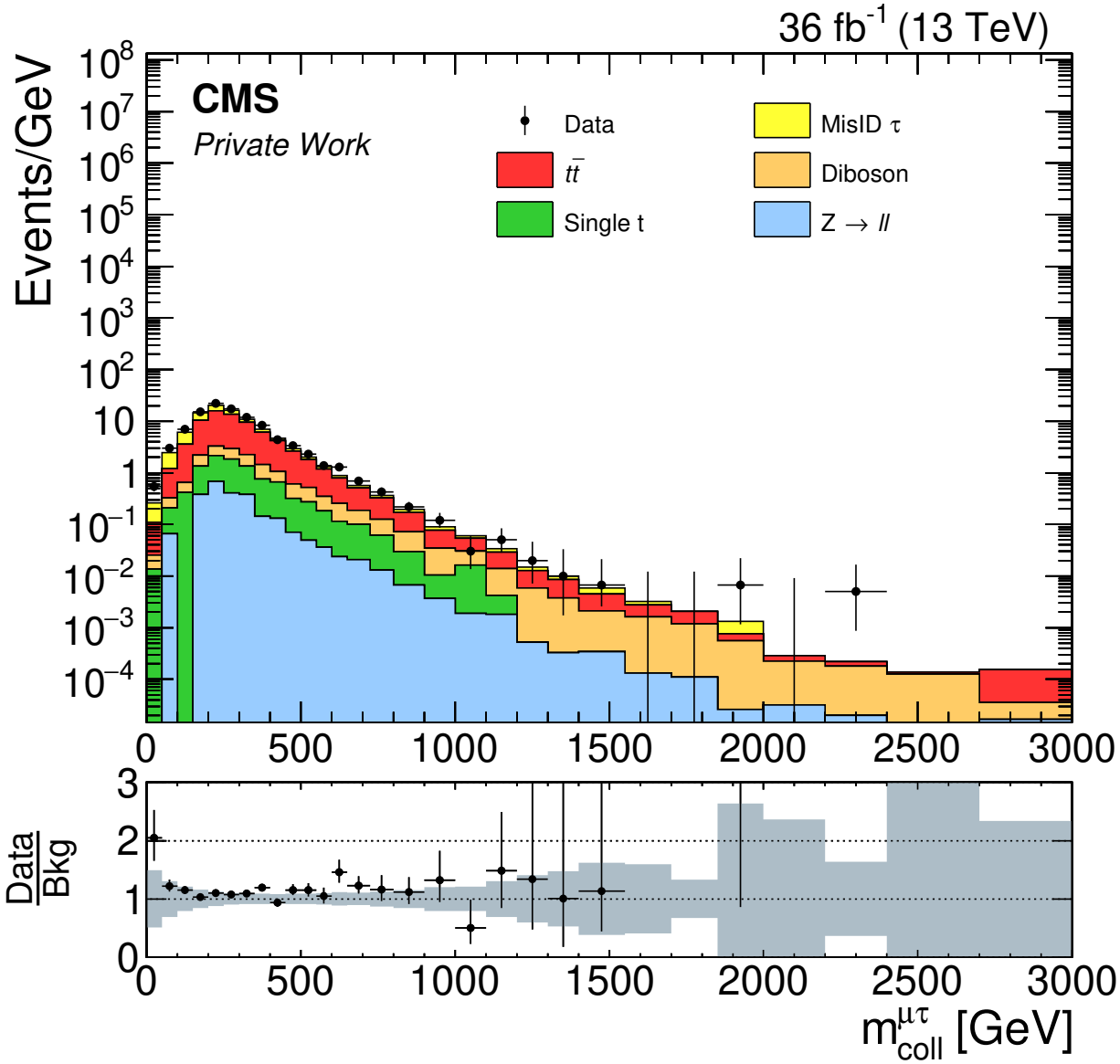

Figure A.7.: Collinear mass distribution of the muon and the tau after all selection steps for 2016. The distribution is shown with a binning following the mass resolution and underlying statistic. Each bin is normalized to its width. The different backgrounds are ordered by their contribution. The lower part of the plot shows the ratio between the measured data and the Standard Model prediction. The grey band in the ratio represents the combined relative systematic uncertainty.

A.4.2 2017

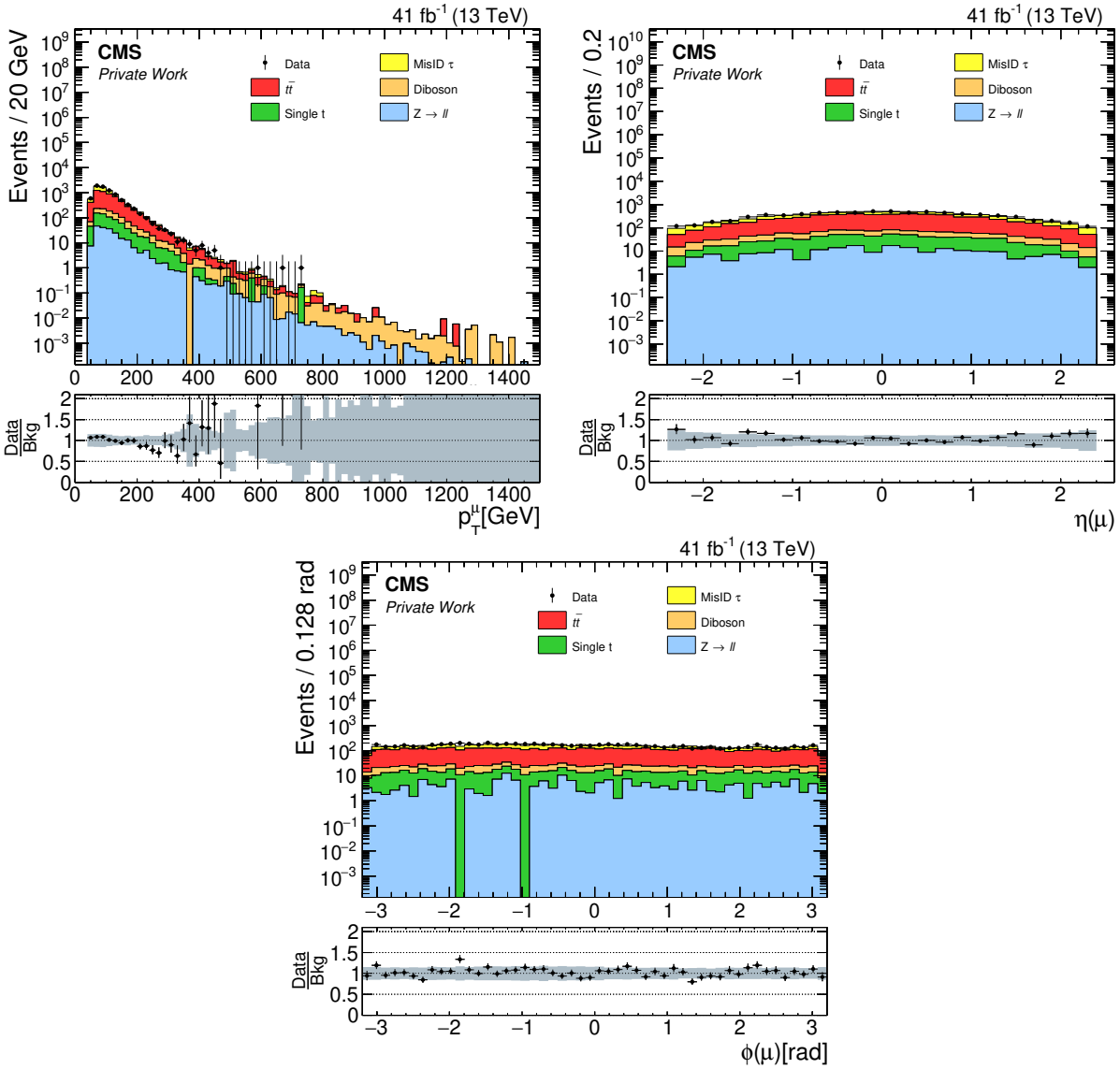

Figure A.8.: Data and the Standard Model prediction using the jet faking taus contribution derived from data for the muon p_T (left), muon η (right) and muon ϕ (bottom) for 2017. In the bottom of each plot, a ratio between the measured data and the Standard Model prediction is shown together with the combined relative systematic uncertainties as a grey band. The distributions do not show any unexpected behaviour nor significant variations from the Standard Model prediction.

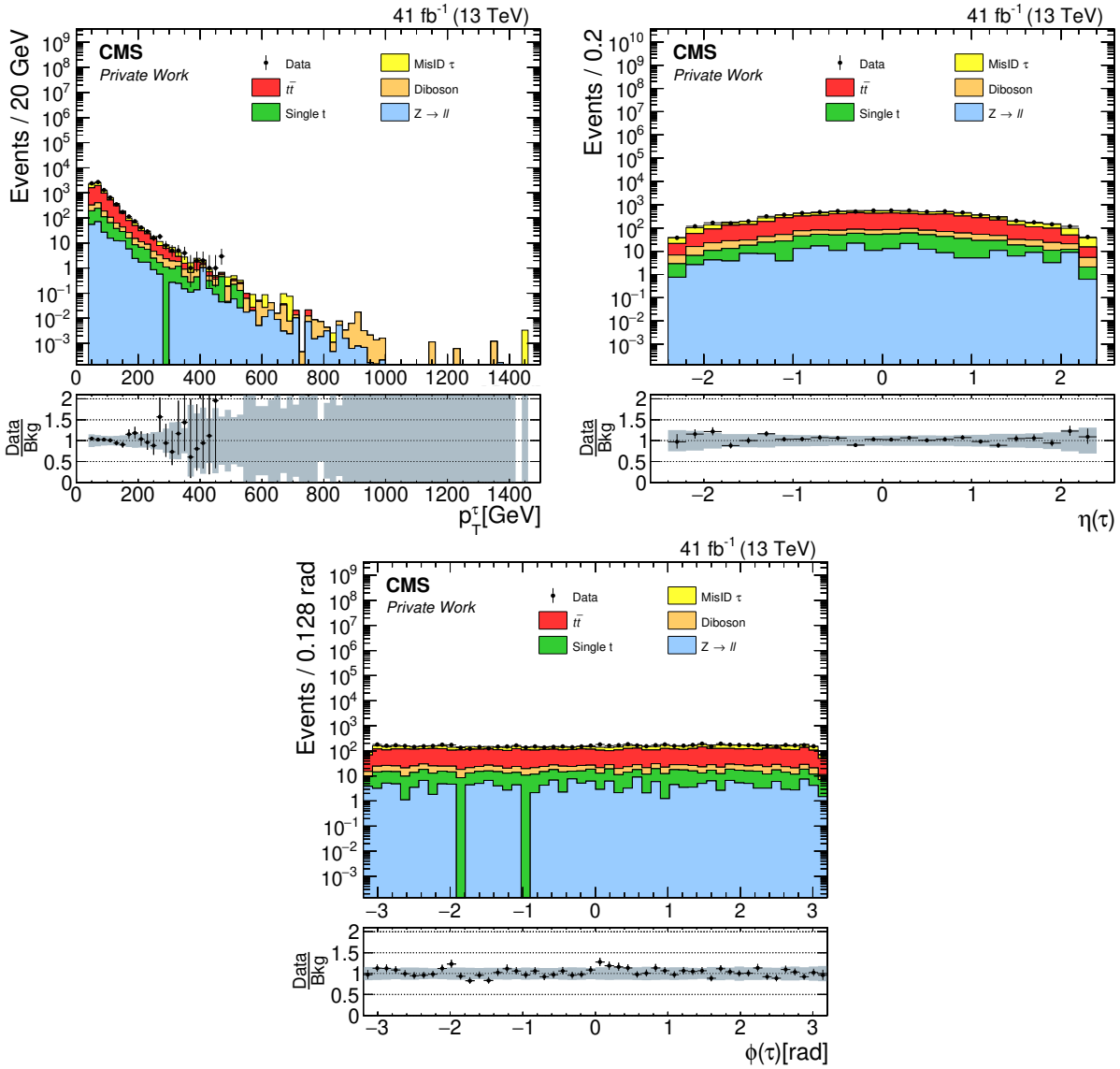

Figure A.9.: Data and the Standard Model prediction using the jet faking taus contribution derived from data for the tau p_T (left), tau η (right) and tau ϕ (bottom) for 2017. In the bottom of each plot, a ratio between the measured data and the Standard Model prediction is shown together with the combined relative systematic uncertainties as a grey band. The distributions do not show any unexpected behaviour nor significant deviations from the Standard Model prediction.

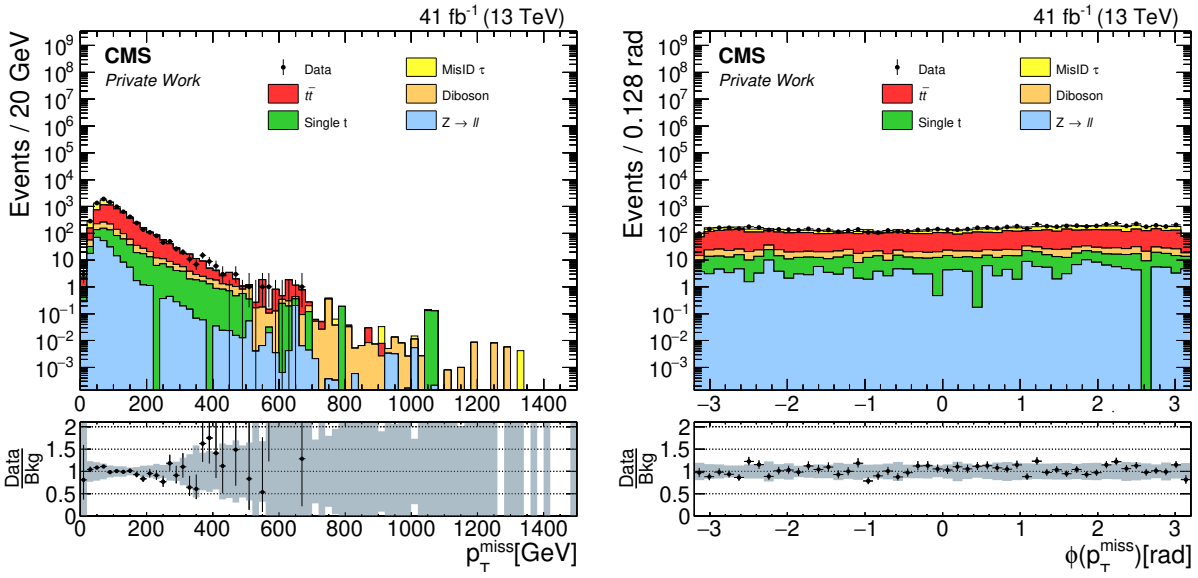

Figure A.10.: Data and the Standard Model prediction using the jet faking taus contribution derived from data for the $\vec{p}_T^{\,\text{miss}}$ (left) and the $\phi(\vec{p}_T^{\,\text{miss}})$ (right) for 2017. In the bottom of each plot a ratio between the measured data and the Standard Model prediction is shown together with the combined relative systematic uncertainties as a grey band. The distributions do not show any unexpected behaviour nor significant variations from the Standard Model prediction.

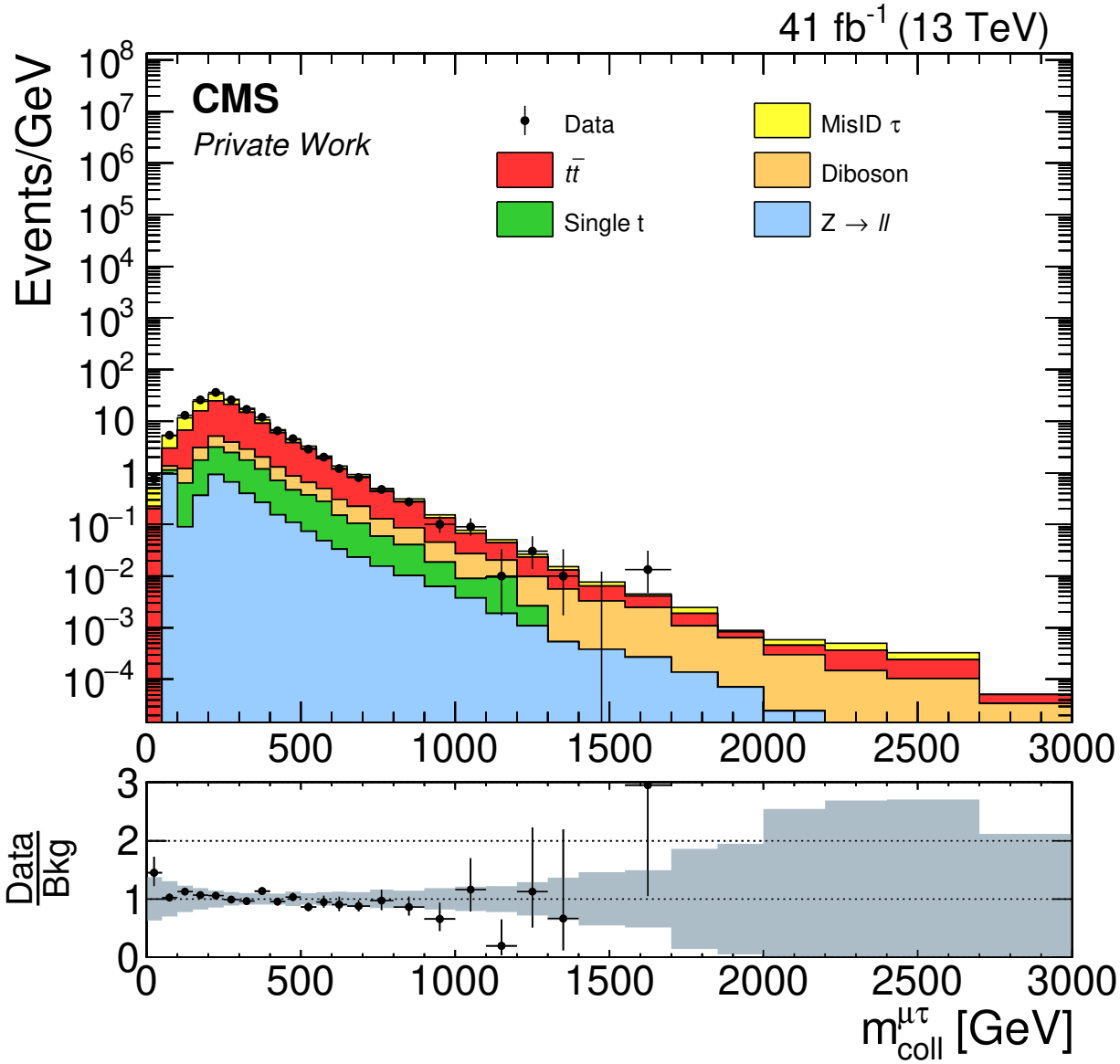

Figure A.11.: Collinear mass distribution of the muon and the tau after all selection steps for 2017. The distribution is shown with a binning following the mass resolution and underlying statistic. Each bin is normalized to its width. The different backgrounds are ordered by their contribution. The lower part of the plot shows the ratio between the measured data and the Standard Model prediction. The grey band in the ratio represents the combined relative systematic uncertainty.

A.4.3 2018

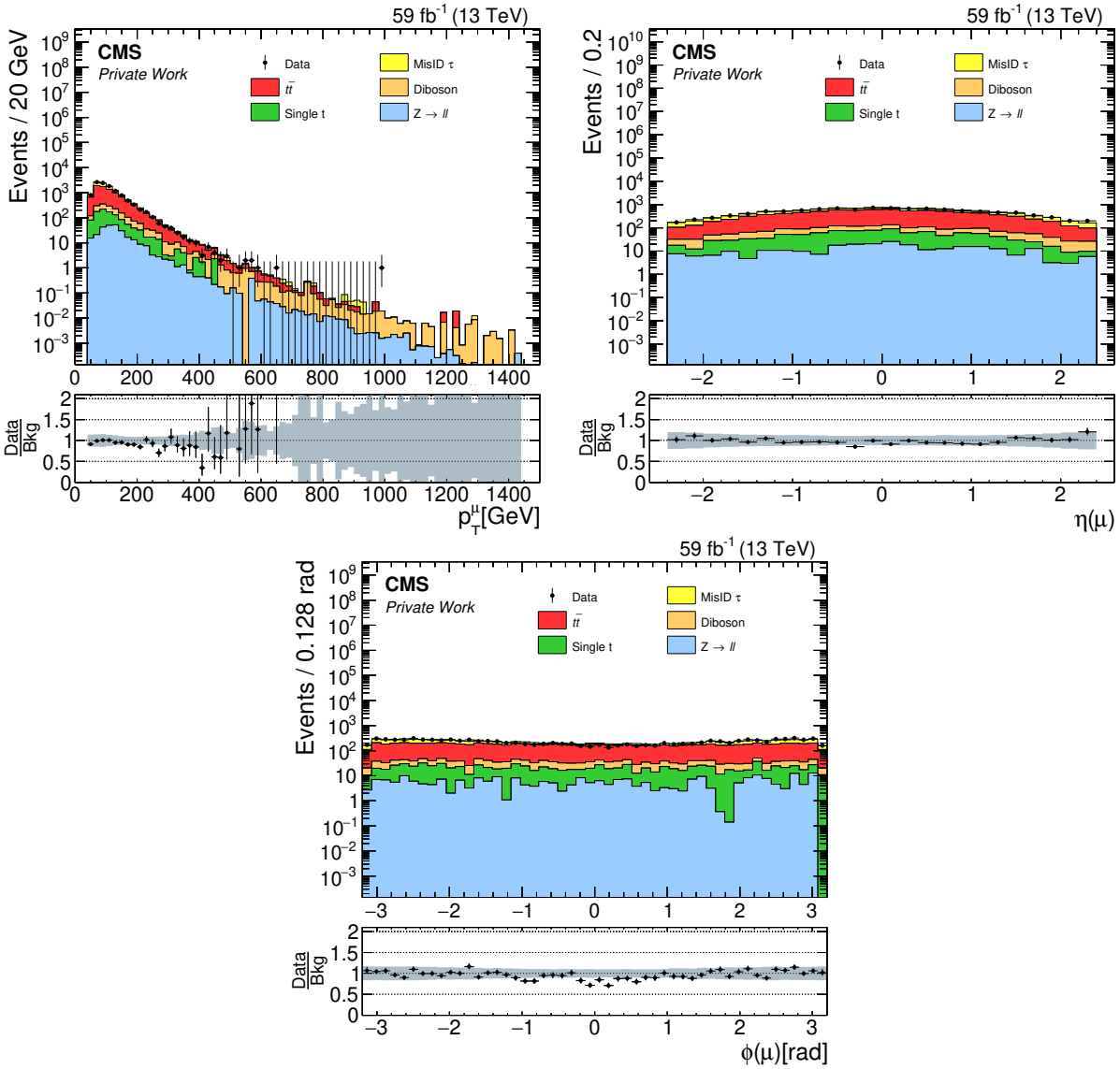

Figure A.12.: Data and the Standard Model prediction using the jet faking taus contribution derived from data for the muon p_T (left), muon η (right) and muon ϕ (bottom) for 2018. In the bottom of each plot, a ratio between the measured data and the Standard Model prediction is shown together with the combined relative systematic uncertainties as a grey band. The distributions do not show any unexpected behaviour nor significant variations from the Standard Model prediction.

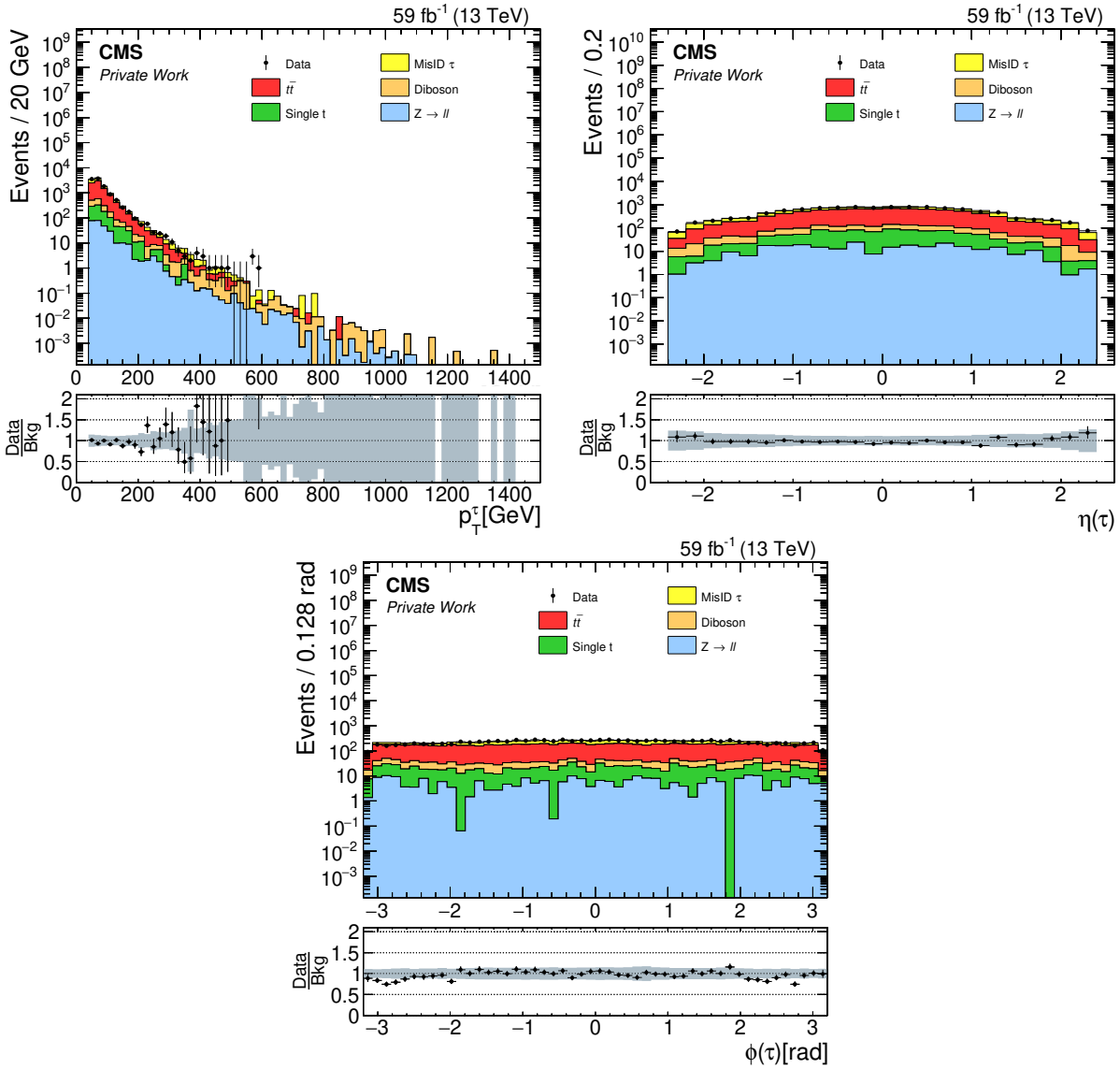

Figure A.13.: Data and the Standard Model prediction using the jet faking taus contribution derived from data for the tau p_T (left), tau η (right) and tau ϕ (bottom) for 2018. In the bottom of each plot, a ratio between the measured data and the Standard Model prediction is shown together with the combined relative systematic uncertainties as a grey band. The distributions do not show any unexpected behaviour nor significant deviations from the Standard Model prediction.

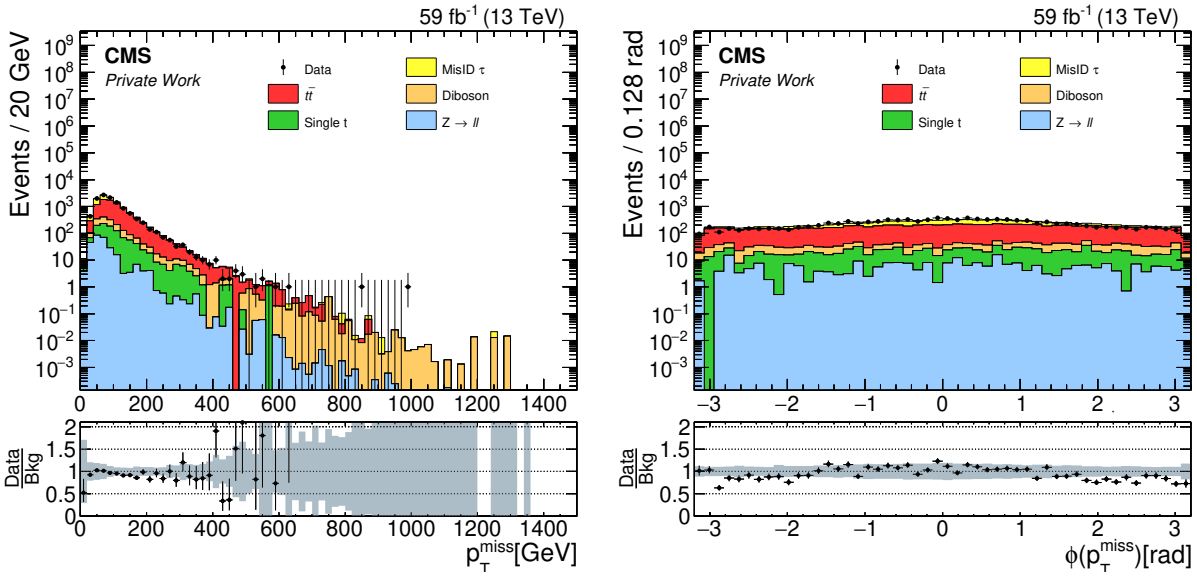

Figure A.14.: Data and the Standard Model prediction using the jet faking taus contribution derived from data for the $\vec{p}_T^{\,\text{miss}}$ (left) and the $\phi(\vec{p}_T^{\,\text{miss}})$ (right) for 2018. In the bottom of each plot a ratio between the measured data and the Standard Model prediction is shown together with the combined relative systematic uncertainties as a grey band. The distributions do not show any unexpected behaviour nor significant variations from the Standard Model prediction.

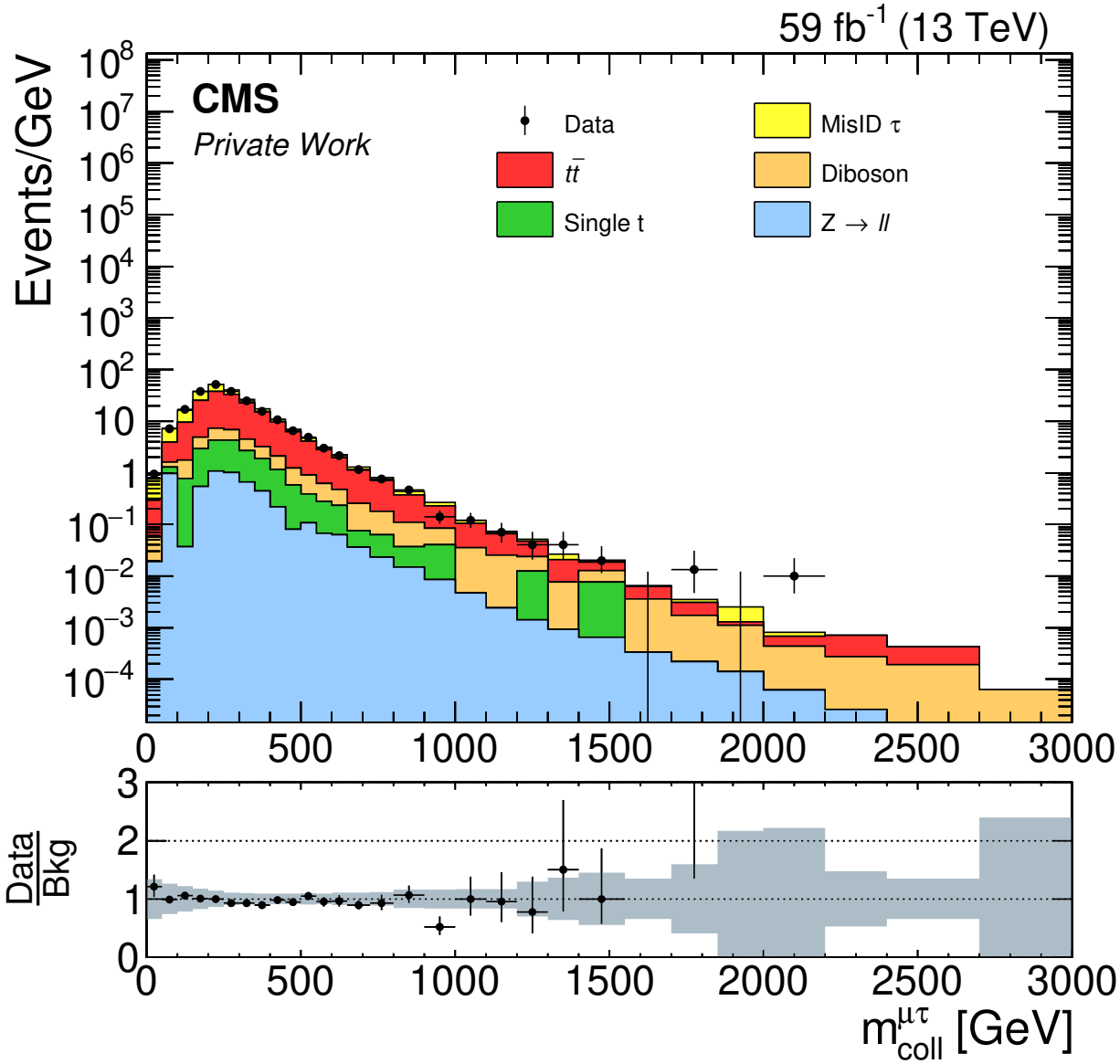

Figure A.15.: Collinear mass distribution of the muon and the tau after all selection steps for 2018. The distribution is shown with a binning following the mass resolution and underlying statistic. Each bin is normalized to its width. The different backgrounds are ordered by their contribution. The lower part of the plot shows the ratio between the measured data and the Standard Model prediction. The grey band in the ratio represents the combined relative systematic uncertainty.

Bibliography

[1] CMS Collaboration, "Search for heavy resonances and quantum black holes in eμ, eτ, and $\mu\tau$ final states in proton-proton collisions at $\sqrt{s}$ = 13 TeV", *JHEP* **05** (2023) 227, arXiv:2205.06709. doi:10.1007/JHEP05(2023)227.

[2] D. Griffiths, "Introduction to Elementary Particles". Wiley, 1st edition, 2014.

[3] Particle Data Group Collaboration, "Review of Particle Physics", *PTEP* **2022** (2022) 083C01. doi:10.1093/ptep/ptac097.

[4] P. Higgs, "Broken symmetries, massless particles and gauge fields", *Physics Letters* **12** (September, 1964) 132–133. doi:10.1016/0031-9163(64)91136-9.

[5] F. Englert and R. Brout, "Broken Symmetry and the Mass of Gauge Vector Mesons", *Physical Review Letters* **13** (August, 1964) 321–323. doi:10.1103/PhysRevLett.13.321.

[6] G. S. Guralnik, C. R. Hagen, and T. W. B. Kibble, "Global Conservation Laws and Massless Particles", *Phys. Rev. Lett.* **13** (1964) 585–587. doi:10.1103/PhysRevLett.13.585.

[7] CMS Collaboration, "Observation of a New Boson at a Mass of 125 GeV with the CMS Experiment at the LHC", *Phys. Lett. B* **716** (2012) 30–61, arXiv:1207.7235. doi:10.1016/j.physletb.2012.08.021.

[8] ATLAS Collaboration, "Observation of a new particle in the search for the Standard Model Higgs boson with the ATLAS detector at the LHC", *Phys. Lett. B* **716** (2012) 1–29, arXiv:1207.7214. doi:10.1016/j.physletb.2012.08.020.

[9] Super-Kamiokande Collaboration, "Evidence for the Appearance of Atmospheric Tau Neutrinos in Super-Kamiokande", *Phys. Rev. Lett.* **110** (2013), no. 18, 181802, arXiv:1206.0328. doi:10.1103/PhysRevLett.110.181802.

[10] Double Chooz Collaboration, "Indication of Reactor $\bar{\nu}_e$ Disappearance in the Double Chooz Experiment", *Phys. Rev. Lett.* **108** (2012) 131801, arXiv:1112.6353. doi:10.1103/PhysRevLett.108.131801.

[11] Daya Bay Collaboration, "Observation of electron-antineutrino disappearance at Daya Bay", *Phys. Rev. Lett.* **108** (2012) 171803, arXiv:1203.1669. doi:10.1103/PhysRevLett.108.171803.

[12] RENO Collaboration, "Observation of Reactor Electron Antineutrino Disappearance in the RENO Experiment", *Phys. Rev. Lett.* **108** (2012) 191802, arXiv:1204.0626. doi:10.1103/PhysRevLett.108.191802.

[13] R. K. Ellis, W. J. Stirling, and B. R. Webber, "QCD and collider physics", volume 8. Cambridge University Press, 2, 2011.

[14] J. C. Collins, D. E. Soper, and G. Sterman, "FACTORIZATION OF HARD PROCESSES IN QCD", in *Advanced Series on Directions in High Energy Physics*, volume 5, pp. 1–91. WORLD SCIENTIFIC, July, 1989.

[15] H1, ZEUS Collaboration, "Combination of measurements of inclusive deep inelastic $e^{\pm}p$ scattering cross sections and QCD analysis of HERA data", *Eur. Phys. J. C* **75** (2015), no. 12, 580, arXiv:1506.06042. doi:10.1140/epjc/s10052-015-3710-4.

[16] J. Rojo et al., "The PDF4LHC report on PDFs and LHC data: Results from Run I and preparation for Run II", *J. Phys. G* **42** (2015) 103103, arXiv:1507.00556. doi:10.1088/0954-3899/42/10/103103.

[17] S. Forte, "Parton distributions at the dawn of the LHC", *Acta Phys. Polon. B* **41** (2010) 2859–2920, arXiv:1011.5247.

[18] S. Forte and G. Watt, "Progress in the Determination of the Partonic Structure of the Proton", *Ann. Rev. Nucl. Part. Sci.* **63** (2013) 291–328, arXiv:1301.6754. doi:10.1146/annurev-nucl-102212-170607.

[19] R. D. Ball, V. Bertone, S. Carrazza et al., "Parton distributions from high-precision collider data", *The European Physical Journal C* **77** (Oct, 2017). doi:10.1140/epjc/s10052-017-5199-5.

[20] CMS Collaboration, "Search for resonant and nonresonant new phenomena in high-mass dilepton final states at $\sqrt{s} = 13$ TeV", *JHEP* **07** (2021) 208, arXiv:2103.02708. doi:10.1007/JHEP07(2021)208.

[21] A. Belavin, A. Polyakov, A. Schwartz et al., "Pseudoparticle solutions of the Yang-Mills equations", *Physics Letters B* **59** (1975), no. 1, 85–87. doi:https://doi.org/10.1016/0370-2693(75)90163-X.

[22] S. H. H. Tye and S. S. C. Wong, "Bloch Wave Function for the Periodic Sphaleron Potential and Unsuppressed Baryon and Lepton Number Violating Processes", *Phys. Rev. D* **92** (2015), no. 4, 045005, arXiv:1505.03690. doi:10.1103/PhysRevD.92.045005.

[23] R. F. Dashen, B. Hasslacher, and A. Neveu, "Nonperturbative methods and extended-hadron models in field theory. III. Four-dimensional non-Abelian models", *Phys. Rev. D* **10** (Dec, 1974) 4138–4142. doi:10.1103/PhysRevD.10.4138.

[24] N. S. Manton, "Topology in the Weinberg-Salam theory", *Phys. Rev. D* **28** (Oct, 1983) 2019–2026. doi:10.1103/PhysRevD.28.2019.

[25] F. R. Klinkhamer and N. S. Manton, "A saddle-point solution in the Weinberg-Salam theory", *Phys. Rev. D* **30** (Nov, 1984) 2212–2220. doi:10.1103/PhysRevD.30.2212.

[26] J. Ellis and K. Sakurai, "Search for Sphalerons in Proton-Proton Collisions", *JHEP* **04** (2016) 086, arXiv:1601.03654. doi:10.1007/JHEP04(2016)086.

[27] BaBar Collaboration, "Evidence for an excess of $\bar{B} \to D^{(*)}\tau^{-}\bar{\nu}_{\tau}$ decays", *Phys. Rev. Lett.* **109** (2012) 101802, arXiv:1205.5442. doi:10.1103/PhysRevLett.109.101802.

[28] BaBar Collaboration, "Measurement of an Excess of $\bar{B} \to D^{(*)}\tau^{-}\bar{\nu}_{\tau}$ Decays and Implications for Charged Higgs Bosons", *Phys. Rev. D* **88** (2013), no. 7, 072012, arXiv:1303.0571. doi:10.1103/PhysRevD.88.072012.

[29] Belle Collaboration, "Measurement of the branching ratio of $\bar{B} \to D^{(*)}\tau^-\bar{\nu}_\tau$ relative to $\bar{B} \to D^{(*)}\ell^-\bar{\nu}_\ell$ decays with hadronic tagging at Belle", *Phys. Rev. D* **92** (2015), no. 7, 072014, arXiv:1507.03233. doi:10.1103/PhysRevD.92.072014.

[30] Belle Collaboration, "Measurement of $\mathcal{R}(D)$ and $\mathcal{R}(D^*)$ with a semileptonic tagging method", *Phys. Rev. Lett.* **124** (2020), no. 16, 161803, arXiv:1910.05864. doi:10.1103/PhysRevLett.124.161803.

[31] Belle Collaboration, "Measurement of the τ lepton polarization and $R(D^*)$ in the decay $\bar{B} \to D^*\tau^-\bar{\nu}_\tau$", *Phys. Rev. Lett.* **118** (2017), no. 21, 211801, arXiv:1612.00529. doi:10.1103/PhysRevLett.118.211801.

[32] LHCb Collaboration, "Measurement of the ratio of branching fractions $\mathcal{B}(\bar{B}^0 \to D^{*+}\tau^-\bar{\nu}_\tau)/\mathcal{B}(\bar{B}^0 \to D^{*+}\mu^-\bar{\nu}_\mu)$", *Phys. Rev. Lett.* **115** (2015), no. 11, 111803, arXiv:1506.08614. [Erratum: Phys.Rev.Lett. 115, 159901 (2015)]. doi:10.1103/PhysRevLett.115.111803.

[33] LHCb Collaboration, "Measurement of the ratio of the $B^0 \to D^{*-}\tau^+\nu_\tau$ and $B^0 \to D^{*-}\mu^+\nu_\mu$ branching fractions using three-prong τ-lepton decays", *Phys. Rev. Lett.* **120** (2018), no. 17, 171802, arXiv:1708.08856. doi:10.1103/PhysRevLett.120.171802.

[34] LHCb Collaboration, "Test of Lepton Flavor Universality by the measurement of the $B^0 \to D^{*-}\tau^+\nu_\tau$ branching fraction using three-prong τ decays", *Phys. Rev. D* **97** (2018), no. 7, 072013, arXiv:1711.02505. doi:10.1103/PhysRevD.97.072013.

[35] Heavy Flavor Averaging Group, HFLAV Collaboration, "Averages of b-hadron, c-hadron, and τ-lepton properties as of 2021", *Phys. Rev. D* **107** (2023), no. 5, 052008, arXiv:2206.07501. doi:10.1103/PhysRevD.107.052008.

[36] LHCb Collaboration, "Measurement of the ratios of branching fractions $\mathcal{R}(D^*)$ and $\mathcal{R}(D^0)$", arXiv:2302.02886.

[37] R. Puthumanaillam, "LHC Seminar: Measurement of $R(D*)$ with hadronic τ^+ decays at $\sqrt{s} = 13$ TeV by the LHCb collaboration". https://indico.cern.ch/event/1231797/, March, 2023.

[38] LHCb Collaboration, "Tests of lepton universality using $B^0 \to K^0_S\ell^+\ell^-$ and $B^+ \to K^{*+}\ell^+\ell^-$ decays", *Phys. Rev. Lett.* **128** (2022), no. 19, 191802, arXiv:2110.09501. doi:10.1103/PhysRevLett.128.191802.

[39] LHCb Collaboration, "Test of lepton universality in beauty-quark decays", *Nature Phys.* **18** (2022), no. 3, 277–282, arXiv:2103.11769. doi:10.1038/s41567-021-01478-8.

[40] LHCb Collaboration, "Measurement of lepton universality parameters in $B^+ \to K^+\ell^+\ell^-$ and $B^0 \to K^{*0}\ell^+\ell^-$ decays", *Phys. Rev. D* **108** (2023), no. 3, 032002, arXiv:2212.09153. doi:10.1103/PhysRevD.108.032002.

[41] P. Langacker, "The physics of heavy $Z^{'}$ gauge bosons", *Rev. Mod. Phys.* **81** (Aug, 2009) 1199–1228. doi:10.1103/RevModPhys.81.1199.

[42] T. G. Rizzo, "Z' phenomenology and the LHC", in *Theoretical Advanced Study Institute in Elementary Particle Physics: Exploring New Frontiers Using Colliders and Neutrinos*, pp. 537–575. 10, 2006. arXiv:hep-ph/0610104.

[43] S. P. MARTIN, "A SUPERSYMMETRY PRIMER", in *Perspectives on Supersymmetry*, pp. 1–98. WORLD SCIENTIFIC, jul, 1998.

[44] H. K. Dreiner, C. Luhn, and M. Thormeier, "What is the discrete gauge symmetry of the minimal supersymmetric standard model", *Physical Review D* **73** (apr, 2006). doi:10.1103/physrevd.73.075007.

[45] R. Barbier, C. Bérat, M. Besançon et al., "R-Parity-violating supersymmetry", *Physics Reports* **420** (nov, 2005) 1–195. doi:10.1016/j.physrep.2005.08.006.

[46] P. W. Graham, D. E. Kaplan, S. Rajendran et al., "Displaced Supersymmetry", *Journal of High Energy Physics* **2012** (jul, 2012). doi:10.1007/jhep07(2012)149.

[47] ATLAS Collaboration, "Search for lepton-flavor violation in different-flavor, high-mass final states in pp collisions at $\sqrt{s} = 13$ TeV with the ATLAS detector", *Phys. Rev. D* **98** (2018), no. 9, 092008, arXiv:1807.06573. doi:10.1103/PhysRevD.98.092008.

[48] CMS Collaboration, "Search for lepton flavour violating decays of heavy resonances and quantum black holes to an eμ pair in proton-proton collisions at $\sqrt{s} = 8$ TeV", *Eur. Phys. J. C* **76** (2016), no. 6, 317, arXiv:1604.05239. doi:10.1140/epjc/s10052-016-4149-y.

[49] T. Kaluza, "Zum Unitätsproblem der Physik", *Sitzungsber. Preuss. Akad. Wiss. Berlin (Math. Phys.)* **1921** (1921) 966–972, arXiv:1803.08616. doi:10.1142/S0218271818700017.

[50] N. Arkani-Hamed, S. Dimopoulos, G. R. Dvali et al., "Infinitely large new dimensions", *Phys. Rev. Lett.* **84** (2000) 586–589, arXiv:hep-th/9907209. doi:10.1103/PhysRevLett.84.586.

[51] G. L. Landsberg, "Black holes at future colliders and beyond: A Review", in *10th International Conference on Supersymmetry and Unification of Fundamental Interactions (SUSY02)*, pp. 562–577. 11, 2002. arXiv:hep-ph/0211043.

[52] P. Meade and L. Randall, "Black Holes and Quantum Gravity at the LHC", *JHEP* **05** (2008) 003, arXiv:0708.3017. doi:10.1088/1126-6708/2008/05/003.

[53] T. Banks and W. Fischler, "A Model for high-energy scattering in quantum gravity", arXiv:hep-th/9906038.

[54] X. Calmet, W. Gong, and S. D. H. Hsu, "Colorful quantum black holes at the LHC", *Phys. Lett. B* **668** (2008) 20–23, arXiv:0806.4605. doi:10.1016/j.physletb.2008.08.011.

[55] D. M. Eardley and S. B. Giddings, "Classical black hole production in high-energy collisions", *Phys. Rev. D* **66** (2002) 044011, arXiv:gr-qc/0201034. doi:10.1103/PhysRevD.66.044011.

[56] H. Yoshino and V. S. Rychkov, "Improved analysis of black hole formation in high-energy particle collisions", *Phys. Rev. D* **71** (2005) 104028, arXiv:hep-th/0503171. [Erratum: Phys.Rev.D 77, 089905 (2008)]. doi:10.1103/PhysRevD.71.104028.

[57] S. Davidson, B. Echenard, R. H. Bernstein et al., "Charged Lepton Flavor Violation", arXiv:2209.00142.

[58] MEG Collaboration, "Search for the lepton flavour violating decay $\mu^+ \to e^+\gamma$ with the full dataset of the MEG experiment", *Eur. Phys. J. C* **76** (2016), no. 8, 434, arXiv:1605.05081. doi:10.1140/epjc/s10052-016-4271-x.

[59] MEG II Collaboration, "The Search for $\mu^+ \to e^+\gamma$ with 10^{-14} Sensitivity: The Upgrade of the MEG Experiment", *Symmetry* **13** (2021), no. 9, 1591, arXiv:2107.10767. doi:10.3390/sym13091591.

[60] U. Bellgardt, G. Otter, R. Eichler et al., "Search for the decay $\mu+ \to e + e + e-$", *Nuclear Physics B* **299** (March, 1988) 1–6. doi:10.1016/0550-3213(88)90462-2.

[61] Mu3e Collaboration, "Technical design of the phase I Mu3e experiment", *Nucl. Instrum. Meth. A* **1014** (2021) 165679, arXiv:2009.11690. doi:10.1016/j.nima.2021.165679.

[62] The SINDRUM II Collaboration, W. Bertl, R. Engfer et al., "A search for $\mu - e$ conversion in muonic gold", *The European Physical Journal C* **47** (August, 2006) 337–346. doi:10.1140/epjc/s2006-02582-x.

[63] Mu2e Collaboration, "Mu2e Technical Design Report", arXiv:1501.05241. doi:10.2172/1172555.

[64] COMET Collaboration, "COMET Phase-I Technical Design Report", *PTEP* **2020** (2020), no. 3, 033C01, arXiv:1812.09018. doi:10.1093/ptep/ptz125.

[65] BaBar Collaboration, "Searches for Lepton Flavor Violation in the Decays $tau^\pm \to e^\pm\gamma$ and $\tau^\pm \to \mu^\pm\gamma$", *Phys. Rev. Lett.* **104** (2010) 021802, arXiv:0908.2381. doi:10.1103/PhysRevLett.104.021802.

[66] BaBar Collaboration, "Search for Lepton Flavor Violating Decays $\tau \to \ell K^0_s$ with the BABAR Experiment", *Phys. Rev. D* **79** (2009) 012004, arXiv:0812.3804. doi:10.1103/PhysRevD.79.012004.

[67] BaBar Collaboration, "Improved limits on lepton flavor violating tau decays to $\ell\phi$, $\ell\rho$, ℓK^* and $\ell\bar{K}^*$", *Phys. Rev. Lett.* **103** (2009) 021801, arXiv:0904.0339. doi:10.1103/PhysRevLett.103.021801.

[68] BaBar Collaboration, "Search for lepton flavor violating decays $tau^\pm \to \ell^\pm\omega(\ell = e, \mu)$", *Phys. Rev. Lett.* **100** (2008) 071802, arXiv:0711.0980. doi:10.1103/PhysRevLett.100.071802.

[69] BaBar Collaboration, "Limits on tau Lepton-Flavor Violating Decays in three charged leptons", *Phys. Rev. D* **81** (2010) 111101, arXiv:1002.4550. doi:10.1103/PhysRevD.81.111101.

[70] BaBar Collaboration, "Search for lepton-flavor and lepton-number violation in the decay $\tau^- \to \ell^\mp h^\pm h'^-$", *Phys. Rev. Lett.* **95** (2005) 191801, arXiv:hep-ex/0506066. doi:10.1103/PhysRevLett.95.191801.

[71] Belle Collaboration, "New Search for $\tau \to \mu\gamma$ and $\tau \to e\gamma$ Decays at Belle", *Phys. Lett. B* **666** (2008) 16–22, arXiv:0705.0650. doi:10.1016/j.physletb.2008.06.056.

[72] Belle Collaboration, "Search for lepton flavor violating τ^- decays into $\ell^-\eta$, $\ell^-\eta'$ and $\ell^-\pi^0$", *Phys. Lett. B* **648** (2007) 341–350, arXiv:hep-ex/0703009. doi:10.1016/j.physletb.2007.03.027.

[73] Belle Collaboration, "Search for Lepton Flavor Violating τ^- Decays into $\ell^- K_S^0$ and $\ell^- K_S^0 K_S^0$", *Phys. Lett. B* **692** (2010) 4–9, arXiv:1003.1183. doi:10.1016/j.physletb.2010.07.012.

[74] Belle Collaboration, "Search for Lepton-Flavor-Violating tau Decays into a Lepton and a Vector Meson", *Phys. Lett. B* **699** (2011) 251–257, arXiv:1101.0755. doi:10.1016/j.physletb.2011.04.011.

[75] Belle Collaboration, "Search for Lepton-Flavor-Violating tau Decays into Lepton and fo(980) Meson", *Phys. Lett. B* **672** (2009) 317–322, arXiv:0810.3519. doi:10.1016/j.physletb.2009.01.058.

[76] K. Hayasaka et al., "Search for Lepton Flavor Violating Tau Decays into Three Leptons with 719 Million Produced Tau+Tau- Pairs", *Phys. Lett. B* **687** (2010) 139–143, arXiv:1001.3221. doi:10.1016/j.physletb.2010.03.037.

[77] Belle Collaboration, "Search for Lepton-Flavor-Violating and Lepton-Number-Violating $\tau \to \ell hh'$ Decay Modes", *Phys. Lett. B* **719** (2013) 346–353, arXiv:1206.5595. doi:10.1016/j.physletb.2013.01.032.

[78] Belle Collaboration, "Search for lepton and baryon number violating τ^- decays into $\bar{\Lambda}\pi^-$ and $\Lambda\pi^-$", *Phys. Lett. B* **632** (2006) 51–57, arXiv:hep-ex/0508044. doi:10.1016/j.physletb.2005.10.024.

[79] Belle Collaboration, "Search for the Lepton Flavor Violating Decays B+→K+$\tau\pm\ell\mp$ (ℓ=e, μ) at Belle", *Phys. Rev. Lett.* **130** (2023), no. 26, 261802, arXiv:2212.04128. doi:10.1103/PhysRevLett.130.261802.

[80] LHCb Collaboration, "Search for the lepton flavour violating decay $\tau^- \to \mu^- \mu^+ \mu^-$", *JHEP* **02** (2015) 121, arXiv:1409.8548. doi:10.1007/JHEP02(2015)121.

[81] LHCb Collaboration, "Searches for violation of lepton flavour and baryon number in tau lepton decays at LHCb", *Phys. Lett. B* **724** (2013) 36–45, arXiv:1304.4518. doi:10.1016/j.physletb.2013.05.063.

[82] LHCb Collaboration, "Physics case for an LHCb Upgrade II - Opportunities in flavour physics, and beyond, in the HL-LHC era", arXiv:1808.08865.

[83] ATLAS Collaboration, "Prospects for lepton flavour violation measurements in $\tau \to 3\mu$ decays with the ATLAS detector at the HL-LHC",.

[84] CMS Collaboration, "The Phase-2 Upgrade of the CMS Muon Detectors",.

[85] OPAL Collaboration, "A Search for lepton flavor violating Z^0 decays", *Z. Phys. C* **67** (1995) 555–564. doi:10.1007/BF01553981.

[86] P. Abreu Et Al., "Search for lepton flavour number violating Z^0-decays", *Zeitschrift für Physik C Particles and Fields* **73** (January, 1997) 243–251. doi:10.1007/s002880050313.

[87] ATLAS Collaboration, "Search for the lepton flavor violating decay Z→eμ in pp collisions at $\sqrt{s}$ TeV with the ATLAS detector", *Phys. Rev. D* **90** (2014), no. 7, 072010, arXiv:1408.5774. doi:10.1103/PhysRevD.90.072010.

[88] ATLAS Collaboration, "Search for charged-lepton-flavour violation in Z-boson decays with the ATLAS detector", *Nature Phys.* **17** (2021), no. 7, 819–825, arXiv:2010.02566. doi:10.1038/s41567-021-01225-z.

[89] ATLAS Collaboration, "Search for lepton-flavor-violation in Z-boson decays with τ-leptons with the ATLAS detector", *Phys. Rev. Lett.* **127** (2022) 271801, arXiv:2105.12491. doi:10.1103/PhysRevLett.127.271801.

[90] ATLAS Collaboration, "Search for the Higgs boson decays $H \to ee$ and $H \to e\mu$ in pp collisions at $\sqrt{s} = 13$ TeV with the ATLAS detector", *Phys. Lett. B* **801** (2020) 135148, arXiv:1909.10235. doi:10.1016/j.physletb.2019.135148.

[91] CMS Collaboration, "Search for lepton-flavor violating decays of the Higgs boson in the $\mu\tau$ and eτ final states in proton-proton collisions at $\sqrt{s}$ = 13 TeV", *Phys. Rev. D* **104** (2021), no. 3, 032013, arXiv:2105.03007. doi:10.1103/PhysRevD.104.032013.

[92] CMS Collaboration, "Search for charged-lepton flavor violation in top quark production and decay in pp collisions at $\sqrt{s}$ = 13 TeV", *JHEP* **06** (2022) 082, arXiv:2201.07859. doi:10.1007/JHEP06(2022)082.

[93] CMS Collaboration, "Search for lepton-flavor violating decays of heavy resonances and quantum black holes to eμ final states in proton-proton collisions at $\sqrt{s} = 13$ TeV", *JHEP* **04** (2018) 073, arXiv:1802.01122. doi:10.1007/JHEP04(2018)073.

[94] CMS Collaboration, "Search for black holes and sphalerons in high-multiplicity final states in proton-proton collisions at $\sqrt{s} = 13$ TeV", *JHEP* **11** (2018) 042, arXiv:1805.06013. doi:10.1007/JHEP11(2018)042.

[95] CMS Collaboration, A. Lopes and M. L. Perrey, "FAQ-LHC The guide". https://cds.cern.ch/record/2809109, 2022.

[96] L. Evans and P. Bryant, "LHC Machine",. doi:10.1088/1748-0221/3/08/S08001.

[97] ATLAS Collaboration, "The ATLAS Experiment at the CERN Large Hadron Collider", *JINST* **3** (2008) S08003. doi:10.1088/1748-0221/3/08/S08003.

[98] CMS Collaboration, "The CMS Experiment at the CERN LHC", *JINST* **3** (2008) S08004. doi:10.1088/1748-0221/3/08/S08004.

[99] ALICE Collaboration, "The ALICE experiment at the CERN LHC", *JINST* **3** (2008) S08002. doi:10.1088/1748-0221/3/08/S08002.

[100] LHCb Collaboration, "The LHCb Detector at the LHC", *JINST* **3** (2008) S08005. doi:10.1088/1748-0221/3/08/S08005.

[101] C. Lefèvre, "The CERN accelerator complex. Complexe des accélérateurs du CERN". https://cds.cern.ch/record/1260465, Dec, 2008.

[102] CMS Collaboration, T. Sakuma, "Cutaway diagrams of CMS detector". https://cds.cern.ch/record/2665537, 2019.

[103] The Tracker Group Of The CMS Collaboration, "The CMS Phase-1 Pixel Detector Upgrade", 2020. doi:10.48550/ARXIV.2012.14304.

[104] CMS Collaboration, "CMS Technical Design Report for the Phase 1 Upgrade of the Hadron Calorimeter",. doi:10.2172/1151651.

[105] CMS HCAL Collaboration, "Design, performance, and calibration of CMS hadron-barrel calorimeter wedges", *Eur. Phys. J. C* **55** (2008), no. 1, 159–171. doi:10.1140/epjc/s10052-008-0573-y.

[106] CMS Muon Collaboration, "GEM detectors for the CMS endcap muon system: status of three new detector stations", *JINST* **18** (2023), no. 07, C07006, arXiv:2303.17244. doi:10.1088/1748-0221/18/07/C07006.

[107] CMS Collaboration, "CMS reconstruction improvement for the muon tracking by the RPC chambers", *PoS* **RPC2012** (2012) 045, arXiv:1209.2646. doi:10.1088/1748-0221/8/03/T03001.

[108] CMS Collaboration, "Calibration of the CMS Drift Tube Chambers and Measurement of the Drift Velocity with Cosmic Rays", *JINST* **5** (2010) T03016, arXiv:0911.4895. doi:10.1088/1748-0221/5/03/T03016.

[109] CMS Collaboration, "Performance of the CMS muon detector and muon reconstruction with proton-proton collisions at $\sqrt{s} = 13$ TeV", *JINST* **13** (2018), no. 06, P06015, arXiv:1804.04528. doi:10.1088/1748-0221/13/06/P06015.

[110] CMS Collaboration, "CMS Trigger Performance", *EPJ Web Conf.* **182** (2018) 02037. doi:10.1051/epjconf/201818202037.

[111] A. Nowack, "CMS tier structure and operation of the experiment-specific tasks in Germany", *Journal of Physics: Conference Series* **119** (07, 2008) 072024. doi:10.1088/1742-6596/119/7/072024.

[112] A. Sirunyan, A. Tumasyan, W. Adam et al., "Particle-flow reconstruction and global event description with the CMS detector", *Journal of Instrumentation* **12** (Oct, 2017) P10003–P10003. doi:10.1088/1748-0221/12/10/p10003.

[113] CMS Collaboration, "Description and performance of track and primary-vertex reconstruction with the CMS tracker", *JINST* **9** (2014), no. 10, P10009, arXiv:1405.6569. doi:10.1088/1748-0221/9/10/P10009.

[114] P. Billoir, "Progressive track recognition with a Kalman-like fitting procedure",. doi:10.1016/0010-4655(89)90249-X.

[115] P. L. DeVries, J. E. Hasbun, and P. L. DeVries, "A first course in computational physics". Jones and Bartlett Publishers, 2nd ed edition, 2011. OCLC: ocn437300527.

[116] CMS Collaboration, "Performance of Electron Reconstruction and Selection with the CMS Detector in Proton-Proton Collisions at $\sqrt{s} = 8$ TeV", *JINST* **10** (2015), no. 06, P06005, arXiv:1502.02701. doi:10.1088/1748-0221/10/06/P06005.

[117] W. Adam, R. Frühwirth, A. Strandlie et al., "Reconstruction of electrons with the Gaussian-sum filter in the CMS tracker at the LHC", *Journal of Physics G: Nuclear and Particle Physics* **31** (jul, 2005) N9–N20. doi:10.1088/0954-3899/31/9/n01.

[118] H. Bethe and W. Heitler, "On the Stopping of fast particles and on the creation of positive electrons", *Proc. Roy. Soc. Lond. A* **146** (1934) 83–112. doi:10.1098/rspa.1934.0140.

[119] CMS Collaboration, "Search for physics beyond the standard model in dilepton mass spectra in proton-proton collisions at $\sqrt{s} = 8$ TeV", *JHEP* **04** (2015) 025, arXiv:1412.6302. doi:10.1007/JHEP04(2015)025.

[120] CMS Collaboration, "Electron and photon reconstruction and identification with the CMS experiment at the CERN LHC", *JINST* **16** (2021), no. 05, P05014, arXiv:2012.06888. doi:10.1088/1748-0221/16/05/P05014.

[121] CMS EGamma POG, "HEEP Electron ID and isolation". https://twiki.cern.ch/twiki/bin/view/CMS/HEEPElectronIdentificationRun2, 2022. Accessed: (2023-07-19).

[122] CMS EGamma POG, "EGamma RunII Recommendations". https://twiki.cern.ch/twiki/bin/view/CMS/EgammaRunIIRecommendations, 2022. Accessed: (2023-07-19).

[123] CMS Collaboration, "Performance of the reconstruction and identification of high-momentum muons in proton-proton collisions at $\sqrt{s} = 13$ TeV", *JINST* **15** (2020), no. 02, P02027, arXiv:1912.03516. doi:10.1088/1748-0221/15/02/P02027.

[124] CMS collaboration, "Performance of CMS muon reconstruction in pp collision events at $\sqrt{s}$ = 7 TeV", *Journal of Instrumentation* **7** (oct, 2012) P10002–P10002. doi:10.1088/1748-0221/7/10/p10002.

[125] CMS Collaboration, "Performance of the reconstruction and identification of high-momentum muons in proton-proton collisions at $\sqrt{s} = 13$ TeV", *JINST* **15** (2020), no. 02, P02027, arXiv:1912.03516. doi:10.1088/1748-0221/15/02/P02027.

[126] M. Cacciari, G. P. Salam, and G. Soyez, "The anti-k_t jet clustering algorithm", *Journal of High Energy Physics* **2008** (apr, 2008) 063–063. doi:10.1088/1126-6708/2008/04/063.

[127] M. Cacciari, G. P. Salam, and G. Soyez, "FastJet User Manual", *Eur. Phys. J. C* **72** (2012) 1896, arXiv:1111.6097. doi:10.1140/epjc/s10052-012-1896-2.

[128] S. Catani, Y. L. Dokshitzer, M. H. Seymour et al., "Longitudinally invariant K_t clustering algorithms for hadron hadron collisions", *Nucl. Phys. B* **406** (1993) 187–224. doi:10.1016/0550-3213(93)90166-M.

[129] Y. L. Dokshitzer, G. D. Leder, S. Moretti et al., "Better jet clustering algorithms", *JHEP* **08** (1997) 001, arXiv:hep-ph/9707323. doi:10.1088/1126-6708/1997/08/001.

[130] CMS Collaboration, "Identification of hadronic tau lepton decays using a deep neural network", *JINST* **17** (2022) P07023, arXiv:2201.08458. doi:10.1088/1748-0221/17/07/P07023.

[131] CMS Collaboration, "Performance of reconstruction and identification of τ leptons decaying to hadrons and ν_τ in pp collisions at $\sqrt{s} = 13$ TeV", *JINST* **13** (2018), no. 10, P10005, arXiv:1809.02816. doi:10.1088/1748-0221/13/10/P10005.

[132] Y. Lecun, L. Bottou, Y. Bengio et al., "Gradient-based learning applied to document recognition", *Proceedings of the IEEE* **86** (1998), no. 11, 2278–2324. doi:10.1109/5.726791.

[133] CMS Collaboration, "Performance of missing transverse momentum reconstruction in proton-proton collisions at $\sqrt{s} = 13$ TeV using the CMS detector", *JINST* **14** (2019), no. 07, P07004, arXiv:1903.06078. doi:10.1088/1748-0221/14/07/P07004.

[134] D. Beghin, B. Clerbaux, B. Dorney et al., "Search for lepton-flavor violating decays of heavy resonances and quantum black holes to $e\mu$, $e\tau$ and $\mu\tau$ final states in proton-proton collisions at $\sqrt{s} = 13$ TeV with 2016, 2017 and 2018 data". CMS Internal note CMS-AN-2018/169, 2021.

[135] CMS PdmV Group, "Physics Data And Monte Carlo Validation (PdmV)". https://twiki.cern.ch/twiki/bin/view/CMS/PdmV, 2022.

[136] CMS PdmV Group, "Lumi Recommendations Run2". https://twiki.cern.ch/twiki/bin/view/CMS/LumiRecommendationsRun2, 2022.

[137] G. Boudoul, G. Franzoni, A. Norkus et al., "Monte Carlo Production Management at CMS", *J. Phys. Conf. Ser.* **664** (2015), no. 7, 072018. doi:10.1088/1742-6596/664/7/072018.

[138] J. Alwall, A. Ballestrero, P. Bartalini et al., "A standard format for Les Houches Event Files", *Computer Physics Communications* **176** (Feb, 2007) 300–304. doi:10.1016/j.cpc.2006.11.010.

[139] J. Allison et al., "Recent developments in Geant4", *Nucl. Instrum. Meth. A* **835** (2016) 186–225. doi:10.1016/j.nima.2016.06.125.

[140] G. Petrucciani, A. Rizzi, and C. Vuosalo, "Mini-AOD: A New Analysis Data Format for CMS", *Journal of Physics: Conference Series* **664** (Dec, 2015) 072052. doi:10.1088/1742-6596/664/7/072052.

[141] CMS Collaboration, "NANOAOD: a new compact event data format in CMS", *EPJ Web Conf.* **245** (2020) 06002. doi:10.1051/epjconf/202024506002.

[142] S. Frixione, P. Nason, and C. Oleari, "Matching NLO QCD computations with Parton Shower simulations: the POWHEG method", *JHEP* **11** (2007) 070, arXiv:0709.2092. doi:10.1088/1126-6708/2007/11/070.

[143] S. Alioli, P. Nason, C. Oleari et al., "A general framework for implementing NLO calculations in shower Monte Carlo programs: the POWHEG BOX", *JHEP* **06** (2010) 043, arXiv:1002.2581. doi:10.1007/JHEP06(2010)043.

[144] P. Nason, "A New method for combining NLO QCD with shower Monte Carlo algorithms", *JHEP* **11** (2004) 040, arXiv:hep-ph/0409146. doi:10.1088/1126-6708/2004/11/040.

[145] S. Frixione, P. Nason, and G. Ridolfi, "A Positive-weight next-to-leading-order Monte Carlo for heavy flavour hadroproduction", *JHEP* **09** (2007) 126, arXiv:0707.3088. doi:10.1088/1126-6708/2007/09/126.

[146] S. Alioli, P. Nason, C. Oleari et al., "NLO single-top production matched with shower in POWHEG: s- and t-channel contributions", *JHEP* **09** (2009) 111, arXiv:0907.4076. [Erratum: JHEP 02, 011 (2010)]. doi:10.1088/1126-6708/2009/09/111.

[147] E. Re, "Single-top Wt-channel production matched with parton showers using the POWHEG method", *Eur. Phys. J. C* **71** (2011) 1547, arXiv:1009.2450. doi:10.1140/epjc/s10052-011-1547-z.

[148] T. Melia, P. Nason, R. Rontsch et al., "W+W-, WZ and ZZ production in the POWHEG BOX", *JHEP* **11** (2011) 078, arXiv:1107.5051. doi:10.1007/JHEP11(2011)078.

[149] T. Sjöstrand, S. Ask, J. R. Christiansen et al., "An introduction to PYTHIA 8.2", *Computer Physics Communications* **191** (Jun, 2015) 159–177. doi:10.1016/j.cpc.2015.01.024.

[150] M. Czakon, D. Heymes, A. Mitov et al., "Top-pair production at the LHC through NNLO QCD and NLO EW", *Journal of High Energy Physics* **2017** (oct, 2017). doi:10.1007/jhep10(2017)186.

[151] J. Alwall, R. Frederix, S. Frixione et al., "The automated computation of tree-level and next-to-leading order differential cross sections, and their matching to parton shower simulations", *JHEP* **07** (2014) 079, arXiv:1405.0301. doi:10.1007/JHEP07(2014)079.

[152] S. Kallweit, J. M. Lindert, S. Pozzorini et al., "NLO QCD+EW predictions for $2\ell 2\nu$ diboson signatures at the LHC", *Journal of High Energy Physics* **2017** (nov, 2017). doi:10.1007/jhep11(2017)120.

[153] F. Campanario, C. Englert, S. Kallweit et al., "NLO QCD corrections to WZ+jet production with leptonic decays", *Journal of High Energy Physics* **2010** (jul, 2010). doi:10.1007/jhep07(2010)076.

[154] F. Cascioli, T. Gehrmann, M. Grazzini et al., "ZZ production at hadron colliders in NNLO QCD", *Physics Letters B* **735** (jul, 2014) 311–313. doi:10.1016/j.physletb.2014.06.056.

[155] E. L. Berger, J. Gao, C.-P. Yuan et al., "NNLO QCD corrections to t-channel single top quark production and decay", *Physical Review D* **94** (oct, 2016). doi:10.1103/physrevd.94.071501.

[156] A. Andonov, A. B. Arbuzov, S. G. Bondarenko et al., "NLO QCD corrections to Drell-Yan processes in the SANC framework", *Physics of Atomic Nuclei* **73** (oct, 2010) 1761–1769. doi:10.1134/s106377881010011x.

[157] CMS Collaboration, "Jet→Tau Misidentification Probability with 2016 pp collision data at $\sqrt{s}$=13 TeV". https://cds.cern.ch/record/2282910, 2017.

[158] CMS Collaboration, "Extraction and validation of a new set of CMS PYTHIA8 tunes from underlying-event measurements", *Eur. Phys. J. C* **80** (2020), no. 1, 4, arXiv:1903.12179. doi:10.1140/epjc/s10052-019-7499-4.

[159] A. Buckley, J. Ferrando, S. Lloyd et al., "LHAPDF6: parton density access in the LHC precision era", *Eur. Phys. J. C* **75** (2015) 132, arXiv:1412.7420. doi:10.1140/epjc/s10052-015-3318-8.

[160] A. Belyaev, N. D. Christensen, and A. Pukhov, "CalcHEP 3.4 for collider physics within and beyond the Standard Model", *Computer Physics Communications* **184** (Jul, 2013) 1729–1769. doi:10.1016/j.cpc.2013.01.014.

[161] J. Pumplin, D. R. Stump, J. Huston et al., "New Generation of Parton Distributions with Uncertainties from Global QCD Analysis", *Journal of High Energy Physics* **2002** (Jul, 2002) 012–012. doi:10.1088/1126-6708/2002/07/012.

[162] H. K. Dreiner, S. Grab, M. Krämer et al., "Supersymmetric NLO QCD corrections to resonant slepton production and signals at the Fermilab Tevatron and the CERN LHC", *Physical Review D* **75** (Feb, 2007). doi:10.1103/physrevd.75.035003.

[163] A. Güth, "Searches for charged lepton flavour violation involving final states with an electron / muon pair in pp collisions at the CMS detector". Dissertation, RWTH Aachen University, Aachen, 2017. Veröffentlicht auf dem Publikationsserver der RWTH Aachen University; Dissertation, RWTH Aachen University, 2017, https://publications.rwth-aachen.de/record/707885.

[164] D. M. Gingrich, "Monte Carlo event generator for black hole production and decay in proton–proton collisions – QBH version 1.02", *Computer Physics Communications* **181** (Nov, 2010) 1917–1924. doi:10.1016/j.cpc.2010.07.027.

[165] E. Boos et al., "Generic User Process Interface for Event Generators", in *2nd Les Houches Workshop on Physics at TeV Colliders*. 9, 2001. arXiv:hep-ph/0109068.

[166] C. Bravo and J. Hauser, "BaryoGEN, a Monte Carlo generator for sphaleron-like transitions in proton-proton collisions", *Journal of High Energy Physics* **2018** (nov, 2018). doi:10.1007/jhep11(2018)041.

[167] S. Wiedenbeck, "Sphaleron cross section calculator". https://github.com/swiedenb/sphaleronxs, 2022.

[168] CMS Collaboration, "Pileup mitigation at CMS in 13 TeV data", *JINST* **15** (2020), no. 09, P09018, arXiv:2003.00503. doi:10.1088/1748-0221/15/09/P09018.

[169] CMS Collaboration, "Measurement of the inelastic proton-proton cross section at $\sqrt{s} = 13$ TeV", *JHEP* **07** (2018) 161, arXiv:1802.02613. doi:10.1007/JHEP07(2018)161.

[170] CMS Collaboration, "Performance of the CMS Level-1 trigger in proton-proton collisions at $\sqrt{s} = 13$ TeV", *JINST* **15** (2020), no. 10, P10017, arXiv:2006.10165. doi:10.1088/1748-0221/15/10/P10017.

[171] CMS JETMET Group, "Reweighting recipe to emulate Level 1 ECAL prefiring.". https://twiki.cern.ch/twiki/bin/viewauth/CMS/L1ECALPrefiringWeightRecipe. internal CMS Twiki Page.

[172] CMS Muon POG, "Muon Physics Object Group". https://twiki.cern.ch/twiki/bin/viewauth/CMS/MuonPOG, 2023.

[173] CMS Collaboration, "Performance of the CMS muon trigger system in proton-proton collisions at $\sqrt{s} = 13$ TeV", *JINST* **16** (2021) P07001, arXiv:2102.04790. doi:10.1088/1748-0221/16/07/P07001.

[174] CMS Muon POG, "Muon recommendations for 2016 Legacy data and Monte Carlo". https://twiki.cern.ch/twiki/bin/view/CMS/MuonLegacy2016, 2022.

[175] CMS Muon POG, "Muon recommendations for 2017 Legacy data and Monte Carlo". https://twiki.cern.ch/twiki/bin/view/CMS/MuonLegacy2017, 2022.

[176] CMS Muon POG, "Muon recommendations for 2018 Legacy data and Monte Carlo". https://twiki.cern.ch/twiki/bin/view/CMS/MuonLegacy2017, 2022.

[177] CMS collaboration, "Determination of jet energy calibration and transverse momentum resolution in CMS", *Journal of Instrumentation* **6** (nov, 2011) P11002–P11002. doi:10.1088/1748-0221/6/11/p11002.

[178] J. Damgov and L. Thomas, "MET report". https://indico.cern.ch/event/759372/, September, 2018.

[179] CMS Exotica Working Group, "EXOTICA". https://twiki.cern.ch/twiki/bin/view/CMS/EXOTICA.

[180] M. Czakon and A. Mitov, "NNLO+NNLL top-quark-pair cross sections ATLAS-CMS recommended predictions for top-quark-pair cross sections using the Top++v2.0 program". https://twiki.cern.ch/twiki/bin/view/LHCPhysics/TtbarNNLO#Updated_reference_cross_sections.

[181] T. Gehrmann, M. Grazzini, S. Kallweit et al., "W^+W^- Production at Hadron Colliders in Next to Next to Leading Order QCD", *Physical Review Letters* **113** (nov, 2014). doi:10.1103/physrevlett.113.212001.

[182] CMS Monte Carlo Generator Group , "Standard Model Cross Sections for CMS at 13 TeV.,". https://twiki.cern.ch/twiki/bin/viewauth/CMS/StandardModelCrossSectionsat13TeV. internal CMS Twiki Page.

[183] N. Kidonakis and N. Yamanaka, "Higher-order corrections for tW production at high-energy hadron colliders", *JHEP* **05** (2021) 278, arXiv:2102.11300. doi:10.1007/JHEP05(2021)278.

[184] S. Kallweit, J. M. Lindert, S. Pozzorini et al., "NLO QCD+EW predictions for $2\ell 2\nu$ diboson signatures at the LHC", *JHEP* **11** (2017) 120, arXiv:1705.00598. doi:10.1007/JHEP11(2017)120.

[185] J. Butterworth et al., "PDF4LHC recommendations for LHC Run II", *J. Phys. G* **43** (2016) 023001, arXiv:1510.03865. doi:10.1088/0954-3899/43/2/023001.

[186] G. Cowan, "Statistical data analysis". Oxford science publications. Clarendon Press ; Oxford University Press, 1998.

[187] D. D. L. Minh and D. L. P. Minh, "Understanding the Hastings Algorithm", *Communications in Statistics - Simulation and Computation* **44** (2015), no. 2, 332–349, arXiv:https://doi.org/10.1080/03610918.2013.777455. doi:10.1080/03610918.2013.777455.

[188] W. M. Bolstad, "Understanding Computational Bayesian Statistics". Wiley, 1st edition, 2009.

[189] CMS Collaboration, "CMS Higgs Combination toolkit". https://github.com/cms-analysis/HiggsAnalysis-CombinedLimit/.

[190] L. Moneta, K. Belasco, K. Cranmer et al., "The RooStats Project", 2010. doi:10.48550/ARXIV.1009.1003.

[191] CMS Collaboration, "CMS Higgs Combination toolkit manual". http://cms-analysis.github.io/HiggsAnalysis-CombinedLimit/.

[192] R. E. Kass and L. Wasserman, "The Selection of Prior Distributions by Formal Rules", *Journal of the American Statistical Association* **91** (1996), no. 435, 1343–1370, arXiv:https://www.tandfonline.com/doi/pdf/10.1080/01621459.1996.10477003. doi:10.1080/01621459.1996.10477003.

[193] L. ATLAS Collaboration, CMS Collaboration, "Procedure for the LHC Higgs boson search combination in Summer 2011", technical report, CERN, Geneva, 2011.

[194] J. S. Conway, "Incorporating Nuisance Parameters in Likelihoods for Multisource Spectra", 2011. doi:10.48550/ARXIV.1103.0354.

[195] R. J. Barlow and C. Beeston, "Fitting using finite Monte Carlo samples", *Comput. Phys. Commun.* **77** (1993) 219–228. doi:10.1016/0010-4655(93)90005-W.

[196] M. Pharr, W. Jakob, and G. Humphreys, "Monte Carlo Integration", in *Physically Based Rendering*, pp. 747–802. Elsevier, 2017.

[197] N. Metropolis, A. W. Rosenbluth, M. N. Rosenbluth et al., "Equation of State Calculations by Fast Computing Machines",. doi:10.1063/1.1699114.

[198] W. K. Hastings, "Monte Carlo sampling methods using Markov chains and their applications",. doi:10.1093/biomet/57.1.97.

[199] G. Cowan, K. Cranmer, E. Gross et al., "Asymptotic formulae for likelihood-based tests of new physics", *Eur. Phys. J. C* **71** (2011) 1554, arXiv:1007.1727. [Erratum: Eur.Phys.J.C 73, 2501 (2013)]. doi:10.1140/epjc/s10052-011-1554-0.

[200] ATLAS Collaboration, "Search for lepton-flavour violation in high-mass dilepton final states using 139 fb^{-1} of pp collisions at $\sqrt{s} = 13$ TeV with the ATLAS detector", arXiv:2307.08567.

[201] S. Erdweg, "Search for charged lepton flavour violation with CMS". Dissertation, RWTH Aachen University, Aachen, 2018. Veröffentlicht auf dem Publikationsserver der RWTH Aachen University; Dissertation, RWTH Aachen University, 2018, https://publications.rwth-aachen.de/record/723166.

[202] J. Sato and M. Yamanaka, "A way to crosscheck μ-e conversion in the case of no signals of $\mu \to e\gamma$ and $\mu \to 3e$", *Phys. Rev. D* **91** (2015) 055018, arXiv:1409.1697. doi:10.1103/PhysRevD.91.055018.

[203] G. Apollinari, I. Béjar Alonso, O. Brüning et al., "High-Luminosity Large Hadron Collider (HL-LHC): Technical Design Report V. 0.1",. doi:10.23731/CYRM-2017-004.

Danksagung

An dieser Stelle möchte ich mich bei allen Menschen bedanken, die mich während der Anfertigung dieser Dissertation unterstützt haben.

Zuerst möchte ich Prof. Thomas Hebbeker danken, der mir die Möglichkeit gegeben hat am III. Physikalischen Institut A meine Dissertation anzufertigen. Ich habe nunmehr meine gesamte akademische Laufbahn in diesem Institut verbracht und in diesen acht Jahren viel erlebt und gelernt. Die Zeit war von sehr vielen Freiheiten und einer äußerst angenehmen Atmosphäre geprägt. Hierfür möchte ich mich sehr herzlich bedanken.

Außerdem möchte ich mich bei Prof. Oliver Pooth bedanken, der sich dazu bereit erklärt hat, meine Arbeit als Zweitgutachter zu betreuen.

Zusätzlicher Dank gilt Arnd Meyer, welcher immer Zeit und ein offenes Ohr für Fragen und Diskussionen hatte und mit seiner Ruhe und Übersicht stets auch in stressigen Situationen eine Lösung parat hatte. Ebenso möchte ich mich bei Kerstin Hoepfner bedanken, welche mich in meiner gesamten Zeit am Institut stets mit ihrem Wissen und ihrem Engagement unterstützt hat.

Ein großer Dank gilt auch Christoph Schuler, mit dem ich die meiste Zeit ein Bürozimmer teilen durfte. Neben der Entwicklung unserer Analyse waren auch Diskussionen und Späße abseits der Physik immer interessant und unterhaltsam. Ich möchte mich auch bei Swagata Mukherjee bedanken. Unsere gemeinsame Arbeit, sowohl für diese Abschlussarbeit, als auch für die W′ Analyse und DT-Calibration, habe ich immer als sehr angenehm und motivierend empfunden. Vielen Dank auch an Markus Merschmeyer, Melanie Strothotte und Sabine Eicker für ihre Hilfestellung bei organisatorischen und bürokratischen Anliegen.

Selbstverständlich möchte ich mich auch bei allen anderen aktuellen und ehemaligen Mitgliedern des Instituts bedanken. Sie haben erst dafür gesorgt, dass die Arbeitsatmosphäre eine derart angenehme war. Namentlich möchte ich mich bei Jonas Roemer, Valentina Sarkisovi, Fabian Nowotny, Francesco Ivone und Shawn Zaleski bedanken, die immer Zeit für Fragen und Diskussionen hatten. Insbesondere Christoph, Jonas und Valentina danke ich für das Korrekturlesen meiner Arbeit. Außerdem bedanke ich mich bei Thomas Kress, Andreas Nowack und der gesamten IT-Abteilung, ohne die das Erstellen dieser Arbeit nicht möglich gewesen wäre.

Zusätzlich möchte ich mich bei den weiteren Mitgliedern der LFV Arbeitsgruppe bedanken.

Ein großer Dank gilt meiner Familie, meinen Eltern Frank und Konny Wiedenbeck, meiner Schwester Angela Wiedenbeck, Matthias Daun und meiner Tante und meinem Onkel Gaby und Ingo Kupschus. Sie haben mich in der gesamten Zeit, während des Studiums und anschließend während meiner Zeit als Doktorand, immer unterstützt und durch interessierte Fragen auch stets motiviert. Ein sehr großer Dank gilt Ana Andrade. Während der zeitweise sehr schwierigen Zeit der Anfertigung dieser Arbeit hat sie mich stets unterstützt und ein Umfeld erschaffen, in dem ich die Arbeit mit der nötigen Entspanntheit fertigstellen konnte. Zu guter Letzt bedanke ich mich bei meinen Freunden, die immer für die nötige Ablenkung gesorgt haben.